UNIVERSITÀ
DEGLI STUDI
DI BRESCIA

DIPARTIMENTO DI INGEGNERIA MECCANICA E INDUSTRIALE

Dottorato di Ricerca in Ingegneria Meccanica e Industriale
DRIMI
TeSE – Energy, Fluid & Thermal, and Manufacturing Systems and
Technologies

Settore Scientifico Disciplinare (SSD): ING-IND/16
CICLO XXXV

Analysis, optimization, FE simulation of micro-cutting processes and integration between Machining and Additive Manufacturing

Dottorando:
Ing. Andrea Abeni

Supervisore: Prof. Aldo Attanasio

2021/2022

Indice

Obiettivo della tesi

La seguente Tesi di Dottorato riguarda i processi di Micro-Machining (MM) applicati su materiali ottenuti per fabbricazione additiva. I processi MM sono un insieme di tecnologie di produzione utilizzate per fabbricare componenti o realizzare features di piccole dimensioni. In generale, i processi di taglio sono caratterizzati da un'interazione meccanica tra un pezzo e un utensile che avviene lungo una determinata traiettoria. Il contatto determina una rottura del materiale lungo un percorso definito, ottenendo diverse forme del pezzo. Più precisamente, la denominazione di microlavorazione indica solo le lavorazioni di taglio eseguite utilizzando un utensile di diametro inferiore a 1 mm. La riduzione della scala dimensionale del processo introduce alcune criticità non presenti negli analoghi processi su scala convenzionale, come l'effetto dimensionale, la formazione di bave, la rapida usura dell'utensile, le forze di taglio superiori alle attese e l'eccentricità del moto dell'utensile. Negli ultimi decenni, diversi ricercatori hanno affrontato problemi relativi alla microlavorazione, ma pochi di loro si sono concentrati sulla lavorabilità dei materiali prodotti per Additive Manufacturing (AM).

L'AM è un insieme di processi di fabbricazione strato per strato che possono essere impiegati con successo utilizzando polimeri, ceramica e metalli. L'AM dei metalli si sta rapidamente diffondendo nella produzione industriale trovando applicazioni in diversi rami, come l'industria aerospaziale e biomedica. D'altro canto, la qualità del prodotto finale non è comparabile con gli standard ottenibili mediante i metodi convenzionali di rimozione del materiale. Lo svantaggio principale dei componenti realizzati mediante AM è la bassa qualità della finitura superficiale e l'elevata rugosità; pertanto, sono solitamente necessari ulteriori trattamenti superficiali post-processo per adeguare le superfici del prodotto ai requisiti di integrità superficiale.

L'integrazione tra le due tecnologie manifatturiere offre opportunità rilevanti, ma la necessità di ulteriori studi e indagini è evidenziata dalla mancanza di pubblicazioni su questo argomento. Questa ricerca mira ad esplorare diversi problemi connessi alla microlavorazione di leghe metalliche prodotte mediante AM. Le prove sperimentali sono state eseguite utilizzando il centro di lavoro ultrapreciso a 5 assi "KERN Pyramid Nano", mentre i campioni AM sono stati forniti da aziende e gruppi di ricerca. L'attrezzatura sperimentale è stata predisposta per eseguire la micro-fresatura e per monitorare il processo in linea misurando la forza di taglio. Il comportamento di rimozione del materiale è stato studiato e descritto per mezzo di modelli analitici e simulazioni FEM. I metodi FE sono stati utilizzati anche per eseguire un confronto tra le forze di taglio previste e i carichi sperimentali, con lo scopo finale di affinare la legge di flusso dei materiali lavorati. La ricerca futura sarà focalizzata sulla simulazione FE dell'usura dell'utensile e dell'integrità della superficie del pezzo.

Thesis purpose

This thesis is focused on Micro-Machining (MM) processes applied on Additively Manufactured parts. MM processes are a class of manufacturing technology designed to produce small size components. In general, cutting processes are characterized by a mechanical interaction between a workpiece and a tool. The contact determines a material breakage along a defined path, obtaining different workpiece shapes. More specifically, the micro-machining designation indicates only the cutting processes performed by using a tool with a diameter lower than 1 mm. The reduction of the process scale introduces some critical issues, such as size effect, burr formation, rapid tool wear, higher than expected cutting forces and tool run-out. In the last decades, several researchers have tackled micro-machining related issues, but few of them focused on workability of Additive Manufactured materials.

Additive Manufacturing (AM) is a collection of layer-by-layer building processes which can be successfully employed using polymers, ceramics and metals. AM of metals is rapidly spreading throughout the industrial manufacturing finding applications in several branches, such as aerospace and biomedical industries. Moreover, the final product quality is not comparable with the standards achievable through the conventional subtractive material removal methods. The main drawback of additively manufactured components in metals is the low quality of the surface finish and the high surface roughness, therefore further post-process surface treatments are usually required to finish and to refine the surfaces of the build product.

The embedding between the two technologies offers relevant opportunities, but the necessity of further studies and investigation is highlighted by the lack of publication about this topic. This research aimed to explore several micro-machining issues with regards to Additive Manufactured metals. Experimental tests were performed by using the ultraprecision 5-axes machining center "KERN Pyramid Nano", while the AM samples were provided by companies and research groups. The experimental equipment was set-up to perform micro-milling and to monitor the process online by measuring the cutting force. The material removal behavior was investigated and described by means of analytical models and FEM simulations. FE methods were employed also to perform a comparison between the predicted cutting forces and the experimental loads, with the final purpose of refining the flow stress law of the machined materials. The future research will be focused on the FE simulation of the tool wear and the workpiece surface integrity by means of specific subroutines.

Summary

In this summary, a brief introduction to the research project and its industrial framework will be discussed. The main objectives of the thesis will be described, and the research activities will be summarized in a flowchart. The structure of the thesis will be described by anticipating the contents of each chapter.

Introduction

AM of metals opens strategic opportunities for high-value industrial sectors, such as aerospace or biomanufacturing. AM allows to overcome the traditional limits of the conventional fabrication methods, also promoting integration and more functionality of components and systems. The sustainability of AM is favored by the possibility to minimize the material usage eliminating the scraps and waste. In addition, the cost for consumable tool and the constraints about the components design are lower for AM then conventional processes. Among the AM techniques for metallic alloys, Laser Based Powder Bed Fusion (LB-PBF) and Beam Based Powder Bed Fusion (BB-PBF) are the most widespread. The components manufactured with these techniques usually requires additional machining operations due to the poor surface quality. The machinability of the samples manufactured via AM must be investigated since the LB-PBF and BB-PBF determines meaningful differences about the microstructure and the mechanical properties of the parts if compared with conventional techniques of material production. The criticalities of turning, milling, and drilling become more relevant as the size of the machining becomes lower. The chip formation mechanism in micro-machining is affected by specific phenomena which have a meaningful influence on tool wear, cutting forces and surface integrity. More in detail, surface roughness and residual stress are strictly related to the machining processes. The chip formation mechanism in turn is affected by the AM process, such as the building direction and the printing settings. It depends also on the post-process thermo-mechanical treatments.

Industrial issues

The demand for miniaturized end-products (examples are visible in **Figure 1**) has been continuously increasing in biomedical, automotive, aerospace, and electronics industries **[1]**. Alting et al. **[2]** defined the miniaturized components as "products whose functional features or at least one dimension is in the order of µm. The products are usually characterized by a high degree of integration of functionalities and components." This definition goes beyond the geometrical and size aspects and involves the concept of integration. Microproducts are frequently characterized by an integration of functions, an integrations of different functioning principles and an integration of intelligence in terms of processing and control of information and data.

Figure 1. MEMS devices compared to a matchstick and a dime coin.

The elevated economic efficiency, accuracy and flexibility guaranteed by the micro-cutting processes justifies their elevated wide spreading [3]. Production system cannot be merely downscaled from macro-industry, but specific processes and materials must be developed. The size reduction carries a huge number of specific issues and effects compared to conventional machining. The specific properties of AM components introduce a further element of variability which must be investigated. Controlling all these aspects is crucial to achieve high-quality products and economic efficiency. The influence of these aspects on the process must be estimated and limited to ensure robust micro-machining.

When the uncut chip thickness becomes equal or smaller than the tool edge radius, extremely negative rake angle values can be promoted [4]. This phenomenon not only increase cutting forces but can also influence the chip formation mechanism. In fact, if the depth of the cut does not reach a specific value, the work material will not be cut. The material compression in this undesired condition is know how ploughing effect [5]. In ploughing regime, the tool scrapes the workpiece without chip formation. Moreover, the ploughing process has a direct impact on the final surface roughness and the residual stress of the machined material, influencing the achievable accuracy of the components.
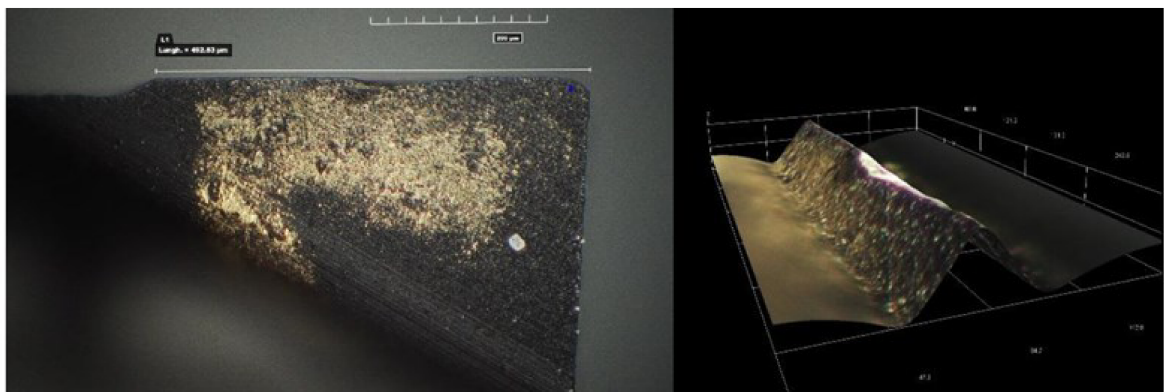
.

Figure 2. An example of tool damage, (a) a 2D image and a (b) 3D picture.

4

Another crucial theme is the tool run-out. This phenomenon occurs due to the sum of the geometrical displacements of the tool axis, the spindle axis, and the tool-holder axis from the ideal axis of rotation [6]. In contrast of the conventional machining, the ratio between this offset and the feed per tooth could be easily high in high-speed micro milling. The deviation of the tool edge trajectories involves an asymmetric cutting condition. A change of undeformed chip thickness, a load imbalance between the flutes, a decrease of the tool life, and a reduction in workpiece quality are the main consequences of tool runout [7]. **Figure 2** shows an example of a damaged two-flutes micro-mill. Only one flute shows a damage of the cutting edge, while the other one is intact. The cutting force signal recording during the micro milling confirmed the unbalance cutting condition due to the tool run-out phenomena.

As previously pointed out, an interesting and suggestive industrial perspective is the integration between AM and micro-machining. The poor product quality of the AM components resulting from a high surface roughness is mostly due to the partially melted powder on the outer surface of the manufactured parts collected during the building process [8, 9]. The rapid cooling of the particles induces high stress in the material, and it have a high impact on the final microstructure of the parts. The machinability is a property of an engineering material that can refer to the ease or difficulty with which the material can be machined using a cutting tool under a determined set of machining parameters such as cutting speed, feed, and depth of cut. Machinability is strongly affected by the properties of the workpiece: in general, AM metallic alloys can result more difficult-to-cut machining operations when compared to their equivalents fabricated by conventional forming technologies, such as casting, forging or hot stamping [10–12].

Project and targets

The PhD Project had as major objective a deeper understanding of the behavior of Additive Manufactured materials employed in micro-machining. The integration between the two processes could bring to a mutual advantage.
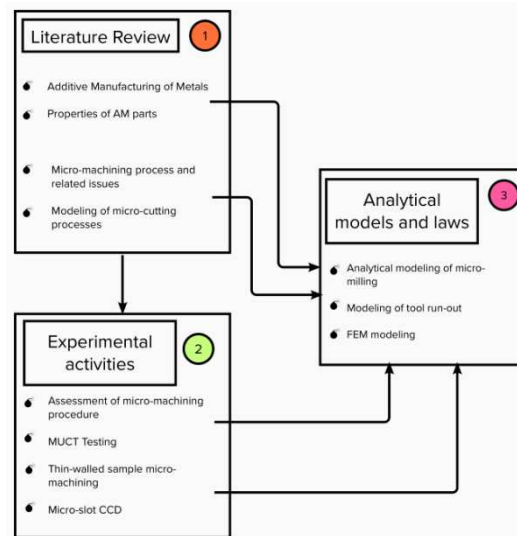

Figure 3. Flow chart illustration of the PhD project.

5

The objective is to combinate the high productivities and flexibility of machining with the geometrical freedom and low scrapes of Additive Manufacturing. The research project is summarized in **Figure 3**. A deeper and comprehensive bibliographic review was performed to investigate the knowledge background about additive manufacturing and machining. The review focused on the AM processes currently available for metallic alloys, with a special regard on LB-PBF and BB-PBF due to their large diffusion [13] and economic sustainability [14]. If compared with other AM technologies, PBF processes allow to achieve better surface quality, higher complexity and they require less post processing [15]. The literature review on micro-milling focused on the most critical issues which affects the processes, such as the ploughing cutting regime, the tool run-out, the burrs formation, the high cutting forces, the tool wear phenomenon, the difficulties about respecting the geometrical and dimensional tolerances [16]. The research regards the experimental procedures and the process modeling both. About the modeling, the literature review concerned the analytical models, the numerical models, the regression analysis, and the response surface methodology. The second chapter of this thesis is dedicated to micro-milling modeling. Furthermore, the numerical models require the correct modeling of some crucial aspects, such as the friction coefficient and the flow stress characterization of the material behavior. A deep and extended review of the models currently utilized in numerical simulations is reported.

(**a**) (**b**)
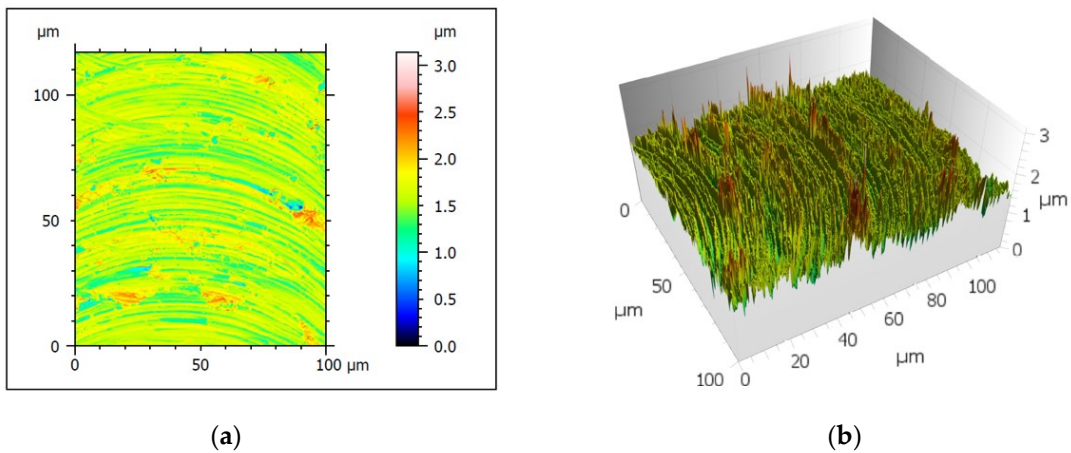
Figure 4. (a) Micromachined surface two-dimensional reconstruction and (b) three-dimensional illustration.

About the experimental tests, the Ultra-Precision Laboratory of the University of Brescia were employed to micro-cut a wide range of AM materials, such as Stainless Steel, Titanium alloy, Aluminum alloy and Inconel. Machining was performed by using an ultra-precision 5-axis KERN Pyramid Nano, equipped with piezometric triaxial sensors to monitor the cutting forces. The experimental procedure was optimized during the Project with the aim of improving the force measurement chain reliability. The loadcell performances were investigated with the purpose to identify the dynamic limits of the Kistler 9317C sensor when it is mounted on the milling-machine. The amplification of the high-frequencies signal components could distort the cutting force trend. The application of filters is useful to avoid the cutting force overestimation and to increase the measurement system reliability. An assessment procedure developed with the purpose of identifying the limits of a machine-tool was

finally published on an international journal [17]. The quality of the machined surface, the roughness, the dimensional and geometrical tolerances were investigated with the Optical Coordinates Measuring Machine (CMMO), a multifocal optical microscope and an Auto Focus (AF) laser probe. **Figure 4** shows an example of a micro-machined surface acquired through the AF laser probe. The Laboratory facilities will be described in detail in the third chapter.

The material removal behavior during micro-milling operations was investigated to select the optimal feed rate value when machining additive manufactured samples. The variation of the specific cutting force was studied as a function of the feed per tooth. The transition from shearing to ploughing regime was analyzed by considering the variation of the specific cutting forces. The Minimum Uncut Chip Thickness (MUCT) can be defined as the value of the chip thickness which corresponds to the behavior transition. It was calculated to identify the transition between the cutting regimes (shearing, ploughing or their combination) that affects the final product quality in terms of surface integrity and dimensional accuracy. The procedure was applied to several materials, such as AM stainless steel [18], AM Inconel 625 [19], AM and conventional Ti6Al4V [20] and AM and conventional AlSi10Mg alloy. Chapter four is dedicated to the description of the experimental tests and to the results.

The MUCT was one of the parameters subsequently utilized to set-up an analytical model able to predict the cutting force in micro-machining. PBF process was employed to build a special design sample with a thin wall with a thickness of 0.15 mm. It was subsequently cut by using a zero-helix micro mill and testing different cutting speed. The 2D cutting configuration facilitated the modeling of the process, which allowed a deeper investigation of the chip formation mechanism. An analytical force model was developed and subsequently optimized through the Particle Swarm Optimization (PSO) technique [19]. The model reliability was improved by defining a second function of error [21]. The effectiveness of the model was proved by calibrating it also on Ti6Al4V samples fabricated via LB-PBF [22]. Therefore, the calibration procedure was repeated also for different building orientation and for samples fabricated via BB-LBF. A comparison with the micromachining on cast Ti6Al4V samples was finally executed.

A new version of the analytical model was subsequently developed. It also considers the effect of the tool run-out on the cutting forces by taking into account the imbalance load on the tool flutes. The tool run-out phenomenon was described by some geometrical parameters which can be experimentally estimated by considering the periodicity of the cutting force signal and the morphology of the machined samples. Once the tool run-out parameters and the MUCT value are known, it is possible to exploit the analytical model for predicting the micro-milling forces, avoiding the need of expensive and time-consuming experimental tests. The analytical model predictions about cutting force constitute an interesting database which can be employed also to calibrate more complex numerical models.
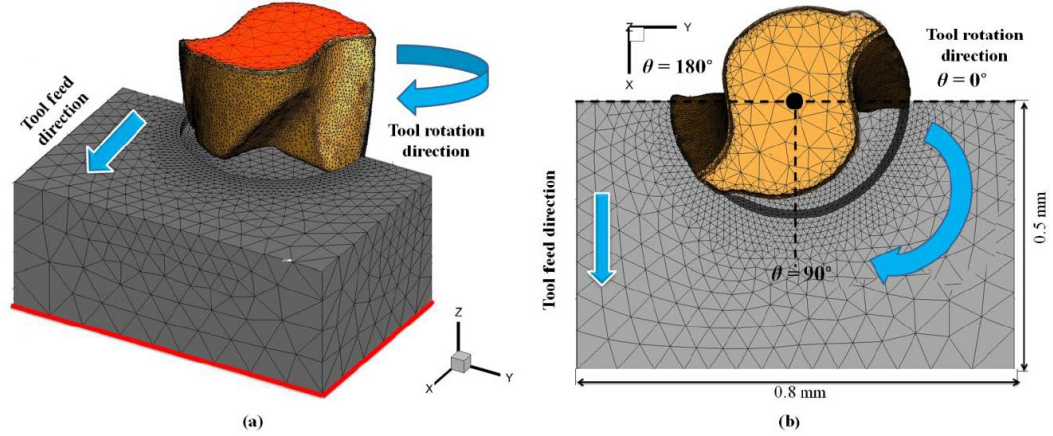
Figure 5. a) 3D FEM setup isometric view, boundary condition (red area), (b) definition of tool engagement angle θ (top view) **[7]**

Among the numerical model, Finite Element Method (FEM) are a powerful instrument to achieve a deeper investigation about several themes, such as the workpiece material behavior, the tool damage and wear, the elastic recovering effects and the thermal aspects of the machining. **Figure 5** shows an examples of FEM simulation of machining. FEM simulation of processes is a powerful instrument, but its diffusion in industry is limited, especially for machining processes. The development of a reliable machining model can promote the adoption of simulation in several sectors. Simulations allow to optimize process in a virtual environment, with a considerable saving in terms of costs and materials. The FEM simulation software DEFORM was utilized to model the experimental test.

The analytical model was used to generate a wide amount of data to calibrate the flow stress model of AM Inconel-625 by performing FE simulation. The cutting force measurements and the micro-chip observation were utilized to calibrate a 2D FEM model which considers ploughing and shearing regimes both. The first simulation was performed by using the flow stress data available in literature and obtained from samples made by casting. Then, it was iteratively adjusted by using the PSO algorithm, an optimization tool implemented in MATLAB. The last iterations allowed to identify a flow stress parameters set which guaranteed a good matching with the experimental results in terms of maximum cutting speed and chip segmentation. Further tests were performed with the final purpose of verifying the reliability of the material flow stress model. Analytical and numerical models developed during the PhD project are collected in the fifth chapter of this thesis.

The last thesis chapter regards some additional research projected related to machining which does not consider AM materials. A three-dimensional FEM model was developed to simulate micro-milling of lead-free brass. It has the purpose to describe and provide some actual aspects, as the burr formation, the chip development, the cutting load, and the temperature distribution. The model was developed also by considering the tool run-out effect on the actual tool edge trajectories **[23]**.
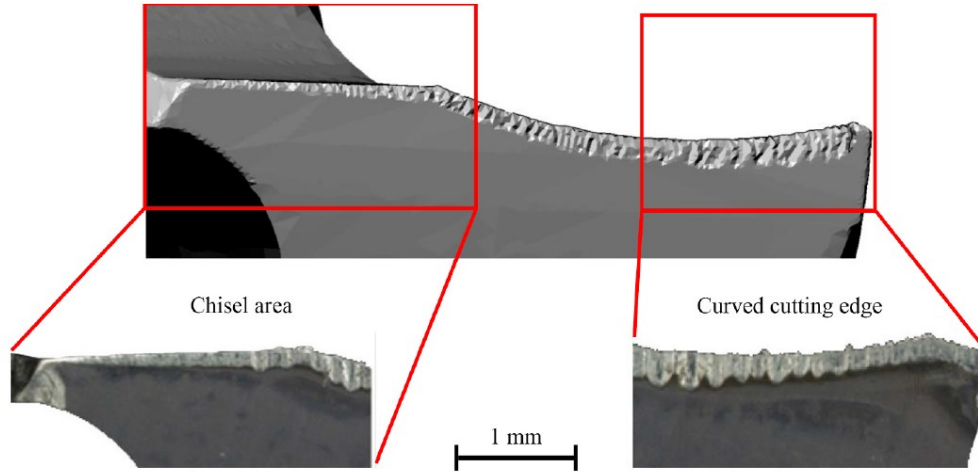
Figure 6. Simulated (upper) and experimental (bottom) tool wear in drilling **[24]**.

Scanning Electron Microscope (SEM) observation of the 3D chip shapes demonstrates ductile deformed surfaces together with localized serration behavior. Cutting force and chip flow results from simulations are compared with force measurements, tool run-out, and chip morphology revealing reasonable agreements.

FEM analysis was employed also to study the tool wear phenomena and how it affects the efficiency of machining and the quality of machined products. The traditional and regulated experimental approach to investigate tool wear requires several time-consuming tests. FEM can be utilized to predict tool wear and tool life as function of process parameters and tool geometry. The commercial software for Finite Element Analysis (FEA) are limited by the impossibility to update the geometry of the worn tool. The research utilizes a self-released subroutine to modify the tool geometry in DEFORM 3D simulations by considering the volume reduction of the tool. Figure 6 illustrates a comparison between the model prediction and the actual worn profile of a drill. The model was validated with experimental data obtained by drilling tests on Inconel 718 using conventional metal working fluids (MWF). The correct profile of the simulated worn tool was individuated by comparing the prediction of the simulation with the real tool geometry.

(**a**)　　　　　　　　　　　　　　　　　　(**b**)

Figure 7. Comparison between the features machined with: (a) original process parameters; (b) optimized process parameters **[26]**

9

The FEM simulation allowed to predict how torque changes during the tool life [25]. In a predictive maintenance perspective, the model can be implemented to optimize the tools replacement. Finally, a research project was focused on one of the most relevant industries for micro-machining, the horology. Final products are typically characterized by high requirements and stricter geometrical and dimensional tolerances. From this perspective, the optimization of the micromachining process parameters assumes a crucial role to increase the efficiency and effectiveness of the process. The optimization of micro machining is indispensable to achieve excellent surface finishing combined with high precision. The cost-saving objective can be pursued by limiting manual post-finishing and by complying the very strict quality standards directly in micromachining. A micro-machining optimization technique was defined during the research. The procedure was applied to manufacturing main-plates and bridges of a wrist-watch movement. Cutting speed, feed rate and depth of cut were varied in an experimental factorial plan to investigate their correlation with some fundamental properties of the machined features. The dimensions, the geometry and the surface finishing of holes, pins and pockets were evaluated as results of the micromachining optimization. The identified correlations allowed to manufacture a wristwatch movement in conformity with the required technical characteristics and by considering the cost and time constraints **[26]**. **Figure 7** shows a comparison to visualize how the optimization was effective.

The following table illustrates an overview of the Thesis, by considering the contents of each chapter.

	Chapter 1 *State of Art* The most impactful Additive Manufacturing technologies for metals are described and the properties which influences the micro-machinability are summarized. The technologies suitable for micro-products manufacturing are listed with a special focus on micromachining and micro-milling of AM parts.

10
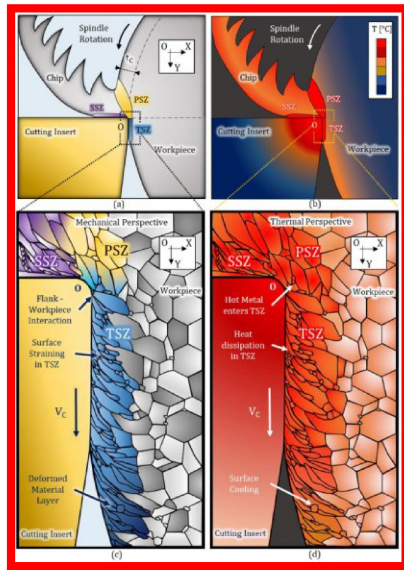
Chapter 2 *Analytical models and laws*

The second chapter deal with a literature review of the most meaningful research about modeling of micro-machining. The focus is on the analytical and numerical models.

The key issues of a Finite Element Model are highlighted, such as the material flow stress computing and the chip formation mechanism and the

Chapter 3 *Experimental set-up*

In this section, the instruments and machines employed during the project are described and classified.

AM machines, the micro-milling machines and the metrological tools are listed in order to better understand the experimental part of this work.
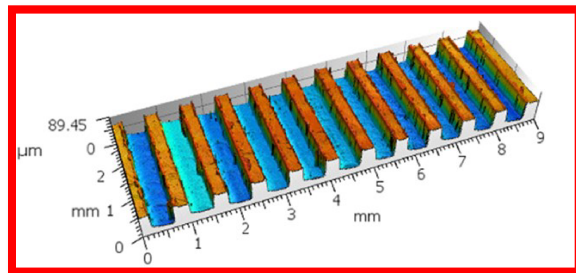
Chapter 4 *Experimental tests and results*

The fourth chapter is dedicate to the experimental activities performed on several AM metallic alloys, such as the 17-4 PH stainless steel, the Ti64 Titanium alloy, Inconel 625 and AlSi10Mg Aluminum alloy.

11
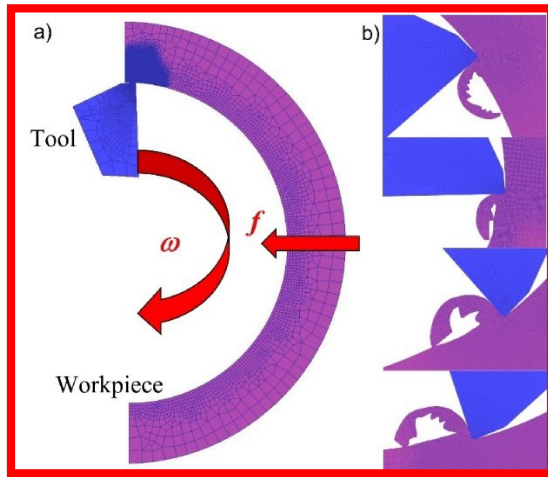
Chapter 5 *Definition and calibration of new models*

The last chapter of the manuscript regards the modeling of the micro-machining process. Different strategies of modeling are described, such as the analytical modeling (without and with tool run-out) and the 2D FE model of micro-cutting.

1.1 Additive Manufacturing of Metals

Nowadays AM techniques allow to successfully fabricate a wide range metallic alloys and high-performance engineering materials since the historical drawback of the large amount of residual porosity **[27]** was significantly improved. AM designates a large collection of different process which can be classified by considering how the raw material is supplied (powder, wire ore sheet shape) or how the energy is provided (laser, electron beam, arc.). Lewandowski and Seifi in **[28]** provided a helpful classification of AM of metals, which is shown in **Figure 8**.
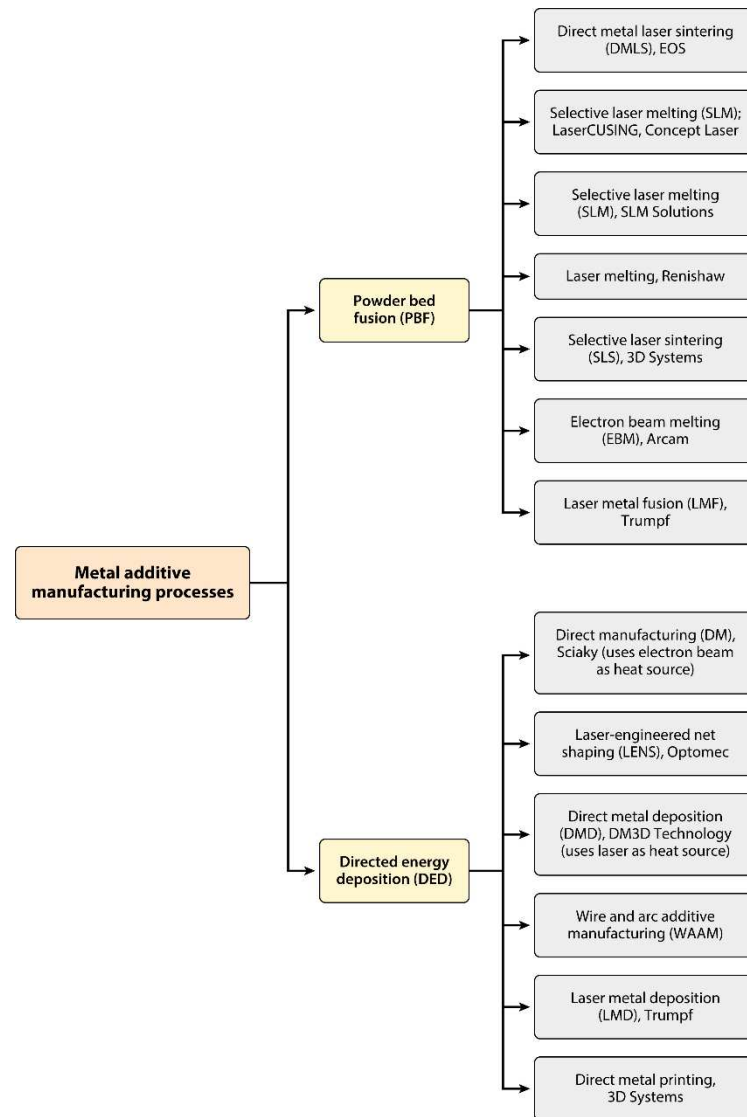
Figure 8. Summary of metal additive manufacturing processes, along with their commercial machine supplier names. **[28]**

The pattern shows how exists two major metal AM process categories, the Powder Bed Fusion (PBF) and Directed Energy Deposition (DED). Other AM techniques are suitable for metallic alloys, but PBF and DED are the only methods which have currently a meaningful spread in industrial context. The **Figure 8** also includes designations for the technologies currently available within each major process category [e.g., direct metal laser melting (DMLM), selective laser melting (SLM), selective laser sintering (SLS), direct metal deposition (DMD)] and current commercial machine suppliers. Although there are different technologies, there is a common basic approach. Firstly, 3D Computer Aided Design (CAD) data is obtained using a CAD software or reverse engineering approach. Then the model is virtually sliced in accordance with AM process by divided it into thin layers overlapped. The AM component is generated by repetitive deposition of single layers of metal powders and locally melting of the workpiece material by a heat source **[29]**. Subsequent layers are formed by lowering the build platform according to layer thickness and building processes are repeated layer by layer until the part is completed.

PBF employs an energy source to consolidate material in powder form to form three-dimensional (3D) objects. The heat source is applied to particles contained within a powder bed, which gradually indexes down as each layer is completed and new powder is spread over the build area **[30]**. PBF includes the following processes: direct metal laser sintering (DMLS), electron beam melting (EBM), selective laser melting (SLM or LB-PBF, which is illustrated in **Figure 9**), and selective laser sintering (SLS). Instead of using binder in the binder jetting process, PBF uses a laser source (SLS, LB-PBF, DMLS) or electron beam (EBM or BB-PBF) to directly and selectively melt or sinter layers of materials together to form a solid part. If a laser source is adopted, the deposition process is carried out in an inert atmosphere such as argon or helium chamber to prevent material from oxidation at elevated temperature. The usage of an electron beam requires a vacuum chamber **[31]**.

PBF processes have a strong advantage over the other AM processes: they do not require support structures, since overhangs are supported by the surrounding unfused powder bed. This allows more complex geometries to be produced, due to the possibility to not consider the support structure removing after the build **[30]**.
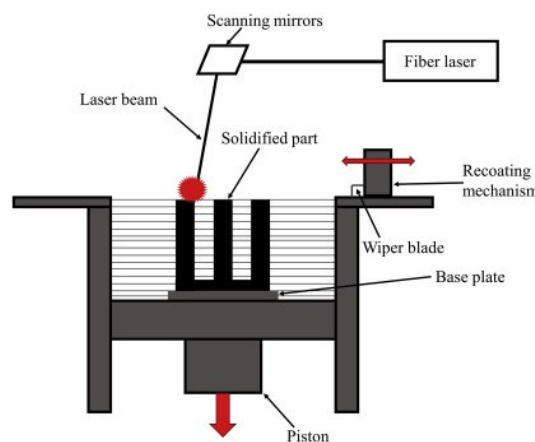
Figure 9. Illustration of the selective laser melting process **[31]**.

Figure 10. A typical laser sintering build set-up consisting of multiple individual parts **[30]**.

The lack of support structures also means that parts can be stacked freely in the powder bed, increasing the number of parts that can be produced in each build and thus increasing the productivity. An example is visible in **Figure 10**.

DED technology employs a heat source such as laser, electron beam or a gas-tungsten arc to create a melt pool. A filler material is added in powder or wire form inside the melt pool. The process follows a toolpath created directly from the CAD geometry and builds up parts in successive layers **[32]** A typical DED machine consists of a nozzle mounted on a multi-axis appendage, which deposits the melted material onto the specified surface. The process is similar to material extrusion, but the nozzle can move in multiple directions and is not fixed to a specific axis. The pattern in **Figure 11** shows how this technique works. The material, which can be deposited from any angle due to 4 and 5 axis machines, is melted upon deposition with a laser or an electron beam **[33]**. DED processes include laser engineering mesh formation (LENS), directional light production (DLF), direct metal deposition (DMD), and 3-D laser coating (LC). DED is a more complex printing process that is often used for repair or adjustment **[34]**.
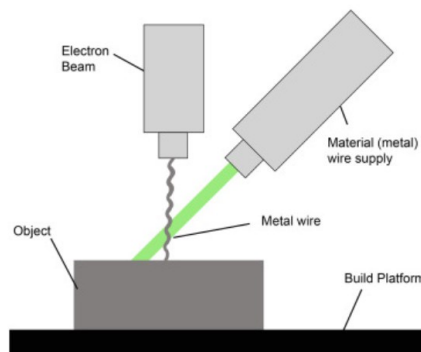
Figure 10. Directed energy deposition process.

When compared with DED technique, PBF achieves less post-processing requirements, better surface quality, and higher complexity [15]. Also, the mechanical properties achievable via PBF are reported to be higher than DED. In 2021 Babuska et al. [35] compared Fe-Co intermetallic alloy processed by L-PBF and laser directed energy deposition (L-DED). They demonstrated how L-PBF material was characterized by high strength (500–550 MPa) and high ductility (35%) in tension. The properties corresponded approximately to 250% increase in strength and an order-of-magnitude improvement in ductility relative to conventional material. On the other hand, L-DED material exhibited similarly poor tensile properties to the conventional wrought alloy, with low strength (200–300 MPa) and low ductility (0–2.7%).

PBF seems to show better proprieties then DED also after heat treatments. In 2022, Kumaran et al. [36] reports the effect of heat treatment on microstructural properties of the Stainless Steel 316L (SS316L) alloy sandwich structure manufactured using Directed Energy Deposition (DED) and Powder Bed Fusion (PBF) technique. The SS316L sandwich structure was treated with two heating methods namely, stress relief at 650 °C (HT1) and solution treatment at 1100 °C (HT2). Both heat treatments are maintained for two hours, followed by furnace cooling. The microstructure and mechanical properties of the heat-treated samples and the as-built sample were compared. It was noticed that the grain size in the interface layer for both the HT1 and HT2 were reported to be of finer, whereas in HT2 sample, the grain size of the DED portion was relatively larger as compared to the grains of the HT1 sample. In 2021 Liu et Al. [37] collected in a paper all the issues and anomalies related to the process which are yet to be suitably understood and resolved. The full list is shown in **Figure 11**. They limit DED applicability and adoption when compared to PBF.
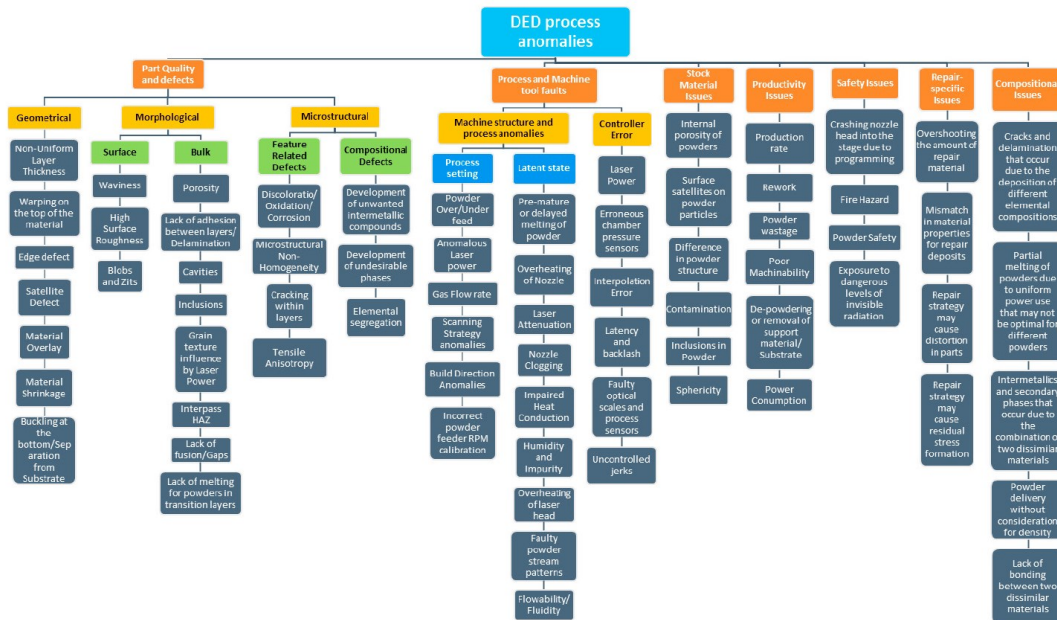
Figure 11. Flow chart of process anomaly classification [37].

For these reasons, the research about machinability of AM formed metallic alloys was limited to PBF process, which are described in more detail in the next paragraph.

1.1.1 Powder Bed Fusion

Powder Bed Fusion processes (PBF) of metals have been analyzed to evaluate the influence of the parameter's optimization on the residual stresses and metallurgical defects directly responsible of the impact on the mechanical performances of the final parts [38]. Further, one of the most studied aspects of the outcomes of PBF techniques is the surface quality of the samples especially with different building direction in relation to the building plate for the obtainment of complex and convoluted structures [39,40].

The most analyzed PBF processes are LB-PBF and BB-PBF, also known as Selective Laser Melting and Electron Beam Melting, respectively. LB-PBF is the most common PBF method. On the other hand, BB-PBF method employs higher power than a laser source [41]. The typical dimensional accuracy of LB-SLM parts is around ± 0.1 mm/100 mm and the average surface roughness (Ra) is usually above 5 μm [42]. Usually LB-PBF outputs are characterized by lower dimensional accuracy and higher Ra, usually in the range of 20–50 μm [42]. For many engineering applications, it cannot be considered acceptable [43]. Some recent investigations aimed to improve surface quality by optimizing the AM process parameters. A realistic lower limit for Ra achievable through PBF process is equal to 1 μm [44] and it implicates that post-processing still be necessary.

About the materials, an interesting case is represented by Ti6Al4V (Ti64) titanium alloy. It is widely used to produce biomedical implants due to its outstanding properties [45]. Besides, the corrosion and fatigue properties of additively manufactured Ti64, critical for the biomechanical outcomes of an implanted device, result affected by the PBF techniques chosen for the production. Similarly, the surface properties of the Ti64 samples fabricated by LB-PBF and BB-PBF, considered crucial for both the biocompatibility and the stress concentration during fatigue cycles, have been demonstrated different and strongly dependent on the energy source utilized for the material melting [46,47]. The surface defects deriving from the PBF processes, and remained even after using Hot Isostatic Pressuring, finishing and passivation, can substantially alter the stress concentration on the implant and the bioactivity of the surrounding tissue during in-vivo applications [48,49].

(a) (b) (c)
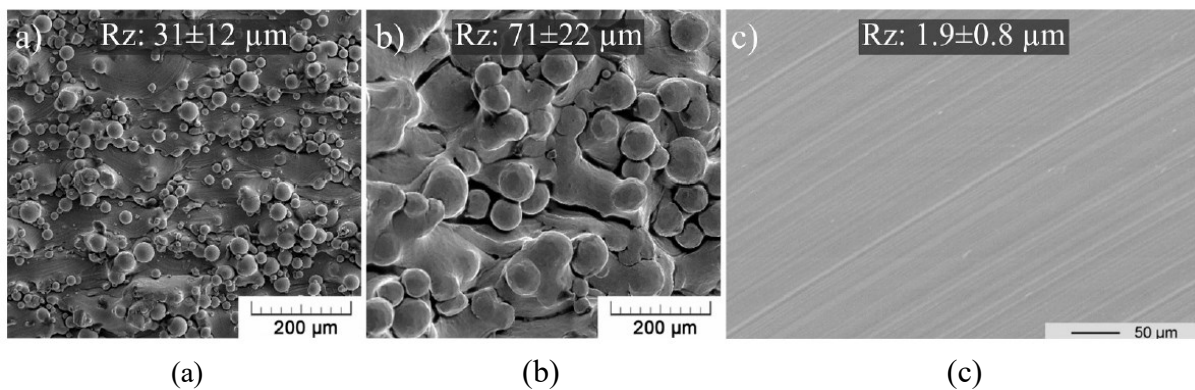
Figure 12. Surface finishing of a) SLM and b) EBM Ti6Al4V [50], and c) milled Ti6Al4V after AM [51].

Precisely, BB-PBF techniques have been observed to cause significant surface irregularities in relation to LB-PBF, with important issues on the surface state of implants.

Nevertheless, process optimization has not been highlighted as a possible way to control and predict the surface properties of PBF samples. An example for the surface morphologies of LB-PBF and BB-PBF Ti6Al4V specimens is given in **Figure 12**. The necessity of post-processing processes to improve the surface quality of PBF samples remains one of the disadvantages of the layer additive manufacturing of metals.

Recently, the building strategy of additive manufacturing processes has been established as the most influencing parameter when dealing with surface features since independent from materials, equipment, and applications. This parameter has also been found to be editable and optimizable even while using machines with constrained possibilities of investigable parameters. Moreover, several studies have been revealed that the building orientation can, in fact, alter different properties of as-built parts [52,53]. The literature focuses on the effect of the building strategy on the microstructure and mechanical behavior of PBF titanium-based blends. On the other hand, a proper comparison between LB-PBF and BB-PBF processes under machining operations has yet to be reported and analyzed although as-built samples have typically to be treated by machining prior to application.

1.1.2 Laser Based-PBF

In this section, further information about LB-PBF is collected. The components fabrication begins with the slicing of the CAD model in several layer by using a proper software. The final product quality depends directly on some input parameters which must be determined as function of the selected workpiece material, the powder properties, and the final shape of the component. The most relevant parameters are the laser power (usually ranging between 100 and 1000 W [41]), the layer thickness (usually ranging between 20 and 100 μm [54]), the layer uniformity, the scanning speed, the hatch spacing and the bed temperature. The laser melt and fuse selective areas of the metal powder, layer by layer, typically in an inert atmosphere to reduce oxidation effects [55].
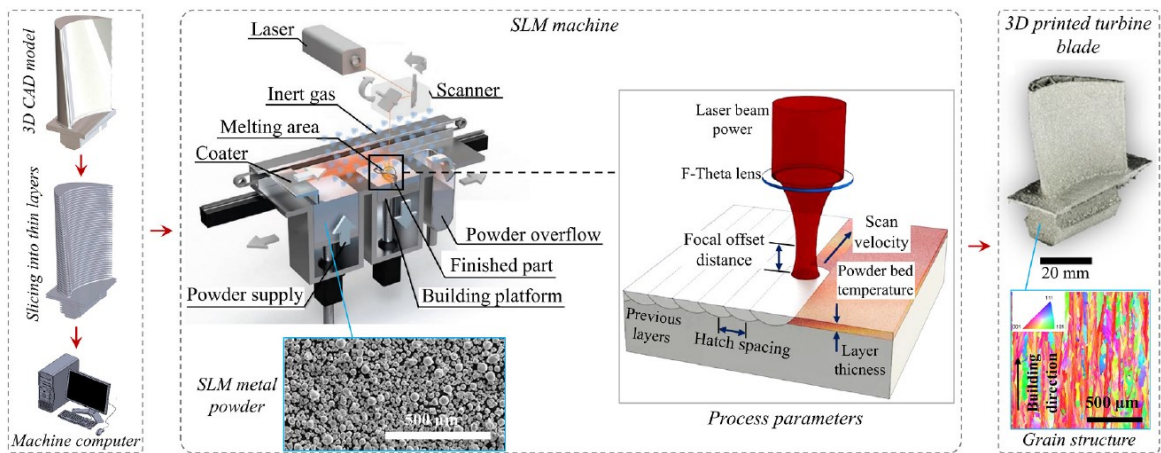
Figure 13. Schematic representations of a LB-PBF process and the process parameters [56]

A schematic representation of LB-PBF process and process parameters is provided in **Figure 13**. The process starts laying out a thin layer of metal powder from powder supply on a building plate inside the building chamber. Once the solidification of the first layer is completed, the building plate moves from top to down with a stroke equal to the layer thickness. A new metal powder layer is iteratively deposited on the previous layer and the laser can scan a new stratum until the final shape is reached. Usually post-processing treatments are performed, such as shot peening, polishing, heat treatment, Hot Isostatic Pressing (HIP) and machining. The objective is increasing the mechanical properties, improve the surface finishing and increase the part density [14].

LB-PBF can lead to several defects if the process parameters are not well calibrated. Balling [55], keyhole formation [57] and deterioration of the quality of the part. Moreover, the high cooling rate and the layer-wise production determines some issues that cannot be eliminated, such as residual stresses, crack formations, warpage, and base plate separation. These problems can be reduced by combination of pre-heating [58], selecting the appropriate laser scanning strategy [59], and heat treatment [60]. In addition, the employed metal powder size and distribution also significantly affect the final part quality [61,62]. In the previous section, a deepening was dedicated to the Ti64 Titanium alloy, but LB-PBF is frequently employed with a wide range of materials such as iron-, titanium-, copper-, aluminum-, cobalt- and nickel-based alloys and their composites. In this Research Project, the machinability of LB-PBF samples in Ti64, Inconel 618 and AlSi10Mg and 17-4 PH stainless steel was investigated. In each case, finishing machining operations are necessary to provide final product requirements in terms of surface quality and dimensional accuracy.

1.1.3 Beam Based-PBF

In this section, further information about BB-PBF is collected. The process shares with LB-PBF the slicing of the 3D CAD model, but an electron beam is employed to melt the metal powder in a vacuum environment. The electrical conductivity is a fundamental requirement for the workpiece material; for that reason, BB-PBF is not available for ceramics and polymers.
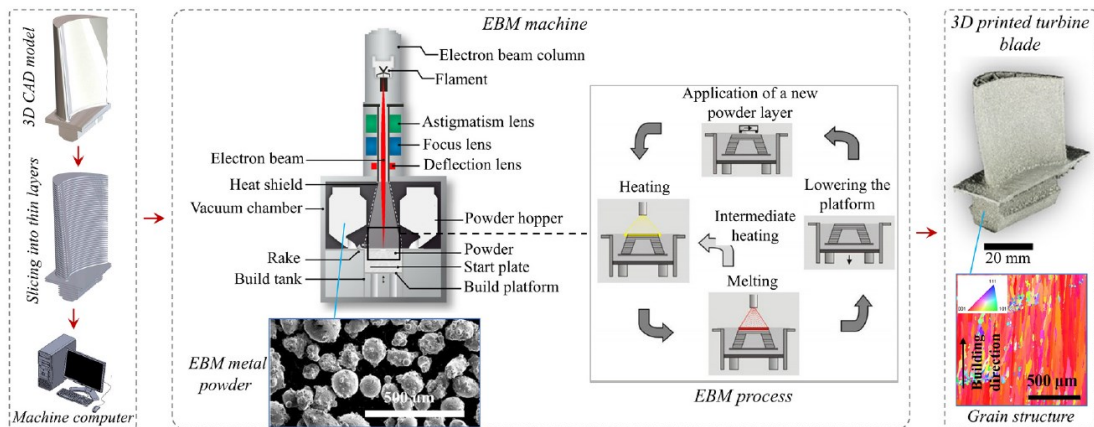
Figure 14. Schematic representations of a BB-PBF process and the process [27,64]

The main advantage of BB-PBF is the elevated limit of velocity and the high power of the electron beam. The electrons are emitted by a hot tungsten filament or a lanthanum hexaboride cathode. Electromagnetic lenses are employed to focus, accelerate and deflect the electron beam. These features allow to apply different melting strategy and higher temperatures, if compared with LB-PBF [27]. BB-PBF is suitable when manufacturing high-performances alloy, with final residual stress lower than LB-PBF. Cobalt-, nickel-based superalloys, aluminum alloys, tool steel, titanium alloys are some of the most employed materials.

The process is schematized in **Figure 14**. The typical vacuum environment exhibits a pression ranging between 10^{-5} and 10^{-4} mbar, while the electron beam reaches a maximum power of 3 kW [27]. The metal powder (size ranging between 40 and 100 μm) is applied on a preheated plate and subsequently it is heated to sinter the particles slightly [64]. The temperature during this phase is strictly dependent on the powder proprieties, but generally the heating rate is increased if compared with the heating rate during the subsequently melting phase. Once the material is solidified, the plate shifts down and a new powder is applied to repeat the described cycle since the part is completed and it starts the cooling phase inside the machine.

Beam power, velocity, focus offset, distance between scan lines, number of contours, and hatching strategy are the most important parameters that must be optimized. The final properties of the AM parts are different if compared with LB-PBF due to the differences about process temperature and cooling rate. Another important difference is about the penetration depth of the electron beam, which is higher than the laser beam. They determine differences about microstructures and consequently about the proprieties [65]. Generally, LB-PBF employs thinner layers, slower scanning speed and finer particles allowing a better surface if compared with BB-PBF. Final parts usually exhibit also residues of un-melted powders which must be removed by sand-blasting.

Machining is necessary to finish the BB-PBF parts. The differences about proprieties also influence the machinability of the alloy. Therefore, innovative machining strategies and perspectives need to be developed to achieve a proper AM component performance and to increase productivity during machining.

1.2 Properties of AM affecting machinability

As previously pointed out, the machinability is the property which indicated how is difficult to machine a specific material under a specific set of cutting speed, feed, and depth of cut. The pattern in **Figure 15** summarized which factors indirectly affect the machinability, which are divided in three prominent groups: the workpiece and tool materials, the cutting condition, and the machined tool proprieties. All these aspects have an influence on the cutting mechanism, and consequently on cutting forces and temperature. The machinability data consists in a set of recommended parameters usable for a specific workpiece material to minimize the production costs and to improve the final quality. About AM metallic parts, is fundamental to individuate which properties have a critical influence on machinability. In general, when compared to their equivalents fabricated by conventional forming technologies, such as forging and casting, AM based metallic work materials can have some distinct difficult-to-cut characteristics in subsequent machining operations.
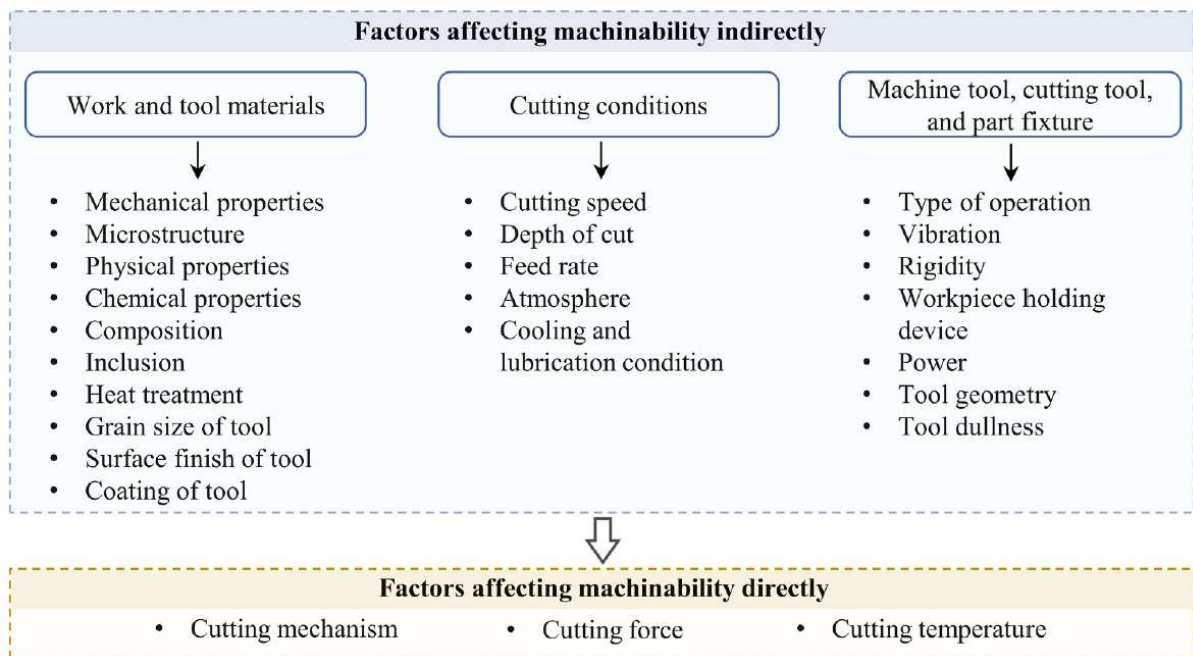
Figure 15. Factors which determine machinability **[66]**.

More in detail, the AM material properties which have a strong influence on machinability will be described underlining their differences in comparison to their conventionally manufactured equivalents. Physical and mechanical properties and microstructure are the most meaningful properties. In addition, the dynamic mechanical and thermal behavior is relevant because the chip formation mechanism in machining which typically involves high temperature and strain rates **[67]**.

1.2.1 Density

The relative density is defined as the ratio between the density of a final AM component and the theoretical density of the bulk material [55]. The relative density is usually lower then 100% due to the porosity which affects parts produced via PBF. High porosity is determined by the absence of a mechanical pressure during the PBF process, and it has a dual negative effect. On one hand, the density directly affects mechanical properties of the components [68] and, on the other hand, porosity also reduces the machinability. In fact, it leads to micro-impacts on the tool [69] and it favorites diffusion wear phenomena [70], causing premature failure of the tool.

The control of the AM process is crucial to maximize the relative density. Porosity increases when the melting of the powder is not sufficient [71] and gas are trapped in the powder bed. The optimization of printing parameters can decrease the porosity up to almost zero [71, 72] but optimal parameters can not be used for all geometry and with all the material. For this reason, the Hot Isostatic Pressing (HIP) post process is usually employed to provide a significant reduction of the porosity [73,74]. The HIP process combines the effect of high temperature and pressure to fuse unmolten powder to reduce the porosity and to improve the microstructure. **Figure 16** shows an example of the porosity reduction in LB-PBF of Ti6Al4V, while **Figure 17** shows the HIP effect on the same material manufactured by BB-PBF.

(a)   (b)   (c)
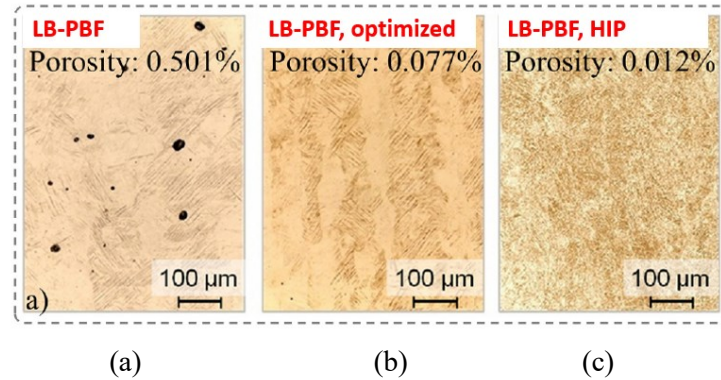
Figure 16. X-ray microtomography of Ti6Al4V part fabricated via LB-PBF in as built condition (a), after the optimization of process parameters (b) and after HIP treatment (c) [73].

(a)   (b)   (c)
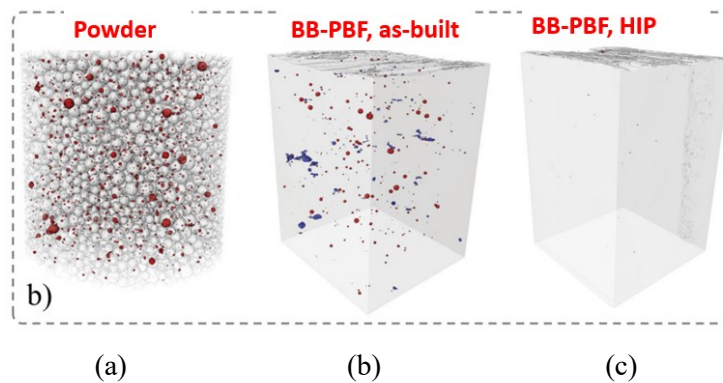
Figure 17. X-ray microtomography of Ti6Al4V part fabricated via BB-PBF, the powder (a), the as built part (b) and after HIP treatment (c) [75].

1.2.2 Thermal aspects

The fast solidification during AM of metallic alloys has a high impact on final microstructure of the workpiece which will be machined. The differences about microstructure with conventionally formed alloys implicate different thermal properties [76], such as thermal conductivity, specific heat, and thermal diffusivity. Furthermore, the porosity, the building direction, and the post-process heat treatments have a non-negligible impact on thermal properties of PBF outputs [77,78,79]. During machining, a portion of the mechanical energy is transformed to heat due to the shearing and friction in deformation zones. This heat is evacuated through the chip, but the temperature of the tool and workpiece in the contact area can increase. The temperature distribution depends also on the thermal properties of the workpiece. More in detail, lower thermal conductivity leads to higher surface temperature, with higher degree of diffusive and adhesive wear formations as consequence. The rise of temperature has negative consequences also on the surface integrity of the machined parts, with formation of micro-cracks, alteration of the hardness and lower accuracy [80, 81]. Therefore, the specific thermal characteristics of AM parts are important properties that need to be investigated from a machinability point of view. The **Figure 18** shows the dependence of thermal conductivity on temperature for Ti6Al4V alloys obtained through PBF (Laser based and Beam Based), heat-treated LB-PBF and the wrought alloy. It can be noticed as the not-treated LB-PBF samples has the lower conductivity, with a negative impact on machinability of this alloy.
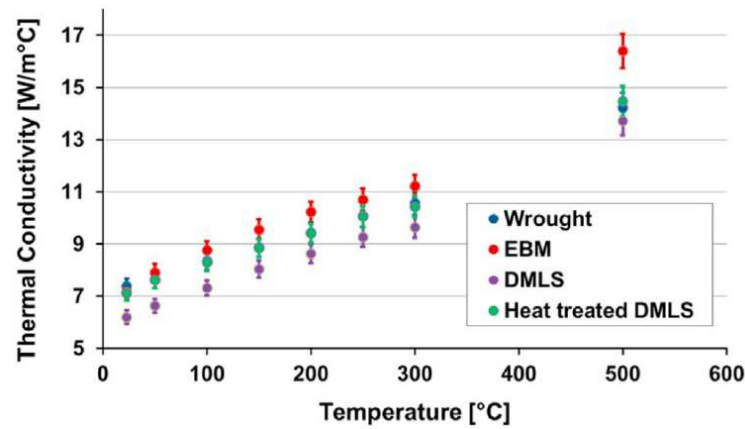
Figure 18. Thermal conductivities of EBM, SLM, heat-treated SLM and wrought Ti6Al4V alloys [77].

1.2.3 Microstructure

The literature states that the microstructure of the parts produced by metal AM technology strongly depends on the process parameters [82] and on the post processes (heat treatment and HIP) [83]. It is well known that AM technologies induce microstructures different from their conventional equivalent materials, with the same chemical composition. The AM technologies are characterized by different combinations of absorbed power (P) and beam velocity (V) [28]. The **Figure 19** shows a pattern of the typical P-V combination for each technology. The P-V combinations influence the cooling rates during and after solidification.
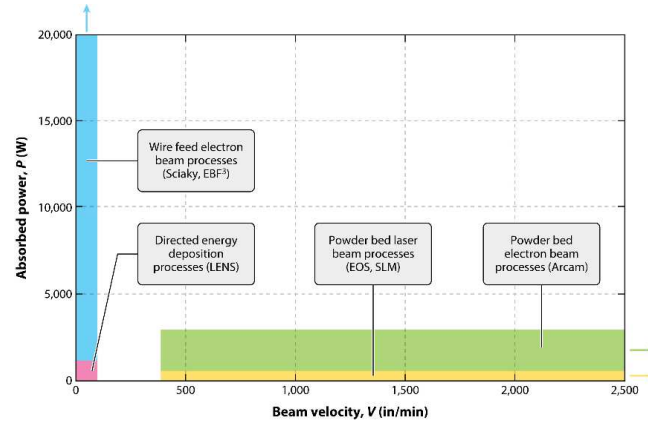
Figure 19. Typical combinations of power (P) and velocity (V) in different metal AM **[28]**.

This variable, along with the subsequent thermal cycles that occur during such layered manufacturing as well as any postprocessing affect the resulting microstructures. Generally, the obtained microstructures predominantly consist of columnar grains with a mix of equiaxed grains having cellular dendrites **[82]**. The columnar grains grow along the building direction of printing; for this reason, AM parts are affected by anisotropy and their properties strictly depend on the building orientation **[28]**. A specific issue which regards LB-PBF is the formation of non-equilibrium microstructures due to the high thermal gradients. BB-PBF is less interested by this phenomenon due to the control of the building chamber temperature in a vacuum environment **[65]**. The interest on microstructure is dictated by the fact that it determines the mechanical properties and consequently it affects machinability at macro **[77]** and micro **[84]** scale.

As seen for other properties, also about the microstructure Ti6Al4V work material represents an interesting example. **Figure 20** shows the microstructure of BB-PBF, LB-PBF, treated LB-PBF and forged alloys. The very fine and acicular morphology of α + β microstructure (7 % β phase) for BB-PBF sample (see **Figure 20 (a)**) is the results of high solidification rate and subsequent annealing **[85,86]** due to high temperature of the building chamber of the process.
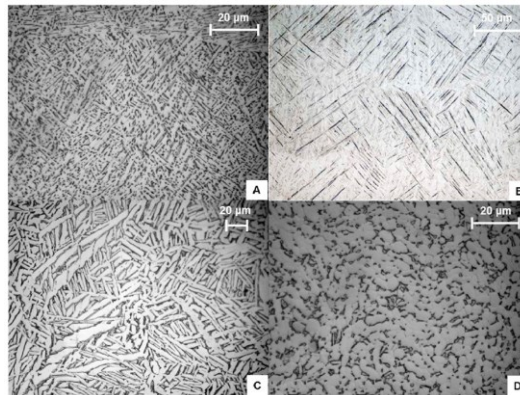
Figure 20. Microstructures of a) BB-PBF, b) LB-PBF, c) heat-treated LB-PBF, and d) wrought Ti6Al4V specimens **[77]**.

In the LB-PBF case, the **Figure 20 (b)** shows the martensitic microstructure (ἀ) with typical needles determined by the very high cooling rates **[65]**. This type of microstructure must be transformed into a biphasic α + β microstructure through the heat treatment (**Figure 20 (c)**) **[77]** due to the high brittleness of the as built part. On the other hand, the as built LB-PBF components exhibit the maximum tensile strength and hardness **[76,87]**. The wrought alloy formed by hot working and annealing shows α + β phases (8 % β phase) visible in **Figure 20 (d)**. The high variability about the structure determines uncertainties on machinability characteristics **[87]**.

1.2.4 Mechanical properties

Among the mechanical properties, hardness and tensile strength are crucial aspect in the material selection process by considering both the final application and the machinability of the alloy. Hardness is defined as the resistance to permanent deformation and the hardness of PBF parts was largely investigated and correlated to the process parameters **[88, 89]**, the post-process heat treatments **[90,91]**, the printing orientation **[92,93]**, and the AM-induced defects **[88]**. As discussed in previous section, usually LB-PBF determines finer microstructure which implicates high hardness if compared with BB-PBF and forged components **[94]**. In machining, low hardness are usually correlated to low cutting forces and cutting temperature in the tool-chip interface. On the other hand, low hardness can determine other issues in machining due to the high ductility, which can determine more burrs and the Built-Up Edge (BUE) phenomenon.

As an example, **Figure 21** lists the hardness values of Ti6Al4V specimens manufactured by different methods (wrought, EBM, SLM, heat treated SLM) as a function of the temperature **[77]**. Although the thermal softening which is shared by all the samples, the BB-PBF and the heat-treated LB-PBF samples are characterized by similar hardness. The as-built LB-PBF is harder, but it is reported that is possible to achieve similar hardness by changing the process parameters **[95,96]**.
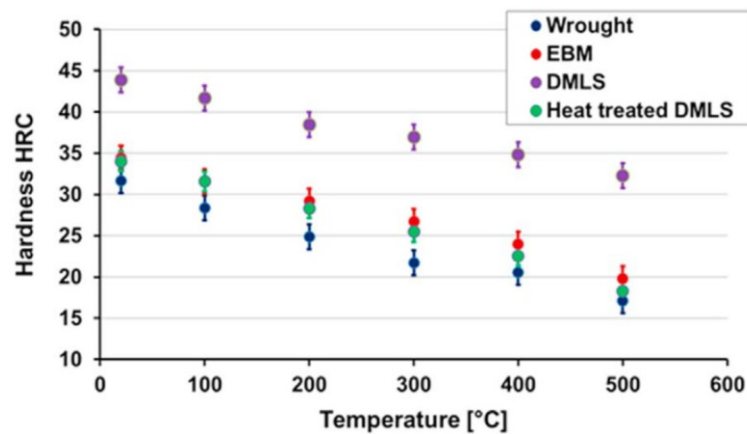
Figure 21. Temperature dependent hardness values of Ti6Al4V specimens manufactured by different methods **[77]**.

The tensile test allows to collect important data about the material characterization, such as the ultimate tensile strength (UTS), yield strength (YS), ductility, elastic modulus, and stress-strain relationship. When testing AM samples, it results clear that the tensile properties are strongly influenced by the AM process. More in detail, the strength depends on 3D printing parameters and strategies [97,98], part density [99], building direction [87]; furthermore, post-process thermomechanical treatments such as HIP [100] and heat treatments [73] directly affect the strength of AM components. When compared with the conventional processed materials, AM alloys exhibit comparable or even better tensile strength values [101].

From a machinability point of view, this leads to differences in chip formation mechanism with a consequence on cutting energy and forces. The anisotropy of AM components must be considered because the machinability strictly depends on building directions [102,103]. Several researchers demonstrated that the building orientation of AM parts ha s strong influence on elongation, while the effect on UTS and YS is lower and less repeatable [100,104]. More in detail, in [105,106] the UTS and YS result higher for samples fabricated in horizontal direction (perpendicular to building direction) in comparison to vertical direction (parallel to building direction), while in [107,108] was obtained the opposite effect. In the first case the correlation was justified by considering a higher amount of interlayer porosity occurrence in vertical specimens due to the higher number of layers than horizontal specimens [106]. In the second case, the inverse trend was associated with the directionality of the microstructure: the columnar grains are aligned parallel to the building direction, affecting the fracture mechanisms and the crack propagation in the part during deformation [106,107].

As anticipated describing the effect of hardness, heat treatments of PBF components are widely spread to improve and homogenize the mechanical strength, especially for LB-PBF. As an example, **Figure 22** shows the effects of different heat treatment on tensile property and microstructure of Ti6Al4V fabricated via LB-PBF [73]. The treatments are significantly affected the obtained microstructure and thus mechanical properties. On the other hand, HIP process provided very close tensile properties with the reference material. This was associated with removal of residual porosity and fusion of unmolten particles after HIP [73].
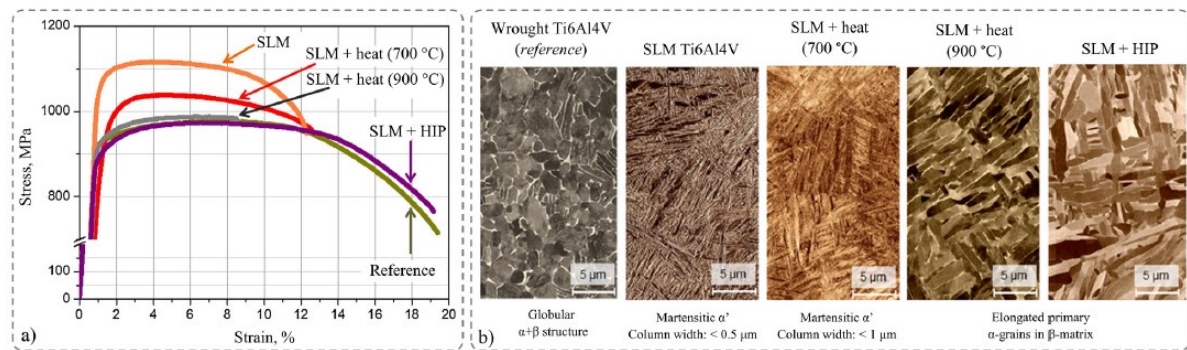
Figure 22. Effects of thermomechanical treatments on a) tensile strength and b) microstructure of SLM Ti6Al4V [73].

The mechanical behavior in static or quasi-static condition of metallic alloys can change the strain rates increases. Usually, at low temperature, the materials are interested by a strain

rate hardening which can meaningfully increases the tensile strength. Machining involves high strain rate, especially in micro-machining. For that reason, the dynamic properties of materials strongly influence machinability [109]. Furthermore, a reliable characterization of material flow stress in an adequate range of temperature and strain rate is necessary to perform numerical simulation of machining through FEM [110].

For these two reasons, the researchers are investigating the dynamic properties of AM metals and they are focusing on the difference induced by the AM process. The building direction [111,112,113], the process parameters [114] and the post-process heat treatments [115] and the energy source [109,116] are the most impacting aspects. In [116] heat treated LB-PBF and as built BB-PBF samples in Ti6Al4V were characterized at a maximum strain rate of 3000 s^{-1}. Both materials exhibit strain rate hardening effect but the increasement of strength was different. In another research [113] the effect of building direction was tested at high strain rate (up to 1500 s^{-1}). It was demonstrated that the vertical samples show higher impact strength than the horizontal ones. Also, the effect of some heat treatments (solution treatment, solution and ageing treatment) on properties at high strain rate (up to 2400 s^{-1}) was studied. The changes on microstructure introduced by heat treatments induced high differences on dynamic properties [112].

The studied described in this introduction about machinability of AM metallic parts usually regards conventional machining, but few of them deal with the micro-machining. On the other hand, micro-machining is a widespread technology useful to product micro-product or micro features on conventional size parts. In the following paragraphs, a brief introduction to the micro production technologies will be presented. It will be followed by a focus on micro-machining and related issues, with a final introduction at micromachining of AM metallic alloys.

1.3 Micro production technologies

In the last decades, there has been a spread of miniaturization of many components. For example, in consumer electronics, circuits have become extremely compact due to the reduction of the final products' size. Devices with micro-dimensions are contained in integrated packages with small size to allow convenient handling and assembly. Numerous medical applications are interested in miniaturization. In particular, the development of reduced size medical tool facilitates the widespread of non-invasive surgery techniques. Biotechnology is another important microproduct field: micro-end-effectors are necessary to handle biological cells and genes. Also, others field like automotive, telecommunications and energy are interested by miniaturization.

A relevant example of microproduct is the MEMS (Micro Electro-Mechanical Systems). These devices are composed by electrical circuits and opto-mechanical equipment integrated on a silicon substrate with dimensions ranging from 1 μm to 100 μm. MEMS can acquire information (position, movement, pressure, temperature, and others) from the environment thanks to some microsensors.

Input data are processed and used to control some actuators, all on the same micro devices. This chain of processes is traditionally ensured by many devices connected each other. MEMS are replacing conventional systems as pressure sensors, accelerometers and gyroscopes due to several advantages: minor energy required, and costs, lower weight and better performance are the mains.

From a geometrical point of view, microproducts can be organized in three different groups:

1. Two-dimensional structures (2D)
2. Two-dimensional structures with a third-dimension dependent on the transversal cross section ($2\frac{1}{2}$D)
3. Actual three-dimensional structures (3D)

The reasons for miniaturizing these geometries can be divided in two groups: on one side, there are products for which reduced size allows more compactness and portability; on the other side there are components whose functionality is achievable only by virtue of their small dimensions.

In more detail, microproducts can be defined as: *products whose functional features or at least one dimension are in the order of μm. The products are usually characterized by a high degree of integration of functionalities and components* [2]. This definition goes beyond the geometrical and size aspects and involves the concept of integration. Microproducts are frequently characterized by an integration of functions and an integration of intelligence in terms of processing and control of information and data. As any other product, microdevices can be constituted by several components. At this scale, handling and assembling the components into a final product is very challenging. For this reason, a high level of integration is necessary. It means that the lowest number of components should be used, and so they must have different functions and features.

Production system cannot be merely downscaled from macro-industry, but specific processes and materials must be developed. Today, many microproducts are successfully realized but high costs do not allow their mass production and commercialization. High precision tolerance and good surface finish are required also with hard-to-machine materials. These aspects promote the development of non-conventional processes characterized by a low material removal rate, as for example laser beam machining. At the same time, conventional manufacturing technologies continue to be used for certain applications. Microproducts can be obtained from a high number of different processes. They can be grouped in categories depending on the main physical and chemical principle adopted:

1. Plastic deformation processes
2. Thermal processes
3. LIGA
4. Micro Ultrasonic Machining
5. Micro-machining

The choice depends on the workpiece material, the geometrical features, the integration level required, the size of the production lot, and the final quality desired. In this regard, quality control is an issue concerning any kind of micro-production. When part dimensions are reduced, conventional equipment might not be suitable anymore and special instrumentation must be developed to identify failures. FEM can be a helpful instrument to perform numerical simulation to investigate the processes and their outputs.

1.3.1 Plastic deformation processes

Plastic deformation processes are considered as mass-production technologies. Metal forming has well-known advantages of high production rates, minimized or zero material loss, excellent mechanical properties of the final product and close tolerances, making it suitable for near net shape or even net shape production [117]. Bending, deep drawing, stretch forming and blanking are processes commonly used in micro-applications. More complex processes, as for example extrusion, are limited by the high accuracy required, especially regarding handling and positioning of the small sized workpiece.

1.3.2 Thermal processes

Thermal processes use heat as high concentrated energetic source to remove typically low quantities of material. Heat can be used to melt or vaporize material subsequently removed by using pressurized gas. These technologies can be applied with several materials, depending on their thermal properties such as melting point and heat capacitance. EDM and LBM are typical thermal processes examples. They are shown in **Figure 23**.

- EDM (Electro Discharge Machining) uses pulsed electrical discharges to provide the heat. Workpiece and tool are used as two electrodes, separated by a dielectric fluid; a voltage is applied to generate a spark which erodes the workpiece material. It must be conductive, and this condition limits the workable materials. Micro-EDM uses small energy for each pulse and precise mechanism to move machine elements, ensuring sufficient accuracy. Most valuable applications of Micro-EDM are WEDM (Wire Electro Discharge Machining, used to realize convex shapes with size around 10 µm) and micro-holes machining [118]. A significant advantage is the possibility to obtain burr free products. Furthermore, tool wear is significant, process is slow, and the choice of materials is limited.

- LBM (Laser Beam Machining) uses as energy source a laser beam. Process is controlled by tuning laser power, wavelength, spot diameter and pulse frequency [119]. Changing the laser type, is possible to deal with different metals, ceramics, glass, polymers, and semiconductors. LBM is mainly used to produce micro-features and micro-channel. His diffusion is limited by some issues, as residual stresses, and micro-structural alterations; to submerge workpiece in water (UWLBM) seems to be a solution to improve the product final quality and it allows to realize also cavities and holes.

<div align="center">(a)   (b)</div>
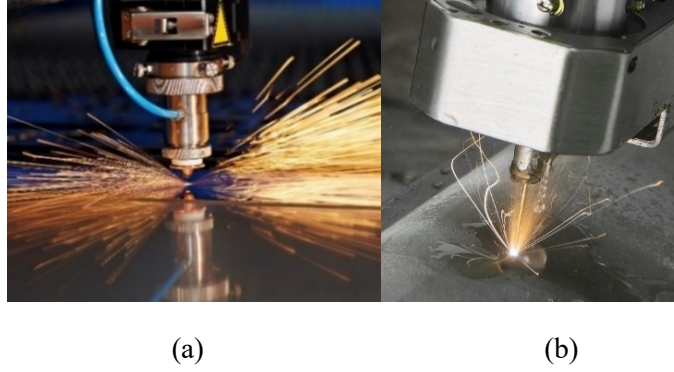
Figure 23. Laser Beam Machining (a) and Electro Discharge Machining (b).

1.3.3 LIGA

The LlGA technology comprises the processes of X-ray lithography, electroforming and molding. LlGA enables the manufacture of micro-components made of non-silicon materials like plastics, metals, and ceramics with almost any kind of lateral geometry **[118]**. Lithography is used to realize an etching pattern in which a metal or an alloy is plated. Molding the plated part, vertical wall can be realized from the starting geometry; $2\frac{1}{2}$D shapes are typical final products realized with LIGA technique.

1.3.4 Micro Ultrasonic Machining (MUSM)

MUSM is the result of the miniaturization of the conventional ultrasonic machining, characterized by the using of a tool and a free abrasive. The material removing is obtained by the tool vibration at high frequency. It drives the abrasive on the workpiece surface (typically ceramics, graphite, silicon, and glass that are also difficult-to-machine materials **[120]**) to generate a brittle breakage. In **Figure 24** some micro-holes are shown. At this scale, the vibrations applied to the tool generate some problems regarding the tool holding and the cutting accuracy. Two solutions were identified during last years: the first one is the on-the-machine tool preparation. It means that a tool fixed on the spindle is machined with the desired shape. Then the workpiece machining took place on the same machine tool. The second alternative is to apply the vibrations on the workpiece. This solution allows to move the tool with the same high-precision mechanism used in micro-EDM process. Micro-holes of 5 μm can be obtained in this way **[120]**. In conventional operations, USM tools are realized in Tungsten carbide. In micro-USM this material can be substituted with sintered diamond to reduce the tool wear and improving the machining rate.
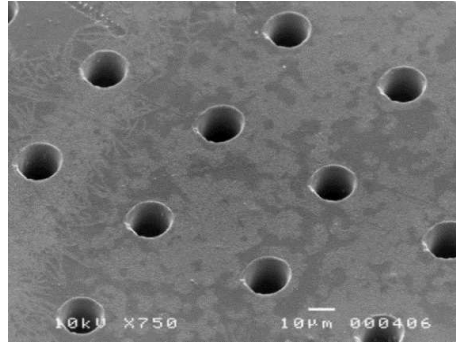
Figure 24. Micro-holes with a diameter equal to 15 μm, an example of MUSM machining.

1.3.5 Micro-cutting

Micro-cutting processes are characterized by a mechanical interaction between a workpiece and a tool. The contact determines a breakage along a defined path, obtaining several possible workpiece shapes. There are two fundamental conditions to achieve a good micro-machining. The first one involves thermodynamic aspects, and it is significant due to the high temperatures that can be reached during the cutting. It consists in the absence of thermal diffusion between tool and workpiece materials. If chemical affinity is strong, high tool wear rate and workpiece deterioration will be the main consequences. The second condition has a mechanical nature: the tool hardness must be higher than the workpiece one. In micro-cutting context, the tool cutting edge radius is significant too. It must be equal or lower than the chip thickness. If cutting edge is higher than the uncut chip thickness, a negative rake angle cutting condition will be realized. The main consequence is an increase of the cutting forces and the resultant tool deflection, which lead to a worsening of the surface quality, a meaningful burr formation and a decrease of the tool life. Available micro tools can reach cutting edge radius equal to some tenths of microns. As a result, minimum depth of cut is limited to some hundreds of nanometers. Tool fabrication technology is an additional limit for the machining miniaturization. Sintered carbide two flutes end mills and drills with a diameter of 25 μm are currently available, but 5 μm diameter micro-mills are at the research phase. In **Figure 25** some examples are shown.

Drilling for micro-holes, milling for micro-grooves and micro-3D shapes, turning for micro-pins are typical examples of processes and products obtainable at this scale. Sub-micrometer tolerances can be realized only with ultra-precision machines with high positional accuracy. Burr formation can be relevant and to remove it with conventional method is not possible due to the burr dimensions. Furthermore, hard or brittle materials are difficult to machine. On the other hand, using small cutting depth is possible to machine these material in a ductile regime. Electrical material properties are no relevant as, for example, with LBM technology. Finally, a huge advantage on the others micro-processes is the high flexibility of micro-machining, which allow to produce 3D complex shapes and not only holes, grooves and 2D shape. For these reasons, micro-cutting processes remain one of the most valuable micro production technologies.

31

<center>(a)   (b)</center>
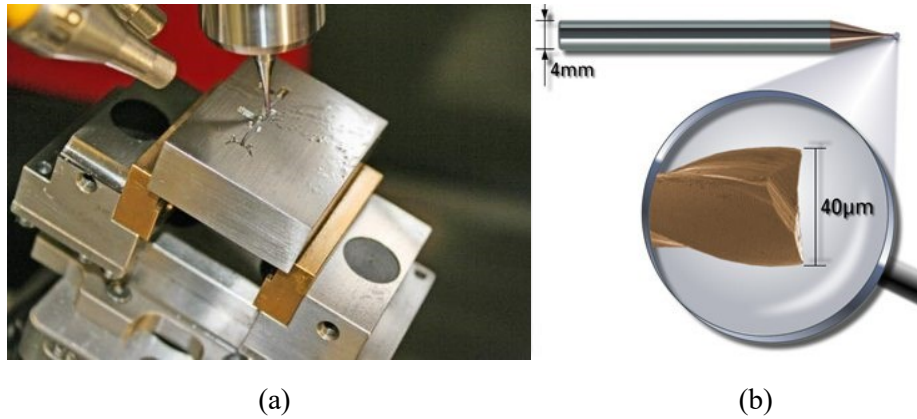
Figure 25. Micro milling operation (a) and a 40 µm diameter micro-mill (b)

1.4 Micromachining and related miniaturization effects

Micro-turning and micro-milling provides high economic efficiency due to high material remove rates and the low material wastefulness **[121]**. Tool diameters are typically smaller than 1 mm, tool edge roundness is about few microns, and chip thickness is in the same order of the magnitude. Micro-milling is among the most important manufacturing processes which have allowed the high spread of components possessing micrometric dimensions. The most important area of application for this technology is surely the dies and molds fabrication, due to the high accuracy and the low surface roughness achievable. Today micro-milling is applied also to realize final products in the aerospace, electronics, and biotechnology fields. High economic efficiency, flexibility, high accuracy, and elevated removal rate are the main causes of this success. On the other hand, micro-milling processes are affected by a large number of technical issues.

At this length scale, phenomena that can be usually neglected involve with a considerable weight: ploughing, size effect, burr formation, rapid tool wear, higher than expected cutting forces and tool run-out are the most common micro milling related issues **[2-5]**. The development of a good model for describing cutting operation on a micro scale is essential to understand how all process variables influence the product final quality. In fact, the experimental approach run into several difficulties at this scale. First research efforts go back to the 1960'. In the following decades several publications were realized. They concerned mainly the process modelling to achieve a greater understanding about cutting forces prevision, workpiece defects, tool run-out effect, thermal stability, and many other issues. Measuring tool temperature and tool wear, evaluating chip morphology, and determining the cutting force values are challenging tasks. Finite Element (FE) simulations can be applied to predict these process variables reasonably well, to analyze the generated surfaces, and to optimize the machining parameters.

In the next paragraphs, the actual micro-milling know-how will be summarized, focusing on workpiece and tools material, size effect and quality.

1.4.1 Workpiece material

Micro-milling applications require the employ of different materials, ductile and brittle both. In **Figure 26** a pie chart shows the most diffused. Workpiece materials can be divided into two main groups regarding their machinability in micro-milling operations:

1. Hard-to-cut materials, as hardened steels, ceramics, glasses, and W-Cu alloys.
2. Easy-to-cut materials, as the most of aluminum and copper alloys and low hardness carbon steels.
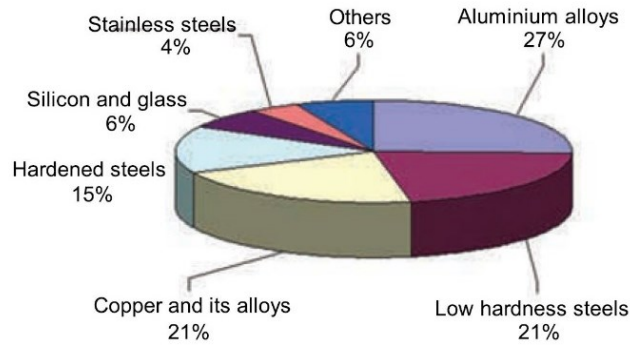
Figure 25. Most common workpiece material in micro-milling.

This first group of materials is clearly more interesting, and many research deal with the issues regarding their cutting. Size effect is certainly among the principal issues **[1,123,124]**. It can be defined as the meaningful increase in the shear flow stress of the workpiece material caused by the decrease in the uncut chip thickness (indicated in **Figure 26** as t_u).
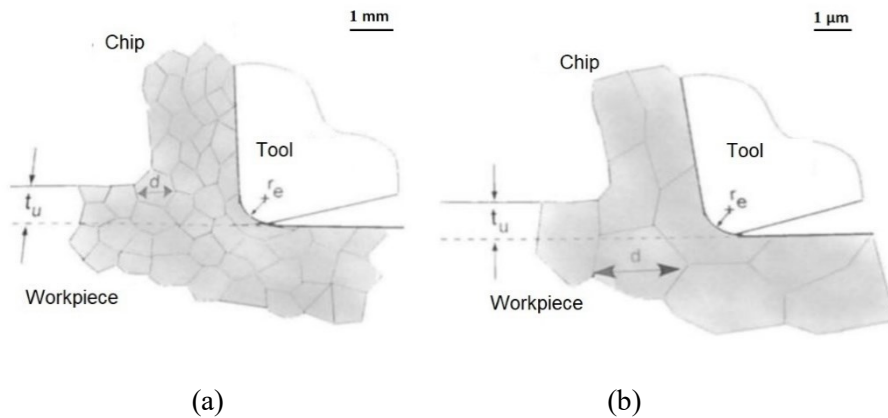
(a)   (b)
Figure 26. Comparison between conventional cutting (a) and micro-cutting (b).

An explanation of this experimental evidence is described as follow: cutting forces decrease with increased concentration of crystalline lattice defects, such as grain boundaries and impurities. Grain boundaries, for example, are zones of lower binding energy; therefore, less then theoretical stresses are adequate to generate intergranular fractures. In the same materials, tools with different size engage with different concentrations of these defects. As shown in **Figure 26**, in micro-cutting the ratio between grain and tool sizes is different from the conventional processes. This condition is equivalent to a situation in which two tools,

with the same size, engage grains with reduced dimensions (for the conventional cut) and higher dimensions (for the micro-cut): in the second case, fewer concentration of boundary grains will increase the forces. When the ratio of average grain size and uncut chip thickness reaches the unit, the cutting edge is forced to fracture a single grain. The consequence is a further increase of specific cutting forces which determines burrs formation, high tool wear rate and lower surface quality.

The increment of the specific forces is attributable also to others two effects: the high elastic recovering effect and negative rake angles. They are both shown in **Figure 27.** The recovery of the elastic deformation, that is negligible in conventional processes, may result at this scale in a high friction between tool and cut surface. Furthermore, when the uncut chip thickness becomes equal or smaller than the tool edge radius, extremely negative rake angle values can be promoted **[124]**. This phenomenon not only increase cutting forces but can also influence the chip formation mechanism. In fact, if the depth of the cut does not reach a specific value the work material will not be cut.
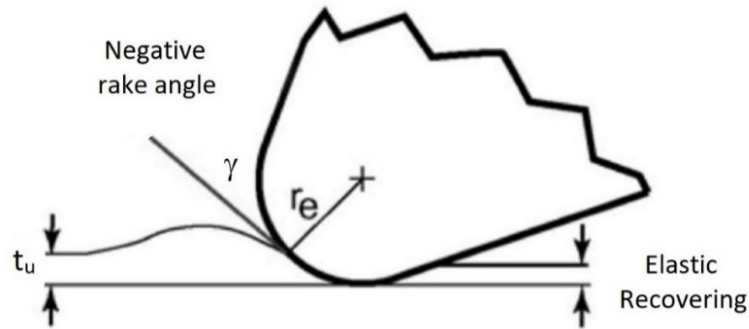
Figure 27. Representation of negative rake angle and elastic recovering effect.

The material compression in this undesired condition is know how ploughing effect **[5]**. In ploughing regime, the tool scrapes the workpiece without chip formation. Ploughing effect can be described by reference to full-immersion micro-milling, described in **Figure 28**. The uncut chip thickness $t_u(\varphi)$ depends on the value of the rotation angle φ, ranging from zero (when $\varphi=0°$) to feed per tooth f_z (when $\varphi=90°$). At the beginning, uncut thickness is not sufficient to form the chip and mostly elastic deformations are induced to the workpiece. Ploughing regime ends when the rotation angle φ reaches a chip formation angle φ_{CFA} corresponding to a minimum uncut chip thickness $t_u(\varphi_{CFA}) = t_{u\_min}$. Subsequently, the standard cutting condition, based on shearing, is achieved.
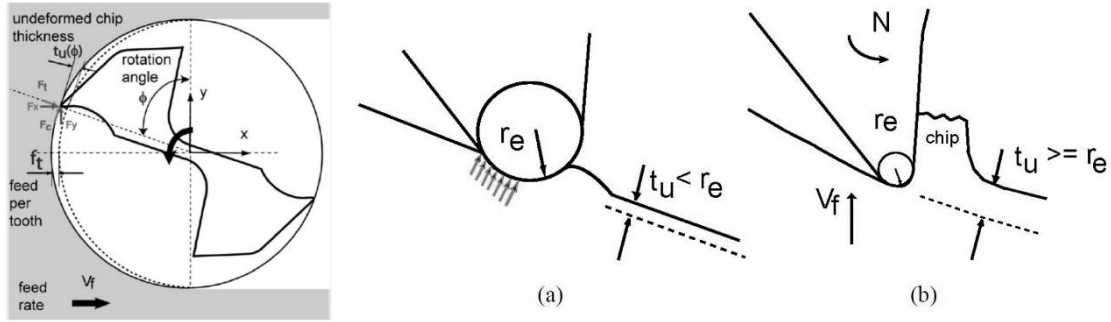
Figure 28. Chip thickness during micro-milling process (a) and conventional process (b) **[5]**.

Several experiments show as a smaller edge radius causes early formation of minimum chip thickness whereas a larger edge radius will result in ploughing of the workpiece. In particular, the minimum uncut chip thickness MUCT is proportional to the cutting-edge radius r_β, as expressed by **Equation 1**:

$$MUCT = k \cdot r_\beta \qquad\qquad\qquad\qquad\qquad\qquad \textbf{Eq.1}$$

For ductile materials, k is fixed between 0.1 and 0.25. Further studies **[124]** experimentally investigated the phenomenon, determining k = [0.35÷0.4] for AL6082-T6 aluminum and k = [0.2÷0.3] for AISI 1018 steel, at a wide range of cutting speed and edge radius.

About thermal aspect of the cut, considerable low temperature values are expected in micro-milling owing to the small uncut chip thickness values. At the same time, workpiece and tool temperatures has not been widely investigated due to the limitations of the traditional measurement methods. For example, thermocouples should not be employed because they influence the cutting conditions. Thermal camera has been used to achieve some temperature data, which result equal to few hundreds of degrees at most. It is generally accepted that the thermal expansion during machining has a negligible effect if compared with tool run-out.

1.4.2 Micro-milling tools

In most cases, micro-milling is carried out with two types of tools:

- Flat end mills, used for two dimensional components.
- Ball end mills, used for three dimensional parts.

In both cases, two-flutes tools are the most widespread. In last years, the tool production technology has considerably improved. EDM, LBM and others non-conventional micro processes allow to accomplish minimum tool diameters of 3 μm **[125]**.

Currently, cuts with few microns diameter tools have unpredictable results due to the tool weakness. Successfully used tools have a minimum diameter of 25 μm, enabling the realization of very small workpiece features. The tool edge radius r_β must be lower than uncut chip thickness. On the other hand, chip thickness may not be too much higher: micro-tools have low stiffness; consequently, high chip load would determine excessive tool deflection. For this reason, tool cutting edge radius must be in the micron magnitude order. Literature

reports r_β ranging from 0.1 μm to 5 μm and underlines the importance of tooling inspection due to the lack of information and compliance frequently found in micro-tools.

Concerning the material selection, fine-grained tungsten carbide (WC) is the most diffused, as shown in **Figure 29**. High speed steel and monocrystalline diamond are less widespread, but while the usage of the firsts is reducing, the seconds should increase in the next years. Tungsten carbide tools can be coated with different coverings (TiN, TiCN and TiAlN) to reduce wear effects. At the same time, the coatings increase the cutting-edge radius. This aspect limits their spread.

One of the most significant issues regarding micro-tools is their unpredictable behavior: often premature failure occurs with a fracture of the tool shank, differently from conventional cutting where usually the wear generates the break of a single flute.
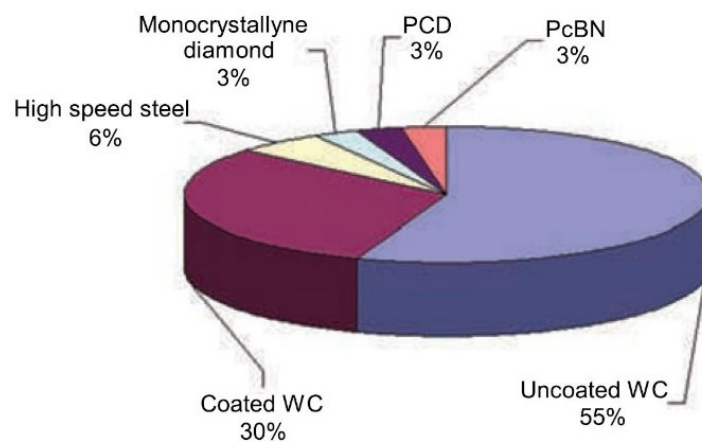
Figure 29. Materials most used for micro-tools.

The main tool failure causes in micro-milling are three:

1. Chip clogging occurs when the removed material hampers the correct tool movement. The related increase of the stress can lead to the tool fracture.
2. Failure by fatigue may take place due to the high spindle speeds employed which determines an elevated number of stress cycles.
3. Tool wear and material adhesion both lead to an increase of the cutting edge. This effect may grow the cutting forces to levels high enough to cause the failure.

An additional interesting phenomenon is tool run-out. It occurs due to the sum of the geometrical displacements of the tool axis, the spindle axis, and the tool-holder axis from the theoretical rotation axis. The ratio between this offset and the feed per tooth could be easily high in micro-milling, contrary to what happens with conventional cutting. The deviation of the tool edge trajectories involves an asymmetric cutting condition. A change of undeformed chip thickness, an imbalanced load between the flutes, a decrease of the tool life, and a reduction in workpiece quality are the main consequences of tool run-out.

1.4.3 Product final quality

The microproducts surface quality is usually investigated by using non-contact measuring systems, as optical equipment, and SEM (Scanning Electron Microscopy). These instruments are used to the surface roughness and the burr sizes. They are the main machining quality parameters in micro-milling processes.

Burr formation is the principal damage phenomenon due to the difficulties concerning its removal. In conventional cutting, burrs can be easily eliminated by suitable machines. The miniaturization makes this process more complicated and costly. The objective should be to minimize burr formation thanks to the process parameters control. At this regard, several studies show as burr size decrease as the uncut chip thickness was elevated during micro-milling. In fact, small feed rates increase the ploughing effect which favors burr development. Minimal quantity lubrication promotes the correct chip formation and consequently it minimizes the burr height. Others process parameters (cutting speed, depth of cut, tool rake angle and corner radius) should be studied to identify optimal values which lead to the reduction of the burrs thickness.

Surface roughness should be limited under a hundred nanometers by controlling the micro-cutting process. The feed rate determines the uncut chip thickness which has effects on the roughness similar to the burr formation problem: ploughing effects increase the roughness. On the other hand, when uncut chip thickness become higher than the edge radius value, the surface roughness increases as in conventional milling. The surface roughness minimum value is obtained when feed rate is equal to the cutting-edge radius. About lubrication, dry cutting led to a drastic deterioration of the tool and it reduces surface quality as consequence. Elevated cutting speeds eliminate built-up tool edge effect reducing the surface roughness. If excessive, cutting speed has the opposite effect. Optimal process parameters values can be determined experimentally because they depend on workpiece and tool material and geometry. FE model can be used to support practical machining tests.

1.5 Micromachining of AM metallic Materials

As described in paragraphs 1.1 and 1.2, the metallic parts fabricated via AM process usually require post treatments and machining. In conventional machining, the differences between traditional metallic alloys and AM materials are limited, while in micro machining the behavior deviation can be significantly higher. In fact, the chip section in micro machining is comparable to average grain size of workpiece material. Therefore, when considering the micro machinability of PBF parts, the microstructure of work material and the AM process parameters have a high impact on the machinability. Several research tackled the topic by investigating how the part building orientation, the AM parameters, the cutting conditions influences the performances of micro machining. Usually the surface integrity, tool wear, tool life, cutting forces and chip formation are considered as the relevant variables which must be monitored and studied.

Micromachining induces compressive residual stresses on AM parts, which usually are characterized by tensile residual stress after the printing. Several studied was performed on LB-PBF Ti6Al4V alloy [126,127,128] and on Inconel 718 [129]. The increasement of cutting speed and feed determine a major magnitude of the residual stress in the machined parts. Micromachining also alters the micro-hardness profile of the AM components. Ji in [129] compared the effects of different cutting speed and feed on micro-hardness between LB-PBF and wrought Inconel 718. In both cases, the increases of the process parameters determine an increase of the micro-hardening on the machined surface. Moreover, the AM alloy exhibits lower hardness if compared with the wrought one due to a higher level of porosity and less volume of precipitation of γ′ and γ ″phases. Moreover, the micro-hardness change post micro-machining of LB-PBF CoCrMo was investigated [130] by testing variable feed per tooth ranging between 0.5 and 10 μm/tooth. The hardness of micro slots increases from 597 HV to 710 HV at feeds of 0.5 and 10 μm/ tooth, respectively. The research also regarded BB-PBF: in [131] Ti6Al4V was micromachined under dry and MQL condition both. Micro-hardness resulted increased, and the improvement was higher for high cutting speeds and for samples cut in dry condition. The microstructure of the PBF components after micro-machining does not seem to reveal any markable alteration, neither in terms of phase transformation nor in terms of dynamic recrystallization. The increasement of temperature and the loads are not sufficient to alter the microstructure of LB-PBF [126,132,133] parts and BB-PBF parts [131,133].

When considering the surface finishing of micro-machined components, it is necessary to consider the ploughing phenomenon. If the uncut chip thickness is lower then the critical value MUCT, the workpiece material undergoes to an intermittently elastic-plastic deformation which lead to surface defects and high surface roughness due to elastic recovery. To evaluate the machined surface integrity, the most meaningful properties are the surface roughness and the surface topography. The final surface properties of machined parts fabricated via AM processes seem to be different if compared with the conventional counterparts: several experimental research have reported lower surface roughness values PBF parts if compared to their conventionally manufactured counterparts. For example, in [12] a comparison about micro milling of BB-PBF Ti6Al4V and extruded Ti6Al4V under different cutting speeds (35, 60, 80 m/min) and feeds (1.25–50 μm) is reported. The higher hardness of the AM material determines less plastic flow during the cut and this phenomenon leads to a lower surface roughness. Similar results were obtained in [134] by comparing the surface finishing of LB-PBF Ti6Al4V with conventionally formed alloy. Analogue trend was reported by comparing the micro-machining of wrought and LB-PBF Inconel 718 [129]. Furthermore, it was demonstrated as the roughness depends on the feed per tooth parameter; generally, Sa decreases as the feed increases due to the reduction of the ploughing effects, regardless the material [129, 133].

The only aspect which can negatively affect the surface integrity of AM metallic alloy is their porosity. It can cause interrupted cutting mechanism which determines high surface roughness if compared with conventional counterpart materials. In [128] this comparison

was performed on Ti6Al4V by machining samples with very high porosity (30% and 60%) and it was demonstrated as the surface of AM samples is worst then the wrought samples.

The surface integrity strictly depends on the cutting condition, such as the tool geometrical features, the lubrication during machining and the tool trajectories. In **[135]** an investigation about the micro-milling performances on LB-PBF AISI 316L was performed by testing two tool geometries (Ø0.6 and Ø0.8 mm) and by changing the feed direction in different angles (60°, 90°, 120°, and 180°). The results of this work demonstrated how, with the smaller tool, there was anisotropy in cutting due to the non-homogeneity of the AM part. The vibration during micro-machining is a major cause of machined surface deterioration and it strictly depends on the micro-tool employed during the cut. In **[133]** it was verified as a four-fluted end mill with a diameter of Ø0.3 mm induced higher vibration if compared with a two-fluted end mill with the same diameter, with a consequent worsening of the surface finishing. In **[131]** BB-PBF Ti6Al4V was micromachined in dry, cryogenic and MQL condition. Although the roughness was comparable regardless the cooling condition, cryogenic lubrication on one hand achieved less burrs, while on the other hand it determined more surface defects and the deterioration of the surface topography. The effect of lubrication must be considered when the tool begins to undergo to wear phenomenon. MQL allows to extend the tool life if compared with dry condition, and consequently it can improve the surface finishing **[127]**.
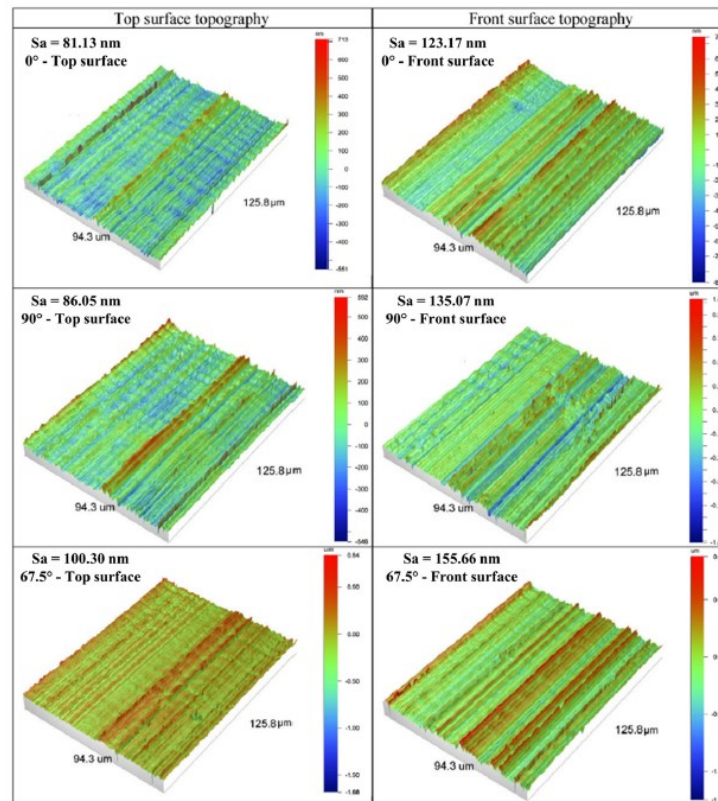
Figure 29. 3D surface topographies of SLM Ti6Al4V parts after micro machining depending on scanning strategy and building direction **[10]**.
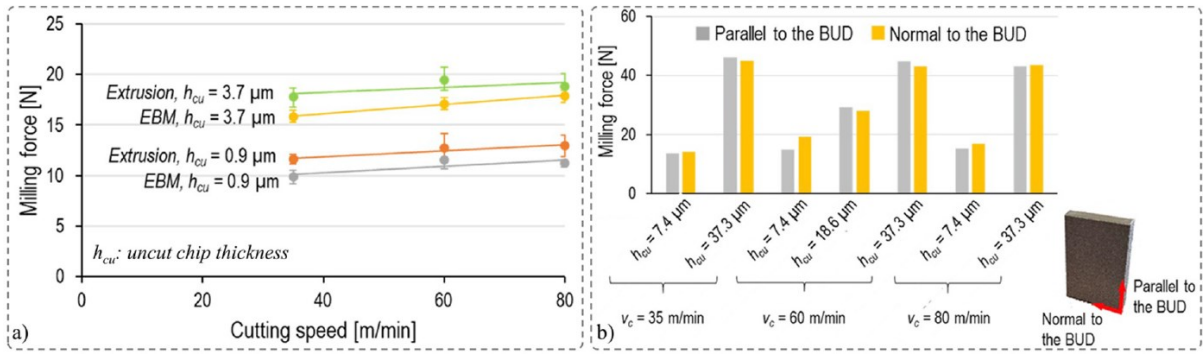
Figure 30. a) Variation of cutting force in micro milling BB-PBF and extruded Ti6Al4V and b) effect of building direction on cutting forces in micro milling BB-PBF Ti6Al4V.

The effect of the AM process parameters on the surface integrity post micro-machining must not be underestimate. In particular, the building direction and the scanning parameters can affect the surface roughness [10]. In **Figure 30** are visible the 3D surface topographies of machined surface with the same machining parameters but built with different building directions. The finishing on top and front surface is compared. According to obtained results, Sa values of front faces are higher than top surfaces of all types of LB-PBF Ti6Al4V parts. The lowest surface roughness (Sa = 81.18 nm) was obtained on top surface of LB-PBF part fabricated with 0°-line scanning strategy, where cutting direction and laser scanning strategy were parallel. On the other hand, the worst surface roughness (Sa = 155.6 nm) occurred on front surface of the LB-PBF part with 67.5°. The obtained results were associated with variation of microstructural characteristics (columnar grains, melt-pool boundaries, and their orientations) depending on cutting direction and cutting parameters.

The peculiarities of AM metallic alloys also influence the cutting force in micro-machining due to the differences about the microstructure and the anisotropic behavior. **Figure 30 (a)** shows the cutting force comparison between micro-milling of BB-PBF and extruded Ti6Al4V [12]. Although the PBF alloy exhibits higher hardness and strength, the cutting forces resulted lower if compared with the extruded alloy. The dependence of cutting force on feed rate and cutting speed is equivalent for both alloys. Similar results were published by Compos et al. [134] in case of micro-milling of LB-PBF Ti6Al4V compared with extruded Ti6Al4V in the technological window of feed per tooth 0.5–4 μm/tooth and cutting speed equal to 28.3 m/min. The effect of cutting parameter is meaningful; In [132] the same milling test were repeated by changing cutting speed between 6 and 500 m/min and feed per tooth between 1 and 20 μm/tooth. With low cutting speeds and feeds, the behavior of LB-PBF Ti6Al4V and extruded Ti6Al4V was comparable, while with high cutting speeds and feeds the LB-PBF Ti6Al4V required 3–24 % higher cutting force to be cut.

Moreover, **Figure 30 (b)** describes the effect of building direction on cutting forces during micro-milling of BB-PBF Ti6Al4V [12]. The comparison between the milling parallel to the building direction and the milling normal to the building direction shows how the effect of anisotropy on cutting force is limited. Analogue tests performed in LB-PBF Ti6Al4V [136] lead to different results. A meaningful difference about cutting force was recorded when

machining top surface and front surface. The effect of anisotropy was not neglectable also when micro-machining LB-PBF CuCrZr on front and top surfaces [137]. Cutting forces resulted higher during the micro-machining of top surface due to the different microstructure determined by different cycles of temperature during the solidification. The same research [137] also tackled the effect of heat treatments on cutting forces. Higher cutting forces were reported when machining the samples treated with solution due to the growing of ductility. On the other hand, ageing treatment caused a significant decrease in cutting forces especially at low cutting speed, thus, this condition is recommended by authors to improve machinability of SLM CuCrZr.

The tool life is a fundamental technological and economical parameter which must be evaluated in machining. Size effect in micro-machining can affect the tool life due to the material spring back, ineffective cutting highly negative rake angles, non-uniformity in material phase and slender geometry of cutting tool [123]. It is important to understand if the specific properties of AM materials can affect the tool life. A comparison on micro-milling of wrought and LB-PBF Inconel 718 allows to verify how the tool wear was 40-45 % lower when machining LB-PBF alloy due to the minor hardness [129]. On the other hand, the same machining tests were performed in [138] and the micro machinability of LB-PBF Inconel 718 resulted lower than conventional Inconel 718. In this case, the AM parts exhibit surface defects, microcracks, partially melted powders and pores which limited the effectiveness of micro-milling. The same paper [138] suggested AlTiN/Si3N4 coated tool in comparison to uncoated and AlTiN tool to improve tool life when micro-machining PBF Inconel 718. The inadequacy of uncoated tools for PBF alloys was demonstrated also by other researchers [139,133] which reported strong adhesion phenomenon.

2 Analytical models and law

Nowadays, in the industrial landscape, the necessity to develop reliable machining models is rapidly growing. The machining process modelling can be applied in several contexts, as the monitoring systems and the adaptive control. A considerable number of models have been developed in machining field in the last five decades by considering different cutting conditions, process parameters, and materials properties. In any case, a machining analytical force model computes cutting forces as a function of cutting parameters and tool geometry. A reliable force model can be used to predict the maximum cutting forces before the execution of machining operations, in order to assess if the tool will undergo excessive stresses. In this chapter an overview of the state of art about analytical modeling of milling will be described, with a special focus on micro-milling process and its specific features.

Besides this, the force model can be used for the generation of reference force data usable for the comparison with finite element method (FEM) predictions. This approach allows to refine finite element (FE) simulations by using the analytical model prediction as benchmark, without the necessity to perform a large number of experimental tests. The force model allows to generate different sets of force data without the need of expensive experimental tests and without the influence of external noise on forces evaluation. The FE simulation methods are complementary to the analytical model because the simulations easily provide additional outputs and predictions such as surface integrity, burrs formation, and stress distributions on the tool [140]. The second part of this chapter regards FE modeling of micromachining.

2.1 Models suitable for micro-machining

Machining includes a vast number of processes characterized by different tool geometries, workpiece-tool interaction and sizes. In particular, the size strongly affects the process modelling. The micro machining modelling is a complicated procedure due to the non-negligible elastic deformation, the tool run-out effect and the material behaviour discontinuity. Moreover, the chip fracture occurs at high and variable strain rates [141], in a field characterized by a relevant lack of material flow stress data. Srinivasa and Shunmugam [142] adapted a classic macro-end milling mechanistic model by considering the material strengthening and the edge radius effects. The comparison between the model prediction and the experimental data revealed an error ranging between 10% and 20%. Attanasio et al. [143] elaborated and calibrated an analytical model with the purpose of predicting the force components in slot micro milling. The tool run-out effect on the cutting edges trajectories was considered and a good matching with the experimental data was achieved. Moges et al. [144] developed a flexible force model by considering the effect of tool deflection on cutting forces. The phenomena substantially modified the tool flutes trajectories in micro machining with a considerable effect on the surface error variation in the tool axial direction.

One of the first effort to model chip thickness in milling was presented by Martellotti [145] for conventional size process. The model is based on the assumption of circular toolpath and a small ratio between the feed per tooth and the tool radius. The uncut chip thickness t_u is expressed by **Equation 2**.

$$t_u = R + f_z \sin \theta - \sqrt{R^2 - (f_z \cos \theta)^2} \qquad \text{Eq.2}$$

where R is cutter radius, f_z is feed per tooth and θ is the tool rotation angle. Several researchers demonstrated as this model allows to achieve good prediction in conventional milling, but it seems to be inadequate in micro-milling. Bao elaborated a new model to predict uncut chip thickness which is suitable for high ratio between feed per tooth and tool radius and by considering the actual trochoidal tool path. The model is expressed by **Equation 3**.

$$t_u = f_z \sin \theta - \frac{N}{2\pi R} f_z^2 \sin \theta \cos \theta + \frac{1}{2R} f_z^2 (\cos \theta)^2 \qquad \text{Eq.3}$$

Where N is the number of cutting edges. An evolution was published by Li et al. in [146,147] by finding the intersection point of the path curve left by the previous tooth and the line passing through the current tooth tip. The uncut chip thickness in expressed by **Equation 4.**

$$t_u = R * \left[1 - \sqrt{1 - \frac{2 f_z \sin \theta}{R + \frac{N f_z}{2\pi} \cos \theta} - \frac{f_z^2 \cos(2\theta)}{\left(R + \frac{N f_z}{2\pi} \cos \theta\right)^2} + \frac{f_z^3 \sin \theta (\cos \theta)^2}{\left(R + \frac{N f_z}{2\pi} \cos \theta\right)^3}} \right] \qquad \text{Eq.4}$$

Once the uncut chip thickness is geometrical computed, it can be used to calculate the chip section and to compute the cutting force. Even in this case, the specificities of micro-machining do not allow to successfully employ a conventional milling model. When considering micro milling operations, a suitable force model should not neglect the presence of different cutting conditions, depending on actual uncut chip thickness. As reported in literature [148], two subsequent stages can be detected during micro-cutting, and different cutting modes are present in each stage.

(a)   (b)
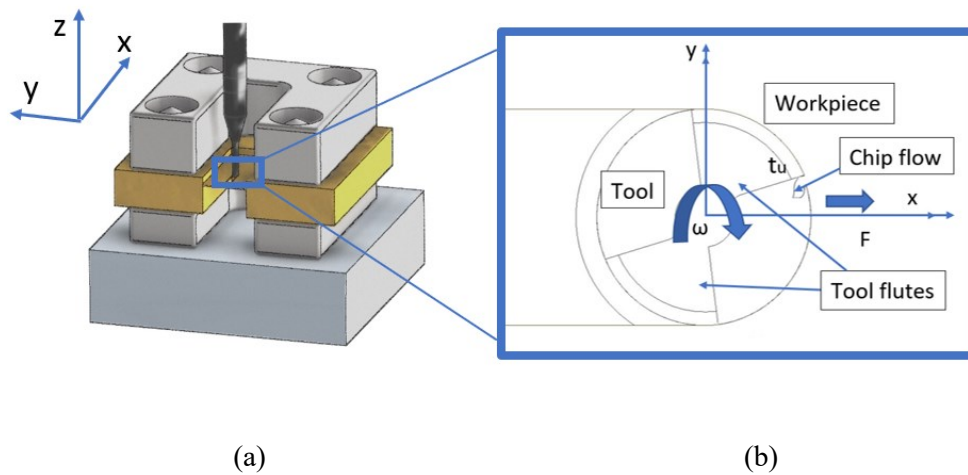
Figure 31. Slot micro machining schematization: **(a)** three-dimensional representation **(b)** two-dimensional detailed view.
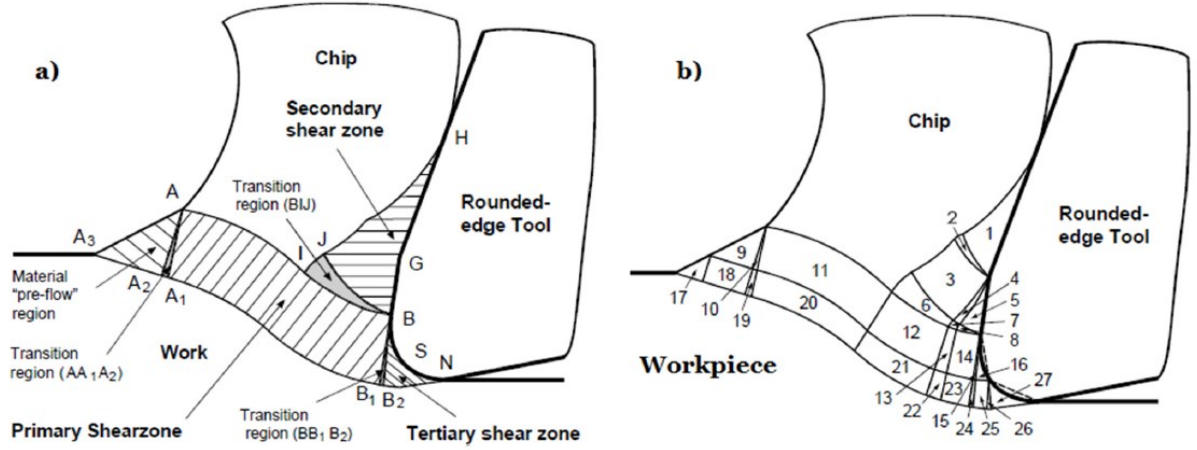
Figure 32. The division of slip-line field. (a) Three major shear zones. (b) A total of 27 slip-line sub regions.

If the uncut chip thickness is lower than the Minimum Uncut Chip Thickness (MUCT), the dominated deformation regime is known as ploughing. In this condition, a ridge of material is deformed and pushed ahead of tool cutting edge without chip formation. If the uncut chip thickness overcomes the minimum uncut chip thickness, the cutting becomes a shearing-dominated process. **Figure 31** illustrates the configuration of the slot micro milling operation. The uncut chip thickness tu ranges from zero to a maximum value equal to the feed per tooth f_z for each flute and each rotation. The ploughing phenomena inevitably characterized the micro slot cutting, regardless of process parameters. The transition to the shearing regime occurs only if the feed per tooth is greater than the MUCT. Moreover, also in this condition, the ploughing affects the process for actual chip thickness ranging between zero and the MUCT value.

Liu et al. **[149]** experimentally identified a sudden variation about thrust force and they associated it to the shift from ploughing to shear dominant cutting regime. On this experimental base, Son et al. **[150]** provided an analytical formulation of the minimum chip thickness by considering the tool edge radius and friction coefficient of workpiece material. Their work was based on an experimental investigation about the effect of friction coefficient on minimum chip thickness. Fang et al. **[151, 152]** investigated elastic recovery associated with ploughing effect in micro-milling. A slip-line field model was employed to estimate shearing and ploughing forces. The presented model consists of slip-line sub-regions, as demonstrated in **Figure 32**, each having its own physical meaning. The model accounts for the effects like shear zone effect, size effect and chip up-curl radius.

Vogler et al. **[153]** proposed the first effort to integrate the transition of cutting regimes in a micro milling analytical model. A slip-line force model was implemented to predict the cutting force when the chip thickness is greater than the minimum uncut chip thickness; in addition, an elastic deformation force model was employed when the chip thickness is smaller than the minimum uncut chip thickness. Since then, numerous force models which consider the presence of ploughing and shearing conditions have been elaborated.

Jin and Altintas **[154]** presented a non-linear model to compute the cutting forces as a function of tool edge radius and uncut chip thickness. The model considers also the tool run-out and dynamometer dynamics and can be expressed by the **Equation 5**.

$$\begin{cases} K_t(t_u, r) = \alpha_t t_u{}^{d_t} + \beta_t t_u{}^{p_t} r^{q_t} \\ K_r(t_u, r) = \alpha_r t_u{}^{d_r} + \beta_r t_u{}^{p_r} r^{q_r} \end{cases} \qquad \textbf{Eq.5}$$

Where factor K_t indicates the force components in tangential direction while K_r indicates the force components in radial direction; r is the tool edge radius and α, β, d, p, q are unknown coefficients.

Rodriguez & Labarga **[155]** proposed an analytical force model by considering the run-out eccentric deviation, the tool deflection and the size effect. The model was expressed through a set of linear equations which considered the MUCT in order to define the entry and the exit angles of the milling tool in the workpiece. Malekian et at. **[156]** developed a ploughing force model which calculates the effect of elastic recovery by considering the interference volume between the tool and the workpiece. A conventional mechanistic model was implemented to calculate the shearing cutting force. The ploughing-shearing transition was identified with the purpose of understanding when each model should be used during the tool flute path. Chen et al. **[157]** proposed an analytical model that alternatively considers ploughing or shearing cutting conditions depending on the value of uncut chip thickness. The model calculates the instantaneous uncut chip thickness by considering the tool run-out and the machine tool system vibrations. Several experimental tests confirm that the model provides more accurate cutting force prediction than conventional models. Zhang et al. **[158]** elaborated a similar model which was validated by performing a series of micro end milling experiments on Al6061 workpieces under different cutting conditions. The real engagement is identified under the tool run out effect, the average uncut chip thickness, actual cutting depth, center position and geometrical relations are analytically established. This leads to better adaptability and eases process modeling and online control.

2.2 FE modeling of micro-machining

From 1970's, Finite Element Method (FEM) has been recognized as a valid technique for reducing trial and error approaches in the design and optimization of numerous processes. In last decades, several studies and research have been involved in the effort to take advantage of FEM also in machining. Traditional analytical models can be defined to describe a machining problem and to predict cutting forces, chip flow, and tool wear. However, they frequently run into several difficulties, regarding the material plasticization, the dynamic hardening, the thermal softening, the chip curvature, and the behavior at the work-tool interface.

Numerical models are an alternative and powerful instrument to solve these issues where the non-linearity is involved. Finite Element (FE) software packages discretize the objects in a high number of delimited elements connected each other by some nodes. Subsequently, they

use numerical methods to solve the complex equation systems and simulate the actual process. An accurate workpiece and tool material behavior characterization must be implemented in the software to achieve reliable results. In machining context, further difficulties arise due to the chip formation, which is a difficult process to analyze even by the Finite Element Method and FE software packages.

In FE framework, the problem modelling assumes a key role. Simulations can be prepared by controlling multiple variables, as the number of the elements, their geometries, the friction, the thermal aspects and several others which are widely discussed in this section. The decisions are frequently a trade-off between accuracy and computational time.

Firstly, it is crucial to decide whether to adopt a 2-dimensional (2D) or a 3-dimensional (3D) method. Two-dimensional FE simulations are suitable only for the processes where the orthogonal cutting hypotheses are verified. The orthogonal cutting model is described in this section. Although 2D FE simulations offer some distinct advantages, 3D FE models provide more realistic oblique configurations, mainly in milling processes with complex cutting tool geometries. Three-dimensional FE simulations present supplementary analysis capabilities to investigate the effect of the helix angle and tool edge radius on chip flow and burr formation, which are almost impossible to be considered by 2D FE models.

2.2.1 Orthogonal cutting

The cutting dynamic is quite often three-dimensional in the actual machining processes. **Figure 33** shows a turning example to illustrate a generic chip formation mechanism. The basic process parameters are three:

1. The cutting speed, v_c, is the relative speed between tool and workpiece in the cutting direction.
2. The feed rate, f, is the relative speed in the tool advancement direction. It allows moving forward the cut along a determined path.
3. The depth of cut, a_p, is the workpiece thickness stock to be removed. It is measured in the orthogonal direction to the feed.

 The contact between the tool and workpiece generates a force, which can be decomposed in three orthogonal components:
1. F_1 has the opposite direction of the cutting speed, v_c, also called cutting force.
2. F_2 has the opposite direction of the feed rate, f, also called feed force.
3. F_3 is orthogonal to F_1 and F_2 also called thrust force. In the turning example, it has the radial direction.
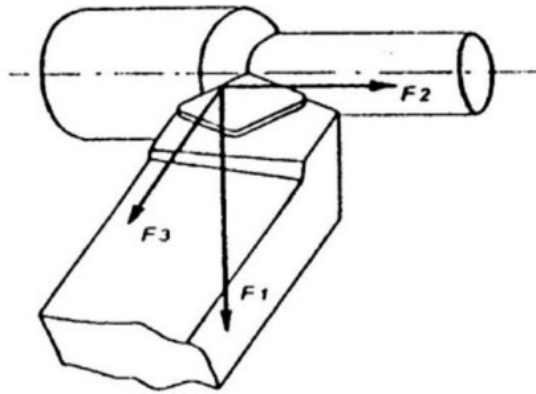
Figure 33. Cutting force components.

If all the relative motions, included the chip flow speed v_t, are in the plane normal to the cutting edge, a simplified situation is achieved. The force resultant belongs to the same plane. In this condition, the cutting configuration is considered "orthogonal". It is a two-dimensional model which allows an easier study of the chip formation process with plane strain assumption for material deformation. It is represented in **Figure 34**.

(a)   (b)
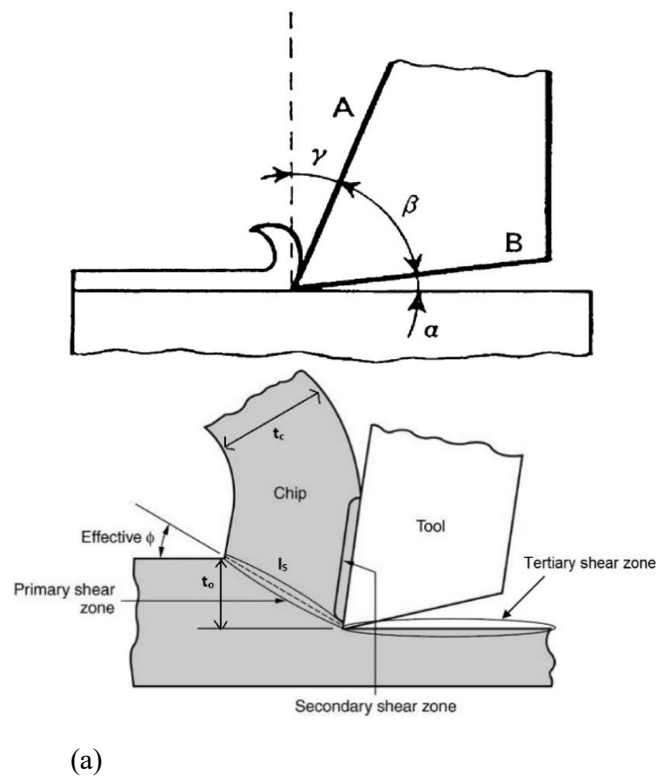
Figure 34. Orthogonal cutting modelling: angles (on the left) and deformation zones (on the right

The single-ended tool inclination in relation to the workpiece can be described by only two angles:

1. Tool rake angle, γ, is the angle between the rake face and the normal to the cutting edge and the workpiece surface. It could be positive, negative, or equal to zero. It has a key role in chip formation process by influencing its speed, curvature, and morphology.
2. Tool side clearance angle, α, is the angle between the side and the workpiece surface. It avoids the friction between the two objects.

Angle $\beta = 90° - \alpha - \gamma$ is the tool solid angle. This angle influences the tool strength and the tool capacity to separate the material. Orthogonal cutting tests can be developed similarly to wood planning process. Experimental evidence shows how the plastic deformation is mostly concentrated in three zones:

1. The primary shear zone extends from the cutting edge to the area where the chip starts to curve. It is the main plastic deformation zone, and it may be approximated by a straight surface inclined at an angle, ϕ, to the cutting speed direction.
2. The secondary shear zone is developed along the tool-chip contact surface. The material deformation is produced by the friction.
3. The tertiary shear zone is localized under the tool side. It is determined by the friction between the tool and the cut surface due to the elastic recovering effect. Angle α influences the extension of this zone.

An analytical model capable to describe the orthogonal cutting may be developed by considering a steady-state operation and by neglecting the secondary and the tertiary shear zones. Its purpose consists in the determination of shear angle ϕ: once ϕ is well-known, others information as the cutting forces, the dynamics, and the deformations can be calculated. The problem should be solved by considering the geometrical modelling shown in **Figure 34**:

* t_o is the uncut chip thickness whereas t_u is the actual chip thickness.
* l_s the length of the straight shear surface.

Trigonometry applied on **Figure 35** allows writing the **Equation 6** and **Equation 7**, while **Equation 8** can be obtained as the ratio between **6** and **7**:

$$t_o = l_s \cdot \sin \emptyset \qquad \qquad \textbf{Eq.6}$$

$$t_c = l_s \cdot \cos(\emptyset - \gamma) \qquad \qquad \textbf{Eq.7}$$

$$c = \frac{t_o}{t_c} = \frac{\sin \emptyset}{\cos(\emptyset - \gamma)} \qquad \qquad \textbf{Eq.8}$$

From **Equation 8**, angle ϕ can be obtained once that ratio c is well-known.

The uncut chip thickness, t_o, is determined by the process control; in end-milling it is not constant but change from 0 to the feed per tooth, f_z, by rotating the tool. Instead, the actual chip thickness, t_c, is unknown. It can be directly determined by measuring some chip samples. In micro-machining, it is difficult due to the length scale; chip thickness is typically

equal to a few micrometers. An indirect measure can be obtained by assuming the volume constancy as shown by **Equation 9**:

$$V_o = t_o w_o L_o = V_c = t_c w_c L_C$$ **Eq.9**

Where w_o is the uncut chip width, w_c is the actual chip width, L_o the uncut chip length and L_c the actual chip length. The uncut chip measurements are all known because they depend on the process parameters. L_c and w_c are easier to measure than t_c due to their bigger size and thus the actual chip thickness could be obtained by using **Equation 9**.

Figure 35. Angles involved in φ calculation.

Once angle ϕ has been calculated, it is possible to determine the cutting forces value. The contact between tool and workpiece produces a force with resultant equal to R. It may be decomposed in three different reference systems, as it is shown in **Figure 36**:

- Along the shear surface and in the orthogonal direction. The components are respectively F_s and F_n, both red colored.
- Along the cutting direction (F_y) and the orthogonal direction (F_x). They are yellow coloured. F_y and F_x can be measured by a loadcell.
- Along the rake face (T) and the orthogonal direction (N). They are blue coloured.

The last decomposition $\vec{R} = \vec{T} + \vec{N}$ is useful for determining the resultant direction ρ: $\vec{T}$ is a frictional force which can be calculated as $T = \mu \cdot N$ by using Coulomb model. Considering that $T = R \cdot \sin(\rho)$ and $N = R \cdot \cos(\rho)$, angle ρ can be obtained as:

$$\rho = \arctan(\mu)$$ **Eq.10**
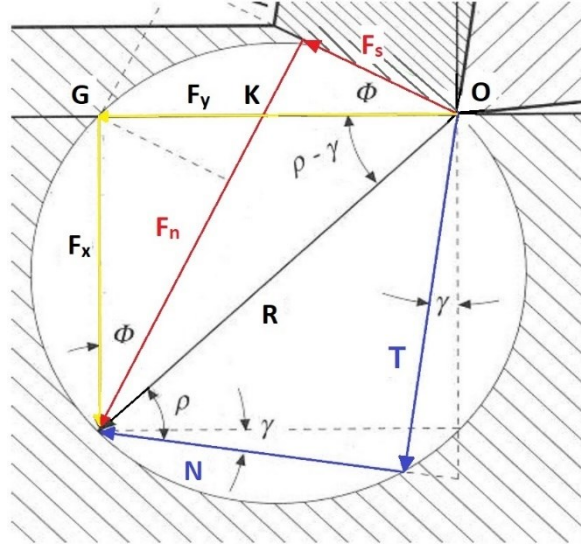
Figure 36. Cutting force R decomposition along three different reference systems.

F_s and F_n can be used to calculate the average stress along the cut plane:

$$\tau_s = \frac{F_s}{w_o l_s} = \frac{F_s}{w_o t_o} \sin(\emptyset) \qquad \textbf{Eq.11}$$

$$\sigma_s = \frac{F_n}{w_o l_s} = \frac{F_n}{w_o t_o} \sin(\emptyset) \qquad \textbf{Eq.12}$$

To obtain F_s and F_n from the measurable forces F_x and F_y some trigonometrical relations must be developed:

$$F_s = \overline{OK} \cdot \cos(\emptyset) = (\overline{OG} - \overline{GK}) \cdot \cos(\emptyset) = (F_y - F_x \tan\emptyset) \cdot \cos(\emptyset) =$$

$$= F_y \cdot \cos(\emptyset) - F_x \sin(\emptyset) \qquad \textbf{Eq.13}$$

$$F_n = F_y \cdot \sin(\emptyset) + F_x \cos(\emptyset) \qquad \textbf{Eq.14}$$

Equation 11 and **Equation 12** can be used to predict F_s and F_n if stress σ_s and τ_s are considered as the material yield strengths. The reliability of the prediction is deeply affected by the angle $\emptyset$ estimate. It can be determined also by using one of the numerous models developed between 1940s and 1970s. Ernst and Merchant (1942) elaborated a model by considering an orthogonal cutting operation with continuous chip. They assumed that the shear surface has the inclination $\emptyset$ which minimizes the cutting power P_t. It can be calculated by using **Equation 15**.

$$P_t = F_y \cdot v_c \qquad \textbf{Eq.15}$$

If the cutting power is minimum, the derivative should be zero.

$$\frac{dP_t}{d\emptyset} = \frac{dF_y}{d\emptyset} v_c + \frac{dv_c}{d\emptyset} F_y = 0 \qquad \textbf{Eq.16}$$

In steady state, v_c is a constant and its derivative is zero. It means that $\frac{dF_y}{d\phi}$ must be zero. F_y can be expressed as a function of angle ϕ considering **Figure 36**.

$$F_y = R \cdot \cos(\rho - \gamma) \qquad\qquad \textbf{Eq.17}$$

$$F_s = R \cdot \cos(\rho - \gamma + \phi) \qquad\qquad \textbf{Eq.18}$$

By using **Equation 11, 17, 18**, it is possible to obtain **Equation 19**:

$$F_y = \frac{\tau_s w_o t_o \cdot \cos(\rho - \gamma)}{\sin(\phi)\cos(\rho - \gamma + \phi)} \qquad\qquad \textbf{Eq.19}$$

The derivative $\frac{dF_y}{d\phi} = \tau_s w_o t_o \frac{\cos\varphi\cos(\rho - \gamma + \phi) - \sin\varphi\sin(\rho - \gamma + \phi)}{(\cos(\rho - \gamma + \phi))^2 (\sin(\phi))^2}$ put equal to zero allows determining the value of angle ϕ as:

$$\phi_{EM} = \frac{\pi}{4} + \frac{\gamma}{2} - \frac{\rho}{2} \qquad\qquad \textbf{Eq.20}$$

This primitive model often predicts results significantly distorted due to the weakness of numerous hypothesis done. As example, stress τ_s depends on temperature, strain rate and other variables. More reliable models (as Merchant modified, Lee and Shaffer, and Huchs) were developed by introducing constants and correction factors experimentally determined. Their spread was limited by the diffusion of the FE method, a powerful instrument which operating principles are addressed in the next section.

2.2.2 FEM foundation

Finite Element Methods is an expression used to indicate a wide range of mechanical and thermal analysis methods. They shall be distinguished by how material stress–strain relations are implemented, how flow variations are described, how the elements are constructed and how some factors more specific to metal machining are dealt with. Generally, FE software have the advantage of dealing with non-orthogonal situation which are very common in the actual processes. For example, the cutting- edge radius does not allow maintaining the chip speed perpendicular to the cutting edge and leading to a violation of the orthogonal cutting hypothesis. FE allows to address three-dimensional problems and to exploit the increasing computational power available.
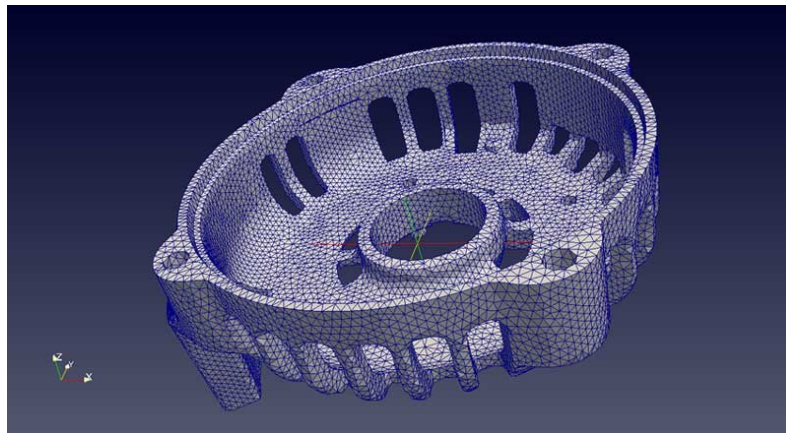
Figure 37. An example of workpiece 3D mesh.

A common feature of all Finite Element Methods is the replacement of a continuum by an assembly of elements named nodes. In the continuum, the problem variables are defined for each point; in the FE object they are determined only on the nodes. Between the nodes, the values of the variables are determined by interpolation. The group of the elements delimited by the nodes is indicated as the object mesh. An example is shown in **Figure 37**. The discretization is necessary to have a limited number of points where stress and strain may be calculated. The mesh density is obviously a trade-off between accuracy and reasonable computational time. For each mesh element, the software elaborates a stiffness matrix $[K_i]$ by using its geometry and the flow stress law. It expresses the relation between stress, strain, strain rate, and temperature and depends on the workpiece material. Then the stiffness matrixes are composed superimposing the parts regarding adjacent nodes. The global stiffness matrix $[K]$ complies with the boundary condition and the relative node displacements. Under the assumption of workpiece elastic behavior, $[K]$ may be used to solve the matrix **Equation 21.**

$$[K] \cdot \{\delta\} = \{F\} \qquad\qquad\qquad \textbf{Eq.21}$$

where $\{\delta\}$ and $\{F\}$ indicate respectively the nodes displacements and the external loads. The column vector $\{F\}$ is a well-known quantity, thus the matrix equation is a set of linear equations for the unknown displacements $\{\delta\}$. Once the matrix equation is solved, strain and stress can be found. In plastic flow conditions, typical of all the machining and forming process, some difficulties arise. In fact, the strains have elastic and plastic parts. The plastic components are proportional to the total stress components, but the elastic parts depend only on the stress increments. If elastic effects are neglected, it is natural to consider nodal velocities $\dot{\delta}$ instead of displacements δ. The matrix **Equation 22** may be resolved to determine the nodal speeds.

$$[K] \cdot \{\dot{\delta}\} \mathrm{d}t = \{F\} \qquad\qquad\qquad \textbf{Eq.22}$$

The **Equation 22** solution is complicated due to the dependence of global stiffness matrix $[K]$ by the displacements. It can be solved by using the implicit method, more precise but time consuming, or the explicit method, faster and reliable for process with small deformation as machining. If elastic effects are not negligible, it is necessary to integrate the solution of **Equation 22** along the element's loading path, from the initially unloaded to the current position. The elasto-plastic analysis ensures a more accurate processes description, but the elevated degree of non-linearity requires high computational power. For this reason, usually only the plastic model is utilized. During chip formation the deformations are localized. In machining, extensive workpiece portions remain in elastic field, thus the plastic hypothesis may be limited. On the other hand, some studies [159] have shown that to neglect elastic effects does not have a negative consequence about forces prediction. Poor results were obtained about tool wear prediction instead.

FE methods are divided between two groups, depending on the adopted technique to discretize the objects:

1. If the mesh flows with the workpiece, the method is called **Lagrangian**. In this case, the target is to calculate how the elements velocity changes in the time. The element shape is not constant, but its geometry is modified during the flow. Consequently, the matrix [K] requires continued updating with an increase of the non-linearity in the problem. The mesh evolution may lead to excessive distortions and thus re-meshing is required.

2. If the mesh is fixed in the space and the material flows through it, the analysis is called **Eulerian**. The attention is focused on how the speed changes from node to node. The mesh element shape constancy simplifies the global stiffness matrix [K] determination. The solution convergence is facilitated by the limited mesh distortions. An issue regarding the Eulerian view is how describe the material properties changes from element to element. For this reason, Eulerian analyses are more common in fluid mechanics because their properties vary less with deformation than solids.

2.2.3 Material flow stress

The material flow stress can be described by different material constitutive laws in plastic field. The choice between the available models is strongly influenced by the process conditions. It is fundamental to distinguish the static working condition from the dynamics. The decisive factors are the strain and the strain rate. In metals, the material hardening with high strain/strain rate is widely common. It means that the stress necessary to deform the work material in plastic field it is not constant, but it increases at high strains and/or strain rates. **Figure 38** shows an example of strain rate influence on the material resistance.
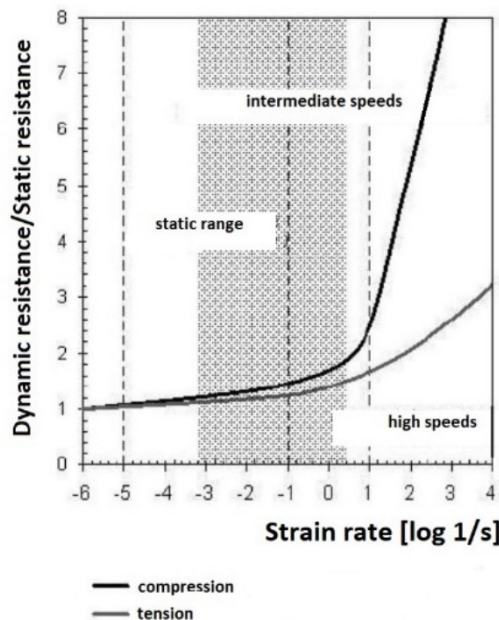
Figure 38. Example of the relation between the resistance and the strain rate in a metal alloy.

Johnson-Cook law allows to consider the stress as a function of the strain ε, the strain rate $\dot{\varepsilon}$, and the temperature T. It is a multiplicative model because the stress-strain relation in static

condition is corrected taking into account of the strain rates and the temperature variations. The Johnson-Cook law is expressed by **Equation 23**:

$$\sigma_{eq} = \underbrace{[A + B(\varepsilon)^n]}_{\text{STRAIN}} \underbrace{\left[1 + C\log\left(\frac{\dot{\varepsilon}}{\dot{\varepsilon}_0}\right)\right]}_{\text{STRAIN RATE}} \underbrace{\left[1 - \left(\frac{T-T_0}{T_{melt}-T_0}\right)^m\right]}_{\text{TEMPERATURE}} \qquad \textbf{Eq.23}$$

Where:

- σ_{eq} Von Mises equivalent stress (MPa)
- ε true strain
- $\dot{\varepsilon}$ true strain rate
- $\dot{\varepsilon}_0$ reference strain rate ($\dot{\varepsilon}_0 = 1\ \mathrm{s}^{-1}$)
- A static yield stress (MPa)
- B, n represent the effects of strain hardening
- C strain rate constant
- m temperature exponent
- T material temperature
- T_{melt} melting material temperature
- T_0 reference material temperature

The law is a product of three factors thus the strain, strain rate and temperature effects are considered independently of each other:

1. The first factor expresses the correlation between stress and strain at environment temperature T=293 K and for $\dot{\varepsilon}_0 = 1\ \mathrm{s}^{-1}$.
2. The second factor reflects the strain rate hardening.
3. The third factor expresses the thermal softening. When T is close to T_m, the material strength is significantly reduced.

Table 1 shows the model parameters value for some material. To determine them, it is necessary to develop some experiments, as tensile, compression and torsion test.

Table 1 Johnson-Cook constants for some material **[160]**.

Material	T_M [K]	A [MPa]	B [MPa]	n	C	m
OFHC Copper	1356	90	292	0.31	0.025	1.09
Nickel 200	1726	163	648	0.33	0.006	1.44
Cartridge Brass	1189	112	505	0.42	0.009	1.68
1006 steel	1811	350	275	0.36	0.022	1.00
2024 T351 Aluminium	775	265	426	0.34	0.015	1.00
7039 Aluminium	877	337	343	0.41	0.010	1.00
4340 steel	1793	792	510	0.26	0.014	1.03
Tungsten alloy	1723	1506	177	0.12	0.016	1.00

The parameter A is equivalent to the tensile yield stress determined in static condition. It is indicated by point 1 in **Figure 39**. Parameters B and n depend only by the plastic segment of the stress-strain curvature (in **Figure 39**, from the point 2 to point 3). If it is plotted in a double logarithmic diagram, B is equal to the difference σ - σ_y calculated when the plastic strain ε_p = 1. The exponent n is the graph slop.

The parameter *C* can be determined by executing several tests with different strain rates, at the same temperature. The coupling effect of stress-strain rate must be plotted in a double logarithmic diagram; *C* is equivalent to the graph slop. The exponent *m* can be obtained by solving the **Equation 24**.
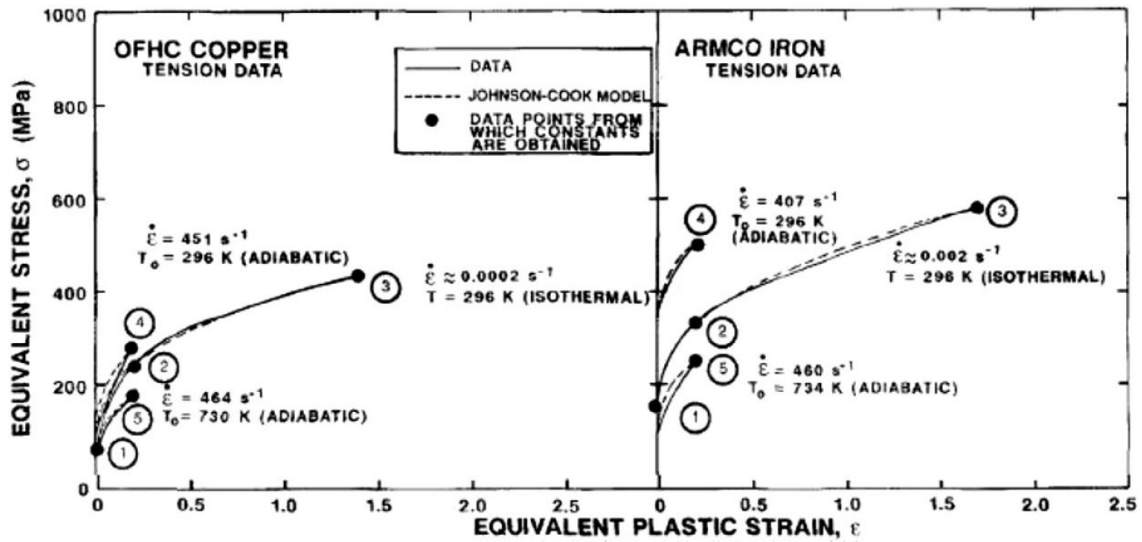
Figure 39. Flow stress for two materials. The point essential to determine the Johnson-Cook parameters are indicated with a number ranging from one to five.

$$m = \frac{\log\left(1 - \frac{\sigma_{eq}}{\sigma_r}\right)}{\log T^*}$$ **Eq.24**

Where σ_r is the stress corresponding to point 2 in **Figure 39**, σ_{eq} is the stress corresponding to the same strain of σ_r, but for the test executed at temperature *T*. The normalized T^* can be calculated by using the **Equation 25**.

$$T^* = \frac{T - T_0}{T_M - T_0}$$ **Eq.25**

A good flow stress model should represent the material behavior with the best accuracy but without being too much complex: the material parameters must be determined with a limited number of simple tests. The Johnson-Cook model offers a good prediction about the stress dependence on the strain. On the other hand, for some metallic alloy, it underestimates the material hardening at high strain rates. For this reason, some model variants were developed.

T.J. Holmquist e G.R. Johnson **[161]** proposed an exponential strain rate dependence instead the logarithmic one. W.R. Rule e S.E. Jones **[162]** suggested an improvement of the original

Johnson-Cook model, suitable with strain rate higher than $10^3 \, \text{s}^{-1}$. It does not deteriorate the law predictions at low and intermediate speeds. The law can be expressed by **Equation 26**:

$$\sigma = \left[A + B(\varepsilon)^n \right] \left[1 + C_1 \log \frac{\dot{\varepsilon}}{\dot{\varepsilon}_0} + C_2 \left(\frac{1}{C_3 - \log \frac{\dot{\varepsilon}}{\dot{\varepsilon}_0}} - \frac{1}{C_3} \right) \right] \left[1 - \left(\frac{T - T_0}{T_{melt} - T_0} \right)^m \right] \qquad \textbf{Eq.26}$$

If compared with **Equation 23**, it is possible to observe three new constants: C_1, C_2 and C_3. The first constant C_1 is equivalent to C in the original model. Constants C_2 and C_3 appear in the section which has been added with the aim to increase the strain rate dependence. The factor $C_2 \cdot \left(\frac{1}{C_3 - \log \frac{\dot{\varepsilon}}{\dot{\varepsilon}_0}} - \frac{1}{C_3} \right)$ tends to infinite if $\log \frac{\dot{\varepsilon}}{\dot{\varepsilon}_0} \rightarrow C_3$, but clearly it is not possible. Thus, Rule and Jones introduced a fourth constant C_4 as a superior limit to the strain-rate factor.

It means that:

$$\left[1 + C_1 \log \frac{\dot{\varepsilon}}{\dot{\varepsilon}_0} + C_2 \left(\frac{1}{C_3 - \ln \frac{\dot{\varepsilon}}{\dot{\varepsilon}_0}} - \frac{1}{C_3} \right) \right] \leq C_4 \qquad \textbf{Eq.27}$$

In FE software packages the flow stress rule may be implemented by using pre-set models or uploading some stress-strain-strain rate-temperature charts.

2.2.4 Chip separation modeling

The simulation of machining requires to separate the chip from the workpiece by implementing a specific strategy. In literature, two methods namely chip separation criterion method and pure deformation method are mostly employed [163]. In the first case, a geometrical or physical separation criteria [163, 164] is used to delete some mesh elements in the workpiece, with the purpose to facilitate the chip formation process by reducing the distortion of the mesh. The geometrical criterion requires that the chip separation occurs when the distance between the tool and the nearest node of the workpiece exceeds a specific limit. The physical criterion allows to separate a pair of coincident nodes or, as an alternative, to delete an element when a physical variable (i.e., stress or equivalent plastic strain) reaches a predefined threshold. In this last case, the FE requires a damage model with a critical value.

The critical value can be considered as the total accumulated damage until failure. It depends on the process and the material. All the fracture criteria are developed from the Freudenthal critical plastic work per unit of volume. It is expressed by **Equation 28**:

$$\int_0^{\varepsilon_f} \sigma \, d\varepsilon = C_1 \qquad \textbf{Eq.28}$$

Where the symbol σ indicates the effective stress, $d\varepsilon$ is the effective strain increment and ε_f is the effective strain at fracture. Cockcroft and Latham suggested an alternative to emphasise the largest tensile stress rule. It is expressed by the **Equation 29**.

$$\int_0^{\varepsilon_f} \sigma_1 \, d\varepsilon = C_2 \qquad \textbf{Eq.29}$$

Where σ_1 indicates the largest tensile principal stress. A normalized version was determined. It is expressed by the **Equation 30**.

$$\int_0^{\varepsilon_f} \frac{\sigma_1}{\sigma} \, d\varepsilon = C_3 \qquad \qquad \textbf{Eq.30}$$

(a)   (b)
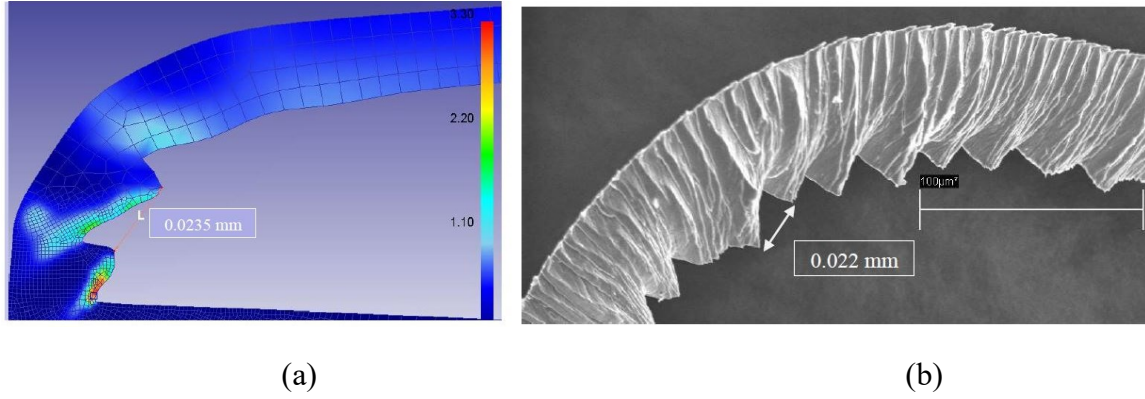
Figure 40. Comparison between FE (a) and experimental (b) chip morphology.

A correct calibration of the fracture criteria allows to determine the chip segmentation for Lagrangian FE methods. The Cockcroft and Latham criterion advantage is its simplicity: only one constant should be determined by experimental tests. FE packages, as DEFORM™, propose several criteria by default and the user only needs to fix the critical value. **Figure 40** shows the correct chip morphology prediction attained by the fracture criterion calibration. An inaccurate chip separation criterion affects the computation of the residual stress in workpiece **[164, 165]**, while the cutting forces are not affected **[165, 166]**.

The second method to achieve chip separation in FE model is the pure deformation method. In that case, the workpiece elements deform around the tool tip and no chip separation criterion is required. However, the deformation in some elements is elevated and the elements distortion is unneglectable. Therefore, Adaptive Remeshing techniques are usually employed to allow the progress of the simulation. The pure deformation method usually employs upgrading/modifying material constitutive models **[167-171]** without employing a damage model.

Calamaz et al. **[167]** firstly developed an upgraded Johnson-Cook model, called TANH material model, with the purpose to simulate discontinuous chips in orthogonal cutting Ti-6Al-4V alloy. The authors modified the plastic strain term by adding a Tangent Hyperbolic function to model the strain softening effect. A second release of the model **[168]** allowed to refine the original version, by providing the softening effect only at high temperature, equal to 0.3 times the melting temperature of the workpiece material.

2.2.5 Literature review about FE modeling of machining

Here it follows a brief description of the most meaningful attempts to simulate machining through FE methods. Ozel and Altan **[172]** developed a methodology to simulate flat end milling operations and to correctly predict chip flow, cutting forces, tool stresses and temperatures using finite element analysis. A flow stress model for P20 steel depending on strain, strain-rate and temperature was used, coupled with a friction model based on shear flow stress of the workpiece at the chip–tool interface. The material data were obtained by

performing conventional turning experiments. Umbrello [173] simulated both conventional and high-speed turning of TiAl6V4 by comparing three different set of flow stress data. The Cockroft-Latham damage criterion ensured to model the chip serration while the best prediction of cutting force was achieved only with flow stress extrapolated by split Hopkinson's bar tests. The methodology permits to cover the ranges strain rate similar to those reached in conventional and high speed turning (10^2-10^4 s-1). Dhanorker and Ozel [5] performed 2D simulation on meso and micro scale slot milling of AL 2024-T6 aluminum and AISI 4340 steel. The Minimum Uncut Chip Thickness (MUCT) effect was considered by using an analytical model developed by Liu et al. [124]; FEM allowed to predict the chip formation, forces, strain, strain-rate and temperature fields without considering process dynamics. In 2010 Afazov et al. [174] employed ABAQUS to develop a new approach for predicting micro-milling cutting forces using the finite element method. Cutting tool radius, feed rate, spindle angular velocity, number of flutes and tool run-out were considered in the orthogonal cutting model. A relationship between the cutting forces, uncut chip thickness and cutting velocity was described by a non-linear equation for AISI 4340 steel. Jin and Altintas [154] perform simulation of orthogonal machining of Brass 260 to calibrate a model capable of predicting cutting force in micro-milling considering the tool trajectory, run-out and the dynamometer dynamics.

In 2011, Calamaz et al. [170] applied their modified version of Johnson-Cook material model to simulate segmented chip formation in orthogonal machining of Ti-6Al-4V alloy. Ducobu et al. [171] compared three different models including ALE with TANH material model, Lagrangian with Johnson-Cook model, and Lagrangian with TANH model to simulate the chip formation in orthogonal cutting of Ti-6Al-4V alloy. The simulated segmented chip had good agreement with the available experimental ones when the third model was used, demonstrating the reliability of the strain softening effect to accurately simulate the chip formation during cutting Ti-6Al-4V alloy. In recent years, Jomaa et al. [175] carried out the simulation and experimental test of orthogonal turning AA7075-T6 aluminum. The simulation was conducted using the DEFORM software, and reasonable agreement between the simulated and experimental chip geometry and segmentation intensity was observed. In the same period, Menezes et al. [176] utilized a damage material model chip fragmentation to simulate discontinuous chip formation in machining. The numerical analysis was utilized to investigate the effects of rake angle and friction factor on the chip breakage.

Few works were dedicated to micro-machining. Ucun and Aslantas [177] deepened the effect of the cutting-edge angle in micro-machining of Inconel 718. The numerical method of analysis was utilized to investigate the chip morphology, the thermal aspects of cutting, the cutting forces and the tool stress distribution. The FE simulation of micro-machining of Inconel 718 were performed also by Shi et al. [178], in order to investigate the ploughing cutting regime and how it influences the surface quality. The numerical model confirms the value of the Minimum Uncut Chip Thickness (MUCT) experimentally determined through the analysis of Acoustic Emission (AE) signal. A larger analysis about the effects of the process parameters on machining outputs was published by Zhou and Sun [179] in 2019. 2D-FE analysis were performed by using ABAQUS and by modelling the Al-Si alloy ZL109

mechanical behavior with the Johnson-Cook model and a shear damage model. In 2020 Sahoo and Patra [180] performed 3D intermittent oblique cutting finite element method (FEM) simulations for micro milling of Ti6Al4V alloy. They predicted the stability limit in micromachining and cutting force more precisely as compared to those obtained by traditional orthogonal cutting simulation. In literature was not found any trial to simulate micro-machining of AM materials.

2.2.6 Software for FE simulation of micro-milling process: DEFORM™

The software DEFORM™ is the Lagrangian FE computer software which was employed for the micro-milling simulations in this doctoral research work. It was developed by Scientific Forming Technologies Corporation (SFTC) from Columbus (Ohio, USA). The FE code was created with the aim to accurately simulate plastic deformation process as metal pressing. DEFORM™ achieves excellent result in that field, but it can be employed also in other context, as machining. The final results and outputs obviously are heavily dependent on the input data accuracy: they must be carefully defined to achieve a reliable simulation.

The process miniaturization introduces a certain number of effects which were illustrated in the Chapter 1. FE software packages may run into several difficulties at this scale. It depends on the software ability to take account of the size effects. An accurate workpiece mesh definition has a great importance, but it is difficult due to the minimal element size which slow down the software and sometimes make it crash. The mesh, as all the other input data, must be defined in a dedicated software section called "Pre-Processor". In this software part, also the problem dimension (2D or 3D) must be defined. Once the simulation database is ready, the simulation may be initiated in "Simulator" section. Finally, the achieved results can be analyzed in "Post-Processor" section. In this paragraph, the main software features are illustrated and discussed.

2.2.6.1 Pre-Processor

The Pre-Processor is the software section dedicated to the simulation setting. In **Figure 41** the user-friendly interface is shown. On the left, it is possible to see a CAD drawing space where the workpiece and the tool can be defined as objects. Their geometry can be imported from an external source (.STL, .GEO, .IGS are some of the available formats) or can be defined by using some basic available shapes.
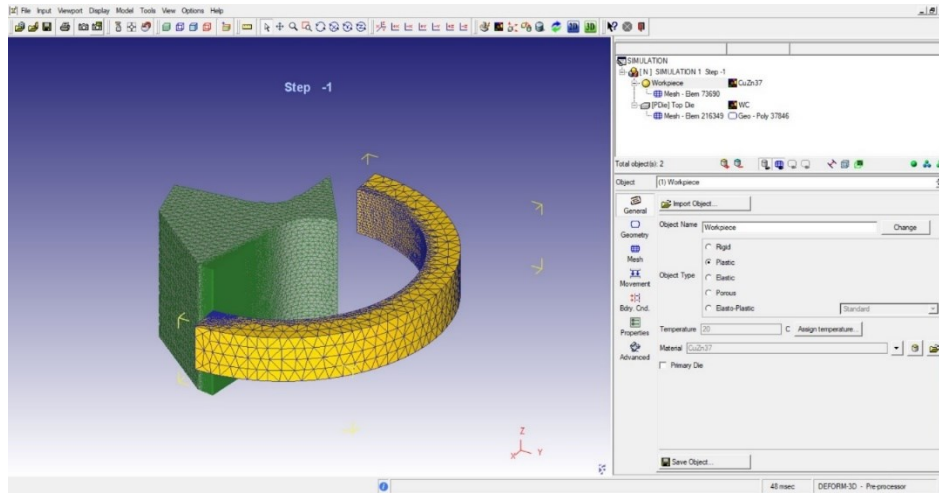
Figure 41. DEFORM^{TM} 3D pre-processor interface window.

With 2D problem, the object geometries can be defined also point by point: the x-y coordinates must be indicated, and the software connects them by using segments. Corner radius may be used to obtain curvatures. On the right and on the top, it is possible to see the five icons of the parts which constitute the Pre-Processor:

- The **simulation control** allows to define many FE general settings. The concerning software windows is shown in **Figure 42**. It is possible to define the unit's type by choosing between International System and English System, to pick the FE typology as the standard Lagrangian or specific settings, to define the simulation mode by activating heat transfer and deformation. The time discretization can be controlled by defining the magnitude which determines the step increment (the time, the die displacement or the temperature) and how much it is incremented between two subsequent steps, the number of steps, the sub-stepping control and finally a simulation stop criteria. In simulation controls, it is possible also to set the re-mesh criteria by choosing between the global and the local re-mesh. A maximum interference between tool and workpiece can be defined with the aim to guarantee a new mesh generation when the two objects have a significant interpenetration. The solver and the iteration method must be selected between some available options.
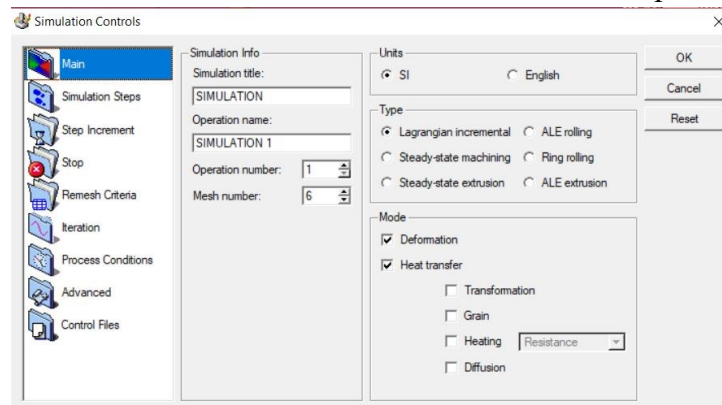
Figure 42. Simulation control window.

The target is the minimization of the computational time to obtain a solution with a low number of iterations for each step. This aspect is influenced also by the convergence error limit, which value is a trade-off between accuracy and reasonable simulation duration. The process condition allows to define environment status as the temperature and the convection coefficient.

- The **object** section allows to implement all the specification concerning workpiece and tool as their geometry. It can be defined or modified by delating some elements. It is fundamental to pick the object type which can be rigid (useful for the tool when the simulation does not aim to predict the damage due to the wear), plastic, elastic or elasto-plastic (the material elastic behavior at low strain is not neglected). In this section, also the objects mesh must be created. If the tool is a rigid body, it needs a mesh only if the thermal exchange is activated. Workpiece and tool should be meshed by two different strategies: the absolute and the relative. With absolute mesh type, it is possible to control the minimum and maximum element size. On the other hand, relative mesh type allows to control the element number and the maximum size ratio. The mesh shape may be defined by balancing the weighting factors: it is possible to assign a weight between zero and one to different variable (surface curvature, temperature distribution, strain or strain rate distribution) with the aim to control the element distribution. An effective instrument is the mesh window; it allows to define several zones with different size elements to have a more concentrated mesh where, for example, the deformation is more significant. An optimal mesh windows definition guarantees accurate results, and it significantly reduces the computational effort. For tool meshes, it is possible to add a coating by defining its material and thickness. Object section allows also to implement the object movement: translation and/or rotation can be defined by picking the control magnitude (speed, hammer, force …), the direction and the magnitude value. It can be fixed as a constant value, or it may be calculated as a function of time or the tool stroke. The boundary conditions are useful to establish some constraints on the tool and workpiece mesh. For example, it is possible to assign some nodes velocity or pressure to model the interference with external elements not included in the simulation as objects. Also, some thermal aspects may be implemented, like some nodes temperature or the possibility to have heat exchange along a defined path. More specific objects features may be defined in properties section, where, for example, it is possible to assign a workpiece volume constant value in order to avoid it transformation during a re-mesh.
- The **material** section (see **Figure 43**) is the place where it is possible to define the workpiece and tool, mechanical and thermal features. DEFORM^{TM} has a rich library with numerous pre-set materials. A material is characterized by some properties, including the flow stress. Johnson-Cook and other laws are pre-configured: only the parameter values must be fixed. If a material behavior may not be expressed by one of the available models, it is possible to load the flow stress by some charts. Stress and strain data must be defined in a wide range of strain rate and temperature.
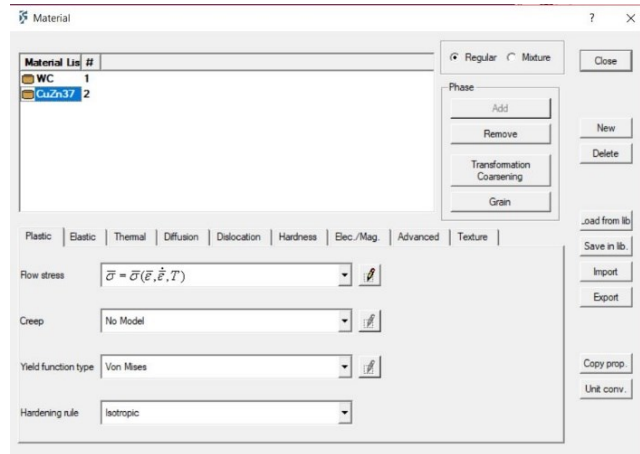
Figure 43. Material window.

In this regard, some of the library materials are not suitable for all the processes because there are characterized only in standard condition. The Poisson ratio, the thermal expansion and conductivity, the heat capacity, the emissivity are some of the material properties which can be defined as a function or as a constant value.

- The **object positioning** is the pre-processor section dedicated to the object's placement in the CAD space. The objects may be offset by indicating the distance vector. If the initial positions are not well-known, it is possible to use the interference command to put in contact two objects. Elements should be rotated by defining a center, an angle and the reference axis.

- The **inter-object** allows to define the thermo-mechanical relation between the objects. After selecting an object couple, it is possible to generate the contacts between them: the adjacent nodes are used to calculate the workpiece-tool interference. As it is shown in **Figure 44**, also a workpiece-workpiece relation should be defined with the aim to simulate the contact between the curly chip and the workpiece. The contact is defined by choosing the friction model between Coulomb, Shear or hybrid and the related coefficients as constant or function. The heat transfer coefficient may be defined to also simulate the thermal aspects of the contact between objects.
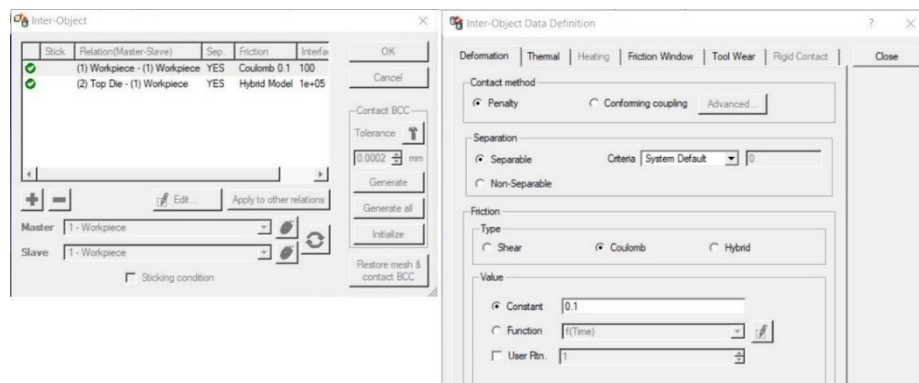
Figure 44. Inter-object windows.

62

Once the simulation is ready, the database may be "checked" to verify the completeness of the input data. If the control has positive result, it is possible to "generate" a new database file. The file size has the GB order of magnitude and it weight increases during the simulation.

2.2.6.2 Solver and Post-processor

The second software part is the tool to manage the FE simulations, named Solver. The main command is "run options". It allows to define how the calculator may simulate the FE database. It is possible to set a single or multiple processors simulation. The second option speed up the simulation running but does not allow to simulate several processes in parallel. The time saving is limited by the re-mesh: it usually takes long time and must be realized by the calculator only with one processor. DEFORM^{TM} cutting simulations should be very time consuming, especially if they are 3D. The duration may reach some hundreds of hours.

Once the last simulation step is calculated, it is possible to analyze the results by using the thirst software section, called Post-Processor. Its interface is shown in **Figure 45**. A single simulation step may be visualized, or it is possible to dynamically follow the workpiece evolution in a time interval. In **Figure 45** the workpiece is colored in accordance with the effective stress for each element. The strain, the strain rate, the temperature, the damage are some of the variables which can be utilized instead of the stress. The scale on the right may be set on global, local or user defined. Cutting forces, speed, energy may be plotted in a graph and subsequently extracted and imported in data-processing software.
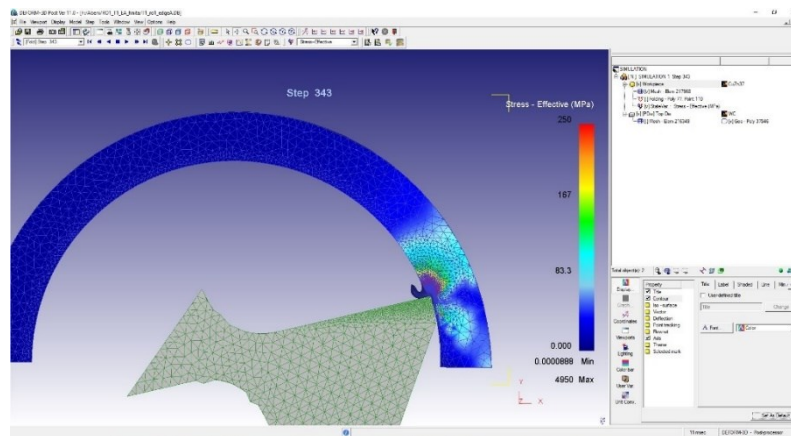
Figure 45. Post-processor window.

3 Experimental set-up

The chapter three is dedicated to the description of the experimental apparatus employed during the PhD project. First section regards the AM machines which were used to manufacture the samples which were subsequently micro-machined. The experimental tests were executed in the Ultra-Precision Laboratory of the University of Brescia by using an ultra-precision 5-axis KERN Pyramid Nano, equipped with piezometric triaxial sensors to record the cutting forces.

The quality of machined surface, roughness, dimensional and geometrical tolerances were investigated with the Optical Coordinates Measuring Machine (CMMO), a multifocal optical microscope and an Auto Focus (AF) laser probe. The final paragraph of this chapter is dedicated to the investigation about the performances of the machine tool and the mounted loadcell which was performed during the PhD project and published on an international journal **[17]**.

3.1 PBF machines

The fabrication of the samples was performed by using Powder Bed Fusion (PBF) process. The principles, the features, the advantages and the limits of PBF is widely described in Section 1.1. In this paragraph will be listed the technical features of the machines which were utilized: the GE Additive Concept Laser M2 Cusing, the 3D System ProX 100, the EOS M290 and the ARCAM EBM Systems Model A2.

3.1.1 LB-PBF machines

Three different LB-PBF machines were utilized during the project in order to process different materials. Inconel 625 samples were fabricated by using a GE Additive Concept Laser M2 Cusing, shown in **Figure 46**.

Figure 46. The GE Additive Concept Laser M2 Cusing.

The machine employs a powerful dual-laser system with a 0.4 kW power and a dedicated thermal control of the optics leads to improved thermal and optical stability. A part vectorization allows for additional flexibility to part parameter design, enabling new geometries and ensuring part quality, especially with increased part complexity. In combination with multiple internal sensors, this ensures a more tightly controlled build environment, resulting in significantly better part quality and consistency. Additionally, all powder handling processes are performed under inert gas to prevent oxidation and safety hazards. The build envelope is equal to 245 x 245 x 405 mm, the layer thickness ranges between 25 and 120 μm, while the maximum scanning speed reaches 4.5 m/s. The focus diameter ranges between 70 and 500 μm, while the spot size ranges between 61 and 72 μm. **Table 2** lists the laser power P, the scan velocity v_s, the laser spot size d, the laser thickness s, the hatch distance h, the stripe width w, and volumetric energy density E which were used to manufacture Inconel 625 samples [19].

Table 2. AM process parameters for Inconel 625.

P (W)	v_s (mm/s)	d (μm)	s (μm)	h (μm)	w (mm)	E (J/mm^3)
370	1200	170	60	110	5	46.7

By using a 3D System ProX 100 (**Figure 47**),17-4 PH stainless steel samples were fabricated. The LB-PBF machine guarantees accuracy on small metal parts equal to ±50 μm, on large parts ±0.2%. Repeatability from part to part is approximately 20 μm. The build volume is equal to 100x100x90 mm, and the laser source power reaches 100 W. The surface finish quality can reach Ra = 5 μm, which can be considered a good result for PBF. **Table 3** lists the laser power P, the scan velocity v_s, the laser spot size d, the laser thickness s, the hatch distance h which were used to manufacture 17-4 PH stainless steel samples [18].

Table 3. AM process parameters for 17-4 PH stainless steel.

P (W)	v_s (mm/s)	d (μm)	s (μm)	h (μm)
50	300	80	50	50

Figure 47. The 3D System ProX 100.

Ti64Al4V samples were fabricated by using a EOS M290, shown in **Figure 48**. The machine is equipped with a 400 W Yb fiber laser which allows high beam quality combined with performance stability. The process occurs in a protective nitrogen or argon atmosphere. A recirculating filter system with self-cleaning reduces the costs related to the system maintenance. The building volume is equal to 250 x 250 x 325 mm while the scanning speed can reach 7.0 m/s. The focus diameter reaches 100 μm. **Table 4** lists the laser power P, the scan velocity v_s, the laser spot size d, the laser thickness s, the hatch distance h which were used to manufacture Ti64Al4V samples [20].

Table 4. AM process parameters for Ti64Al4V printing.

P (W)	v_s (mm/s)	d (μm)	s (μm)	h (μm)
340	1250	70	30	40

Figure 48. The EOS M290.

3.1.2 BB-PBF machines

Ti64Al4V samples were fabricated by using a ARCAM EBM Systems Model A2, shown in **Figure 49.** The high-power beam source (up to 3500 W) allows to provide high melting capacity. Parts are built in vacuum at elevated temperatures resulting in stress relieved parts with high material properties. The machine is equipped with a powder recovery system which allows to recover 95% of the un-melted powders and to re-use them. The build size is equal to 200 x 200 x 350 mm. The accuracy is equal to ± 0.20 mm, the beam spot size ranges between 0.2 to 1.0 mm and the scanning speed can reach 8 m/s. **Table 5** lists the laser power P, the scan velocity v_s, the laser spot size d, the laser thickness s, the hatch distance h which were used to manufacture Ti64Al4V samples [20].

Table 5. AM process parameters for Ti64Al4V BB-PBF printing.

P (W)	v_s (mm/s)	d (μm)	s (μm)	h (μm)
1250	4530	80	50	100

Figure 49. The ARCAM EBM Systems Model A2.

3.2 Micro-milling

The ultra-precision 5-axis machining center Kern Pyramid Nano it is a CNC (iTNC530 HEI-DENEIN) machining center, developed for nano precision applications with high-quality workpiece surface. It is a five-axes machine, and each axis is hydrostatically supported and driven. This configuration is virtually wear-free and thus it guarantees life-long precision. In addition, hydrostatics allows high acceleration coupled with excellent vibration damping. The machine is equipped with a tool pre-setting laser system called BLUM Laser Control Nano. It allows positioning accuracy of few tenths of micrometers, which is a necessary condition to achieve high precision tolerance. A thermal management system allows to dissipate heat very quickly by ensuring temperature stability. High CNC machine performances are guaranteed by its positioning in a temperature and humidity-controlled room ($20 \pm 0,5°C$; 50%). The Kern Pyramid Nano is built with a symmetrical basement which guarantees maximum rigidity and thermal symmetry. It is made by a material (KERN ARMORITH developed by the same manufacturer of the machine) with high tensile strength and with an excellent damping power. There are also additional components such as the fume extraction unit system, the lubrication system, the chip conveyor, the CO_2 fire extinguishing system, which can be integrated without requiring additional space. Another feature that can be very useful for saving time is the automated tool change and piece change system. Tools with internal lubrication-cooling channels can also be installed, with the only constraint of implementing suitable spindles supplied by the company.

Table 6. Kern Pyramid Nano features.

Positioning accuracy (VDI/DGQ 3441)	± 0.3 μm
Minimum surface roughness (VDI/DGQ 3441)	0.05 μm
Maximum spindle rotational speed	50000 RPM
Maximum axes acceleration	10 m/s^2
Maximum axes speed	30 m/min
Workspace size	500x500x300 mm
Maximum workpiece hardness	HRC 64

Finally, it is equipped with a laser measurement system, an integrated unit for tool presetting, and a calibration spindle is included. **Table 6** summarizes the main features of Kern Pyramid Nano.
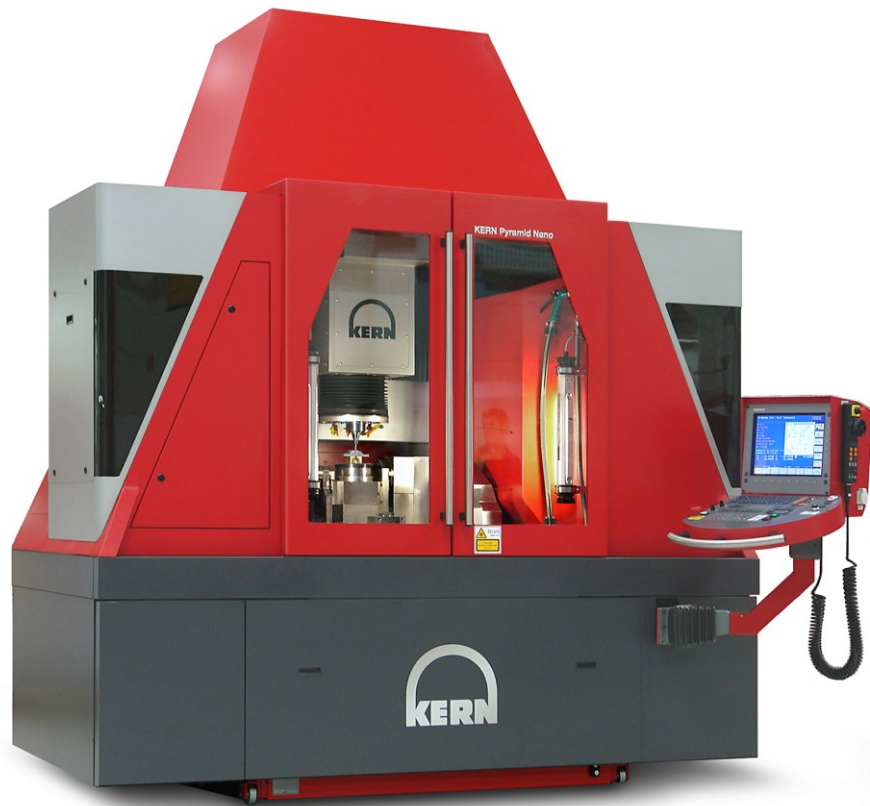
Figure 50. The KERN Pyramid Nano.

3.3 Geometrical and dimensional inspection

The Ultra-Precision Laboratory is equipped with some instruments useful to inspect the machined surface, to measure the machined features (such as the holes diameters, the pockets width, the pockets depth), to acquire profile, to virtual reconstruct surfaces and to measure linear and surface roughness. The machines are an Optical Coordinates Measuring Machine (CMMO), a multifocal optical microscope and an Auto Focus (AF) laser probe.

The CMMO is a Mitutoyo Quick Scope QS300 with a measuring range of 200 x 250 mm and 150 mm in z-direction. It is shown in **Figure 51**. In addition to contour and surface illumination, Quick Scope is equipped with a fiber-optic ring light to aid in reproducing color images more clearly. This illumination enables measurement and observation of images under optimal conditions. The AF (Auto focus) tool allows focusing without personal error, therefore achieving high-accuracy height measurement. Zooming from low to high magnifications can support from wide-field observation to high-magnification measurement without changing lenses. Additionally, the automatic light control function associated with a

zooming operation and automatic correction functions, such as for image displacement and pixel calibration, are available. The resolution is equal to 0.1 μm.

Figure 51. The Mitutoyo Quick Scope.

The multifocal optical microscope is a Hirox RH-2000 is equipped with a camera to capture up to 50 fps with the continuous high-quality resolution of 1920×1200 pixel. The high intensity LED light source provides 5700K temperature, which closely portrays day light color temperature (5460K) to re-produce true sample color image as well as full illumination immediately with no warmup time. The high-speed algorithm and accurate motorized Z-axis movements (50 nanometer per step) allows to acquire focus images in a wide z-range. The RH-2000 offers accurate and calibrated measurements in real-time, including length, area, angle, diameter or automatic surface area. The combination of encoded optics and powerful software reduces human errors by automatically selecting and displaying the correct lens, adapter, and scale on the screen at any time. The magnification ranges between 1:1 to 10000x. It is shown in **Figure 52**.

Figure 52. The Hirox RH-2000 microscope.

The Auto Focus (AF) laser probe is a Mitaka PF60 is visible in **Figure 53**. The instrument is characterized by large measuring areas and high precision measurement (measuring range

60x60x10mm, positioning resolution: x and y is 0.1µm, z is 0.01µm). The scan AF enables fast measurements of 2D and 3D roughness (128000 points in 6 minutes). The automatic system of micro-scan utilizes a spot laser with a diameter of 0.5 µm and it allows to scan thin films and surfaces with high reflectivity or high light absorption.
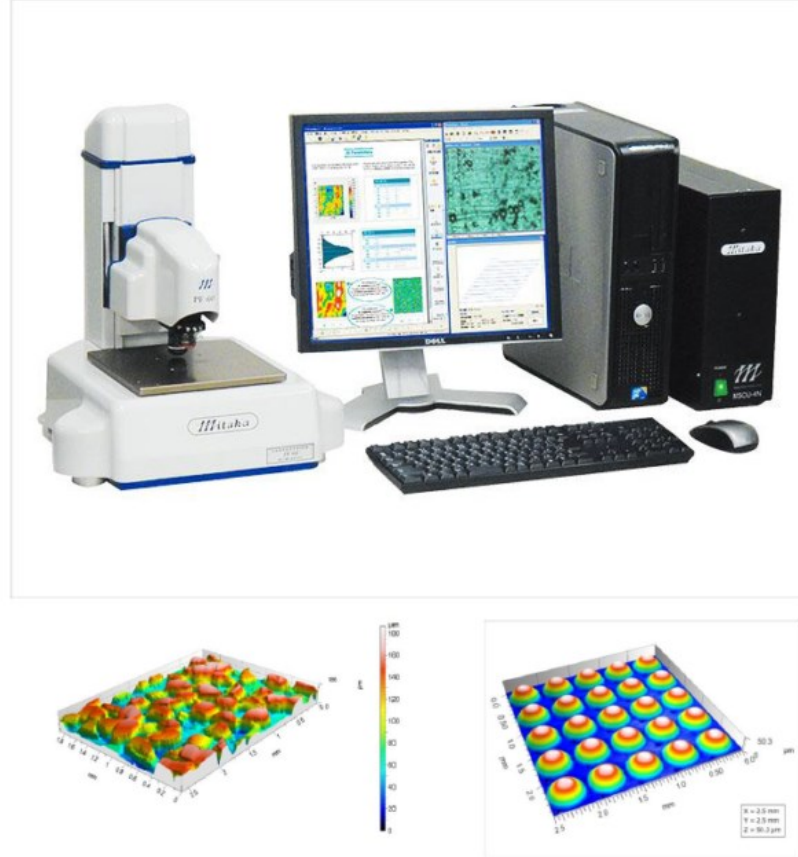
Figure 53. The Mitaka PF60 laser probe.

3.4 Load measurement system

During the Project, the Kern Pyramid Nano was equipped with a system to measure the cutting forces. The selected loadcell is a piezoelectric three-component force sensor Kistler 9317C may be used to measure tensile and compressive loads both. **Figure 54** shows the load cell and his reference system. The working principle is based on the piezoelectric material capacity to generate electrical charges when they are deformed. This principle is reversible because if a voltage is applied on a piezoelectrical material it will deform. The load cell is constituted by a portion of this material blocked between two metal plates which store the electrical charges, as in a capacitor. The potential difference generates an electric current and it allows the dynamic force measurement of a signal variable in the time. In fact, the high piezoelectrical crystals stiffness increases the natural frequency and the bandwidth. In static condition (i.e., force constant), the load cell presents a drift of about 1 N in one minute. Milling force signals is time-variable, thus this issue does not regard the acquisitions realized in this research. The list of the features is reported in **Table 7**.

Table 7. Main load cell features declared by the producer.

Range Fx, Fy [N]	-1500 ÷ 1500 N
Range Fz	-3000 ÷ 3000 N
Threshold	< 0.01 N
Sensitivity Fx, Fy	-26 pC/N
Sensitivity Fz	-11 pC/N
Cross talk Fz → Fx, Fy	< ±1 %
Cross talk Fx → Fy	< ±3 %
Cross talk Fx, Fy → Fz	< ±3 %
Natural frequency for x, y	5 KHz
Natural frequency for z	20 KHz
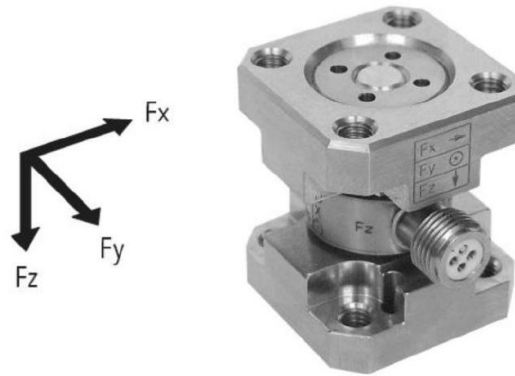
Figure 54. Load cell and the related reference system.

Three Kistler Charge Meter Type 5015 are connected by coaxial cables to the load cell. They amplify the electric charge signals in a voltage in the range of ±10 V. The usage of amplifier is necessary due to the low energy associated to load cell signals. These devices can be used also to set the acquisition sampling rate and to filter the data with low-pass or high-pass filters, digital and analogical both. It is shown in **Figure 55**. The Data Acquisition device is an integrated system to realize the signal conditioning and the analogic-to-digital conversion. It is constituted by a voltage input module NI 9205, with 32 channels and a 16 bits resolution, mounted on a chassis NI DAQ-9174. The chassis controls the timing, synchronization, and data transfer between C Series I/O modules and the external host.

(a)   (b)

Figure 55. Kistler Charge Amplifier Type 5015 (a) and NI 9205 mounted on NI DAQ-9184 (b).

3.5 Assessment procedure for ultra-precision machine tool

Industrial application of processes based on micro-cutting is limited by some issues concerning the geometrical scale. The process performance is significantly affected by milling machine, tool holder, tool, workpiece material microstructure, workpiece fixtures, and process parameters. At present, an ultimate micromachining assessment procedure is not available. This study aimed to propose and conduct an experiment on a testing procedure suitable for micro-milling. The set up to be implemented and the output to be considered were defined and they are described in this section. Three major stages were identified: estimation of the effective bandwidth of the load cell–tool holder system, the milling machine natural frequency measurement, and micro-milling test execution in order to evaluate the machine performance. The entire procedure is performed, and its robustness is demonstrated.

The process quality alteration due to tool run-out phenomenon was evidenced from the experiment and the simulation. Control and optimization of milling machine performance are crucial to achieve adequate micromachining processes. In this context, high productivity and elevated cutting speed are ensured by high spindle rotational speed. Tool run-out and vibration intensity are affected by cutting dynamics. Shi et al. [181] investigated the influence of milling machine structure on micro-milling in terms of roughness. The analysis was performed to identify the natural frequencies of the machine tool and compare them with tooth passing frequency. The effects of the spindle high-speed must be considered in engineering of a cutting force acquisition system. As discussed in [182], a limited load cell bandwidth can distort the measured signals. If harmonic vibration overlaps the natural frequency of the instrument, then the measured cutting force would be amplified. Despite relevant research efforts over the last years, a standard for testing micro-milling performance remains lacking. Garbellini et al. [183] pointed out that although several standards and guidelines have been defined for macroscale machining, they appear inadequate to be downscaled unless appropriate adjustments are made.

The proposed assessment procedure for evaluating the performance of a micro-milling process involves some steps. First, the dynamic performance of the load measurement system was determined through an experimental modal analysis. A similar procedure was employed to compute the relevant natural vibration frequencies of the milling machine. Once the acquired cutting forces were considered reliable, the signal was utilized as a quality index. The surface quality was also found to be suitable for evaluating the instrument and process performance of a milling machine when micro-milling features were realized. An experiment was conducted to test the procedure on a nano-precision milling machine.

3.5.1 Equipment definition for the procedure

These guidelines were developed specifically for ultra-precision milling machine but can also be applied to conventional milling machine and custom-built milling machine. The tool must be a micro-end mill characterized by a diameter lower than 1 mm. Tool run-out should be limited using a chuck tool holder with precision collets instead of other types of holders.

In addition to the standard milling machine equipment, the assessment procedure requires a data acquisition system for forces. The cutting forces are indispensable data to understand the cutting dynamics and estimate tool run-out. Developing a reliable measurement system is challenging due to several issues. The load cell must have an accuracy of at least 0.01 N. The load cell sampling rate must be chosen as the best possible trade-off between acceptable file size and acquisition quality. Aliasing must be avoided by setting sufficiently high sampling rate.

The positioning of the sensor is certainly not insignificant. Smith et al. **[184]** developed a torque measurement system built onto a milling machine. The rotating systems increase the inertia of the measurement system and have a limited frequency bandwidth that is dependent on each tool holder used. A similar condition could distort force signals and must be absolutely avoided. Table dynamometers are commonly used to measure milling forces. In this configuration, the workpiece is mounted on the top of the dynamometer, which is clamped to a milling machine table **[185]**.

Some piezo accelerometers are necessary to complete the machine modal analysis. The standard identified pattern is shown in **Figure 56.** A triaxial piezo-accelerometer must be placed on the tool holder by using a suitable and high-strength fixture **(Figure 56 b).** Another triaxial accelerometer must be placed on the top of steel block simulating the piece to be held, positioned on the force sensor, and fixed on the piece holder.

(a)   (b)

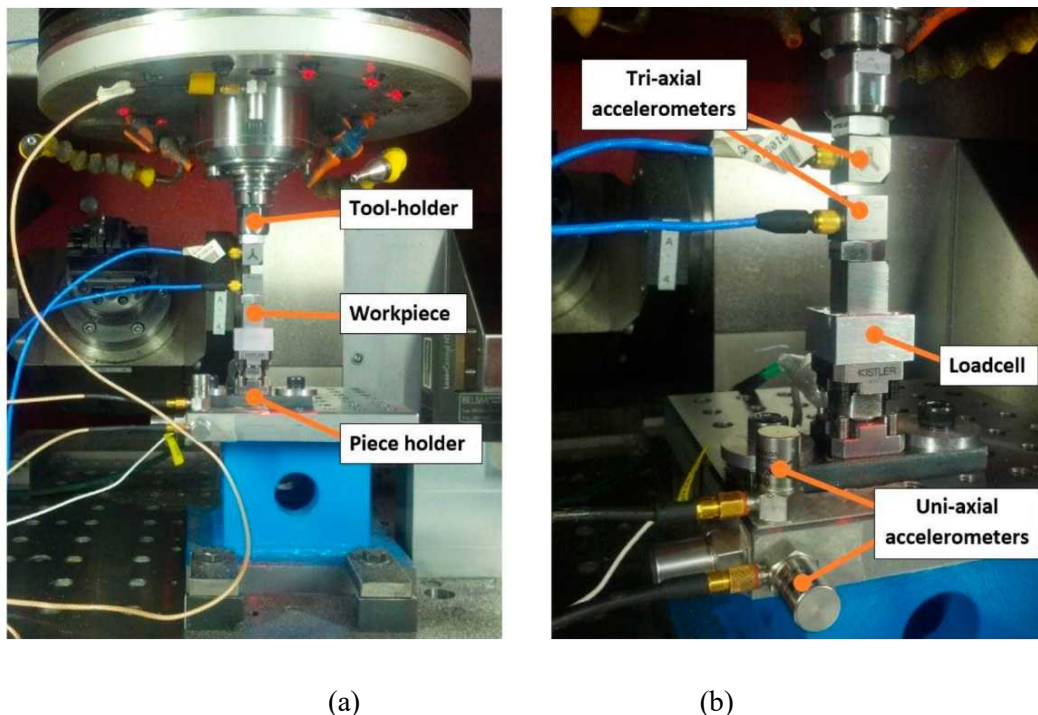**Figure 56.** Test setup: (a) workspace area with the tool holder and the piece holder; and (b) the load cell and the piezo accelerometers.

A third accelerometer must be placed on the machine frame. To provide redundant data should be useful to minimize mode measurement errors. This condition could be obtained with six additional uniaxial accelerometers; three accelerometers should be fixed to the piece

holder in orthogonal configuration and the other three should be fixed on the machine frame by using thin adhesive tape in orthogonal configuration.

The accelerometers and the load cells are all connected to a data acquisition device, which is an integrated system for signal conditioning and analogic-to-digital conversion. The natural vibration frequencies of the system should be determined through several techniques. A modal analysis must be performed on the micro milling machine and the load cell. An impact hammer is also required to conduct the test.

3.5.2   Assessment steps

The machine must be tested after a warm-up phase and characterized through experimental modal analysis to identify frequencies of mode shapes involving vibrations of the load cell, the tool, and the piece holder. A specific micro-milling operation is then executed on appropriate workpiece samples. The first phase consists of identifying the modal parameters of the load cell. The natural frequency of the sensor is declared and certified by the manufacturer. Nevertheless, characterization must be performed due to the influence of constraints on the dynamic behavior of the sensor. Detection can be obtained through impact tests and measurement of output forces in each direction. First, only the load cell, without the workpiece and brackets, must be hit to validate the procedure. The identified natural frequencies can be compared with the value declared by the manufacturer.

Once the procedure can be considered reliable, the entire system comprising a dynamometer fixed on the machining center, workpiece, and brackets must be tested with the same methodology. The frequency response of the force sensing system is influenced by the stiffness and the mass of each component. The constraints decrease the dominant mode and bandwidth. The force measurement system can be considered reliable if the bandwidth remains larger than the maximum tooth passing frequency.

A maximum spindle rotational speed n_{MAX} can be identified using **Equation 31:**

$$n_{MAX} = \frac{f_n \cdot 60}{z} \ [RPM] \qquad\qquad\qquad \textbf{Eq. 31}$$

where f is the natural frequency (Hz), and z is the number of tool flutes. Once the force signals should be considered reliable, machine dynamics will be characterized. The mechanical structure **[186]** and the control system of the milling machine **[187]** are usually optimized during the design phase and validated experimentally to reduce the influence of vibrations during milling on the final product. The techniques used for validation mainly focus on vibrations affecting the tool due to their relevance to the process. As suggested by Altintas et al. **[188]**, such vibrations could be predicted through numerical simulation of the machine body up to the tool holder and coupled with an experimental modal analysis of the tool performed independently from the machine itself.

Numerical simulation would require a complete solid model of the machine, and material properties to be assigned to its elements: the actual results of the simulation would largely depend on the accuracy of these data. A complete experimental solution in which the tool is tested directly in its working configuration is preferred to provide a simpler approach to validation.

Considering that the dimensions of the tools used for micromachining are comparable with those of most accelerometers and the high-speed rotation of the spindle, Gagnol et al. [189] suggested using laser distance sensors or laser Doppler vibrometers. Zaghbani et al. [190] proposed an easier approach of applying contact sensors to the nonrotating parts of the machine combined with operational modal analysis.

Given that this study aims to propose a standard procedure for evaluating machine performance and not to simulate and optimize dynamic behavior. The procedure was also simplified, focusing on the identification of natural frequencies only and neglecting damping and modal mass estimation. An impact hammer was used to hit the piece holder. The frequency transfer function (FRF) of each acceleration signal must be computed to detect the natural frequencies of vibrations involved in the tool holder and piece holder with the force signal of the impact hammer as reference. The most relevant peaks can be identified by picking. This technique is prone to operator-induced errors; as such, the procedure should be repeated several times to further confirm the selection, and each result must be compared with one another using the Modal Assurance Criterion (MAC) matrix [191] considering only the frequencies identified by most of the tests.

Finally, a cutting test must be performed to verify machine performance in terms of final product quality. This procedure suggests realizing a 2D feature, which is directly machined on the top flat surface of a slab workpiece. The geometry is designed as multiple micro slots. In particular, the feature is composed of 16 micro slots, performed on 360°, as visible in **Figure 57**.

The cut is realized by moving the tool from the surface center of the sample in the radial direction. The shape is easy to produce and performing measurements can be effortless.
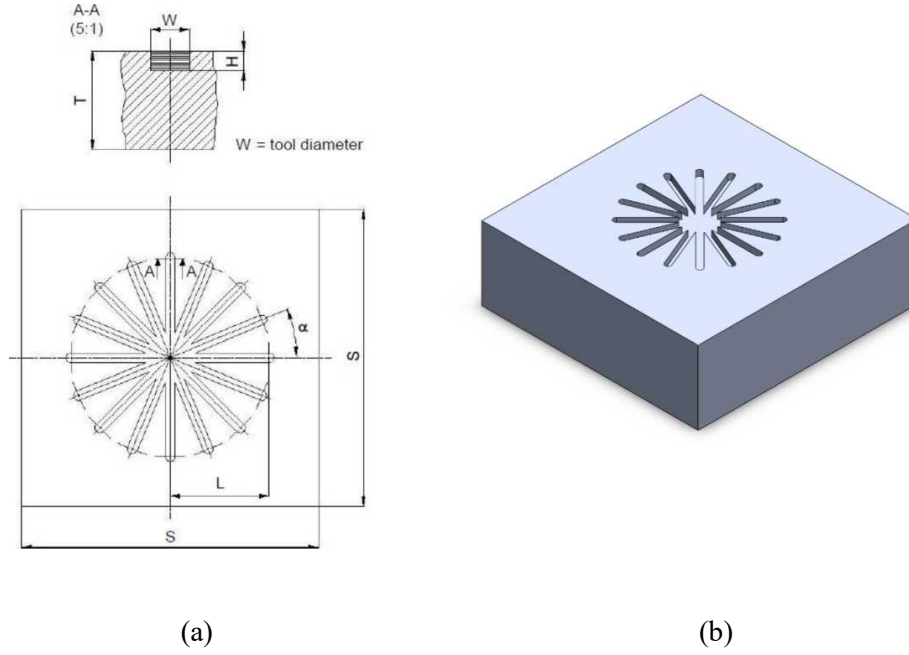
Figure 57. Proposed feature: (a) 2D view and (b) 3D view.

The length (L) of the feature should be 10 times greater than the tool diameter. The depth of the channels (H) should be standardized by setting its value equal to the tool radius and obtained through 10 constant passes (i.e., $ap = 1/10H$).

The minimum dimensions of the sample are set as follows to avoid undesired boundary effects:
• minimum side length $S = 3 \times L$;
• minimum sample thickness $T = 10 \times$ tool diameter or $T > 5$ mm.

Process parameters (cutting speed v_t, axial depth of cut ap, and feed per tooth) must be chosen according to the tool maker guidelines to avoid ploughing regime during cutting. During micro-slotting, cutting forces must be measured through a triaxial force sensor for analysis of force peak values. The measured force components should be composed through **Equation 32** for calculating cutting force Fc acting on the tool cutting edges.

$$F_c = \sqrt{F_x^2 + F_y^2 + F_z^2}$$
<div align="right">**E q . 32**</div>

In the microscale, tool run-out strongly affects the process, and force on the two cutting edges should be separately investigated to highlight the presence of this phenomenon. General surface integrity and burr dimensions must be measured on the inner and outer sides of the microchannels. Dimensions, burr dimensions, and cutting force peaks (for each cutting edge of the tool) related to microchannels must be plotted in a Kiviat chart to show a possible relation with milling direction.

3.5.3   Validation of the procedure on KERN Pyramid Nano

The described procedure was applied on the Kern Pyramid Nano in order to preliminary analyze the milling machine performance. The general overview of the milling machine type and the involved equipment is summarized in **Table 8.**

Table 8 Study case description.

Milling machine	Kern Pyramid Nano©
Load cell	Kistler© 9317C
Triaxial piezo-accelerometers	356A15 PCB© fixed by Dytran® high-strength magnetic fixture
Monoaxial piezo-accelerometers	736 Wilcoxon©
Impact hammer	086c03 PCB©
Tool	Mitsubishi© two-flutes end-mill
Tool diameter (nominal)	200 µrn
Sample material	Ti-6Al-4V alloy with fully lamellar microstructure

(a)   (b)
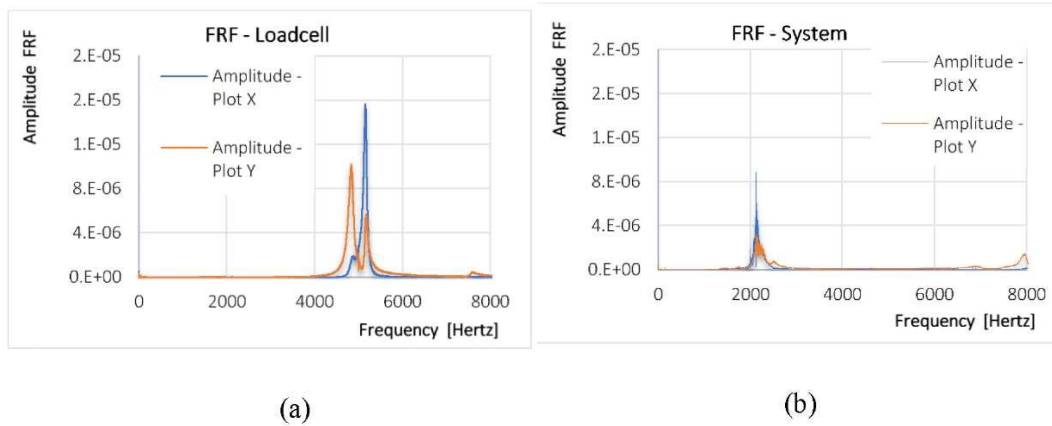
Figure 58. FRF (units in 1/kg) analysis of natural frequency test on **(a)** a load cell and **(b)** the entire system

The natural frequency of the load cell declared by the manufacturer for the x and y directions is equal to 5000 Hz. The sensor was hit three times by the impact hammer, and load data were acquired through a National Instrument cDAQ-9174 with National Instrument 9215 board (BNC type). The sampling frequency was set to 50 kHz. In **Figure 58 a**, the frequency response function (FRF) shows a peak around the natural frequency of the load cell. The effective natural frequency was identified as 5156 Hz for Fx and 4991 Hz for Fy, consistent with the declared data. The entire system (dynamometer fixed on machining center, work-piece and brackets) was then tested with the same methodology. A smaller bandwidth is the result of the dominant mode decrease at 2145 Hz for Fx and 2192 Hz for Fy. **Figure 58 b** shows the decrease in the bandwidth. The maximum spindle speed n_{mca} for two-flute tool determined by **Equation 31** is 64350 RPM, which is higher than the maximum spindle speed of the milling machine (i.e., 50000 RPM).
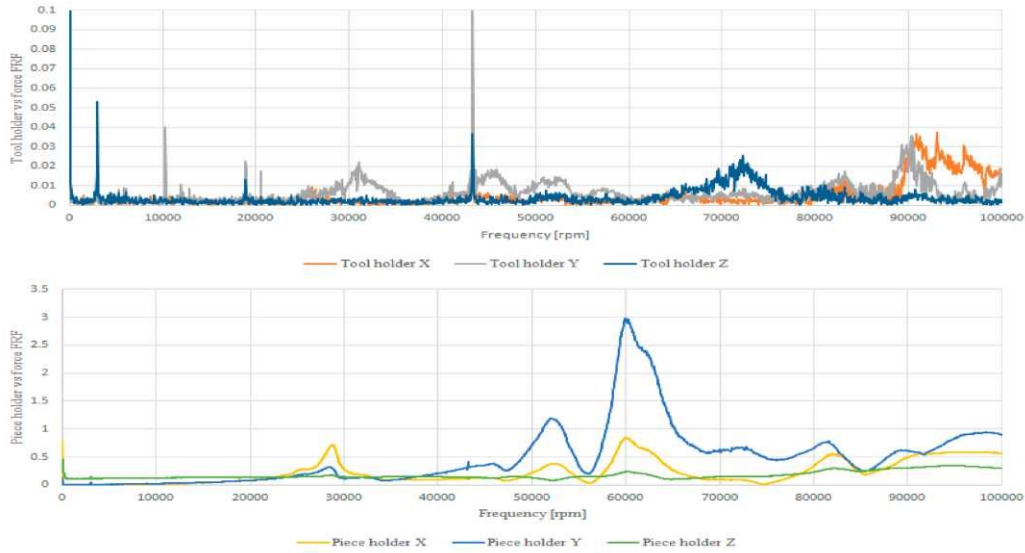
Fig. 59. FRFs of vibrations on the tool holder (upper) and piece holder (lower) recorded during an impact hammer hit on the piece holder.

After a warm-up phase, the milling machine was excited using an impact hammer applied manually to the piece holder. Force sensor and accelerometers were synchronously used for recording. The frequency transfer function (FRF) of each acceleration signal was computed using the force signal of the impact hammer as reference to detect the natural frequencies of vibrations involving the tool holder and the piece holder. FRF was estimated using the H3 FRF mode available in Labview©.

The results of the analysis are presented in **Figure 59**, where only a subset of the recorded quantities is shown to improve clarity. The force applied is limited to avoid damage to the piece holder, and vibration transmission between the two elements is low, leading to low amplitude of the tool holder response signals. A cross examination hitting the tool holder instead of the workpiece holder was not performed to avoid damage to the machine. All frequencies are reported in their revolutions per minute (rpm) equivalents to simplify data interpretation. Both charts display resonance peaks in frequency ranges, and the peaks could be excited during vibration; in particular, the ranges around 43000, 53000, 83000, and 90000 rpm show peaks in both charts.

Mode n°	Frequency [RPM]
1	2949
2	5100
3	8970
4	10260
5	14991
6	18862
7	20521
8	27464
9	30167
10	41779
11	43192
12	50811
13	53207
14	64451
15	86385
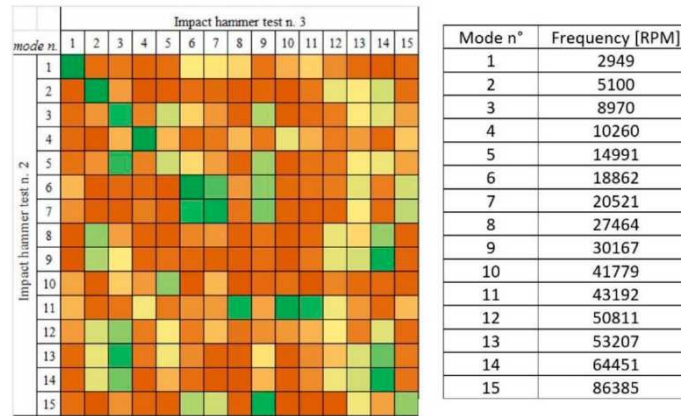
Figure 60. MAC matrix between two repetitions.

As stated previously, the peak-picking identification of the resonant frequencies was confirmed by repeating the tests five times and by using the MAC matrix to compare the results with only the frequencies detected by most of the tests. An example of comparison is shown in **Figure 60**. A good correlation between the two tests can be assessed based on the matrix diagonal up to the seventh frequency identified, whereas the 8th, 9th, and 10th frequencies show an incorrect identification. All other comparisons led to similar results. This procedure is necessary because of the following: peak picking is operator dependent; and the excitation force used is limited compared with the size of the machine structure, making the result sensitive to ambient vibrations unrelated to the test performed. Given these considerations, the frequency ranges that could induce higher vibrations if excited, being present in all the FRF analysis performed, should be from 40000 rpm to 50000 rpm and from 90000 rpm to 100000 rpm.

The third procedure was performed by cutting the 2D feature described in **Figure 61**. Process parameters were chosen according to the tool datasheet and previous modal analysis to stress the machine around its previously determined natural frequency. The feed rate was set to 1170 mm/min and the spindle speed to 45000 rpm. The selected spindle speed generates forces with frequency components within the range of the frequencies of the measured vibrations modes.

As indicated in **Table 8**, the nominal tool diameter is 200 µm. The channel depth (*H*), which is equal to the tool diameter, was obtained through 10 constant passes with a depth of cut of 20 um each one.
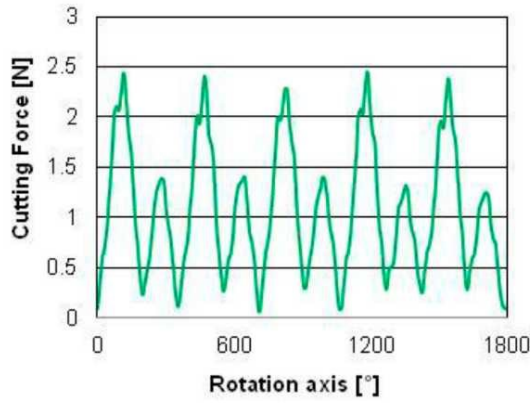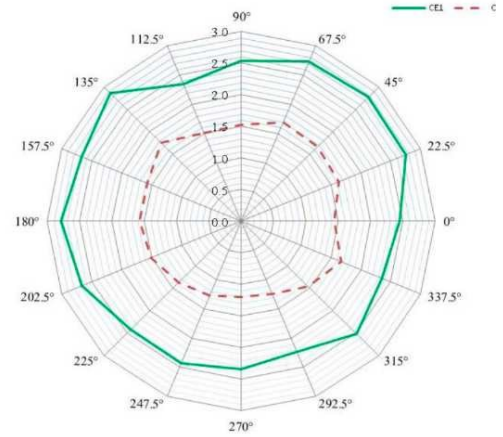
(a)   (b)

Fig. 61. Actual cutting force (a) on 5 mill-rounds with tool run-out effect (b) versus milling direction.

During micromilling, cutting force was acquired through the load cell. **Figure 61 a** shows a cutting force chart, indicating how the process is affected by the tool run-out and determining unbalanced loads on the cutting edges. The same behavior was observed for each step and for each channel (**Figure 61 b.**) The Kiviat graph shows how the feed direction does not significantly affect the cutting force. Even if close to the natural frequencies of the system, the cutting speed does not influence the process stability. In fact, no relevant vibrations were found from the force signal (**Figure 61 a).**
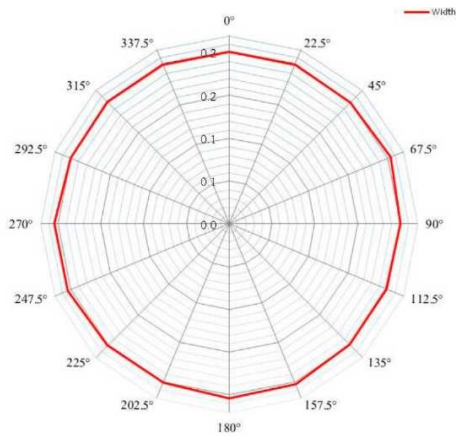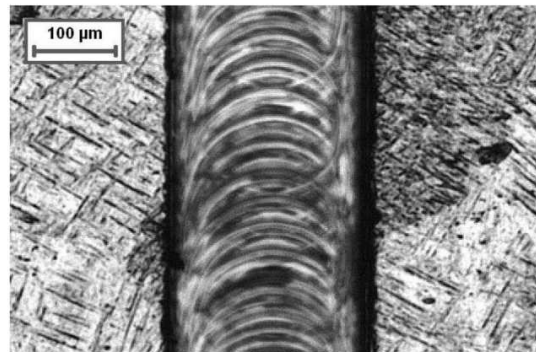
(a)   (b)

Figure 62. (a) Milling direction versus microchannel width (b) burrs on performed feature.

Figure 62 a presents the Kiviat chart of the width of the microchannels. Width is quite constant along every direction. The measured average width is equal to 202±2 μm. Given that the actual tool diameter is equal to 189 μm, the presence of tool run-out effect, which increases the actual width of the channels, could be confirmed. Constant burrs were observed

for each microchannel, regardless of the milling direction. Typical burrs (**Figure 62 b**) are wider on the outer side. Burr dimension was measured by using an optical coordinate measuring machine made by Mitutoyo (Quick Scope QS200Z). The average value is equal to 16 µm.

3.6 Conclusion

This Chapter describes the features of the experimental equipment employed during the PhD Project. It includes also the guidelines for a standard testing procedure used to verify the performance of a micro-milling system (i.e., milling machine, tool, tool holder, material, and process parameters). The proposed feature was realized through consecutive passes. Cutting force, channel geometry, and burr dimensions were considered as the main outputs. The procedure was tested and validated on the Ultra-precision CNC Machining Center (Kern Pyramid Nano). A Ti-6Al-4V alloy sample was utilized during the milling test. A 200 µm diameter two-flute flat end-mill was used during the test, and the process parameters were chosen according to previous modal analysis of the milling machine with the tool datasheet. The milling machine structure and its equipment can be considered adequate for micro-milling. The installed load measurement system is suitable for standard micromachining application. Good results in terms of vibrations were observed from the force signal even if the test was run with cutting speed that matched with the resonance frequency. The cutting force is independent from the working direction. Force analysis and channel width measurements revealed the presence of tool run-out during the test. In general, limited burr dimensions were observed, confirming the good quality of the final feature.

The procedure can be considered reliable and suitable for checking the status of a milling machine and related measurement system. Possible machine issues can be identified and corrected:

- If the tests highlight an excessive run-out, the first action consists in the cleaning of the parts which constitute the tool holder system. The removing of chips and powder is essential to assure the correct functioning of the system. It is important to limit the tool overhang in order to minimize the tool bending during machining. If the machine utilizes ER tool holder, the elastic clamp must be periodically substituted due to the effect of the wear. Finally, more accurate system can be utilized to hold the tool, such as the Weldon holder or hydraulic chuck. These systems reduce tool run-out but can require special equipment to clamp the tool or special designed tool, with a consequent increase of the costs.

- If the tests highlight a distortion of the cutting signal due to the loadcell resonance, the system to block the workpiece on the loadcell must be stiffened and the number of components utilized must be minimized.

- If the vibrations are excessive, the process must be re-designed by selecting tools with different geometries and by changing the process parameters, such as the depth of cut. The mechanical stiffness of the tool machine cannot be easily increased.

- If the quality of the machining is not constant in each direction, the machine axes must be revised in order to correct the alignments.

Furthermore, the test allows the identification of the best range of spindle speed to limit machine vibration and load cell resonance.

Characterization of machine tools and measurement system for micromilling

Andrea Abeni *, Matteo Lancini, Aldo Attanasio

Department of Mechanical and Industrial Engineering, University of Brescia, Italy

ARTICLE INFO

ABSTRACT

Technological progress has led to increased demand for small components with tiny features, which cannot be achieved through conventional machining. Industrial application of processes based on microcutting is limited by some issues concerning the geometrical scale. The process performance is significantly affected by milling machine, tool holder, tool, workpiece material microstructure, workpiece fixtures, and process parameters. At present, an ultimate micromachining assessment procedure is not available. This study aims to propose and conduct an experiment on a testing procedure for micromilling. The set up to be implemented and the output to be considered are defined and described. Three major stages are identified: estimation of the effective bandwidth of the load cell–tool holder system, the milling machine natural frequency measurement, and micromilling test execution. The entire procedure is performed, and its robustness is demonstrated.
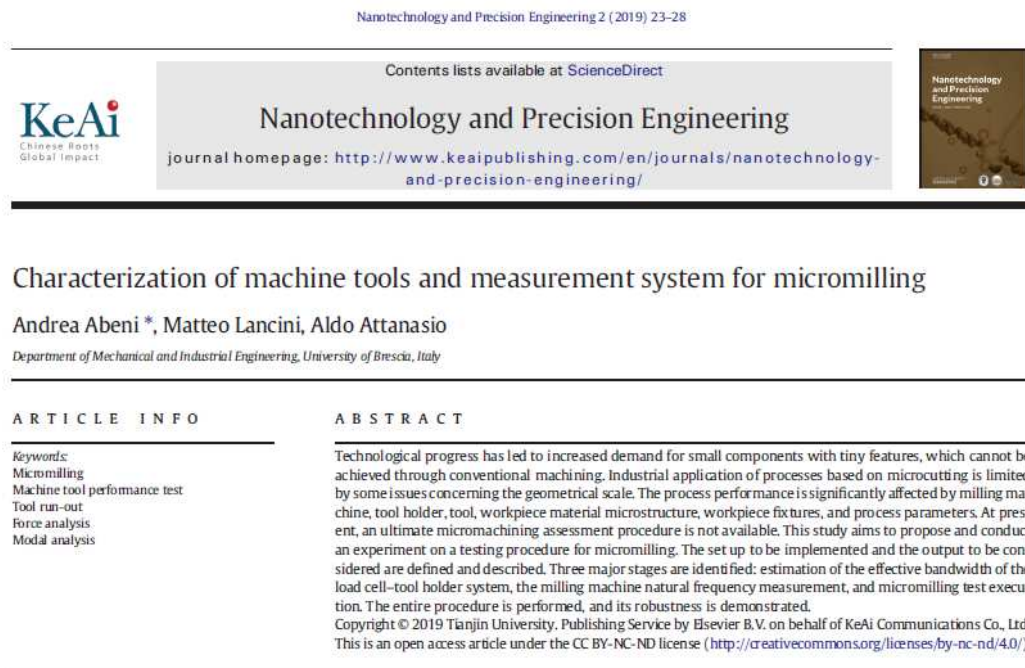
Figure 63. Published paper on NPE international journal **[17]**.

4 Experimental tests and results

The Chapter 3 provides a complete description of the experimental apparatus and how it was tested and evaluated. The experimental system allows to produce AM samples with custom geometry in order to perform subsequent micro-milling tests. The assessment procedure guarantees the precision of the micro-machining system and the reliability of cutting force measurement chain. Other useful experimental outputs, such as the burrs dimensions, the feature actual size, the surface roughness can be collected and used for further investigation about micro-machinability of AM alloys and for the comparison with the conventionally formed counterparts.

In this chapter a full reportage about the experimental tests performed during the PhD project on AM metallic alloys and their results will be described. The information is categorized by considering the workpiece material. Four typologies of materials were micro-machined:

- Additively Manufactured Stainless Steel 17-4 PH.
- Additively Manufactured Inconel 625.
- Additively Manufactured and wrought Ti6Al4V.
- Additively Manufactured and wrought AlSi10Mg.

For each workpiece material, the samples geometry, the experimental set-up, the micro-tool features, the process parameters, the experimental outputs will be listed and described in this section. The experimental tests were performed on four different materials to cover a wide range of industrial application, from aerospace to biotechnology, from electronics to precision mechanics. The data were utilized to model the process and to validate the models with different materials, which determines peculiar cutting conditions and phenomena. These approach allowed to investigate the micro-machinability of AM metallic alloys with different mechanical, chemical and electric properties.

4.1 Micro-milling of LB-PBF Stainless Steel

An analysis of the material removal behaviour during micro-milling operations for the selection of the optimal feed rate value was performed on 17-4 PH additive manufactured samples studying the variation of the specific cutting force as a function of the feed per tooth. The proposed analysis is based on the manufacturing of microchannels with 800 μm width by using coated tungsten carbide micro end mills on the top surface of the samples. The cutting force was acquired at a high sampling rate to avoid any aliasing effects. Moreover, the Specific Cutting Force (SCF) has been computed by considering the ratio between the cutting forces and the chip section. The average SCF peak was plotted as a function of the feed per tooth to identify the occurring transition from ploughing to shearing cutting regimes. A proper analytical model to consider the tool run-out effects while calculating the SCF was applied. The minimum uncut chip thickness was calculated to identify the transition between

the cutting regimes (shearing, ploughing or their combination) that affects the final product quality in terms of surface integrity and dimensional accuracy. Moreover, the roughness (Ra) and the burrs dimension of the microchannel were analysed to relate the surface finishing to the material deformation mechanism during the process.

4.1.1 Experimental procedure

In this paragraph, the production and machining operations of the LB-PBF 17-4 PH stainless steel samples are reported. The manufacturing parameters and the experimental plan followed for the micro milling tests are defined. Micro-machining tests were carried out fabricating twenty channels by using a constant cutting speed and twenty different feed per tooth (f_z) values. Once the cutting forces were acquired and normalized by dividing it with the chip section, the ploughing-shearing transition was determined through the MUCT quantification. Moreover, the roughness and the burrs were measured and the data were evaluated as a function of the parameter f_z.

The chemical composition of the 17-4PH stainless steel powder used as printing material is reported in **Table 9**.

Table 9. Chemical composition of 17-4PH stainless steel powder.

17-4 PH	C	Cr	Ni	Cu	Mn	Mo	Nb	Si
Wt (%)	<0.07	16.71	4.09	4.18	0.8	0.19	0.23	0.53

The samples were produced using the laser-based powder bed fusion machine 3D System ProX 100 (see section 3.1.1). The geometry of the samples was designed to allow the positioning of the samples on the load cell Kistler© 9317C (see section 3.4). The samples were printed as squares with a side equal to 25 mm and a thickness equal to 5 mm with four holes with a diameter of 4.20 mm on the corners of the squares. The absence of impurities is necessary to avoid negative effects of embrittlement. Therefore, the laser process is carried out in a Nitrogen atmosphere with a controlled O_2 content less than 0.1 vol.%. The optimized parameters for the SLM of 17-4PH steel of the process are reported in **Table 3** (see section 3.1.1). The as built samples were subjected directly to the micromachining tests without heat treatment.

The cutting tests were performed on the five axis Nano Precision Machining Centre KERN Pyramid Nano (see section 3.2). The loads generated by the interaction between tool and workpiece were measured through a force acquisition system, as reported in section 3.4. The samples were directly constrained to the load cell through four bolts. The loadcell was blocked to the machine work table. The experimental procedure about the first group of tests consisted in two different milling operations: (i) a roughing to prepare a planar surface on the workpiece and (ii) micro slot machining, executed varying the f_z at each test. The force acquisition was performed during the micro slot machining. The roughing was performed through four identical consecutive passes with a depth of cut of 100 μm for each step. A four-flutes flat-bottom mill with a nominal diameter of 6 mm was employed to prepare the samples setting a cutting speed equal to 40 m/min and a feed per tooth of 10 μm/tooth.

The microchannels were produced using a coated two flutes micro mill with a nominal diameter of 0.8 mm. The actual tool geometry was acquired using a confocal microscope Hirox RH 2000 (see section 3.3). Further tool information are reported in **Table 10**. The tests were designed with the purpose of identifying the MUCT as a function of the feed per tooth. On each side of the 17-4 PH stainless steel workpiece, five cuts were performed moving the tool from the outer to the centre at a constant depth (a_p) of 200 μm. A cutting speed (v_c) of 40 m/min was kept constant for each cut. An actual tool diameter of 789 μm was measured by means of the BLUM laser measuring system mounted on the CNC machine.

Table 10. Data of the micro-mill.

Properties	Value
Nominal (μm)	800
Effective diameter (μm)	789 ±2
Nominal cutting-edge radius (μm)	5
Effective cutting-edge radius (μm)	6.3
Helix angle (°)	20
Rake angle (°)	4
Material	Tungsten Carbide
Material coating	Titanium Nitride

Figure 64 illustrates the machining pattern and the loadcell reference systems that was aligned to the KERN machine tool. Twenty micro channels were machined by using twenty feed per tooth values ranging between 0.5 μm and 10 μm with an increment equal to 0.5 μm. The tool wear has been measured with a digital optical microscope and resulted negligible. Between two consecutive tests the tool has been properly cleaned to remove any stick material as confirmed by the optical microscope observations.
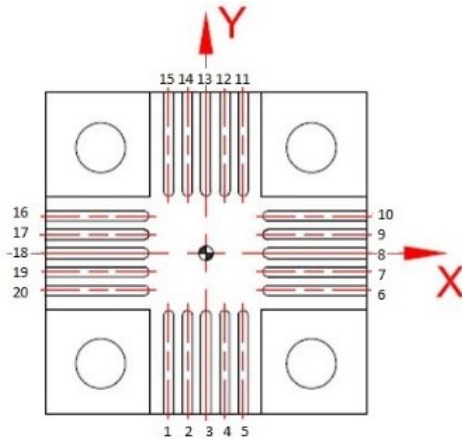
Figure 64. Micro-slot pattern with the related reference systems.

4.1.2 Experimental outputs

The force acquisition system allows to measure the cutting load component along each direction. The single components were subsequently composed to calculate the cutting force (F_c) through **Equation 32** (see section 3.5.2) directly in LabVIEW, the integrated development environment for the National Instruments graphic programming code. LabVIEW code

was integrated by a Butterworth 20th order low-pass filter with a cut-off frequency of 1000 Hz. The tooth pass frequency corresponding to cutting speed and the tool can be calculated by **Equation 33**.

$$f_{TP} = \frac{n}{60} * z$$

<div align="right">**Eq. 33**</div>

Considering the number of tool flutes ($z = 2$) and the spindle speed ($n = 15923$ rpm), the tooth pass frequency is equal to 530 Hz and consequently it is lower than the cut-off frequency. The signal was filtered to identify the cutting force maximum peak on the flutes for each rotation. As shown in **Figure 65,** the maximum peaks of the signal were not substantially altered.
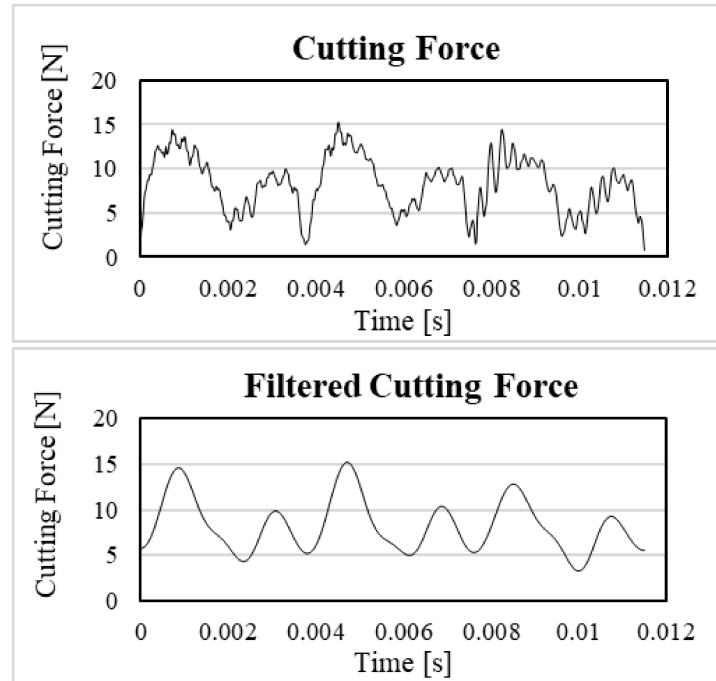
Figure 65. Comparison between the original cutting force and the filtered cutting force.

The roughness was evaluated by means of a Mitutoyo SJ300 profilometer with a 2 μm tip. The width (W_B) and the height (H_B) of each burr were measured for inner (where the chip starts to form) and outer channel side. An illustration is visible in **Figure 66**. The burrs width was measured by using a Mitutoyo Quick Scope optical coordinate measuring machine (see section 3.3), while the burrs height was measured by using a Hirox RH-2000 optical microscope. The width and the height were combined supposing the absence of curvatures of the burrs to obtain a unique value of the length (L_B) of the burrs on each side according to the **Equation 34**:

$$L_B = \sqrt{(W_B)^2 + (H_B)^2}$$

<div align="right">**Eq.34**</div>

The collected data were reported as function of the feed per tooth in order to evaluate the dependence of roughness and burrs in relation to the feed rate.
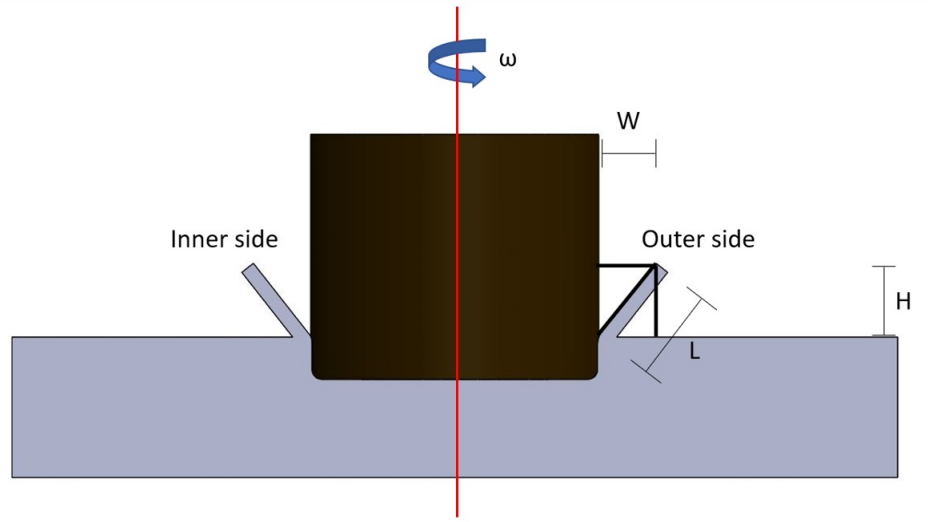
Figure 66. Schematic representation of the geometry of the burrs.

4.1.3 Specific Cutting Force (SCF) computation

The experiments allowed to investigate the regime transition as a function of the process f_z. The cutting force cannot be directly used in this analysis, and it must be normalized regarding the chip cross-section (S). **Equation 35** shows the relation between chip section and feed per tooth:

$$S = a_p * t_u$$

Eq.35

Where a_p is the axial depth of cut while the chip thickness t_u can be calculated by **Equation 3** described in section 2.1, and reported to

$$t_u = f_z \sin \theta - \frac{N}{2\pi R} f_z^2 \sin \theta \cos \theta + \frac{1}{2R} f_z^2 (\cos \theta)^2$$

Eq.36

In particular, the maximum cross section ($\theta = \pi/2$) is expressed by the product between the axial depth of cut (a_p) and the feed per tooth (f_z). The decrease of f_z between two consecutive test determines a section (S) reduction which has a considerable effect on the cutting force value. To highlight the dependence of the cutting force in relation to the deformation mechanism, the *SCF* must be calculated by **Equation 36**:

$$SCF = \frac{Fc}{S}$$

Eq.36

Where F_c is the cutting force resulting from the combination of all the force components including the cutting-edge component. The specific cutting force allows to identify the MUCT. During ploughing regime, the workpiece material elasto-plastic deformation determines a load increment. The phenomenon is enhanced by the accumulation of uncut material against the cutting edge. When shearing regime is prevalent, the correct chip formation causes the *SCF* decreases. A direct correlation between the regime transition and the specific cutting force must be identified without neglecting the tool run-out effects. The tool run-out

causes a difference between the effective chip thicknesses on each flute, determining an un-balanced load condition on the flutes. Considering two flutes, the maximum chip thickness for one flute (t_{u_Amax}) will be greater than the thickness for the other flute (t_{u_Bmax}). The asymmetric condition causes two cutting force peaks ($Fcmax_A$; $Fcmax_B$) which should be normalized by considering the effective thickness. The simplest approach is based on the hypothesis of a direct relation between chip section and force peak. **Equation 37** was implemented to calculate the effective chip thickness for tool flute A:

$$t_{u\_Amax} = \frac{2*Fcmax_A}{Fcmax_B + Fcmax_A} * f_z \quad t_{u\_Bmax} = 2f_z - t_{u\_Amax} \qquad \textbf{Eq.37}$$

Where $\frac{Fcmax_B + Fcmax_A}{2}$ is the average force peaks between edge A and edge B (Fc_{av}). Supposing that the average undeformed chip thickness is equal to f_z, **Equation 37** derived from the proportion $t_{u\_Amax} : Fcmax_A = Fc_{av} : f_z$. The signal of the Fc was considered in order to select a uniform portion corresponding to thirty tool rotations. For each spindle rotation the effective chip thickness t_{u_Amax} was calculated and subsequently an average value was obtained. The average value was finally utilized for the force normalization.

4.1.4 Results and Discussion

In this section, the results related to the evaluation of the transition regime of deformation are reported. **Table 11** shows the values of the average *SCF* calculated considering both the actual depth of cut (a_{peff}) and the force peaks ($Fcmax_A$, $Fcmax_B$).

Table 11. Results of the micro-milling tests performed at different feed per tooth values.

n	f_z [μm/tooth]	a_{peff} [μm]	$Fcmax_A$ [N]	$Fcmax_B$ [N]	SCF [N/mm²]	n	f_z [μm/tooth]	a_{peff} [μm]	$Fcmax_A$ [N]	$Fcmax_B$ [N]	SCF [N/mm²]
1	10	205.4	18.7	14.1	8016.0	11	5	200.5	12.2	4.1	8175.1
2	9.5	205.7	14.0	9.9	6127.6	12	4.5	199.3	10.5	3.6	7960.0
3	9	201.3	13.2	9.1	6177.5	13	4	198.9	11.7	2.5	9007.8
4	8.5	203.1	15.1	10.0	7266.7	14	3.5	199.1	11.0	2.1	9515.1
5	8	203.3	10.4	8.6	5887.3	15	3	198.7	10.9	2.1	10994.4
6	7.5	199.9	12.5	4.2	5595.4	16	2.5	209.8	10.6	1.6	11766.8
7	7	198.1	11.0	1.9	4684.5	17	2	206.3	15.2	3.1	22277.7
8	6.5	198.3	11.1	2.4	5251.8	18	1.5	200.8	15.6	4.3	33253.7
9	6	200.7	11.4	2.5	5840.3	19	1	205.8	17.3	3.0	49514.9
10	5.5	203.4	13.0	4.5	7857.1	20	0.5	202.6	17.8	1.9	97726.5

Figure 67 shows the measured cutting force peaks for each flute. The difference between the force peaks can be related to the tool run-out. It is possible to observe that when the feed per tooth is higher than 2 microns, the tool run-out influence slightly increases as the feed per tooth decreases. In fact, it is evident that the difference between the force peak of the flute A and the force peak of the flute B increases as the feed rate decreases. When the feed per tooth is equal or lower than 2 microns, the difference between the cutting force peaks strongly increases as the feed per tooth decreases. This behaviour can be related to a ploughing condition involving flute B that causes an increment of the undeformed depth of cut for flute A. Consequently, the normalization performed on the resulting cutting force values

allowed to investigate the cutting regime of the AM material by making the tool run- out effects negligible.
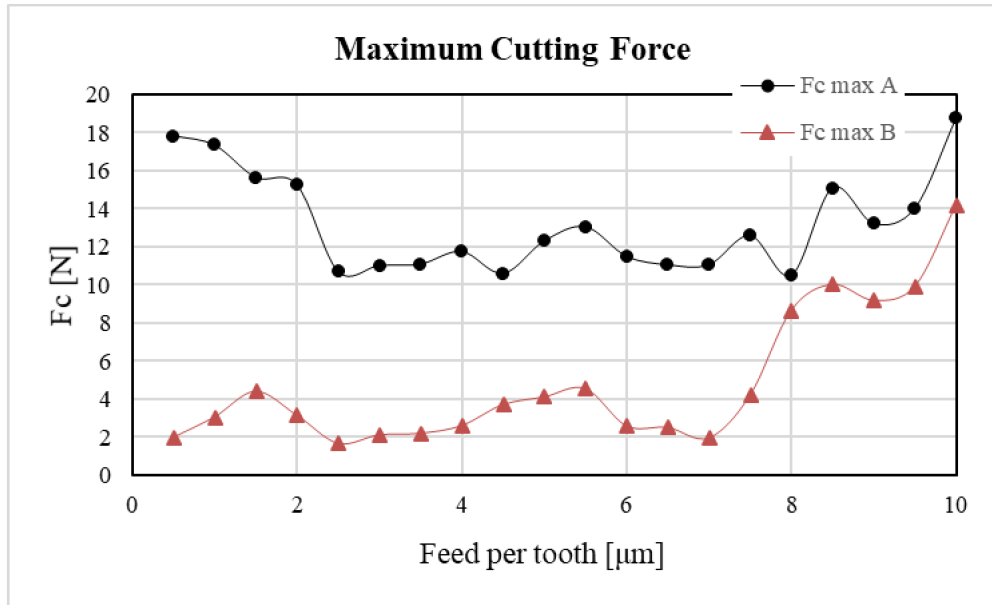
Figure 67. The maximum cutting force value for each flute versus feed per tooth.
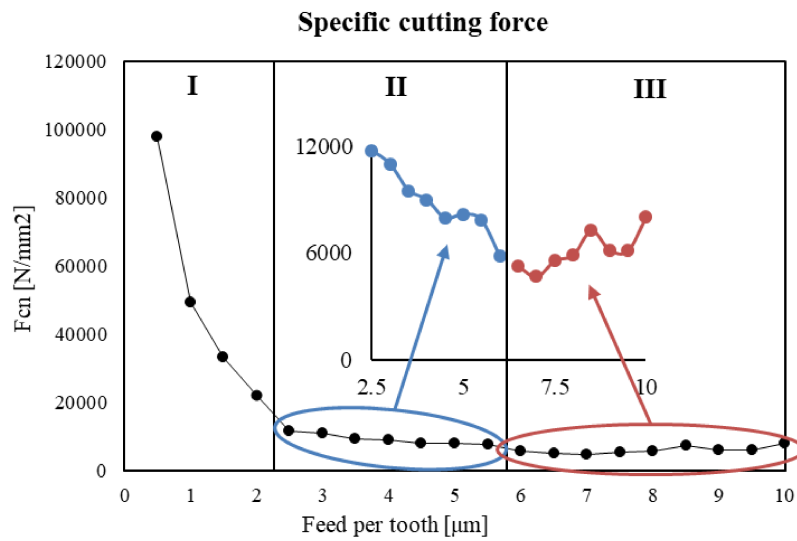
Figure 68. Specific cutting forces versus feed per tooth.

Observing **Figure 68**, the specific cutting force is not constant thorough the tests due to the presence of different deformation mechanisms. It shows an increase of the normalized cutting force when the feed per tooth decreases from 2.5 μm/tooth to 2 μm/tooth. This trend allows to set the MUCT value to 2.5 μm/tooth. Considering the deformation mechanisms, region I corresponds to a ploughing dominated regime extended to a feed per tooth value of 2.5 μm/tooth according to literature, which identifies the MUCT value as the 20% - 40% of the cutting-edge radius. The identified MUCT value is also in accordance with the behaviour observed in **Figure 67**. On the other hand, region III is related to the shearing deformation regime characterized by an independence of the specific cutting forces from the feed per

tooth values, as visible from the reported magnification of the specific cutting force. The region II can be identified as a transition zone between the two dominant deformations mechanism where the ploughing effects are progressively increasing as the feed per tooth decreases.

The roughness of the as built LB-PBF parts was measured on three replica of the same samples and resulted in 12.85±0.18 µm. The micro machining tests significantly improved the surface quality as required by standard mechanical application. The effects of the occurring of the ploughing regime are visible on the evaluation of the roughness trend reported in **Figure 69**
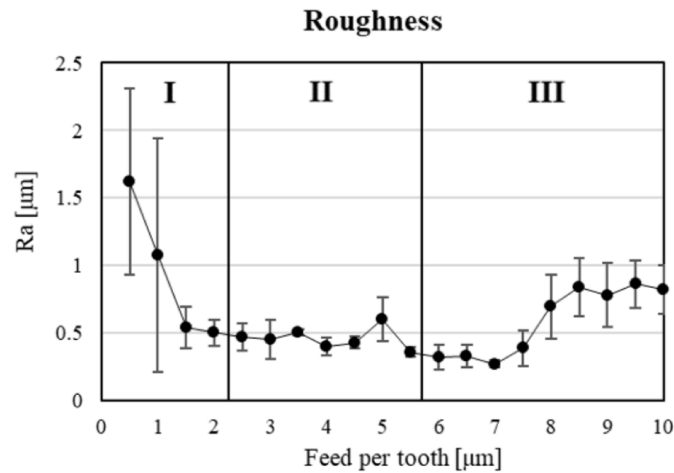
Figure 69. Average roughness versus feed per tooth.

As shown, high average roughness values are also related to the higher sensitivity to run out of the kinematic roughness at lower values of f_z. Moreover, the increased variability of the results is probably due to the incorrect chip formation mechanism during ploughing that is responsible of uncontrollable irregularities and accumulation of material thought the flute path. On the other hand, when the shearing regime is dominant, the mean roughness values depend on the feed per tooth values according to the typical trend of cutting tests. Moreover, the reduced variability of the data demonstrates the transition to a more regular deformation mechanism.
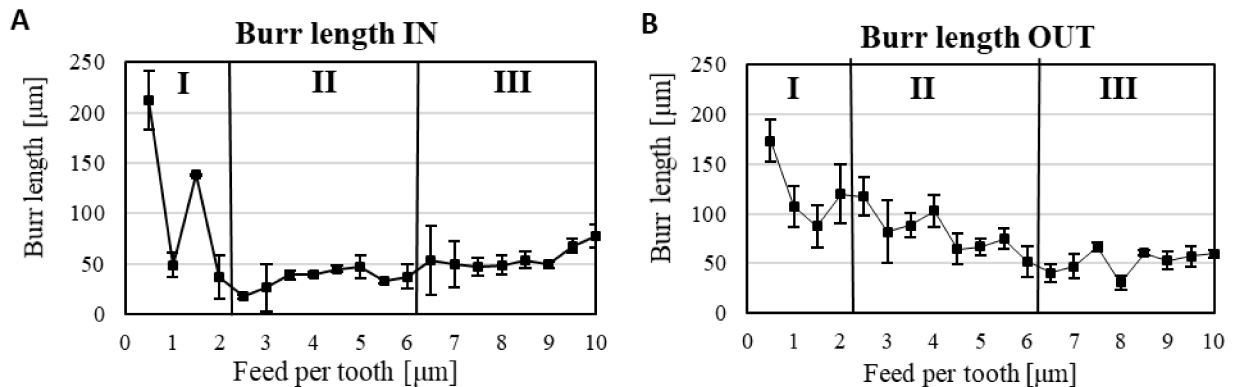
Figure 70. Burr length on the inner side (A) and burr length on the outer side (B) vs feed per tooth.

The burr length was considered to evaluate the influence of the ploughing regime on the feature quality (**Figure 70**). As expected, the length of the burrs on the outer side is higher compared to the length on the inner side. The burr length on the inner side of the channels is strongly influenced by the occurring of the ploughing regime as highlighted from an increase of the average values. As the shearing regime is dominant, the length of the burrs begins to be dependent on the feed rate as visible from the trend of the data. On the other hand, the burr length on the outer side is more variable probably due to the instability of the ploughing regime and the presence of compressed AM material.

4.2 Micro-milling of LB-PBF Inconel 625

Nickel-based superalloys (Ni-Cr, Ni-Co-Cr, Ni-Fe-Cr, or Ni-Co-Fe type) are some of the metal alloys which can be utilized in AM processes in the powder form. Such materials are widely used in aerospace and power industries, as well as in biomedical industry, due to their high strength, high temperature resistance, super-elasticity behavior and good properties in terms of bioactivity **[192]**. The trademark name "Inconel" commonly identifies a specific class of Nickel-Chromium alloys with superior mechanical proprieties, such as high resistance to corrosion and temperature **[193]**. Moreover, Inconel superalloys are known to be very difficult-to-cut **[194]** due to their ability to retain their very high yield strength and the low thermal conductivity. The Inconel superalloy proprieties and difficulty in workability make these alloys more suitable for the integration between the metal AM and the conventional subtractive material removal processes. Complex-shaped and miniaturized parts could be built via metal AM methods and subsequently their surfaces could be finished or polished through micro milling operations **[195]**. The main objective of this work was to investigate the machinability of a specific Ni-Cr-Mo superalloy, Inconel 625, a superalloy characterized by high temperature resistance, high corrosion resistance, and good wear resistance properties **[196]**. Micro milling experimental tests were performed on an additively manufactured workpiece obtained via LB-PBF. The experimental tests can be divided in two categories: the first one corresponds to some micro-slots micro-machining finalized to compute the MUCT (see section 4.1), the second group of test consists in micro-machining of thin-walled samples. The second group of tests was designed with the specific purpose of operating micro machining under orthogonal cutting condition, collecting data useful for an analytical model calibration which will be described in Chapter 5.

4.2.1   Experimental procedure

The tests were executed on Inconel 625 samples fabricated via LB-PBF process with the AM machine GE Additive Concept Laser M2 Cusing described in section 3.1.1. The laser power P, the scan velocity v_s, the laser spot size d, the laser thickness s, the hatch distance h, the stripe width w and volumetric energy density E are listed in **Table 2**.

Table 12 summarizes the chemical composition of the certified Inconel 625 provided by the supplier, while **Table 13** shows the mechanical properties of this material "as-built" in Z

direction. The powder particle size was ranging between 15 μm and 45 μm. The samples were not heat treated (or hot isostatically pressed).

Table 12. Chemical composition of Inconel 625.

	Ni	Cr	Mo	Cb	Fe	Si	Al	Ti
Wt (%)	61.6	22.0	9.0	4.0	3.0	<0.3	<0.2	<0.2

Table 13. Mechanical properties of Inconel 625 **[28]**.

Specimen orientation (X, Y, Z)	Yield strength (MPa)	Ultimate tensile strength (MPa)	Elongation (%)	Hardness (HRC)
Z	410	750	44	14

Figure 71 shows the geometry of the sample utilized for the test finalized to the MUCT identification **(Figure 71 a)** and the geometry of the thin-walled sample used to calibrate the analytical model coefficients **(Figure 71 b)**. The thin wall had a nominal thickness of 0.1 mm.

(a)　　　　　　　　　　　　　　　　(b)
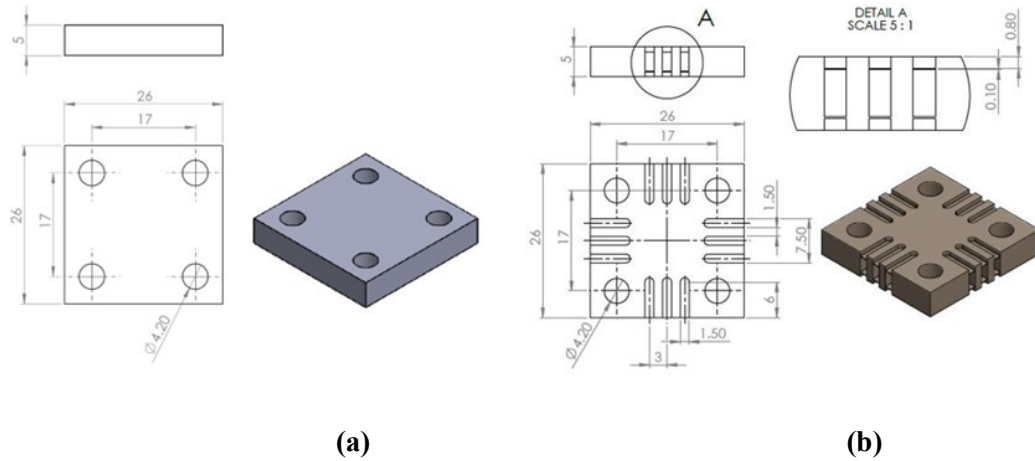
Figure 71. The workpiece geometries: (a) for the MUCT test (b) for the thin-wall cuts.

The sample shapes were designed in order to directly constrain the samples on the loadcell. Both experimental procedures were performed by using the 5-axis nano-precision milling center Kern Pyramid Nano equipped with a cutting force measurement system. The machining was performed in dry condition, without using cooling lubricant.

The micro-machining tests finalized to determine MUCT consist in the fabrication of twenty channels by using a constant cutting speed and twenty different values of feed per tooth f_z, ranging between 0.5 μm/rev*tooth and 10 μm/rev*tooth. The channels were fabricated on a flat surface which was obtained through a face milling operation. The surface roughing was performed by using a two-flute carbide end-mill with a diameter of 6 mm. A cutting speed of 54 m/min, a feed rate of 50 mm/min and an axial depth of cut a_p of 0.1 mm were utilized to execute the rough machining. All slots were machined by using a two-flute micro mill under the same run-out condition. The cutting speed was set at 40 m/min and the depth of cut was fixed at 200 μm, as suggested by the tool manufacturer for hard-to-cut non-ferrous

material. The actual tool geometry was acquired and checked by using a 3D digital microscope Hirox RH 2000. **Table 14** presents further details about the micro end mill.

Table 14. Features of the micro-end mill.

Feature	Value
Manufacturer	SECO
Model code	SECO905L008-MEGA-T
Nominal diameter (μm)	800
Effective diameter (μm)	791 $\pm$1
Nominal cutting edge radius (μm)	5
Helix angle (°)	20
Rake angle (°)	4
Material	Tungsten Carbide
Material coating	Titanium Nitride

Five consecutive slots were fabricated on each side of the sample (see **Figure 64**). The length of the slots kept constant as 8 mm. Between two consecutive cuts, the tool flutes were cleaned to remove sticking material and to avoid the build-up edge phenomena.

The cutting force components were acquired with the loadcell during the whole channel fabrication. The resultant cutting force was obtained and smoothed by using a low-pass filter with a cut-off frequency of 1000 Hz. The maximum peaks of the cutting force were not modified by the filter because the tooth passing frequency is lower than the cut-off frequency. The tooth passing frequency can be calculated by using **Eq. 33** and it is equal to 530 Hz. The **Equation 3** and the **Equations 35-37** (see section 4.1.3) were employed to compute the average peaks of the Specific Cutting Force (SCF).

In addition, a second group of micro-machining tests was performed on Inconel 625 samples. The orthogonal cutting tests were executed to collect experimental data useful for the calibration of an analytical model able to predict cutting forces. Experimental tests have been carried out assuming a thin-wall channel-milling configuration.
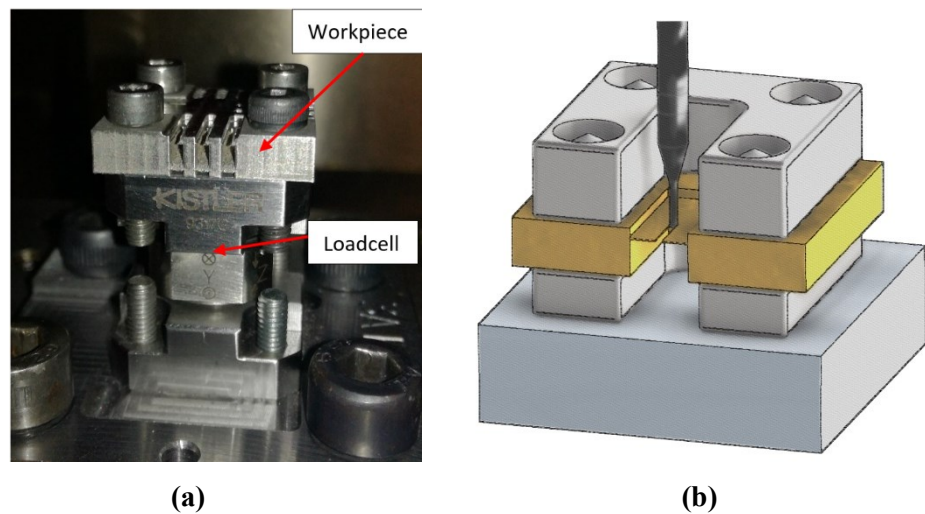

(a)   (b)

Figure 72. The geometrical configuration of the thin-wall micro-cuts, a picture (a) and an illustration (b).

93

The thin-wall configuration, as well as the use of end-mill tools with 0° helix angle, has been assumed in order to replicate orthogonal cutting conditions and it is visible in **Figure 72**. **Table 15** presents further details about the zero-degree helix micro end mill used in actual thin-wall milling tests.

Table 15. Zero-degree helix angle micro end mill features.

Feature	Value
Manufacturer	SECO
Model code	103L008R005-MEGA-64T
Nominal (μm)	800
Effective diameter (μm)	789 ± 3
Nominal cutting edge radius (μm)	4
Helix angle (°)	0
Material	Tungsten Carbide
Material coating	Titanium Nitride

The analytical force model allows to compute cutting forces as a function of uncut chip thickness by considering the presence of different cutting regimes. Therefore, a validation procedure was performed by machining several samples with different combinations of feed per tooth and cutting speed. The machining tests consist in the fabrication of a through-channel for each thin-wall. Three feed per tooth values (2.5, 5, and 10 μm/rev*tooth) and two cutting speeds (30, 40 m/min) were combined while the channel length was set constant and equal to 5 mm. Each test was repeated three times to statistically validate the analytical model. During the machining, the load measurement system was utilized to acquire the cutting force F_c. A uniform portion corresponding to thirty tool rotations was considered for each test, and an average cutting force signal was finally computed for each slot fabrication.

Table 16 summarized the process parameters combinations. The depth of cut a_p, which corresponds to the thickness of the thin-wall was measured before performing the cutting test. The measurements were executed with five repetitions along each thin wall by using the

microscope Hirox RH-2000 and the average thickness was found to be 171 ± 17 μm. **Table 17** summarized the actual thickness with the standard deviation and the deviation from the nominal value of 200 μm. The results highlight on one hand a uniform thickness along each thin wall, moreover the thickness differ from one another by a non-negligible quantity. For this reason, the effective thickness of each thin wall was utilized in the analytical model calibration and validation instead of the average value.

Table 16. Process parameters combinations.

Test	Cutting speed (m/min)	Feed per tooth (μm/rev*tooth)
A	30	2.5
B	40	2.5
C	30	5
D	40	5
E	30	10
F	40	10

Table 17. Process parameters and samples actual dimensions.

Test	Actual thickness (µm)	Deviation (µm)	Test	Actual thickness (µm)	Deviation (µm)
A1	171±2	29	D2	176±4	24
B1	180±2	20	E2	177±4	23
C1	200±3	0	F2	199±2	1
D1	174±3	26	A3	168±2	32
E1	150±2	50	B3	178±1	22
F1	137±3	63	C3	175±3	25
A2	154±3	46	D3	186±2	14
B2	165±2	32	E3	187±1	13
C2	155±3	45	F3	149±2	51

4.2.2   Results and Discussion

The numerical results and the relation between the specific cutting force and the feed per tooth is visible in **Figure 73**. The specific cutting force is not constant, and it decreases as the feed rate increases. The results are qualitatively comparable with the trend of conventional fabricated workpiece [197]. For feed per tooth higher than 6 µm, the specific cutting force is almost constant. During the tests performed with the highest feed rate, the transition from ploughing to shearing regime occurs when the tool rotation angle θ is nearly zero. In shearing dominant zone, the ploughing effect cannot affect the cutting force peak. The tests performed with feed per tooth lower than 2.5 µm are characterized by the presence of a single cutting regime, hence the ploughing. The SCF increases as the feed rate decreases. When ploughing is the dominant regime, the cutting process becomes instable due to the unaccounted material removal behavior, therefore, SCFs are more variable as demonstrated by a larger standard deviation of the data, visible as the error bars in the graph of **Figure 73 b**. During the transition between ploughing and shearing, the correlation between specific cutting force and feed per tooth is linear. The minimum uncut chip thickness was identified as the feed per tooth value corresponding to the beginning of the ploughing dominant zone. Therefore, the value of the MUCT was set equal to 2.5 µm.

n	f_z (µm/rev*tooth)	Fc_n (N/mm²)	n	f_z (µm/rev*tooth)	Fc_n (N/mm²)
1	10	13354.9	11	5	21405.3
2	9.5	11466.1	12	4.5	23145.3
3	9	12057.0	13	4	24285.3
4	8.5	13626.0	14	3.5	26631.2
5	8	13736.9	15	3	29045.6
6	7.5	15096.9	16	2.5	35357.0
7	7	16142.6	17	2	36210.1
8	6.5	15345.3	18	1.5	45648.43
9	6	16238.0	19	1	69289.2
10	5.5	17543.9	20	0.5	112590.9
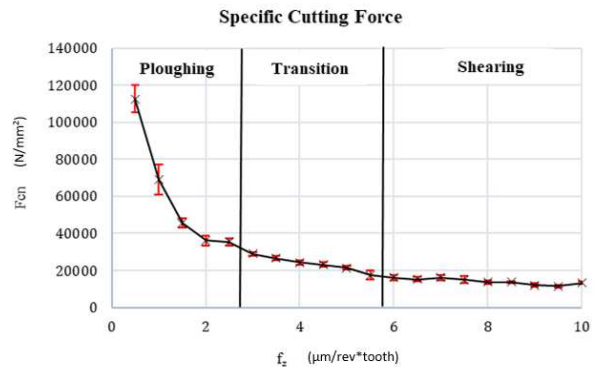
(a)   (b)

Figure 73 The average maximum SCF (a) and the correlation between the maximum specific cutting force and the feed per tooth (b).

Figure 74 shows the average cutting force, with lower and upper bounds, measured during the thin wall machining executed with a cutting speed of 30 m/min at different feed per tooth f_z. Tests A (**Figure 74 a**), C (**Figure 74 b**) and E (**Figure 74 c**) are characterized by increasing feed per tooth, from 2.5 µm/rev*tooth to 10 µm/rev*tooth.

The tool run-out determines unbalanced cutting condition between the flutes, but it is clear that cutting force peaks increase as the feed rate increases. The tests performed with a cutting speed of 40 m/min show an analogue trend (Test B, D, and F). **Table 18** summarizes the average cutting force peak for each cutting edge (*Fc CE1* and *Fc CE2*) and the ratio between peaks**Table 18.** Average peaks of the cutting force for each tool flute and their ratio.

Test	f_z (µm/rev/tooth)	F_c CE1 (N)	F_c CE2 (N)	F_c CE1/F_c CE2
A1	2.5	3.43	1.06	3.2
C1	5	5.21	2.73	1.9
E1	10	6.08	4.05	1.5

The ratio between the cutting force peaks on the flutes is equal to 1.5 for Test E, while the ratio for Test A is equal to 3.2 and for Test C is equal to 1.9. The load unbalance between the tool flutes is higher at low feed rate where the ploughing effects are more relevant.

The highest f_z combined with a cutting speed of 30 m/min allows minimizing tool run-out effects and consequently reducing the approximation about the model parameters calculation. Therefore, the more reliable model calibration was executed by using the experimental data measured during Tests E. The machining test performed in different conditions were utilized to provide the analytical model validation by comparing the model prevision with the experimental data.
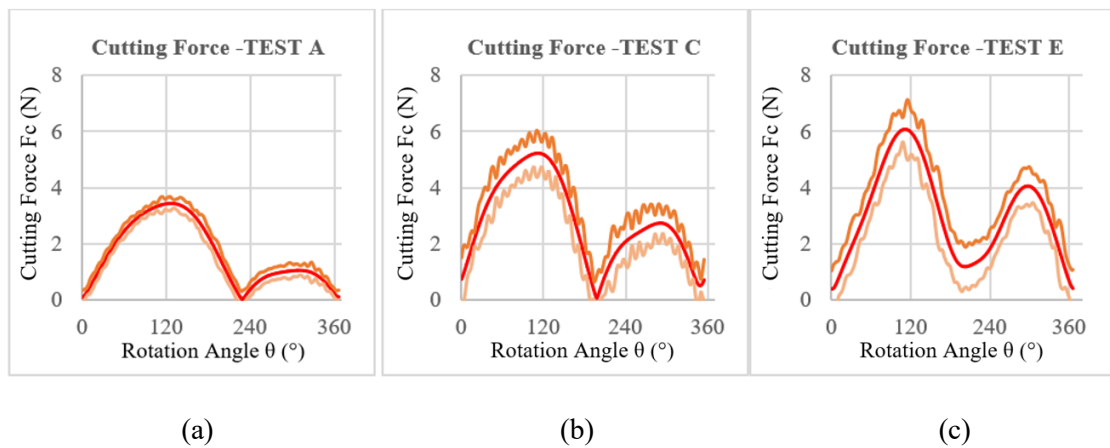

(a)   (b)   (c)

Figure 74 Average cutting force with lower and upper bounds for Test A1 (a), Test C1 (b) and Test E1 (c).
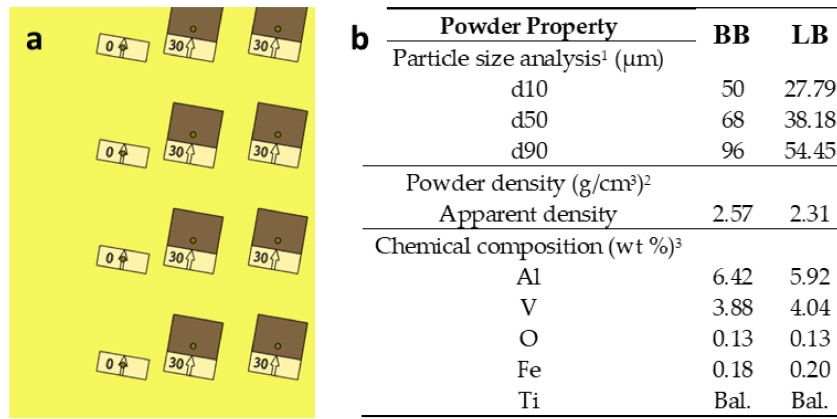
4.3 Micro-milling of PBF and conventionally formed Ti6Al4V alloy

A deep and extensive researcher work about the micro-machinability of Ti6Al4V alloy was performed. Several tests were done in order to experimentally compare the micro-machinability of additively manufactured samples with the micro-machinability of conventionally fabricated samples with mill annealed structure. Laser Based Powder Bed Fusion and Beam Based Powder Bed Fusion processes were used to produce samples with a building direction of 0° and 30° in relation to the plate. Micro machining operations require a proper process characterization depending on the microstructure of the processed material. Specifically, due to the high cooling rates that PBF Ti64 undergoes to, the microstructure of LB-PBF parts is typically characterized by a dominant martensitic microstructure while BB-PBF samples demonstrate a microstructure composed of an α phase and a small amount of β, resulting in a fine α + β dual phase. However, β remains the primary mode of solidification as expected for Ti64 alloys **[65, 198, 199]**.

Specific cutting force in milling of Ti64 alloy decreases as the cutting speed increases **[200]** but a lack of data affected the behavior in micro milling, where size effect is not neglectable. The Minimum Uncut Chip Thickness (MUCT) was determined to investigate the removal behavior during slot machining with rounded-edges micro-tools. The cutting forces were measured, and the loads were utilized to calculate Specific Cutting Force (SCF). It was reported as a function of the feed per tooth (f_z) to investigate when the transition between shearing and ploughing occurs. Once the MUCT was identified, further micro machining tests were performed by changing the feed rate and cutting speed. The surface roughness (*Sa*) and cutting force of the machined samples were measured to deeply investigate the effects of ploughing regime. The dependence of roughness on the sample fabrication technique and on the process parameters of micro milling was highlighted.

4.3.1 Experimental procedure

In this section, the fabrication and machining operation of the LB-PBF, BB-PBF and as received Ti64 samples are reported. The as received microstructure of Ti6Al4V bars (20 mm diameter) was verified and observed under optical microscope. The samples show the presence of a mill annealed microstructure, resulting from cooling after plastic deformation, without any recrystallization annealing **[201]**.

Powder Property	BB	LB
Particle size analysis[1] (µm)		
d10	50	27.79
d50	68	38.18
d90	96	54.45
Powder density (g/cm³)[2]		
Apparent density	2.57	2.31
Chemical composition (wt %)[3]		
Al	6.42	5.92
V	3.88	4.04
O	0.13	0.13
Fe	0.18	0.20
Ti	Bal.	Bal.

[1] ASTM B214 and B215 [20]. [2] ASTM B212 [21]. [3] ASTM F2924 and F1472 [22]. Bal., balance.

Figure 75. (a) Building orientation of the PBF-LB and PBF-BB samples on the printer plate; (b) Ti64 powders compositions and properties. Related ASTM international standards are reported.

About AM process, cubical samples have been fabricated by LB-PBF and BB-PBF additive manufacturing. The AM samples have been produced with two building orientations. The chosen angles were 0° and 30° in relation to the building plate for both the BB-PBF and LB-PBF processes (**Figure 75**). Parameters have been set along with the lab experience with the used machines and powders. The building angles were chosen to replicate the design features that can be inserted on an implant for promoting osseointegration and affect the surface functionalization without a time-consuming post-processing technique. The building orientation has been varied to assess whether the powder bed fusion process can modify the surface characteristics of the metal samples and influence the cellular interaction and adhesion for a target application.

Ti64 samples with cubical geometry (10x10x10 mm³) have been produced using Ti6Al4V powders (EOS Titanium Ti6Al4V for LB-PBF and ARCAM Ti64Al4V for BB-PBF). The properties of the atomized powders are reported in **Figure 75b** according to ASTM B214, B215, B212, F2924 and F1472 **[53]** as reported on the required datasheets. The BB-PBF samples and LB-PBF samples have been fabricated using an EBM SYSTEMS MODEL A2 (see section 3.1.2) and an EOS M290 (see section 3.1.1), respectively. The LB-PBF performs a scanning strategy with an alternating angle between each layer of 67°. The LB-PBF parameters for the samples production were listed in **Table 4**, while the LB-PBF parameters for the samples production were listed in **Table 5**. The BB-PBF process operates a scanning strategy alternating an angle of 90° between the layers. Both the PBF manufactures were carried on in a controlled argon gas atmosphere to reduce the oxygen pick-up to <0.1%. The samples, after supports removal, have been cleaned with sonication in acetone and isopropanol and left to dry.

The machining tests were carried out with the five axis Nano Precision Machining Centre KERN Pyramid Nano. The samples were constrained to the loadcell through brackets. A roughing operation was performed to obtain a planar surface on the samples through a single

cut of 100 μm depth with a three-flutes flat-bottom mill (nominal diameter: 3 mm), cutting speed set to 100 m/min and a feed per tooth of 7.5 μm/tooth.

(a)
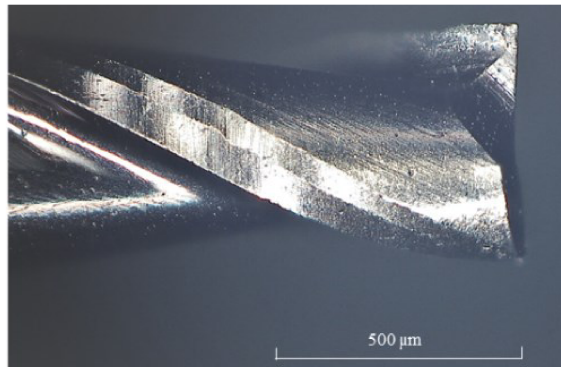
(b)

Figure 76. Micro mill with a diameter of 0.5 mm, top view (a) and lateral view (b).

Microchannels have been subsequently machined with a coated two-flutes micro mill (nominal diameter: 0.5 mm) visible in **Figure 76**. The micromachining was performed in dry condition. The details of the tool geometry acquired with the Hirox RH-2000 confocal microscope are reported in **Table 19** with the information about the materials of tool and coating. The tool manufacturer suggests the coating in Titanium Nitride for machining lightweight alloys in dry condition. The micro milling tests can be divided in two groups. In each case, the tool was moved from the outer part of the samples to the centre at a constant depth of cut equal to $a_p = 0.03$ mm.

Table 19. Properties of the tool used for the micro slot machining.

Proprieties	Value
Model	Rime HM79/05
Nominal (μm)	500
Effective diameter (μm)	475 ±4[*]
Effective cutting-edge radius (μm)	5 ±2
Helix angle (°)	30
Material	Tungsten Carbide
Material coating	Titanium Nitride

*Measured by the BLUM laser measuring system mounted on the CNC machine.

Test	f_z [um]	Vc [m/min]
1	4.0	40
2	3.5	45
3	3.5	35
4	3.0	50
5	3.0	40
6	3.0	40
7	3.0	40
8	3.0	30
9	2.5	45
10	2.5	35
11	2.0	40

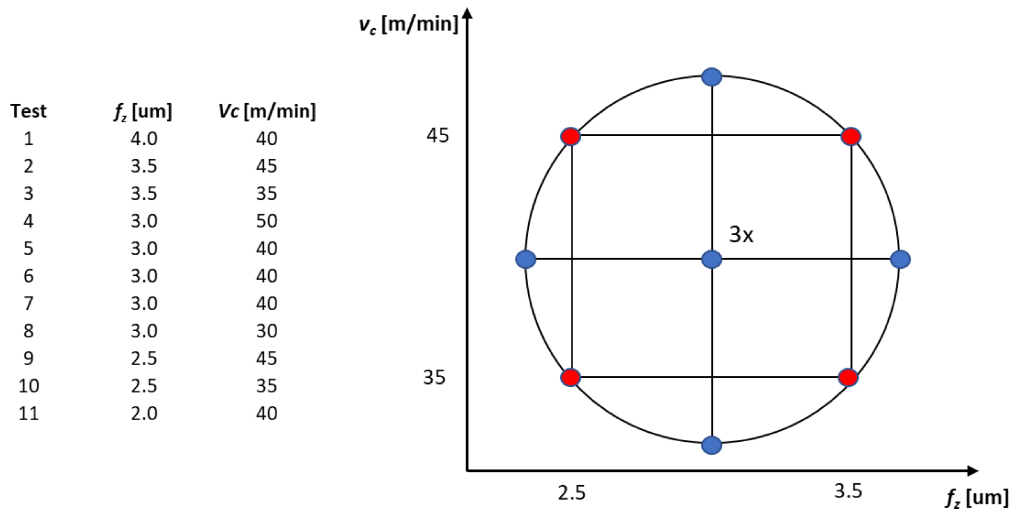v_c [m/min]

45

35

3x

2.5   3.5 f_z [um]

Figure 77. Summarization of the process parameters and illustration of CCD plan.

Constant cutting speed ($v_c = 40$ m/min) tests were performed to measure the cutting forces necessary to determine the ploughing-shearing transition with the MUCT quantification. The cutting forces were acquired by machining ten channels on the samples top surface with different feed per tooth values (f_z) ranging from 0.25 μm/tooth to 4 μm/tooth. This range has been defined experimentally and has been observed that feed per tooths higher than 5 μm/tooth cause the total breaking of the tool. Once the MUCT was determined, a second group of micro machining tests were performed to evaluate the influence of the process parameters on the specific loads acting on the tool and the surface roughness of the parts.

Two values of feed per tooth in shearing regime and two cutting speeds were combined maintaining a depth of cut (a_p) set to 0.03 mm. The test plan was implemented by using the centered composite design (CCD). **Figure 77** summarizes the process parameters of the CCD model.

The standard 2^2 experimental plan (2 factors varied on 2 levels, the red points in Figure 77) is completed by testing further three levels for each factor (the blue points in Figure 77), for a total of nine actual combination of the factors. As required by the CCD model, only the central point was repeated three times. The tool has been properly cleaned by using a silicone rubber after each test to remove any adherent material. The tool was substituted after the machining of a single sample. The tool wear was verified with a digital optical microscope and it resulted negligible.

4.3.2 Experimental outputs

The cutting force (F_c) was calculated as a combination of the single components of the cutting load along each direction that have been measured by the force acquisition system. A Butterworth 20th order low-pass filter based on a cut-off frequency of 1300 Hz was introduced in the code to filter the cutting force in relation to the tooth pass frequency. The tooth

pass frequency can be calculated by **Equation 33** in relation to the cutting speed; cconsidering the unfavorable condition of two flutes and a spindle speed of 31831 rpm, the f_{tp} results 1062 Hz and thus lower than the cut-off frequency. The filtered signal allows the correct identification of the cutting force maximum peak on the flutes during each rotation. As described in section 4.1.2, the average peaks of SCF were computed by using **Equation 3** and **Equation 35-37**. The surface roughness of the samples was observed with the PF60 (see section 3.3) according to ISO 25178. Optical imaging was performed at 400x magnification with a scanning size of 0.5×1.5 mm^2 selected at the central point of the surface. The scanning was carried out between the minimum and maximum focusing points of the height (z) of the BB-PBF and LB-PBF sample surfaces. The Digital Surf MountainsMap® Premium software (v.8 ©1996-2021 Digital Surf, Besançon, France) was used to process the images and obtain the S_a and S_q values.

4.3.3   Results and Discussion

The first group of micro machining tests were performed to identify for each material the transition between ploughing and shearing i.e. the Minimum Uncut Chip Thickness value.
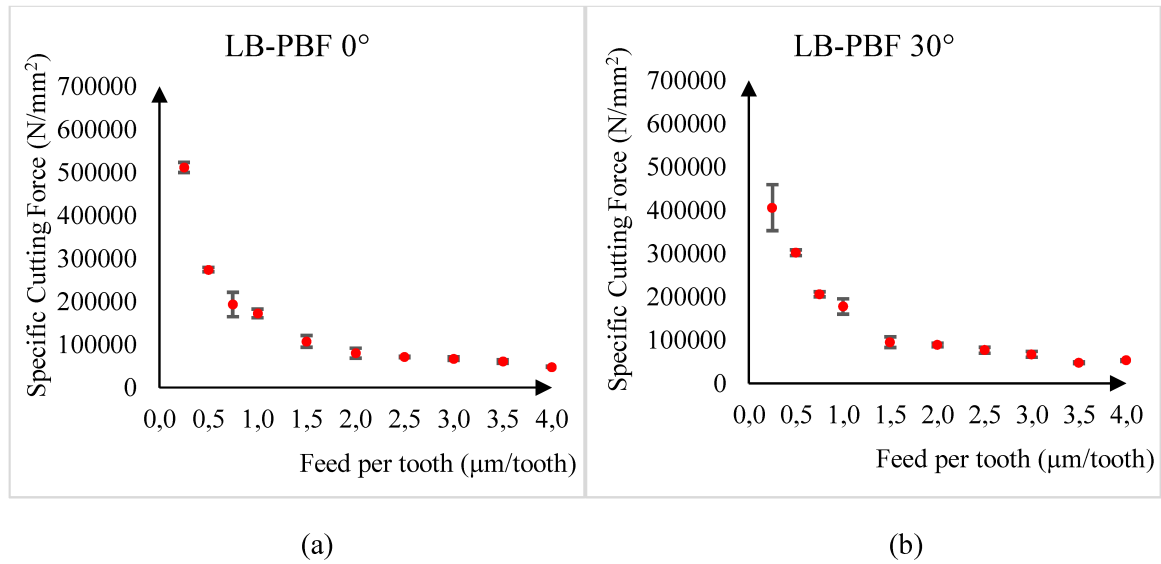

(a)   (b)

Figure 78. LB-PBF, SCF versus feed per tooth with error bars, building angle 0° (a) and building angle 30° (b).
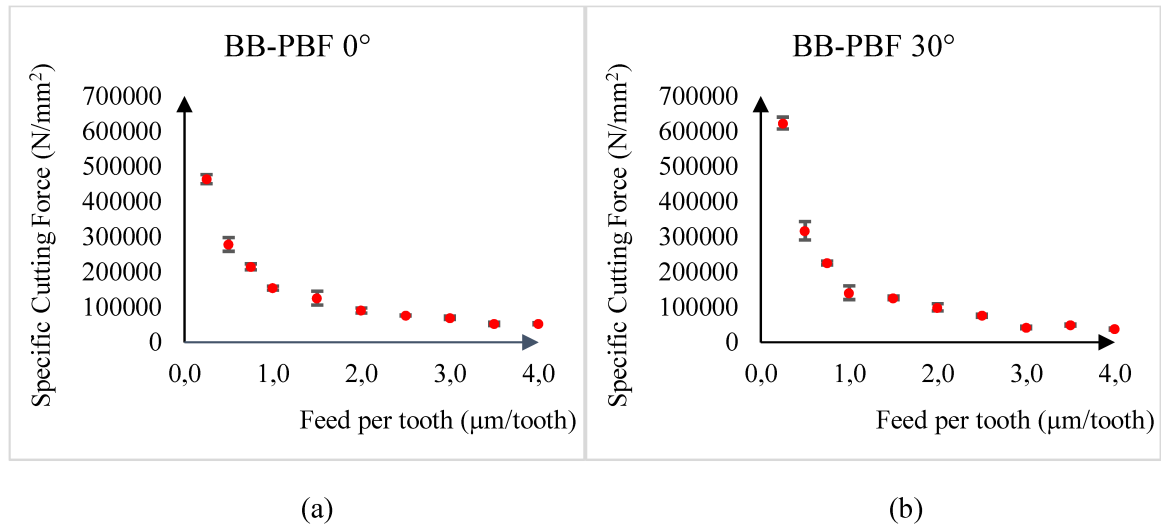
Figure 79. BB-PBF, SCF versus feed per tooth with error bars, building angle 0° (a) and building angle 30° (b).
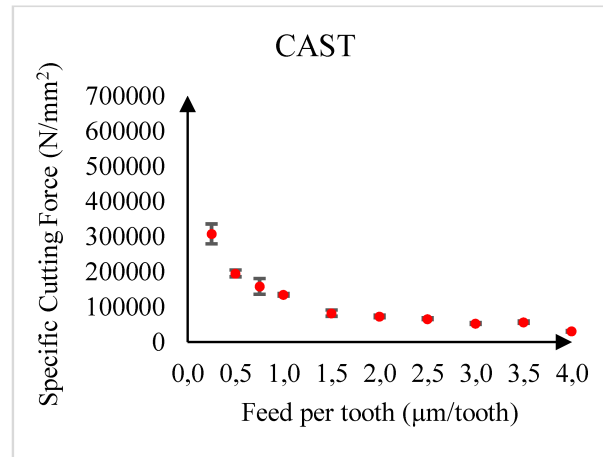

Figure 80. Cast alloy, SCF versus feed per tooth with error bars.

The cutting force signal was elaborated by considering a signal portion corresponding to thirty micro mill rotations. The previous figures show the average of the thirty peaks of the SCF measured cutting the LB-PBF (**Figure 78**), BB-PBF (**Figure 79**) and mill-annealed samples (**Figure 80**). Error bars refer to an interval of confidence equal to 99% ($\pm 3\sigma$). As reported in all figures, the specific cutting force decreases as the feed per tooth is increased. The transition between the ploughing and shearing regime occurs approximately at 1.5-2.0 μm/tooth for all the materials tested. Despite the analyzed materials have different microstructures, this value depends only on the tool geometry and, in this case, is equal to the 40% of the tool cutting edge radius, according to previous studies [197]. Precisely, the SCF during ploughing reaches a value that is ten times higher than in shearing, causing sever tool wear problems. Furthermore, when ploughing is dominant, the variance and the instability of the data between the different materials increases as visible from the deviations standard of the data measured at 0.25 μm/tooth. Moreover, observing the specific cutting force trends after MUCT (from 2 μm/tooth to 4 μm/tooth) it is evident that the plateau normally present

at high feed rates was not reached. This behavior is due to the co-presence of ploughing regime and sharing regime. As the feed rate increases the shearing regime become predominant causing a constant decrease of the specific cutting force as the feed per tooth increases.
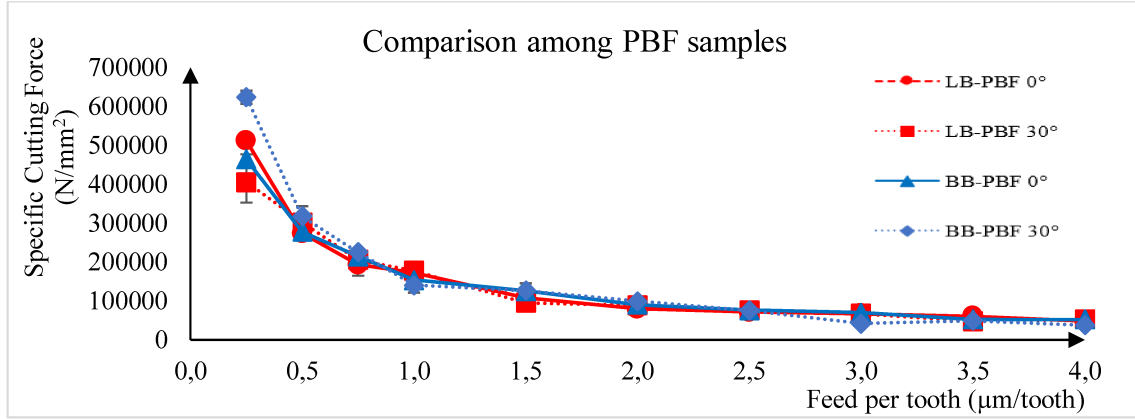

Figure 81. Comparison among the PBF samples, SCF versus feed per tooth with error bars.

As reported in **Figure 81**, the SCF results neither related to the additive manufacturing process nor to the building strategy used for the powder bed fusion process. A meaningful difference is visible only at $f_z = 0.25$ μm/tooth, but it is caused by the large variability in ploughing dominant regime. As expected, the forces are not influenced by the source of the powder fusion process but by the microstructure determined by the typical solidification process of Ti6Al4V alloys that despite being different after LB-PBF and BB-PBF processes, is similar among the powder bed fused titanium powders **[65]**.

Figure 82 reports the comparison between the PBF samples and the cast. In this case, a different behavior between PBF and mill-annealed samples is visible in ploughing regime while in shearing the trends converge. Precisely, the specific cutting forces during ploughing are lower for the mill-annealed samples. This behavior is due to the different microstructure of the mill-annealed in relation to the PBFs that is characterized by lamellar structures. In fact, being the hardness of lamellar structures higher than the mill-annealed ones [77], the specific cutting forces are increased in case of PBF samples.
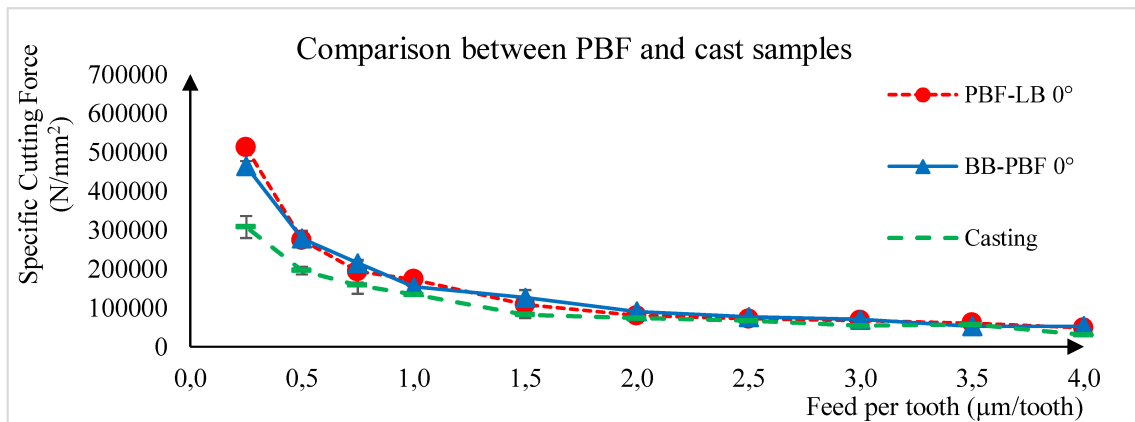

Figure 82. Comparison between the PBF samples and the cast samples, SCF versus feed per tooth with error bars.

On the other hand, during shearing, the ductility of the mill-annealed samples can cause the adhesion of the material increasing the contact length during the cutting. This phenomenon can promote an alignment of the specific forces calculated for the different materials during shearing.

The second group of tests were performed by varying feed per tooth and cutting speed. The experimental tests were conducted by using the Centered Composite Design (CCD). **Figure 83** reports the surface plot of the specific cutting force. As confirmed by the statistical analysis performed on the results of the CCD model, the SCF is not influence by the cutting speed (p value>0.05 for PBF and mill-annealed samples). While, the feed rate has a significant influence on the normalized load as demonstrate by the p values calculated for each samples. The p value for feed rate parameter is equal to 0.01 for the LB-PBF, 0.021 for the BB-PBF and 0.008 for the mill-annealed parts. In all cases, the specific cutting forces decrease with the increasing of the feed per tooth values, confirming the presence of ploughing regime especially for low f_z.
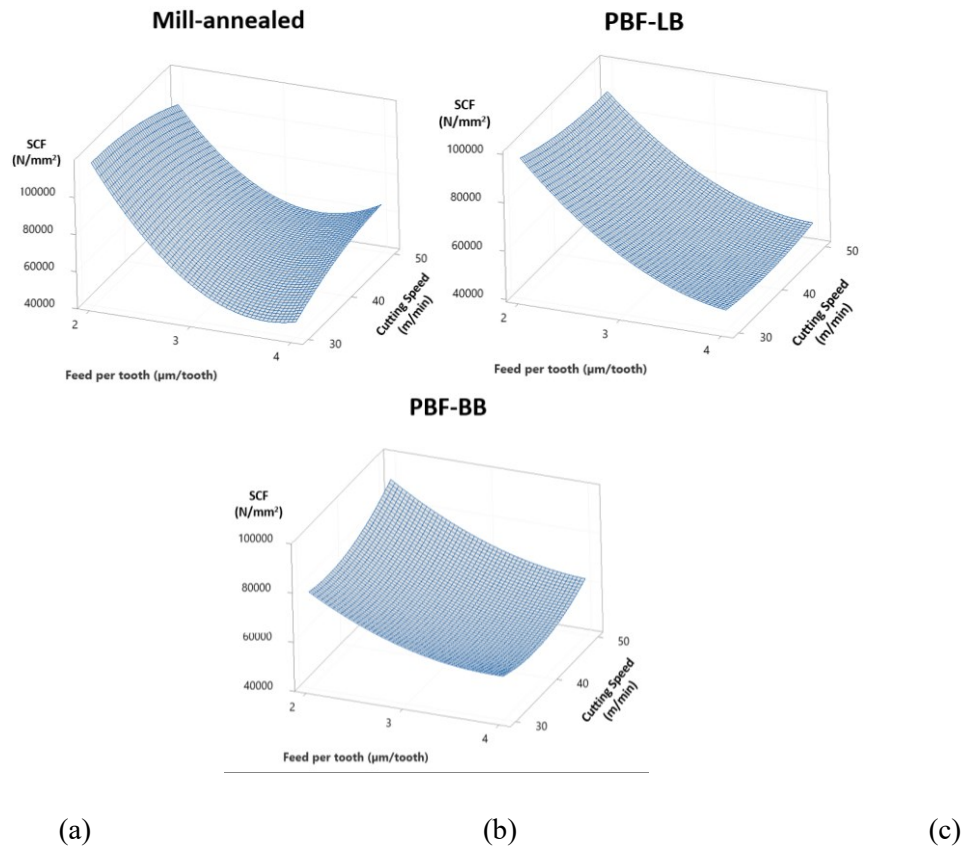

(a)   (b)   (c)

Figure 83. Surface plot of specific cutting force as function of feed per tooth and cutting speed, for cast (a), LB-PBF (b) and BB-PBF (c).
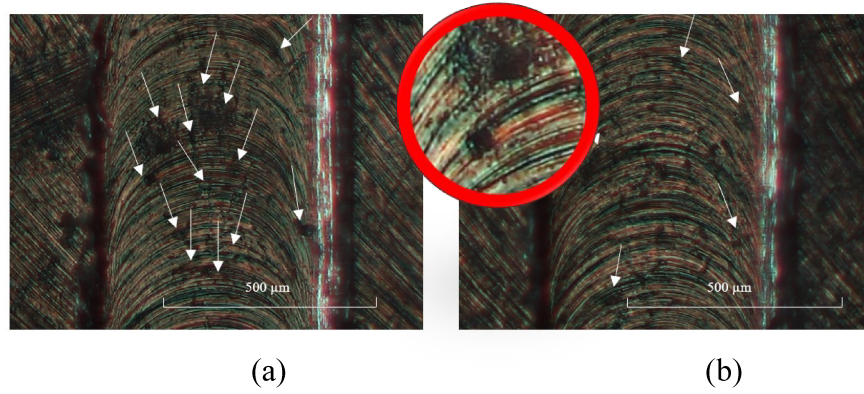
Figure 84. Surface quality of micro-slots machined with $f_z = 2$ µm/tooth (a) and $f_z = 4$ µm/tooth on PBF-BB.

Figure 84 shows an example of micro slots obtained on the BB-PBF with f_z equal to 2.0 µm/tooth (a) and f_z equal to 4.0 µm/tooth (b). As visible, the sample cut with a feed per tooth of 2.0 µm/tooth demonstrate more irregularities than the sample cut at a higher f_z.

The surface roughness of the samples has been analyzed before and after the micro machining tests. Specifically, the LB-PBF and BB-PBF as built parts are characterized by a high surface roughness due to the additive manufacturing process as reported in **Table 20**. Moreover, the LB-PBF samples are generally smoother of the BB-PBF specimens. As expected, the building orientation can influence the surface roughness by increasing the Sa of the PBF samples built at 30° in relation to the building plate. The surface roughness of the as-received mill-annealed samples has not been considered since the bars have been cut prior to investigations.

Table 20. Surface roughness (Sa) of the as built PBF samples.

Sample	Sa (µm)
PBF-LB 0°	12.11±1.0
PBF-BB 0°	24.86±4.7
PBF-LB 30°	14.78±0.5
PBF-BB 30°	35.85±0.4
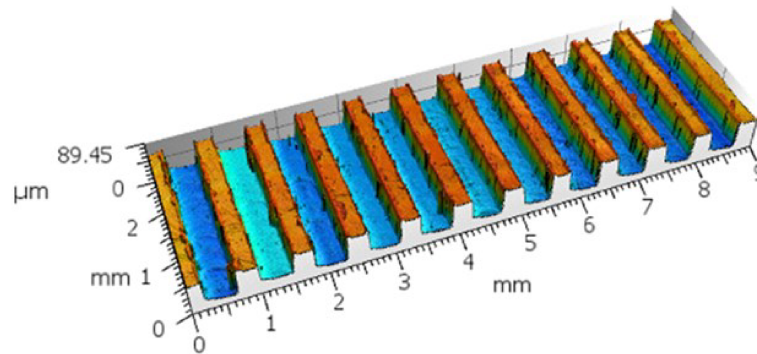
Figure 85. Three-dimensional surface of micro slots on PBF sample

For an optimal comparison of the surface roughness resulting from the micro milling tests, only the Sa of the PBF samples built at 0° has been taken into account. A proper example of the Sa calculated on the channels produced by micro milling tests is reported in **Figure 85**.

Generally, for the Ti6Al4V samples, an interesting trend is observed considering the influence of the feed per tooth and the cutting force on the surface roughness (**Figure 86-88**). The roughness of the PBF and mill-annealed samples decreases at higher values of feed per tooth confirming the presence of ploughing at lower values of f_z. The roughness is also decreased at high cutting speed values. On the other hand, a higher roughness is observed on the machined surface of the mill-annealed material in relation to the LB-PBF and BB-PBF that demonstrate a comparable surface roughness.
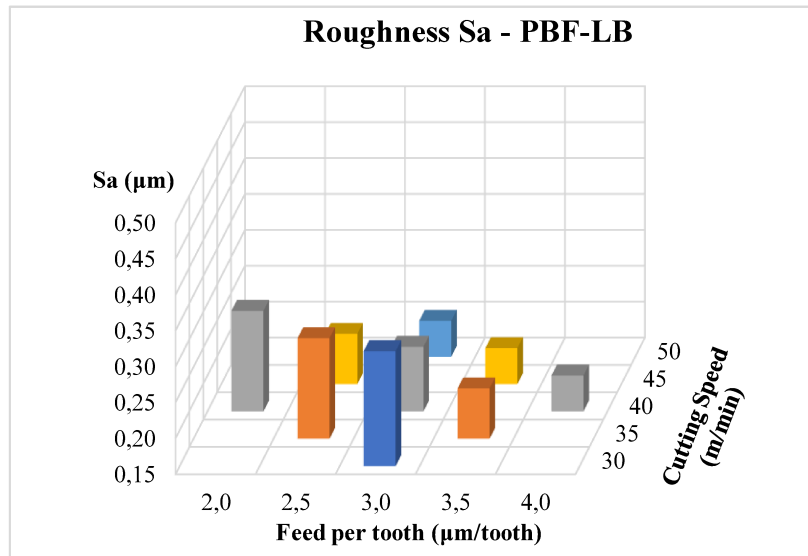
Figure 86. Roughness Sa measured on the top surface of the slots machined on PBF-LB sample.

Figure 87. Roughness Sa measured on the top surface of the slots machined on PBF-BB sample.

106
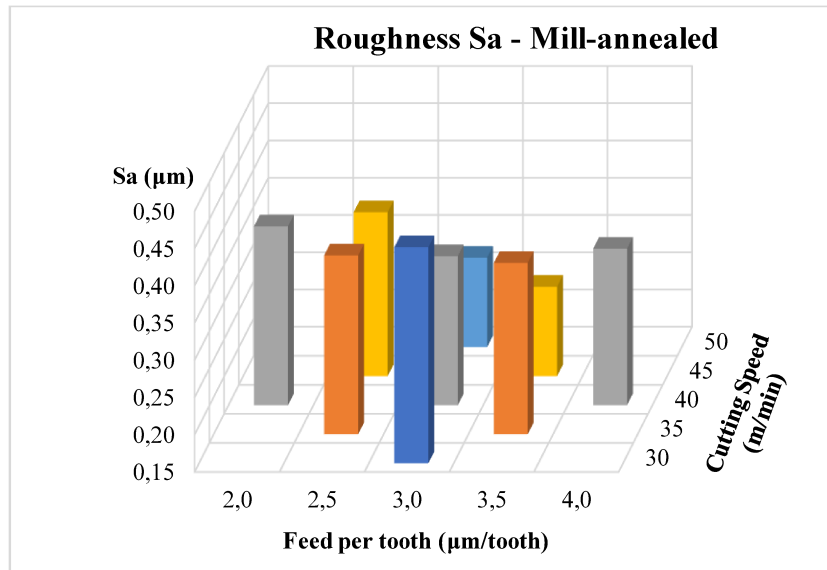
Figure 88. Roughness Sa measured on the top surface of the slots machined on mill annealed sample.

4.4 Micro-milling of LB-PBF and conventionally formed AlSi10Mg alloy

The AlSi10Mg alloy was investigated by performing several micro-milling tests. The experimental study was finalized to investigate the differences about micro-machinability of wrought alloy and LB-PBF alloy. Furthermore, the LB-PBF samples were fabric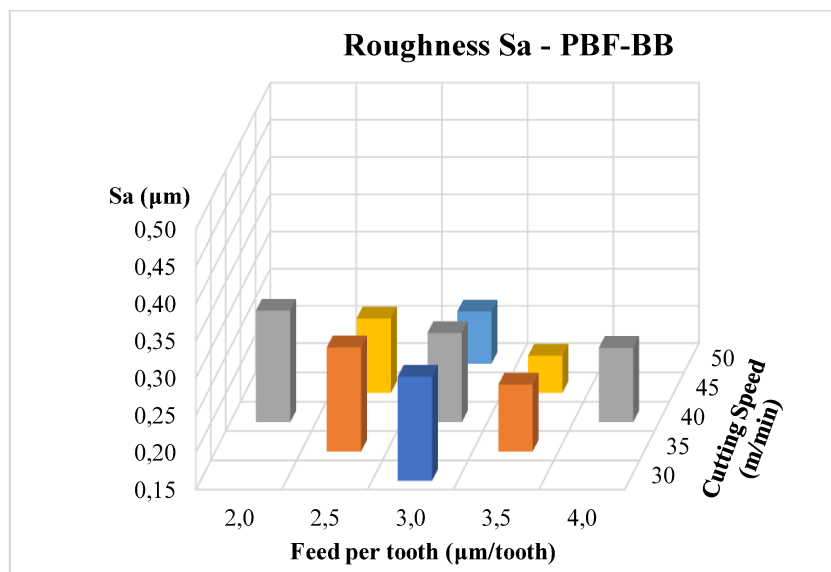ated with two alternatives building direction, 0° and 90°. The tests on LB-PBF samples were repeated on as built samples, stress relieving heat-treated samples, industrial T6 heat-treated samples, industrial T6 heat-treated + HIP treated samples. The tests on wrought samples were performed on cast samples and on industrial T6 heat-treated samples. Industrial T6 consists in a solution heat treatment and then artificially aging. This treatment is used to improve the microstructural anisotropy inducted by the production process; it allows to achieve better ductility and strength, due to the precipitation of hardening phases (Mg2Si) uniformly distributed in the material matrix.

Micromachining tests were finalized to the computation of the Minimum Uncut Chip Thickness (MUCT), by recording the cutting forces and computing the SCF average peaks as a function of the feed rate.

4.4.1 Experimental procedure

The LB-PBF samples were produced using the laser-based powder bed fusion machine EOS M290 (see section 3.1.1). The process parameters were a laser power of 370 W, a scanning speed of 1300 mm/s, a hatching distance of 190 μm, a layer thickness of 30 μm, a temperature of the building platform equal to 80 °C.

The chemical composition of the AlSi10Mg aluminum powder used as printing material is reported in **Table 21**.

Table 21. Chemical composition of AlSi10Mg aluminum powder.

AlSi10Mg	Si	Fe	Mn	Mg	Ti	Zn	Cu	Ni
Wt (%)	10	0.55	0.45	0.35	0.15	0.10	0.05	0.05

Figure 89 shows how the samples were printed (**Figure 89a**), by distinguishing the vertical sample and the horizontal samples. Each sample was subsequently cut in two parts, and it was drilled in order to constrain the samples to the loadcell. **Figure 89b** shows a pattern of the micromachined slot on the sample. The vertical samples were machined on the front face, while the horizontal sample was machined on the top face.

(a)   (b)
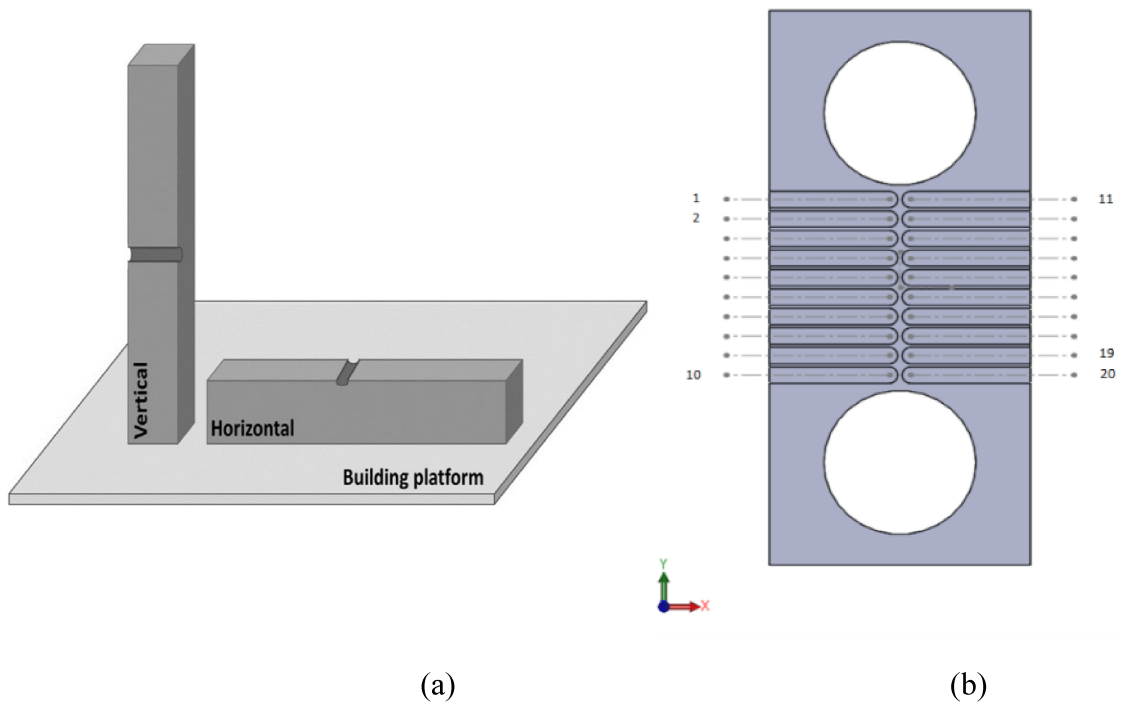
Figure 89. Building orientation of LB-PBF samples (a) and frontal view of the machined samples (b).

The cast samples had the same geometry, but they were fabricated by gravity die casting. The AlSi10Mg alloy is widely employed for gravity casting: it has a chemical composition close to the eutectic and the melting temperature is low; furthermore, the low shrinkage and good fluidity of the alloy make it an excellent candidate for the production through the smelting process. About the heat treatments, the treated samples were processed before micromachining. The thermo-mechanical treatment HIP was performed by applying a pressure ranging between 100 MPa and 150 MPa at a temperature of 500°C for two hours. The industrial heat treatment T6 was performed by keeping a temperature of 540° for 7 hours for solubilization and a temperature of 160° for 4 hours for the aging.
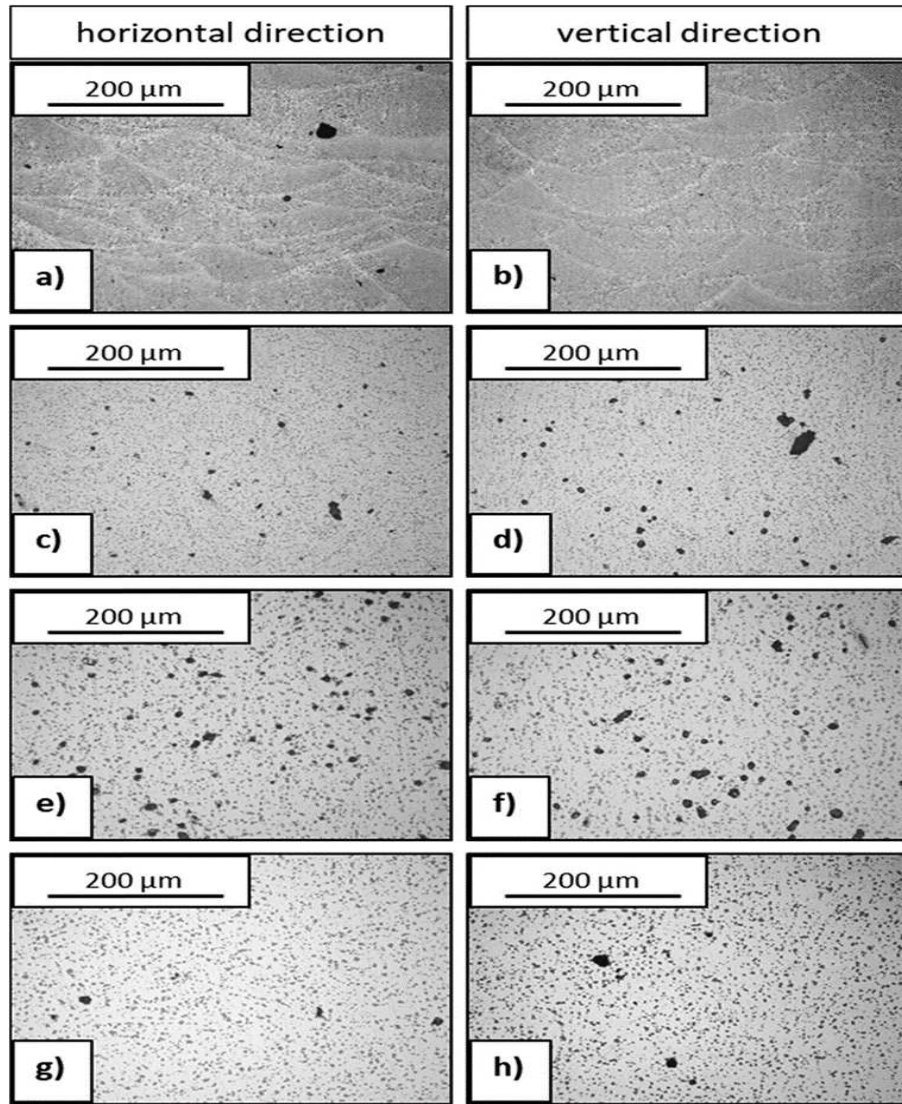
Figure 90: Comparison about the microstructure and porosity for samples (a-b) as-built (c-d) 540°C 1h – 180°C 2h (e-f) 540°C 9h – 160°C 4h (g-h) HIP 540°C 9h – 160°C 4h, with building direction (a-c-e-g) horizontal e (b-d-f-h) vertical.

About the microstructure pre-machining, LB-PBF process determines a fine microstructure, not obtainable by gravity casting. **Figure 90** summarizes the microstructure of the alloy after different treatments. The characteristic microstructure derives by the small sized melt pools, which prevent the growth of the grain due to the rapid solidification. The phenomenon of rapid cooling is called self-quenching and it is determined by the laser which melts a small part of material. It is rapidly cooled from the adjacent areas, obtaining the effect of a hardening. The subsequent laser scanning, which leads to the melting other particles, causes a slight heating causing an artificial aging and favoring the precipitation of Mg2Si. The as-built material has excellent properties, and heat treatments can determine higher porosity and silicon coalescence, with a consequent worsening for the mechanical properties. Furthermore, the silicon spheroidization reduces the mechanical properties and a coarse microstructure is determined. **Figure 91** shows how density and hardness are influenced by the heat treatments. The heat treatment T6 is commonly utilized to reduce anisotropy and to

anneal the residual stress induced by the LB-PBF process. The microstructure results coarser but more uniform, and the subsequent aging treatment increases the material strength due to the precipitation of Mg_2Si.
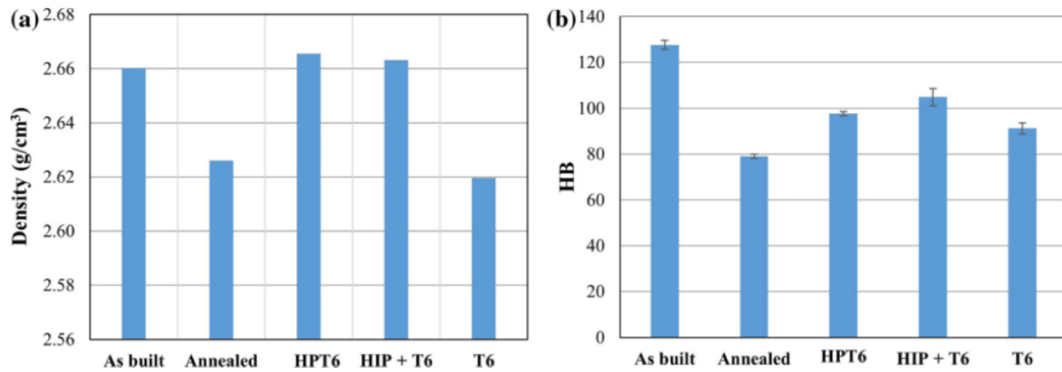
Figure 91. Comparison about the density (a) and the Brinell hardness (b) for PBF samples in different condition.

Cast samples exhibits different microstructure: the cooling rate of the melt material is approximately equal to $10 \div 10^2$ K/s, while in PBF it is equal to $10^5 \div 10^6$ K/s. On one hand, it determines coarse microstructure, but on the other hand the porosity is low. The mechanical properties are low if compared with the PBF properties and T6 heat treatment is utilized to improve the material strength. The solubilization determines the coalescence and the spheroidization of the silicon atoms, as well as it homogenizes the microstructure. After T6, the hardness of the cast samples and the PBF samples is comparable despite the difference about the microstructures. **Table 22** lists the samples hardness.

Table 22. Hardness of the AlSi10Mg samples.

AlSi10Mg	AM-As Built	AM-Stress Relieved	AM-T6	AM-T6+HIP	Cast	Cast+T6
Hardness Brinell	125	87	96	111	64	104

Only the breaking elongation is higher for PBF-T6 samples if compared with cast-T6 samples. **Figure 92** summarizes the mechanical properties of the samples before and after T6 treatment.
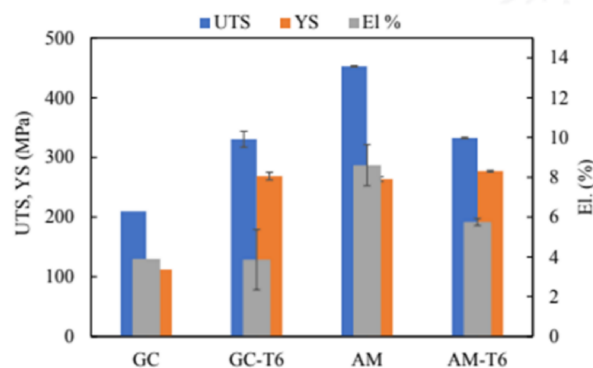
Figure 92. Comparison about the strength and the elongation at breakage for PBF samples and cast samples, before and after T6 heat treatment.

Cutting tests consist in the micro-machining of fourteen slots with a constant width equal to the tool diameter (i.e., 0.8 mm). Tests were performed with constant cutting speed equal to 80 m/min and a constant depth of cut equal to 0.25 mm, while the feed per tooth ranged from 0.5 μm/tooth to 7 μm/tooth. The loads generated by the interaction between tool and work-piece were measured through a force acquisition system, as reported in section 3.4. The average peaks of SCF were computed by using **Equation 3** and **Equation 35-37**. The machined surface was previously prepared by a roughing machining in order to achieve a planar surface for micro-slots. The roughing was performed through a single pass with a depth of cut of 100 μm by using a four-flutes flat-bottom mill with a nominal diameter of 6 mm. A cutting speed of 100 m/min and a feed per tooth of 10 μm/tooth were employed. The micro slot machining was executed with a 103L008R005-MEGA-64-T micro-mill with a nominal diameter of 0.8 mm. The actual features of the mill are listed in **Table 10**.

4.4.2   Results and Discussion

The micromachining tests were performed on several samples: vertical and horizontal AM as-built, vertical and horizontal AM-stress relieved, vertical AM-T6, vertical AM-T6+HIP; cast as built and cast-T6. **Figure 93** shows the results about SCF on feed per tooth for the AM samples before and after the stress relieving. The building orientations were both tested in order to investigate how anisotropy affects the cutting forces in micro-machining. Error bars refer to an interval of confidence equal to 99% (±3σ). The specific cutting force decreases as the feed per tooth is increased and the behavior transition between the ploughing and shearing regime occurs approximately at 1.5 μm/tooth, regardless the building orientation and the heat treatments. The building orientation has a not neglectable impact on SCF in as-built condition: the horizontal sample requires higher forces to be cut. In this condition, the cut involves several sample layers, while when cutting vertical sample, it regards only the top layer. After stress relieving, the homogenization of the properties cancels the differences about SCF. The material cutting require less force in the case of the horizontal sample, but the confidence intervals are overlapped and it means that the difference is not statistically relevant.

(a)   (b)
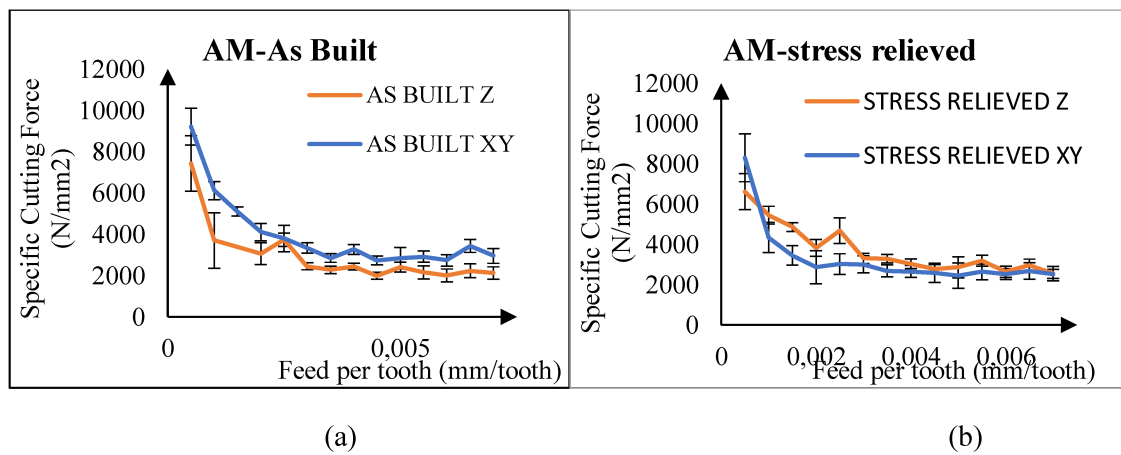
Figure 93. Trend of SCF on feed per tooth for vertical and horizontal AM samples (a) in as-built condition (b) after stress relieving heat treatment.
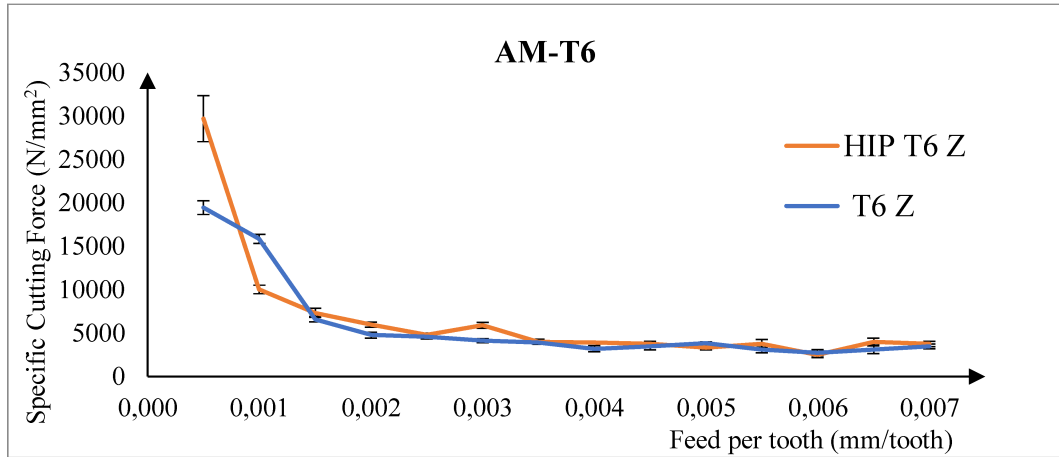
Figure 94. Trend of SCF on feed per tooth for vertical AM samples with T6 treatment.

Figure 94 shows the SCF dependence on feed per tooth for the AM samples treated with T6. It is visible how the specific forces are quite high in ploughing, especially when machining the specimen that has received the hot isostatic pressing treatment. T6 treatment leads to a coarser structure than the as-built condition. Coarse grains imply an average reduction of the grain edges present, which, being areas of discontinuity, facilitate chip removal mechanism during the cutting process. In addition, the HIP treatment helps to reduce porosity by making the material more compact; it favorites a significant increase in specifc cutting forces compared to the not HIP treated sample with feed per tooth lower than Minimum Uncut Chip Thickness. On the other hand, in shearing dominant regime the porosity closure guaranteed by HIP does not produce significant changes about specific cutting force.

To better highlight the cutting force changes determined by the treatments, a full comparison was provided in **Figure 95**.
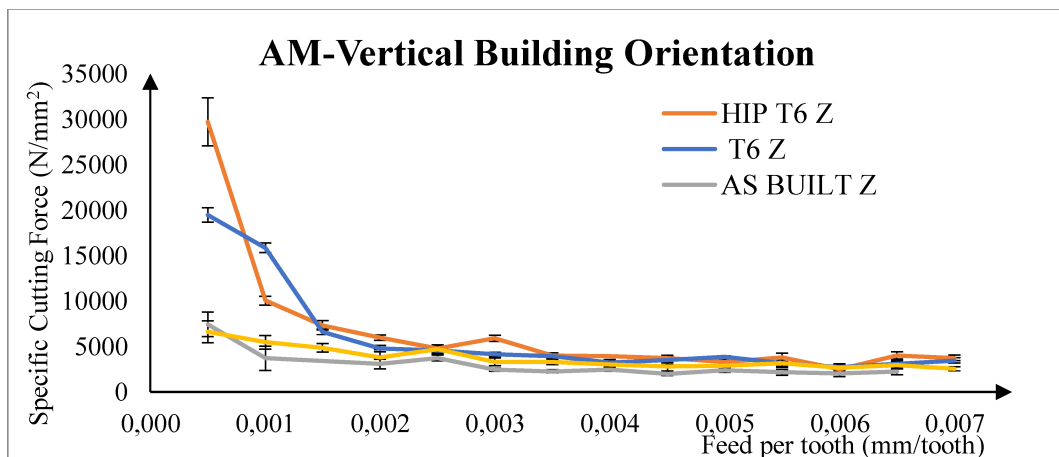
Figure 95. Trend of SCF on feed per tooth for vertical built AM samples.

The heat treatment T6 determines a meaningful increment of SCF in ploughing regime for AM samples, despite the as-built sample exhibits the highest hardness (as visible in **Table 22**). The stress-relieving reduces the hardness by the 30%, but the SCF does not change.

112

It is a further demonstration that in micromilling the hardness does not have a direct correlation with the SCF peaks, especially in ploughing regime. Furthermore, the SCF values can be explained by considering the microstructure. The as-built samples have a fine microstructure due to the rapid cooling of the melt material during the LB-PBF process. The chip removing is favorited by the low ductility of the brittle material. Furthermore, in ploughing the chip thickness is lower than in shearing regime due to the low values of feed per tooth, but it still higher than the average grain size of as-built sample. The presence of a high number of grain boundaries facilitates the chip breakage by determining a decrease of the specific cutting forces. The effect of the grain size disappears in shearing regime due to the increasing of the chip thickness size. Stress relieving does not increase the grain size; it only homogenizes the microstructure, and it eliminates the residual tensions. The behavior of the alloy does not change in ploughing, while in shearing the SCF are slightly higher than the as-built sample. Further consideration can be pointed out by considering **Figure 96**, which shows a comparison about machining of the samples treated with T6 and treated with T6 plus HIP.
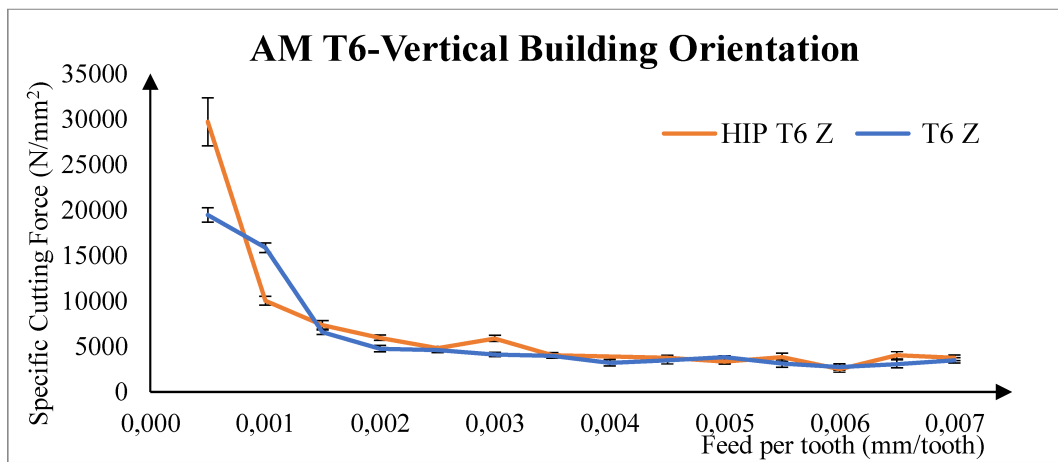
Figure 96. Trend of SCF on feed per tooth for vertical built AM samples with T6 heat treatment.

The charts highlight how in ploughing the Specific Cutting Forces reaches high peaks, with an absolute maximum recorded during the machining with the minimum feed per tooth of the sample that has received the hot isostatic pressing treatment. The T6 heat treatment makes the structure coarser than the as-built condition, with a consequent reduction of the grain boundaries, which being areas of discontinuity facilitate the cutting process. In addition, the HIP treatment helps to reduce porosity by making the material more compact, and it favorites a significant increase in cutting forces compared to the other specimen. On the other hand, in shearing dominant regime, the porosity closure guaranteed by HIP does not produce significant changes about the material removing behavior.
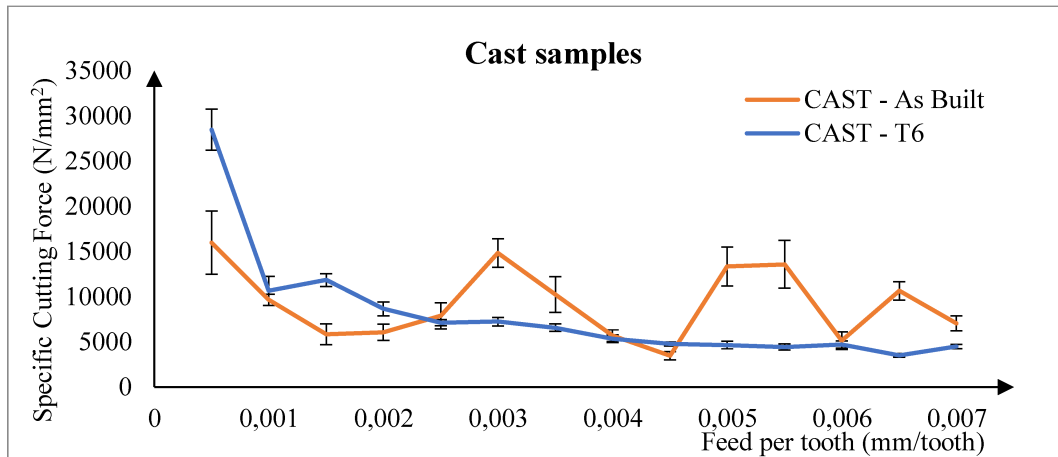
Figure 97. Trend of SCF on feed per tooth for cast samples, with and without T6 heat treatment.

The **Figure 97** shows the SCF for the cast samples. The as-built sample shows an unusual trend, with a random relation between SCF peaks and feed per tooth. The absence of a dependence of SCF peaks on feed rate is related to the high ductility of the cast alloy, which is characterized also by the minimum hardness. The workpiece material adheres to the tool cutting edge by changing the tool edge roundness. The phenomena, known as Built Up Edge (BUE), causes high cutting forces and determines poor surface finishing. The sudden detachments of the adherent material cause the variability of the cutting forces, with the consequent randomicity of the SCF peaks. After the T6 heat treatment, the gravity casted alloy exhibits a completely different machinability. The typical trend of SCF on feed per tooth is adhered and the peaks values are quite similar to the values recorded during machining of AM samples with T6 treatment. The heat treatment on cast samples determines a refinement of the coarse microstructure, with a consequent increase of the hardness and machinability. A comparison between the T6 samples (AM and cast) is visible in **Figure 98**. Although the SCF are comparable in ploughing, a not neglectable difference is visible in shearing, where the cast samples require higher cutting forces.
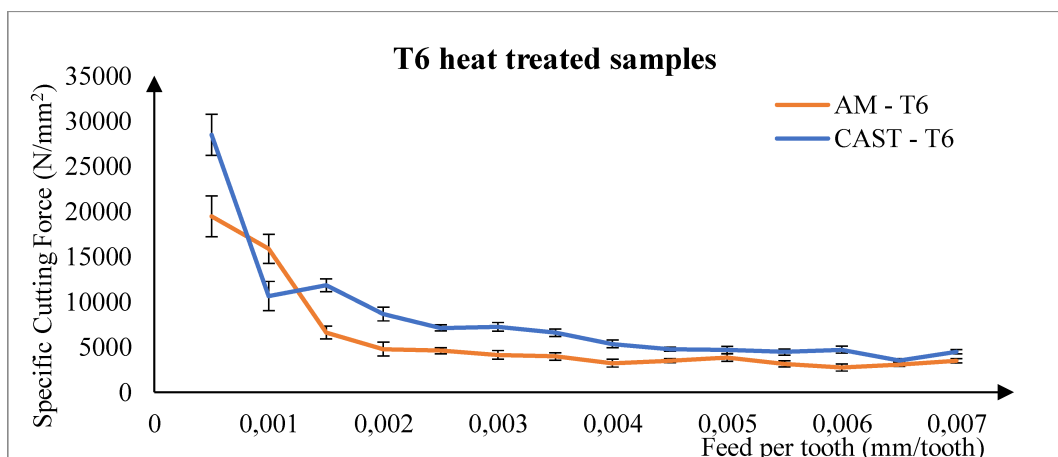
Figure 98. Trend of SCF on feed per tooth for T6 heat treated samples.

4.5 Conclusion

In this chapter the experimental activities and the results were collected and commented. The procedure to test the micro-machinability of the metallic alloys was refined and optimized. Actually, the MUCT determination can be performed through a robust and reliable experimental procedure. Furthermore, specific additional tests were designed to investigate the dynamic effects by changing the cutting speed, to study the final surface finishing and to collect cutting force data useful for the calibration of analytical and numerical models.

About PBF 17-4 PH stainless steel, the specific cutting forces related to the ploughing regime resulted ten times higher than the forces calculated when shearing regime is present. As expected, at the highest feed per tooth values the specific cutting force was found to be independent on the feed rate value. The results showed a behavior transition of the material at the 30-35% of the effective tool edge radius. Thus, the study allowed to identify an optimal feed per tooth range related to reduced cutting forces with the aim of minimize the tool damage probability and consequently the tool wear rates. Furthermore, the highest values of roughness were measured on the surface of the channels machined at low feed rates. The variability of the data showed a progressive decrease corresponding to a more dominant shearing regime. The dimension of the burrs calculated both on the inner and outer channel sides resulted higher at low feed per tooth values. Therefore, a high value of the feed rate is recommended to reduce the extension of the burrs and assure a correct mechanical coupling between the micro-sizes components. The complete data and results are collected in a book chapter **[18]**; the abstract is shown in **Figure 99**.

Micro-milling of Selective Laser Melted Stainless Steel

Andrea Abeni, Paola Serena Ginestra, and Aldo Attanasio

Abstract This paper deals with micro mechanical machining process of 17-4 PH stainless steel samples fabricated by selective laser melting. An analysis of the material removal behaviour during micro-milling operations for the selection of the optimal feed rate value was performed on 17-4 PH additive manufactured samples studying the variation of the specific cutting force as a function of the feed per tooth. The transition from shearing to ploughing regime was analysed by considering the variation of the specific cutting forces. The minimum uncut chip thickness was calculated to identify the transition between the cutting regimes (shearing, ploughing or their combination) that affects the final product quality in terms of surface integrity and dimensional accuracy. Moreover, the surface roughness and the burr extension were analysed as a function of the feed rate.

Keywords Selective laser melting · Micro machining · Minimum uncut chip thickness

Figure 99. Published paper on book chapter **[18]**.

About Inconel 625, the experimental investigation allows to compute a MUCT value equal to 2.5 μm. This parameter is an important information about micro-machinability of the superalloy, and, at the same time, it covers a key role in the analytical model formulation which will be described in the next chapter. The micro-slots fabrication was combined with some micromachining of thin-wall with 0° helix angle in order to perform quasi-orthogonal cutting tests. Cutting force data were collected at different cutting speed and feed rate in order to calibrate the analytical model in a complete range of the process parameters. The complete data and results are collected in a paper **[19]**; the abstract is shown in **Figure 100**.

Analytical force modelling for micro milling additively fabricated Inconel 625

Andrea Abeni[1] · Dario Loda[1,2] · Tuğrul Özel[2] · Aldo Attanasio[1]

Abstract
In recent years, miniaturization of components has been concerned with several industrial fields including aerospace, energy, and electronics. This phenomenon resulted in increasing demand of micro-components with complex shape and high strength, often in high-temperature environment. Nickel-based superalloys such as Inconel 625 are a class of material suitable to aforementioned applications and can be successfully processed with Additive Manufacturing (AM). Moreover, micro-milling can be employed to manufacture micro-scale features on the additively fabricated parts or to achieve better surface finishes, as required for high-precision mechanical assemblies. In micro machining, it is possible to notice a lack of scientific study focusses on the material removal behavior of difficulty-to-cut alloys produced via Additive Manufacturing. This paper describes an analytical cutting force model suitable also for AM'd parts which considers the presence of ploughing- and shearing- dominated cutting regimes. A refinement procedure of the cutting force model was defined and applied by performing an experimental work on Inconel 625 samples fabricated by LaserCUSING™. A search algorithm was employed to develop an iterative methodology to determine the unknown cutting force model parameters. The model was successfully utilized to predict how the cutting force is affected as the process parameters change.

Keywords Micro milling · Cutting force model · Nickel-based superalloy · Minimum cutting thickness · Selective laser melting

Figure 100. Published paper on international journal **[19]**.

About Ti6Al4V, the specific cutting force resulting from the production of micro-slot on PBF samples produced by Laser Based and Beam Based PBF was evaluated as a function of the feed per tooth. The transition behavior from ploughing to shearing deformation regime was investigated and compared with the wrought alloy formed with conventional processes. Furthermore, two different building orientation of the PBF samples have been considered for the experimental tests to identify the minimum uncut chip thickness. Moreover, the surface roughness of the as-received, as built and machined workpieces were measured to investigate the effects of the process parameters on the surface final finishing. Interestingly, from the results it is possible to notice a ploughing dominated regime at low feed per tooth values (< 2.0 μm/tooth) followed by a transition to a shearing dominated regime at higher feed rates. This deformation mechanism is observed to be equivalent for PBF samples and mill-annealed ones with a visible difference between the specific cutting pressure during

ploughing. At lower feed per tooth values the specific cutting force is higher for the PBF samples than the mill-annealed ones. The results showed a behavior transition of the material at the 40% of the effective tool edge radius. Thus, this novel study allowed to identify an optimal feed per tooth range related to conventional and additively manufactured samples of Ti6Al4V. Furthermore, the statistical analysis carried out on the process parameters showed that the dynamics aspects of the micro cutting process has no influence on the specific cutting forces, regardless of the sample production process. Contrarily, higher cutting speeds have been found to improve the surface roughness of all the samples. The complete data and results are collected in a book chapter [20]; the abstract is shown in **Figure 101**.

XV Convegno dell'Associazione Italiana delle Tecnologie Manifatturiere
Milano, 17-19 gennaio 2022

Sessione Giovane Ricercatore

Please restrict your document to:
- "Sessioni Scientifiche Tradizionali": maximum 15 pages
- "Sessione Giovani Ricercatori": maximum 20 pages
- "Sessioni Work in Progress e Laboratori": maximum 10 pages

- - - - - - - - - - - - - - - - - -

Andrea Abeni[1], Paola Serena Ginestra[1] and Aldo Attanasio[1]

[1] University of Brescia, Department of Mechanical and Industrial Engineering, V. Branze 38, Brescia 25123, Italy

Comparison between micro machining of Additively Manufactured and conventionally formed samples of Ti6Al4V alloy.

Abstract. The paper deals with micro mechanical machining process of Ti6Al4V alloy. A comparison between additively manufactured samples and conventionally fabricated samples with mill annealed structure was performed. Powder Bed Fusion Laser Based (PBF-LB) and Beam Based (PBF-BB) processes were used to produce samples with a building direction of 0° and 30° in relation to the plate. The Minimum Uncut Chip Thickness (MUCT) was determined to investigate the removal behavior during slot machining with rounded-edges micro-tools. The cutting forces were measured, and the loads were utilized to calculate Specific Cutting Force (SCF). It was reported as a function of the feed per tooth (f_z) to investigate when the transition between shearing and ploughing occurs. Once the MUCT was identified, further micro machining tests were performed by changing the feed rate and speed rate. The surface roughness and cutting force of the machined samples were measured to deeply investigate the effects of ploughing regime. The dependence of roughness on the sample fabrication technique and on the process parameters of micro milling was highlighted.

Keywords: Additive Manufacturing, Ti6Al4V alloy, Micro machining.

Figure 101. Published paper on international book chapter [20].

Finally, the micro-machinability of AlSi10Mg was investigated by testing several samples in different condition and built with different orientation. The main results of the comparison were the difference among the SCF in ploughing dominant regime, where it was seen that materials with a fine microstructure (such as the T6 treated samples) offer a higher resistance if compared with the samples with coarse microstructure. The gravity cast sample machining

was affected by BUE phenomena, which does not regard PBF micro-machining. Furthermore, it has been observed that the T6 treatment tends to induce a similar micro-structure for the specimens manufactured with traditional and innovative techniques, which therefore exhibit a similar behavior during micromachining. The results will be published on an international journal.

Generally, the experimental tests highlight an interesting relation between machinability and the sample manufacturing technology. The transition between ploughing and shearing was clearly identified in each case, and MUCT shows a strong dependence on the tool geometry. The cutting force values are strongly affected by the microstructure of the alloys, and it depend on the material processing. When a comparison with conventionally formed materials was performed, interesting results were found.

5 Definition and calibration of new models

In the second chapter a brief analysis of the most employed models in micro-machining was described. The analytical model provides the computation of the chip thickness in order to calculate the portion of material which resists to the tool passage. This part of the model is based on geometrical modeling of the process, and it can be enhanced by the tool run-out modeling and the tool bending effect. Once the geometrical modeling is complete, the chip cross section can be employed to compute the cutting forces. Literature demonstrates that the cutting behavior has a great impact on the cutting forces. The experimental tests described in chapter four validate this statement also for AM metallic alloy. As consequence, a reliable analytical model must consider ploughing and shearing regimes and how they contribute to the cutting force computation. As reported in chapter two, some models **[157, 158]** alternatively considers ploughing or shearing regime in order to compute the cutting force as a function of the chip thickness, but few of them consider the concomitant presence of both regimes which typically regards micro-machining. In this chapter, an analytical force model able of predicting the cutting force by considering both ploughing and shearing regimes will be described. It was previously calibrated for micro-machining of Inconel 625 by using the experimental data listed in chapter four, and subsequently it was tuned also for Ti6Al4V. Finally, a second version of the model was released by adding the tool run-out geometrical computation.

The chapter two also includes a collection of research about machining performed by using FE methods. As previously stated, few works regard micro-machining, despite FEM can provide information about chip morphology, thermal aspects, cutting force, stress distribution on tool and residual stress on workpiece. In this chapter some FEM simulation models will be described. A 2D-model suitable for quasi-orthogonal cutting was elaborated and tuned on the Inconel 625 experimental data and analytical model. An iterative procedure allowed finally to calibrate the flow stress model for micro-machining of AM Inconel 625.

5.1   Analytical modeling of micro-machining

This section describes the structure and the calibration of an analytical cutting force model suitable also for AM parts which considers the concomitant presence of ploughing- and shearing- dominated cutting regimes. A refinement procedure of the cutting force model was defined and applied by exploiting the experimental work on Inconel 625 samples fabricated by LB-PBF. The micro-slot machining and the micro-cut of the thin-walled samples were both employed: the Minimum Uncut Chip Thickness (MUCT) is an input parameter of the model, because it determines the passage from ploughing to shearing; the cutting force data collected during the cut of the thin-wall are used to compute the model parameters which determines the cutting force value. A search algorithm was employed to develop an iterative methodology to determine the unknown cutting force model parameters. The model was

successfully utilized to predict how the cutting force is affected as the process parameters change.

5.1.1 Model structure

This section provides a detailed description of the analytical model structure. The mechanistic-based force model is suitable to predict the cutting force for slot micro milling. A two-dimensional micro milling of slots on thin-wall structure was considered as a reference configuration. The geometrical model corresponds with the experimental set-up.
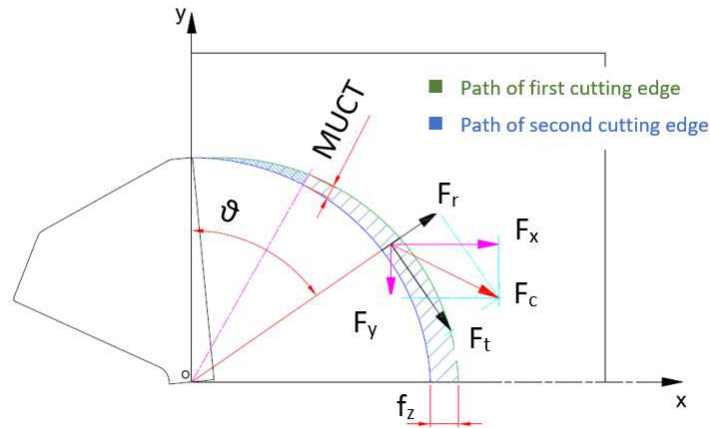

Figure 102. Representation of MUCT, cutting area and cutting force decomposition.

A 2-flutes, zero-degree rake angle and zero-degree helix angle end-mill was employed to perform the milling tests. The tool deflection was considered neglectable due to the stiffness of the tool compared with the intensity of the cutting forces. In accordance with this hypothesis, the interaction between the tool cutting edge and the workpiece at a specific uncut chip thickness t_u determines the cutting force F_c. As showed in **Figure 102**, F_c can be decomposed in the tangential component (F_t) and the radial component (F_r).

Furthermore, the resultant force can be decomposed in *X-Y* reference system as the sum of F_x and F_y components. In the proposed model the tangential and radial components of cutting forces can be computed as function of the actual tool rotation angle θ.

The angle θ depends on time *t* as expressed by the **Equation 38**:

$$\theta(t) = \omega * t \qquad \text{Eq. 38}$$

At steady state, the first contact between tool and workpiece occurs when the tool rotation angle θ is equal to zero and the cutting edge is aligned along *Y* axis. Specific force parameters K_{tp} and K_{rp} are the ploughing force coefficients in tangential and radial directions (N/mm^3) respectively, while parameters K_{ts} and K_{rs} are the shearing force coefficients in tangential and radial directions (N/mm^2) . The force coefficient values depend on the material properties, and they should be determined through a refinement procedure. The cutting force components F_t and F_r can be computed through **Equation 39** and **Equation 40**:

$$F_t(\theta) = \left(K_{tp} * A_p(\theta) + K_{ts} * t_u(\theta)\right) * a_p \qquad \text{Eq. 39}$$

$$F_r(\theta) = \left(K_{rp} * A_p(\theta) + K_{rs} * t_u(\theta)\right) * a_p \qquad \text{Eq. 40}$$

The coefficient t_u is the actual uncut chip thickness, while A_p is ploughed area and the parameter a_p is the axial depth of cut and it is equal to the thin wall thickness. F_x and F_y components can be calculated from F_t and F_r by means of simple trigonometrical calculations, as shown by **Equation 41** and **Equation 42**:

$$F_x = F_t * cos(\theta) + F_r * sin(\theta) \qquad \text{Eq. 41}$$

$$F_y = -F_t * sin(\theta) + F_r * cos(\theta) \qquad \text{Eq. 42}$$

With the assumption of neglectable tool run-out:

- the thickness t_u ranges between zero and a maximum value, which is equal to feed per tooth f_z. The actual value of t_u can be computed as a function of the angle θ, as shown in **Equation 3**.

$$t_u = f_z \sin\theta - \frac{N}{2\pi R} f_z^2 \sin\theta \cos\theta + \frac{1}{2R} f_z^2 (\cos\theta)^2 \qquad \text{Eq.3}$$

The variable R indicates the tool radius as the half of the micro mill diameter. The ploughed area A_p is calculated as the area spanned by the tool cutting edge until t_u reaches the MUCT. When t_u becomes higher than the MUCT, A_p is kept constant until t_u decreases to the MUCT again. In the final portion of the cut, A_p decreases down to zero as cutting edge disengages from the workpiece material. The contribution of ploughing effect in the central portion of cut area (i.e. when t_u is higher than MUCT) is considered constant. The ploughed area A_p was calculated as the portion of the cutting area A_c which remain in the elastic deformation field. The cutting area A_c is defined as the amount of the material removed by a tool flute from 0° to θ, as expressed by the **Equation 42**:

$$A_c(\theta) = \int_0^\theta \left(\frac{t_u(\theta)+t_u(\theta+d\theta)}{2}\right) R d\theta \qquad \text{Eq. 42}$$

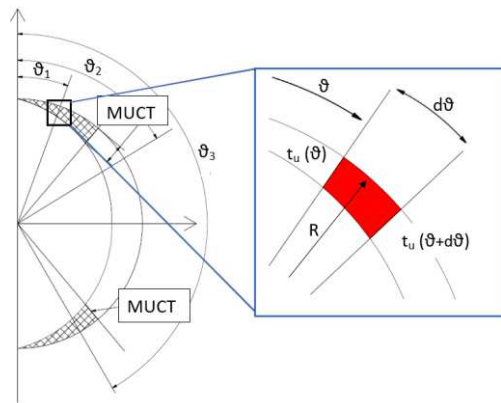The **Figure 103** offers a representation of the cutting area $Ac(\theta)$.

Figure 103. A schematic representation of three possible positions of the tool cutting edge (θ_1, θ_2 and θ_3) with a detailed view of the infinitesimal cutting area (red colored).

Once $Ac(\theta)$ is calculated, the **Equation set 43** can be used to compute A_p:

Eq. set (43)

$$\begin{cases} if \; t_u(\theta) < MUCT \; and \; \theta < \theta_{max} \; then \; A_p(\theta) = A_c(\theta) \\ if \; t_u(\theta) < MUCT \; and \; \theta > \theta_{max} \; then \; A_p(\theta) = A_c(\pi) - A_c(\theta) \\ if \; t_u(\theta) > MUCT \; then \; A_p(\theta) = A_{pMAX} \end{cases}$$

Figure 104 (a) shows how the uncut chip thickness changed during a tool rotation while **Figure 105 (b)** shows how the ploughed area changed during a tool rotation. The geometrical model does not consider the effect of tool run-out. The aim of the model is to predict the cutting force as a function of the material properties, without including the influence of external effects such as the tool run-out.

The calibration procedure consists in two main phases. The first step is finalized to identify the MUCT while the second phase is designed to identify the analytical model coefficient K_{ts}, K_{rs}, K_{tp} and K_{rp}.

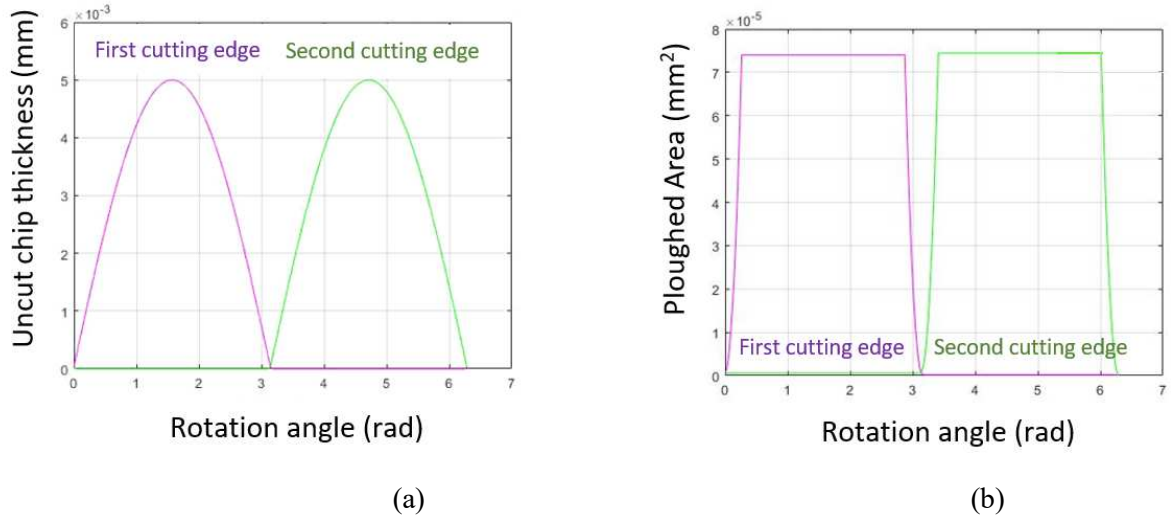(a)   (b)

Figure 104. Trend of (a) uncut chip thickness vs rotation angle and (b) ploughed area vs rotation angle.

The minimum uncut chip thickness can be experimentally determined by fabricating several channels on a sample by using a constant cutting speed and different feed per tooth (f_z) values, as stated in chapter four. The cutting force normalization is performed through the **Equation 35-37**. The MUCT can be identified by considering the SCF as a function of the feed per tooth. **Figure 105** shows an example of the typical trend of the SCF in micro milling. It shows meaningful increments of the specific cutting force when the feed per tooth decreases. At low feed per tooth the transition between ploughing and shearing does not occur. The only material removing mechanism is ploughing and consequently it determines a pronounced specific cutting force increase compared to the test performed with higher feed rates. Therefore, the MUCT is equal to the feed per tooth value that is related to the change of the specific cutting force function.

The second phase of the model refinement procedure consists of finding the optimal parameter set for the analytical force model. The purpose is to best fit the experimental cutting force data by minimizing the prediction error of the model.
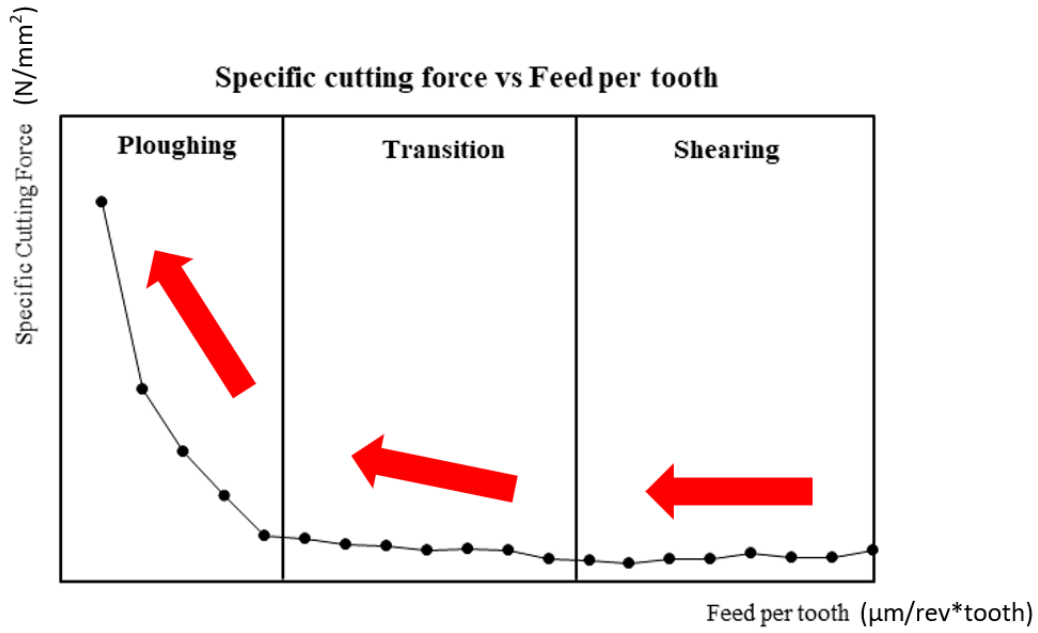
Figure 105. An example of the SCF peaks as function of the feed per tooth for conventionally formed materials.

(a)   (b)

(c)
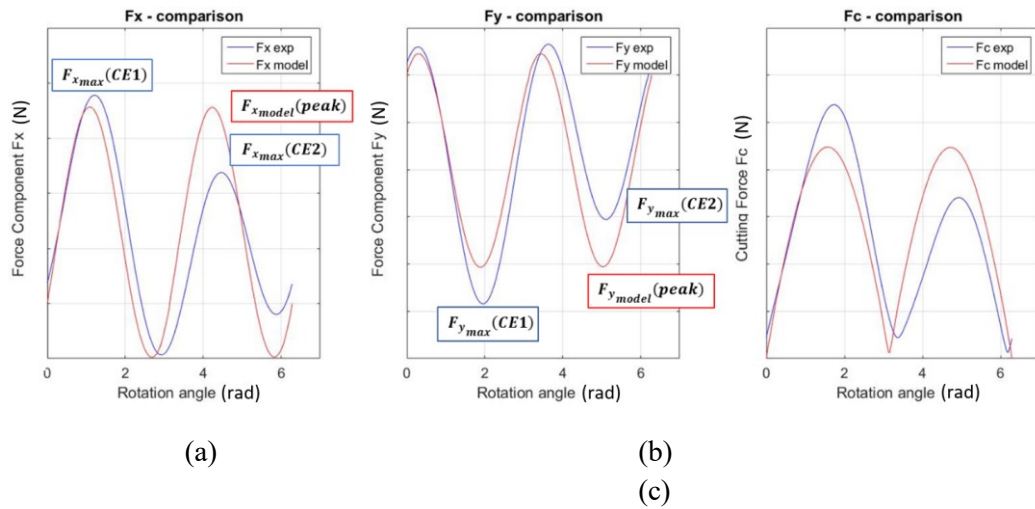
Figure 106. A comparison between the experimental signal and the model prediction for the force component Fx (a); Fy (b) and the resultant cutting force Fc (c).

Figure 106 shows an example of the cutting force components (F_x, F_y) and the resultant cutting force F_c. The force trends are representing the micro milling of a thin-walled sample that was described as a reference system given in **Figure 102**. The F_z component is neglectable due to the tool helix angle, which is equal to zero degrees. The model considers tools with two flutes, indicated as Cutting Edge 1 (*CE1*) and Cutting Edge 2 (*CE2*). Observing the experimental values of F_x, F_y and F_c, they show two different peaks height for a

single tool round due to the tool run-out effect. Each peak could be associated with one of the two flutes. Moreover, the analytical model does not consider tool run-out and it provides two identical force peaks. The model refinement was performed through an iterative method. It was adopted by implementing a search algorithm. Several set of values must be tested until the minimum of an objective function is found. The objective function is defined as the difference between the cutting forces provided by the analytical model and the forces measured during the experimental tests. The implemented optimization algorithm is the Particle Swarm Optimization (PSO) by Eberhart and Kennedy [202], an optimization algorithm for continuous non-linear function which was used in other research related to the optimization of analytical model parameters as well as optimization of process parameters in different applications [203, 204].

An objective function which estimates the error as the difference between the average force peaks and the analytical model peak was defined. The average experimental F_x and F_y peaks are computed by the **Equation 44** and **Equation 45**. The error for F_x and F_y components is calculated through **Equation 46** and **Equation 47**. The **Equation 48** can be used to calculate the total error as the sum of the error for F_x and the error for F_y.

$$\overline{F_X(peak)} = \frac{F_{x_{max}}(CE1) + F_{x_{max}}(CE2)}{2} \qquad \text{Eq. 44}$$

$$\overline{F_y(peak)} = \frac{F_{y_{max}}(CE1) + F_{y_{max}}(CE2)}{2} \qquad \text{Eq. 45}$$

$$E_x = \overline{F_X(peak)} - F_{X_{model}}(peak) \qquad \text{Eq. 46}$$

$$E_y = \overline{F_y(peak)} - F_{y_{model}}(peak) \qquad \text{Eq. 47}$$

$$Err = |E_X| + |E_y| \qquad \text{Eq. 48}$$

The algorithm is based on the definition of a population of particles in a space with a dimension equal to the number n of the function parameters which must be optimized. Each particle is a n-dimensional vector and it represents a possible problem solution. For each particle, the algorithm calculates the objective function and it memorizes the results before changing the function parameters. The particles can be moved in a limited portion of the defined n-dimensional space through some parameters bounds. The geometrical and the analytical models were integrated in a Matlab function which calculates the cutting force components, the resultant and the error through **Equation 38** - **Equation 48**. In particular, the error Err was used as the algorithm objective function. The algorithm begins to compute the analytical cutting force by assuming some initial sets of model parameters K_{tp}, K_{rp}, K_{ts} and K_{rs}, and it calculates the error by using the experimental data. Moreover, the algorithm iteratively changes the model coefficients by overwriting the particles vector components. The particles variation is not arbitrary, and it was controlled through an algorithm set-up.

The inertial factor ω influences the maintenance of the particle direction between two consecutive iterations, enabling a control of the movement freedom. The particle movement is influenced by its own current position and by the global position of the swarm. A cognitive parameter C_1 and a social parameter C_2 are the weights respective of the current particle

position and the swarm position. The Particle Swarm Optimization algorithm requires the experimental cutting force data as benchmark.

A second approach was proposed in order to achieve a better prediction of the model [21]. The new objective function was computed as the sum of the prediction error of all the tests, as expressed by **Equation 49**:

$$Objective\ Function = \sum \left(\frac{|F_{model.c\ MAX} - F_{exp.c\ MAX}|}{F_{exp.c\ MAX}} \right)_i \qquad \textbf{Eq. 49}$$

where $F_{model.c\ MAX}$ is the peak of predicted cutting force for the i-th test, while $F_{exp.c\ MAX}$ is the average experimental peak of cutting force.

5.1.2 Model calibration for AM Inconel 625

The next section describes the procedure to calibrate the model described in section 5.1.1 for the machining of AM Inconel 625. The analytical model refinement and validation were performed through the execution of several micro milling tests, which are described in section 4.2. As previously described, the tests can be divided in two categories: the micro slots at different feed rate to determine the MUCT and the thin-walled samples milling to calibrate the analytical model coefficient K_{ts}, K_{rs}, K_{tp} and K_{rp}. As stated in section 4.2.2 and visible in **Figure 73**, the MUCT resulted equal to 2.5 µm/tooth.

The refinement of the analytical force model was performed by using the PSO. After several preliminary trial optimizations, the cognitive parameter C_1 and the social parameter C_2 were set at 1.2 and 0.012, while the inertial factor W was set at 0.0004. The number of particles and iterations were defined as a trade-off between the error minimization and the computational time. A stable solution was found by the algorithm after 1000 iterations with 150 particles. **Table 23** summarizes the model coefficient bounds. The bounds were changed until the particles did not find the optimal solution in correspondence of their limits. The last column of **Table 23** reports the optimized model coefficients resulting from the optimization procedure. The calibrated analytical force model was utilized to predict the cutting force F_c for all the combinations of cutting speed, feed per tooth and thickness. The results are summarized in **Table 24**. The comparison between the model predictions and the experimental forces allowed to validate the analytical force model refinement. The most important term of comparison is the cutting force peaks. A correct prediction of the maximum force during the process allows estimating the maximum bending force of the tool and predicting a possible failure in the micro-end mill.

Table 23. Lower and upper limits and optimum set of the analytical force model coefficients.

Parameter	Lower Bound	Upper Bound	Optimum set
K_{ts}	0	10000	2595
K_{tp}	0	5000	4625
K_{rs}	0	10000	1870
K_{rp}	0	5000	3000

The experimental cutting force and the analytical force model peaks are listed in **Table 24**. The maximum value of the experimental cutting force was calculated as the average value between the two cutting edge force peaks. The process parameters of each tests are listed in section 4.2.1. The last column expresses the percentage error about the prediction. The model provided accurate results, since the error ranged between 0.8% and 14.6%. The prediction of the cutting force peaks is acceptable regardless the dominant material removing behavior. In fact, the percentage error is lower than 15% for the tests performed in a shearing dominant condition (f_z = 10 μm/rev*tooth), during the material behavior transition (f_z = 5 μm/rev*tooth) and also when the ploughing regime is dominant (f_z = 2.5 μm/rev*tooth).

Table 24. The average peak of the experimental cutting force and the analytical model prediction.

Test	Fc MAX experimental (N)	Fc MAX analytical model (N)	Error (%)	Test	Fc MAX experimental (N)	Fc MAX analytical model (N)	Error (%)
A1	2.24	2.28	-1.7	D2	3.51	3.06	12.8
B1	2.37	2.43	-2.3	E2	5.60	5.83	-4.1
C1	3.97	3.48	12.7	F2	6.29	6.48	-3.0
D1	3.35	3.02	9.9	A3	2.21	2.25	-1.8
E1	5.07	4.92	3.0	B3	2.36	2.38	-0.8
F1	4.39	4.47	-1.9	C3	3.30	3.04	7.9
A2	1.98	2.06	-4.0	D3	3.78	3.23	14.6
B2	2.16	2.21	-2.3	E3	5.86	6.10	-4.1
C2	3.02	2.69	10.9	F3	4.97	4.86	2.2

The analytical force model can be employed also to verify the accuracy of the MUCT identification procedure. In fact, the analytical force model was also utilized to predict the experimental cutting force with different MUCT values, in particular with MUCT' = 2 μm and MUCT'' = 1.5 μm.

The prediction error obtained setting the MUCT at 1.5 μm increased with respect to the errors achieved when setting MUCT equal to 2.5 μm. The average error increment was equal to 22% with MUCT' and 64% with MUCT''.

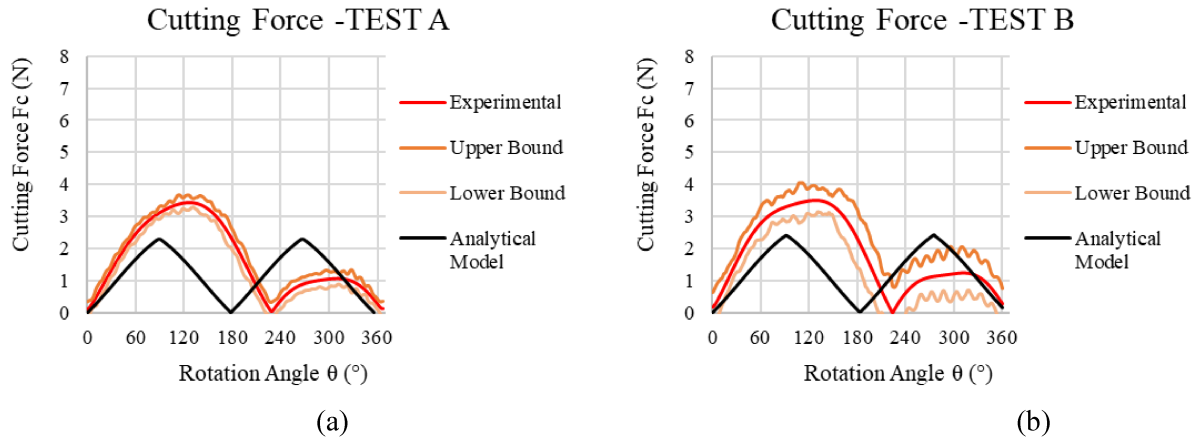**Figure 107** shows the comparison for the Tests A and Tests B.

Figure 107. Comparison between the experimental data and the model prediction for Test A1 (a) and Test B1 (b).

The experimental limits were built by adding or subtracting the average value with the standard deviation. The tool run-out strongly affects the experimental data since it is comparable with the feed per tooth. The deviation of the tool trajectories determines a meaningful difference between the two peaks and between the periods of engagement of the tool flutes. The analytical force model does not consider this imbalance, which has a significant role in ploughing regime also due to the formation of build-up edge material accumulation on the tool flute. The analytical model prediction was calculated by considering the effective thickness of the samples. The average percentage error for each combination of the process parameters was calculated. The results are visible in **Table 25**.

Table 25. Average error of the analytical model.

Test	Cutting speed (m/min)	Feed per tooth (μm/rev*tooth)	Average Error (%)
A	30	2.5	-2.5
B	40	2.5	-1.9
C	30	5	10.4
D	40	5	12.4
E	30	10	-1.7
F	40	10	-0.9

The best model prediction occurs when the cutting dominant mode is shearing. The average error for Tests E is -1.7 % while for Tests F is -0.9 %. The imbalance between the tool cutting edges is almost negligible, as visible in **Figure 74 (c)**. The advantageous experimental condition allowed to calculate the average cutting force between the tool flutes for the entire signal, and not only for the peaks as made for the test in ploughing regime. However, the model offers a very accurate prediction of the cutting load peaks in ploughing dominant regime since the error is equal to -2.5 % for Tests A and -1.9 % for Tests B. During the transition between shearing and ploughing the prediction is less accurate since the tests performed with feed per tooth equal to 5 μm/rev*tooth exhibit the highest error. The error on peaks is 10.4 % for Tests C and 12.4 % for Tests D. The model is less reliable than ploughing

and shearing dominant regime. Moreover, also in transition zone the prediction can be considered enough accurate because of the variability of micro milling process, which is strongly influenced by several factors.
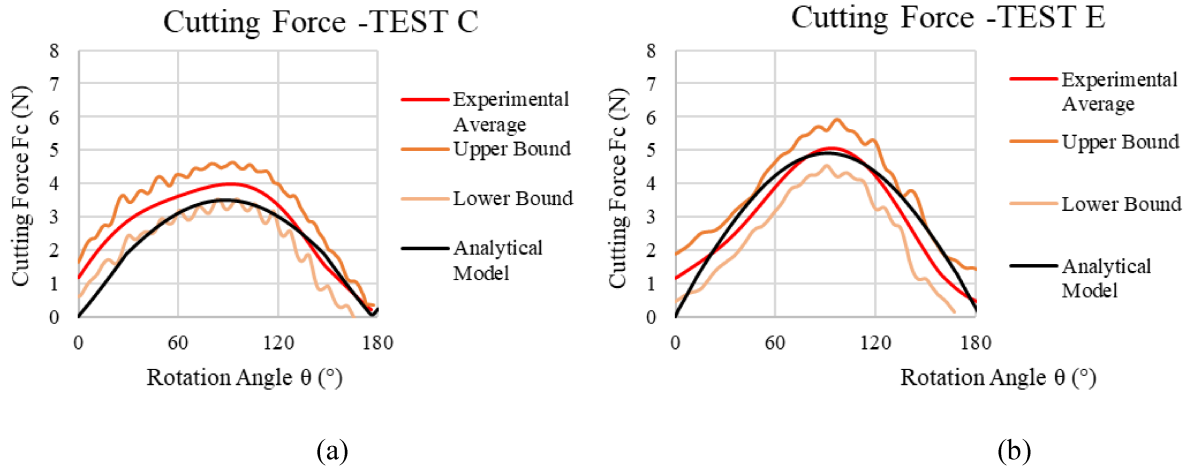

(a)   (b)

Figure 108 Comparison between the experimental data and the model prediction for Test C1 (a) and Test E1 (b)

Figure 108 shows the comparison between two tests with same cutting speed (v_c equal to 30 m/min) and different feed per tooth (f_z equal to 5 μm/rev*tooth for test C and 10 μm/rev*tooth for test E). Tests C (**Figure 108 a**) shows an example of prediction in transition zone while Tests E (**Figure 108 b**) considers the shearing dominant zone. An analogue trend was obtained at higher cutting speed for Tests D and Tests F. The analytical force model provides an accurate cutting force prevision since that F_c is included between the experimental upper and lower limits. Moreover, the model is more powerful in shearing regime since the error about force peaks is minimum and the prediction is extremely accurate along the entire tool rotation.

Here it follows the results achieved by the calibration with the 2nd strategy, expressed by **Equation 49**. The best solution was identified by using 150 particles after 1500 algorithm iterations and it is reported in **Table 26** as optimum set with 2nd strategy.

Table 26. Bounds and optimum sets of the analytical model coefficients.

Parameter	Lower bound	Upper bound	Optimum set 1st strategy	Optimum set 2nd strategy
K_{ts}	0	10000	2595	1559
K_{tp}	0	5000	4625	2187
K_{rs}	0	10000	1870	2933
K_{rp}	0	5000	3000	4415

A comparison between the two strategies was performed in terms of percentage error of the model prediction for each repetition of each test. The result is expressed by **Table 27**, as an average prediction error calculated by considering the three repetitions of each test listed in **Table 25**.

Table 27. Average errors of the analytical model.

Test	Cutting speed (m/min)	Feed per tooth (μm/rev*tooth)	Average Error 1st strategy (%)	Average Error 2nd strategy (%)
A	30	2.5	-2.5	0.6
B	40	2.5	-1.9	-0.1
C	30	5	10.4	10.2
D	40	5	12.4	7.3
E	30	10	-1.7	0.3
F	40	10	-0.9	-1.3

The absolute values of percentage errors oscillate between 0.9 % and 12.4% with the model calibrated with first strategy, while the second strategy slightly improves the model accuracy. The percentage errors of the model calibrated by using the second strategy oscillate between 0.1% and 10.2%. With the new coefficient set, the model achieved the best results for Tests A and B and Tests E and F. By considering a MUCT of 2.5 μm, Tests A and Tests B did not involve a transition of cutting regimes during the tool rotation. Ploughing was the unique and exclusive cutting regime, since the feed per tooth was equal to 2.5 μm/rev*tooth. At the same time, Tests E and Tests F were characterized by shearing and the ploughing effect is neglectable. The model accuracy is maximum for tests in shearing and ploughing dominant region, while the accuracy reduces in transition cutting condition. Tests C and Tests D share a feed per tooth of 5 μm/rev*tooth. The transition from ploughing to shearing occurs at not-neglectable rotational angle of the tool edge.
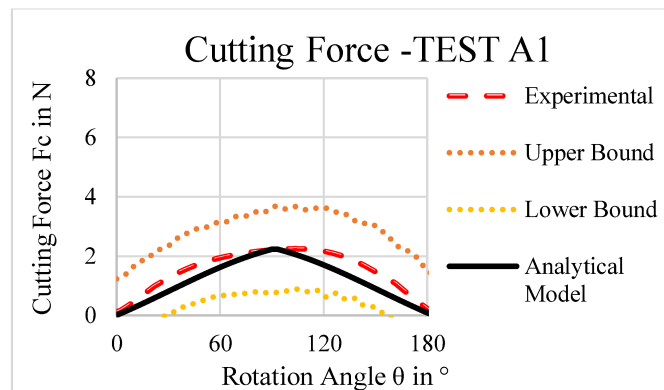
Figure 109 Comparison between the experimental data and the model prediction for Test A1.

Figure 109 shows a comparison between experimental data and the model forecasting for Tests A. The experimental data are presented with a confidence interval of 95%. Process variability appears meaningful in Tests A if compared with Test C and E (see **Figure 108**) due to ploughing regime. The material is not correctly removed, but it is compressed and ploughed. Nevertheless, the model well fits the cutting force signal along the entire machining phase.

5.1.3 Model calibration for LB-PBF Ti6Al4V

The analytical cutting force model described in section 5.1.1 was calibrated also on the experimental data obtained by micro-machining the LB-PBF Ti6Al4V samples with 0° building orientation (see section 4.3). The efforts to tuning the model also for Ti6Al4V were performed mainly for two reasons: on one hand, the necessity to test the reliability of the model also on a second class of material, in order to validate the quality of the model prediction and of the calibration procedure. On the other hand, the Inconel 625 was tested in a special condition to calibrate the model, i.e., the thin-walled cutting with special designed tool with zero-helix angle. Ti6Al4V samples were micro-machined by performing micro-slots by employing a more conventional 30° micro-mill. The axial component of cutting force resulted neglectable if compare with -x and -y components. The calibration was performed also to verify if the model is suitable for this geometrical condition of cutting. Furthermore, Ti6Al4V was tested with a Ø 0.5 mm micro-mill instead of the Ø 0.8mm micro-mill employed for micro-machining of Inconel 625. It is important to verify the reliability of the model also by changing the geometrical size of the process.

As seen in section 4.3, the first group of experimental tests allows to identify the MUCT value. They were performed at constant speed and with decreasing feed rate. The same data set was utilized also to calibrate the analytical model by applying the PSO algorithm. The second group of micro-milling tests was carried out to acquire additional force data for analyzing how the process parameters affect cutting forces, and the related specific loads, and for validating the developed model, by a comparison between experimental and analytical results. **Figure 110** consists in a magnification of **Figure 78 (a)** to better visualize the transition of behavior through the SCF peaks as function of the feed per tooth. A clear change of slope is highlight by the linear regression of the experimental data and it allows to set the MUCT equal to 1.5 μm. The calibration procedure was performed by considering a domain for parameters K_{ts} and K_{rs} equal to [0;100000], while for parameters K_{tp}, and K_{rp} the domain was considered equal to [0;1000000]. The PSO algorithm was set with a population of 100 particles and a number of iterations equal to 1000.
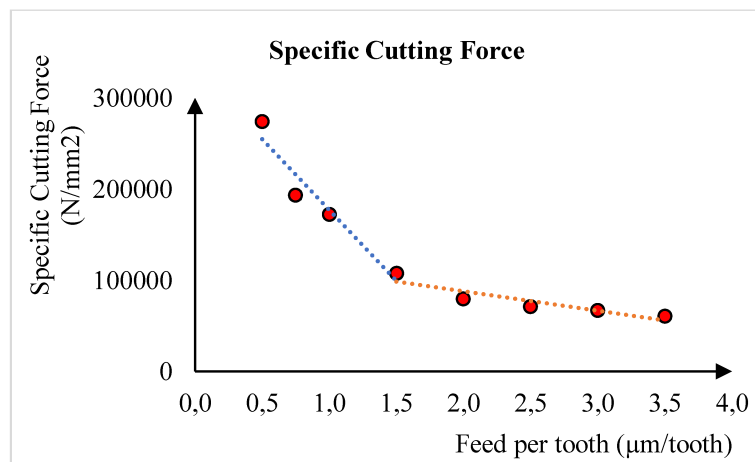

Figure 110. Specific Cutting Force value as function of feed per tooth.

The algorithm was run ten times to find a better solution. In the best iteration, the function *Err* defined by **Equation 49** resulted equal to 0.731. The calibrated model is defined by **Equation50**:

$$F_t(\theta) = \Big(61543 \cdot h(\theta) + 519097 \cdot A_p(\theta)\Big) \cdot a_p$$
$$F_r(\theta) = \Big(79479 \cdot h(\theta) + 733193 \cdot A_p(\theta)\Big) \cdot a_p$$

Eq .50

The model well fits the experimental data, regardless the feed rate. The experimental cutting force signal shows a good balance between the two tool flutes due to a low tool run out. The percentage error on the cutting force peak prediction oscillates between a minimum of 0.01 % (Test f_z=0.75 μm/tooth) and a maximum of 28.5% (Test f_z=0.50 μm/tooth). The average percentage error was calculated as the mean of the percentage error of each test, and it resulted equal to 9.14%. It can be considered a good result having regard of the high extension of the domain of the feed rate, which covers both ploughing and shearing regimes.
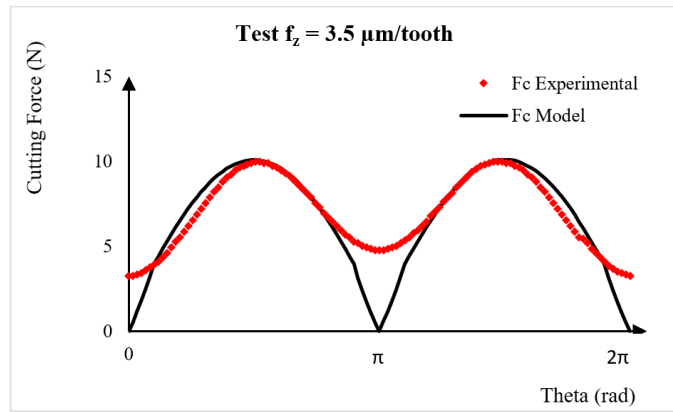
Figure 111. Comparison between the experimental signal of cutting force and the model prediction for test with feed per tooth equal to 3.5 μm/tooth.

Figure 112. Comparison between the experimental signal of cutting force and the model prediction for test with feed per tooth equal to 0.75 μm/tooth.

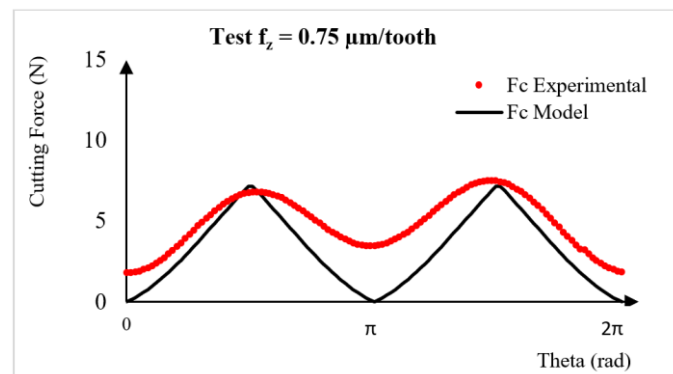**Figure 111** and **Figure 112** shows two examples of comparison between experimental data (as average of thirty cutting tool rotations) and the model. The remaining six tests show similar trends. The model well fits the signal around the cutting force peaks, while the shape

of the curve is different where the cut begins and ends. When ploughing regime is dominant, the model predicts a cutting force sharper then the experimental data. The experimental cutting force results smoother, and the model generally underestimates the signal.

Further tests were performed by following a CCD experimental plan, by changing feed per tooth and cutting speed on five different levels. The experimental cutting force were collected in order to evaluate the dynamics effects of the cutting and to validate the calibrated analytical model. During the experimental tests with different cutting speed the tool run-out increased and only one tool flute was engaged with workpiece. The phenomena of tool run-out is a random effect and it was in complete opposition with the results of the constant cutting speed tests.

However, the model described by **Equation 50** ensured a good prediction also in this condition. The average error about the prediction of the maximum cutting force resulted equal to 6.05%. The error oscillates between a minimum of 1.1 % for the test with a cutting speed of 45 m/min and a feed per tooth of 2.5 µm/tooth, and a maximum of 21.4% for the test with the maximum cutting speed (40 m/min) and the maximum feed per tooth (4.0 µm/tooth). The complete results are listed in **Table 28**.

Figure 113. Comparison between the experimental signal and the model prediction for test with f_z = 3.5 µm/tooth and v_c = 45 m/min.

Table 28. Percentage error of the model prediction.

Test ID	f_z (mm/rev)	v_c (m/min)	Err (%)
1	0,0040	40	21,4
2	0,0035	45	6,3
3	0,0035	35	2,9
4	0,0030	50	1,2
5	0,0030	40	6,4
6	0,0030	40	3,1
7	0,0030	40	6,2
8	0,0030	30	2,5
9	0,0025	45	1,1
10	0,0025	35	8,4
11	0,0020	40	7,2

Figure 113 and **Figure 114** show an example of the comparison between the experimental data and the model prediction. The cutting force exhibits only one peak due to the run-out effect which determines the engagement of only one tool flute with the workpiece. The transition between ploughing and shearing regimes is marked by a sharp edge in the predicted curvature, as visible in **Figure 113**. When ploughing become more relevant, the peak of the predicted cutting force is less smooth, and the concavity is not according with the experimental data.

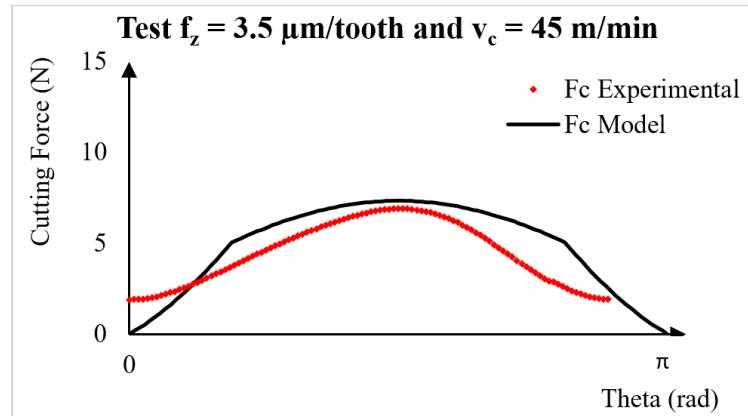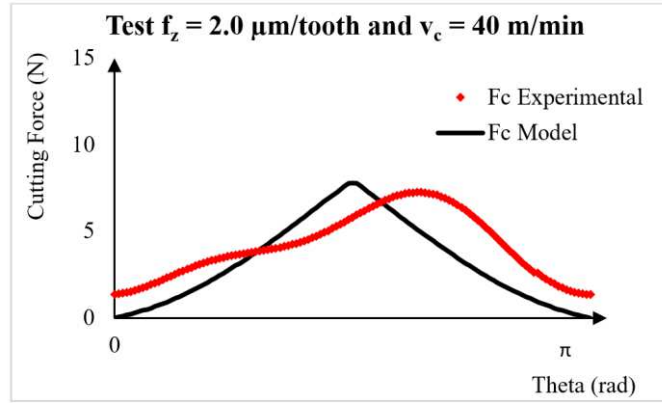**Figure 114.** Comparison between the experimental signal and the model prediction for test with f_z = 2.0 µm/tooth and v_c = 40 m/min.

5.1.4 Model refinement: tool run-out prediction

The accuracy in micro-milling is strongly affected by the phenomena of tool run-out. The discordance between the tool edge effective and theoretical trajectories increases the tool wear and it negatively affects the quality of the machined surface. The tool run-out should be considered in machining modelling in order to accurately predict how the cutting force changes as the process parameters change. This section describes the structure of an analytical model obtained by refining the model described in section 5.1.1. The second version of the model computes the cutting force by considering the tool run-out and the concurrent presence of ploughing- and shearing- dominated cutting regimes. The model was finally calibrated by considering micro-machining on difficult-to-cut material.

Figure 115. Geometrical representation of tool run-out.

The tool run-out phenomena were described by some geometrical parameters which can be experimentally estimated by considering the periodicity of the cutting force signal and the morphology of the machined samples. Tool run-out is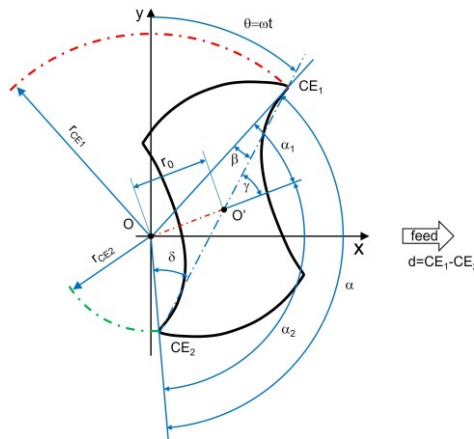 defined as the deviation of the theoretical tool rotational axis from the physical actual one. In conventional milling operations the effect of tool run-out can be considered negligible, but in micro-milling processes, due to the extreme precision required by the machining process, it cannot be neglected, and its analysis is mandatory to achieve the expected reliable quality. Tool run-out can be defined by the run-out length r_0 and the run-out angle γ, as shown in **Figure 115**, representing the topology of tool run-out for a two flute micro-mill, on a plane normal to the tool rotational axis.

In presence of tool run-out, the phase angle α between the mill cutting edges (CE_i), and the cutting edge radii r_{CEi} are functions of r_0 and γ parameters. It has been demonstrated in **[6]** that, once the radius of the first cutting edge r_{CE1}, α, and tool diameter d, are known, it is possible to evaluate all the geometrical parameters. This assessment permits to estimate the chip cross-sectional area evolution, on which the proposed micro-milling tool force model is based, hence it is of fundamental importance for its development. Considering **Figure 115**, the tool rotational angle $\theta(t)$ is defined in **Equation 51**:

$$\theta(t) = \omega \cdot t \qquad \textbf{Eq. 51}$$

where ω is the tool rotational speed [rad/s] and t is the cutting time [s]. The cutting edges trajectories are expressed by their components on x-axis and y-axis by **Equation 52**:

$$
\begin{aligned}
x_{CE1} &= r_{CE1} \cdot \sin\theta + \frac{f}{60} \cdot t \\
y_{CE1} &= r_{CE1} \cdot \cos\theta \\
x_{CE2} &= r_{CE2} \cdot \sin[\theta + \alpha] + \frac{f}{60} \cdot t \\
y_{CE2} &= r_{CE2} \cdot \cos[\theta + \alpha]
\end{aligned}
\qquad \textbf{Eq. 52}
$$

where f is the feed [mm/min] and r_{CE2} is the CE_2 radius [mm] calculated by **Equations 53** and **54** respectively:

$$r_{CE2} = \sqrt{r_{CE1}^2 + d^2 - 2r_{CE1}d\cos\beta} \qquad \textbf{Eq. 53}$$

$$f = f_z \cdot z \cdot N \qquad \textbf{Eq. 54}$$

Where f_z is the feed per tooth [mm/tooth], z the number of flutes of the mill, and N the spindle speed [rpm]. Once the temporal trajectories of $CE_1(x_{CE1}, y_{CE1})$ and $CE_2(x_{CE2}, y_{CE2})$ are derived, the calculation of the instantaneous uncut chip thickness (IUCT) for each one of them is obtained by their difference, leading to **Equation 54** for IUCT of CE_1 (h_{CE1}) and CE_2 (h_{CE2}):

$$
\begin{aligned}
h_{CE1} &= \sqrt{(r_{CE1}\sin\theta + \Delta s_{CE1})^2 + (r_{CE1}\cos\theta)^2} - r_{CE2} \\
h_{CE2} &= \sqrt{(r_{CE2}\sin\theta + \Delta s_{CE2})^2 + (r_{CE2}\cos\theta)^2} - r_{CE1}
\end{aligned}
\qquad \textbf{Eq. 54}
$$

Where Δs_{CE1} is the distance covered by the rotational axis between the passage of CE_2 and the consecutive passage of CE_1 in the θ angular position, while Δs_{CE2} is the distance covered between the passage of CE_1 and the consecutive passage of CE_2 in the θ angular position. These distances are evaluated by **Equation 55**:

$$\Delta s_{CE1} = \frac{f}{60} \cdot \frac{\alpha}{\omega}$$
$$\Delta s_{CE2} = \frac{f}{60} \cdot \frac{2\pi-\alpha}{\omega}$$

Eq. 55

As understandable from **Equation 54** and from **Figure 116**, tool run-out leads to a difference amongst the IUCT of first and second cutting edge. Therefore, the related cutting forces will be different as well. The proposed model deals not only with the tool run-out effect, but also with the contribution of shearing and ploughing cutting regimes to the generated forces. Thus, detecting the transition between ploughing and shearing regimes, and calculating the cutting area A_C covered by each cutting edge is mandatory. **Figure 116** reports the schematization of the cutting edges trajectories in presence of tool run-out and the cutting force components in a plane normal to the tool rotational axis.
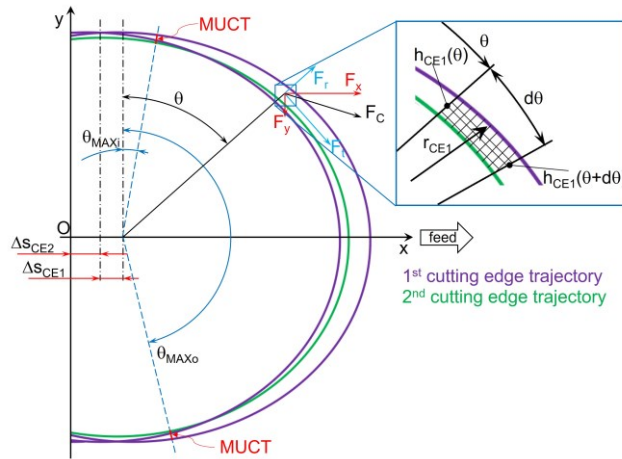
Figure 116. Trajectories and cutting forces for micro-milling operation.

The cutting area of the i-th cutting edge can be estimated by **Equation 56**

$$A_{ci}(\theta) = \int_0^\theta \left(\frac{h_{CEi}(\theta)+h_{CEi}(\theta+d\theta)}{2}\right) r_{CEi} \, d\theta$$

Eq. 56

where $d\theta$ is the infinitesimal variation of the rotational angle.

The transition between ploughing and shearing cutting regimes is detected by the value of the minimum uncut chip thickness (MUCT), related to cutting edge radius and workpiece material, and must be experimentally determined. The total cutting force F_C is the combination of its three axial components F_x, F_y, and F_z (this last not visible in **Figure 116**), and the resulting one in the plane can be subdivided in its tangential F_t and radial F_r components. These latter can be expressed by **Equation 57**:

135

$$F_{t1} = \left(K_{ts} \cdot h_{CE1}(\theta) + K_{tp} \cdot A_{pCE1}(\theta) \right) \cdot a_p$$

$$F_{r1} = \left(K_{rs} \cdot h_{CE1}(\theta) + K_{rp} \cdot A_{pCE1}(\theta) \right) \cdot a_p$$

$$F_{t2} = \left(K_{ts} \cdot h_{CE2}(\theta) + K_{tp} \cdot A_{pCE2}(\theta) \right) \cdot a_p$$

$$F_{r2} = \left(K_{rs} \cdot h_{CE2}(\theta) + K_{rp} \cdot A_{pCE2}(\theta) \right) \cdot a_p$$

Eq. 57

Where K_{ts} and K_{rs} are the specific force coefficients [N/mm^2] for the shearing regime, K_{tp} and K_{rp} are the specific force coefficients [N/mm^3] for the ploughing regime, a_p [mm] is the axial depth of cut, and $A_{pCE}(\theta)$ is the ploughed area [mm^2].

Once MUCT is individuated, $A_{pCE}(\theta)$ can be assessed applying the set of **Equation 58**:

$$h_{CEi}(\theta) < MUCT \wedge \theta < \theta_{MAXi} \quad \Rightarrow \quad A_{pCEi}(\theta) = A_{ci}(\theta)$$

$$hCEi(\theta) > MUCT \quad \Rightarrow \quad A_{pi}(\theta) = A_{piMAX}$$

$$h_{CEi}(\theta) < MUCT \wedge \theta > \theta_{MAXo} \quad \Rightarrow \quad A_{pCEi}(\theta) = A_{ci}(\pi) - A_{ci}(\theta)$$

Eq. 58

Where θ_{MAXi} is the tool rotational angle at which IUCT reaches the value of MUCT in the entering phase, and θ_{MAXo} is the tool rotational angle at which the IUCT becomes smaller than MUCT in the exiting phase.

5.1.5 Experimental calibration of the model with tool run-out

The refined analytical model was calibrated on the experimental data collected while machining the LB-PBF Ti6Al4V samples built with an orientation angle equal to 0°. The summary of the experimental activities and results is collected in section 4.3. The model calibration was performed by assuming a MUCT equal to 1.5 μm, the same value used for the calibration of the previous version of the analytical mode. The evaluation of r_0 and γ concerns the estimation of d, r_{CE1}, and α. The value of the effective tool diameter was measured by the BLUM laser measuring system mounted on the CNC machine. As reported in [6], r_{CE1} was derived by halving the measurements of the machined micro-channels widths (**Figure 117**), while α was detected, by analyzing the acquired force signal as a function of the rotational angle of the tool, and evaluating the angle between the F_C local minima, that indicates the transition amongst one cutting edge and the other (**Figure 118**).
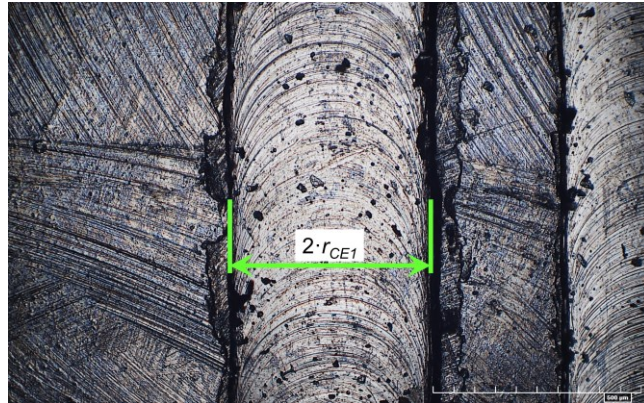

Figure 117. Experimental measurement of r_{CE1}.

The optimization of the model coefficients K_{ts}, K_{rs}, K_{tp}, K_{rp} was attained employing the Particle Swarm Optimization (PSO) algorithm. The error function to be minimized (**Equation 49**) was the normalized difference between the model peak force and the peak of the experimental one for each cutting edge and each performed test. For the evaluation of the forces and of the function *Err*, the **Equations**. from **51** to **58** of the analytical model were implemented in a Matlab® function. By applying on it the PSO search algorithm, *Err* was iteratively minimized, permitting the calibration of K_{ts}, K_{rs}, K_{tp}, K_{rp} coefficients. An initial assumption of these latter led to a first *Err* estimation by the comparison with experimental data. Subsequently, the algorithm iteratively adjusted the coefficients by respecting the constraints related to their modification, until achieving the *Err* minimized value. This process concerned a domain for K_{ts} and K_{rs} of [0;100000], while a domain for K_{tp} and K_{rp} of [0;1000000]. A population number of 100 particles and an iteration number of 1000 was set for the PSO algorithm. In order to attain a more accurate solution, the PSO was executed ten times. Amongst all the iterations performed by the applied PSO algorithm, the one furnishing the best result provides the lowest value of *Err* equal to 4.187. The resulting calibrated coefficients are: $K_{ts} = 99521$ N/mm², $K_{rs} = 4723$ N/mm³, $K_{tp} = 259364$ N/mm², and $K_{rp} = 27275$ N/mm³.

Table 29 reports the percentage errors for each performed test and for each cutting edge. The error $e_\%$ is calculated by **Equation 59**:

$$e_\% = \frac{|F_{C,modMAX,CEi} - F_{C,expMAX,CEi}|}{F_{C,expMAX,CEi}} \cdot 100 \qquad \textbf{Eq. 59}$$
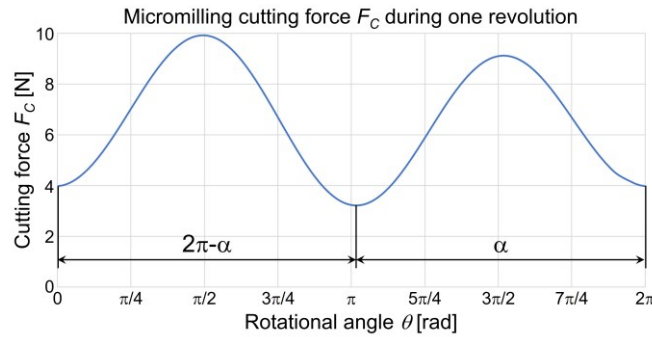
Figure 118. Phase angle α [rad] measurement from the acquired force signal.

Table 29. Percentage error $e_\%$ for each performed test and cutting edge.

First cutting edge (CE_1)		Second cutting edge (CE_2)	
f_Z [µm/tooth]	$e_\%$	f_Z [µm/tooth]	$e_\%$
4.0	0.32	4.0	3.03
3.5	13.98	3.5	9.60
3.0	20.34	3.0	22.22
2.5	4.93	2.5	8.39
2.0	7.13	2.0	6.13
1.5	30.01	1.5	75.55
1.0	0.16	1.0	24.80
0.75	12.18	0.75	22.97

Figures 119-126 report the evolution of the experimental and modeled cutting forces as a function of the rotational angle of the tool. These figures show the capability of the proposed model to correctly estimate the asymmetric behavior of the forces as a consequence of the tool run-out. More in detail, the model correctly forecast the phase angle between the first and the second cutting edge, and it is able to predict which one, amongst these two, will generate the higher cutting force and which one the lower.

The precision of the model is higher at higher feed per tooth, in a range of f_Z values from 4.0 µm to 2.0 µm, and this is noticeable by observing **Table 29** as well. For f_Z values lower than 2.0µm, $e_\%$ increases up to a value of 75.55 %, for the second cutting edge, when f_Z is equal to 1.5 µm, that is the value indicating the transition between ploughing and shearing cutting regime. This behavior is ascribable to the increment of ploughing regime contribution. In these circumstances in fact, the machined material is mainly deformed instead of being sheared, leading to a more discontinuous cross-sectional area of the chip, that makes difficult its correct calculation by the analytical geometrical model. For all the other values of f_Z, $e_\%$ is lower than the 25 %, indicating the capability of the analytical model to calculate the cutting forces in a suitable way. Therefore, the proposed technique can be profitably employed for considering the presence of tool run-out in the prediction of micro-milling cutting forces.
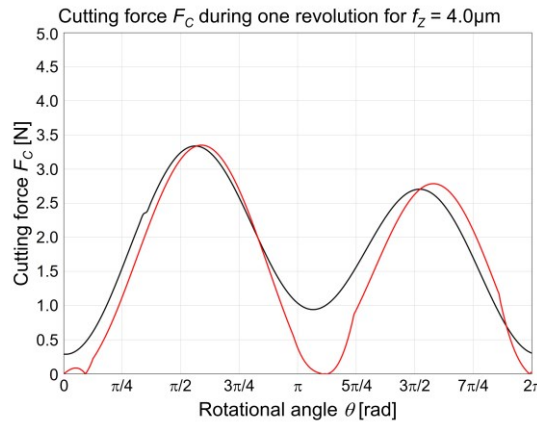
Fig. 119. Experimental vs. modeled F_C for $f_Z = 4.0$ µm.
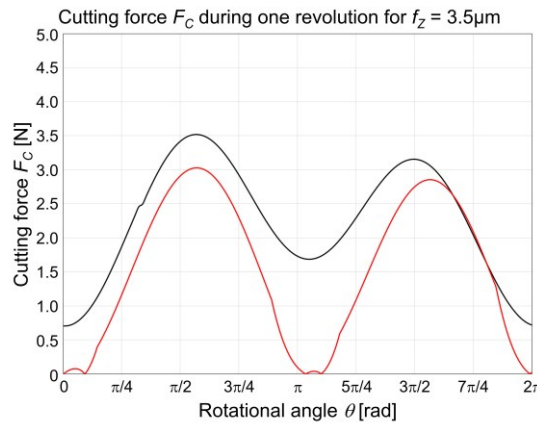
Fig. 120. Experimental vs. modeled F_C for $f_Z = 3.5$ µm.

138

Fig. 121. Experimental vs. modeled F_C for $f_Z = 3.0$ μm.

Fig. 122. Experimental vs. modeled F_C for $f_Z = 2.5$ μm.

Fig. 123. Experimental vs. modeled F_C for $f_Z = 2.0$ μm.

Fig. 124. Experimental vs. modeled F_C for $f_Z = 1.5$ µm.

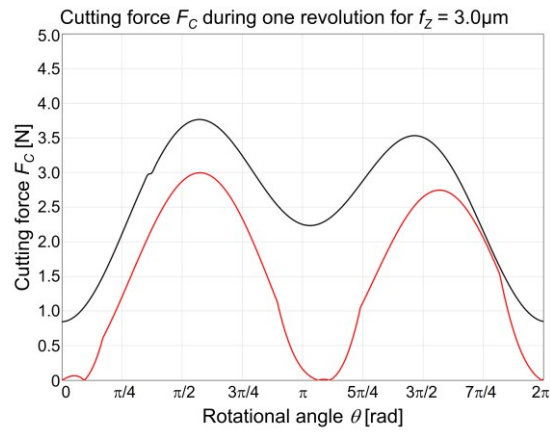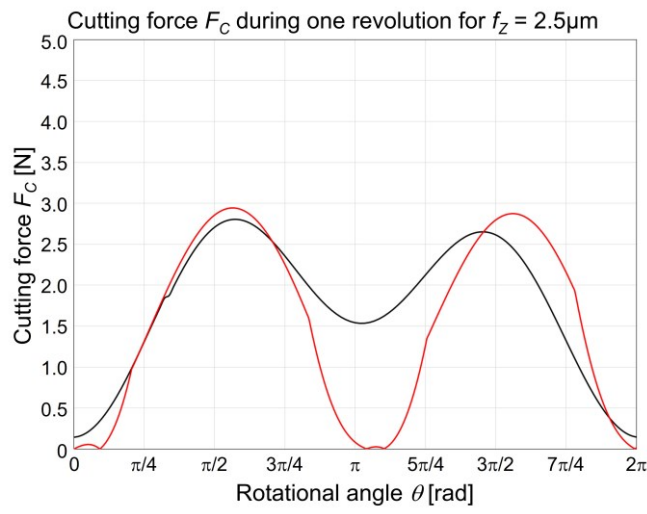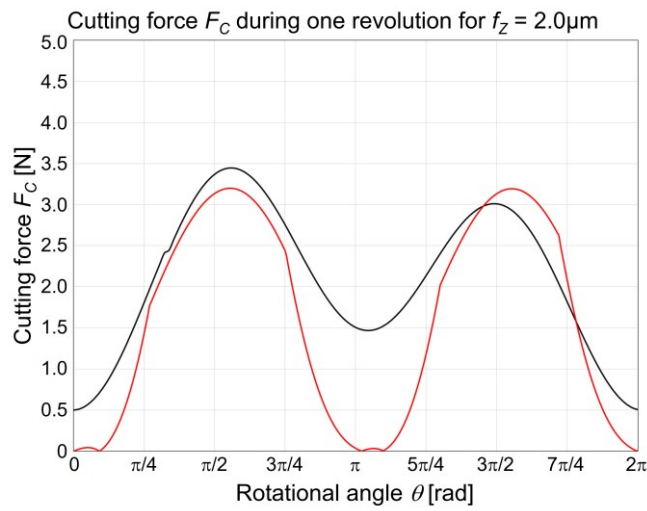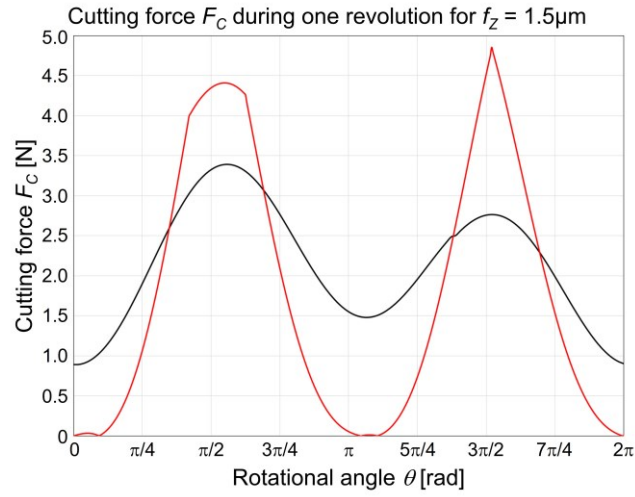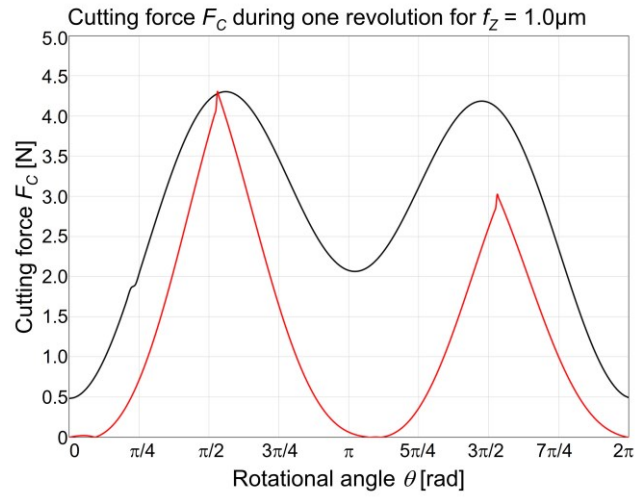**Fig. 125.** Experimental vs. modeled F_C for $f_Z = 1.0$ µm.
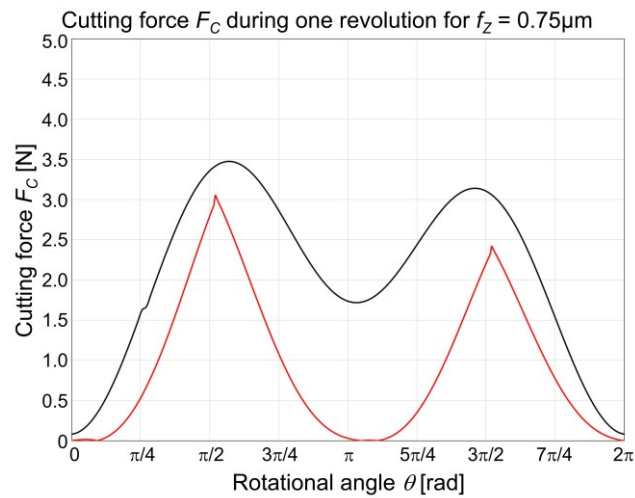
Fig. 126. Experimental vs. modeled F_C for $f_Z = 0.75$ µm.

5.2 FEM modeling of micro-machining

In this section will be introduce a novel 2D micromachining Finite Element Method simulation strategy for micro-milling forces evaluation. Particle Swarm Optimization method was employed for optimizing the flow stress parameters of the workpiece material by comparing the model prediction with experimental data, providing good agreement. FEM reliability is subjected to its correct setup, concerning the implementation of cutting parameters, friction, material behavior, characterized by flow stress law.
Once these inputs are correctly set, this strategy permits the micro-milling process predictive analysis, avoiding costly optimization experimental tests.

The 2D FEM model was tuned on the experimental data collected while micro-milling additive manufactured Inconel 625 specimens. In particular, the micro-cut of the thin-walled samples was modeled by exploiting the semi-orthogonal cut configuration in order to simplify the model and performing 2D-FEM simulation. Starting from the comparison of the simulated cutting forces with the ones calculated by means of a force analytical model (see section 5.1.2) the parameters of a modified Johnson-Cook (J-C) flow stress law were calibrated by applying a Particle Swarm Optimization (PSO) algorithm. The good agreement amongst FEM and model results implies the predictive capability of the proposed methodology.

5.2.1 Structure of the model

Considering the null value of the tool helix angle, 2D FEM simulations can be exploited for modeling purpose. Therefore, the experimental tests were faithfully reproduced by thermo-mechanical simulations in the Deform2D® FEM environment. In order to correctly characterize the intrinsic chip thickness variation during the micro-mill rotation, the workpiece geometry was represented as a semi-tubular section having an internal boundary corresponding to the hypothetical trajectory of the previous cutting-edge passage, and a circular arc for the external boundary. With the aim of reducing computational times, only the portion of the tool geometry closely in contact with the workpiece was considered.
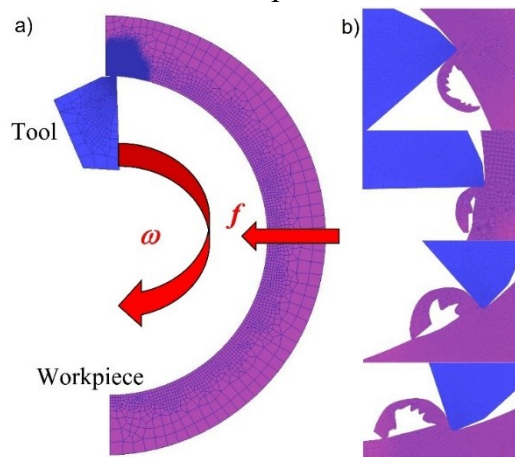
Fig. 127. FEM cutting simulation setup, a) overview, b) chip at different times.

Figure 127 shows the beginning of the proposed cutting simulation, where workpiece and tool geometry are visible. Moreover, the cutting speed movement was assigned to the tool, by putting it into rotation around tool rotational axis, with a rotation speed ω [rad/s] corresponding to the desired V_C [m/min]; while the workpiece was moved against the tool with a feed rate f [mm/s] equivalent to the required f_Z [μm/tooth*rev], in consideration of a micro-mill diameter of 789 μm. **Table 30** summarizes the computed values for f and ω for each experimental configuration.

The tool was considered as a rigid object. For correctly estimating its temperature distribution during the process, the material thermal properties of WC from Deform database were assigned. It was discretized with a mesh consisting of 1500 quadrangular linear elements and a sequence of mesh windows providing an element size at the tool edge region lower than 0.5 μm. An elasto-plastic mechanical behavior was assigned to the workpiece. Temperature-dependent Inconel 625 elastic and thermal properties derived from **[205]** were used. The workpiece was meshed with 15000 quadrangular linear elements, employing a dynamic mesh window following the tool movement, giving a minimum element size lower than 1 μm. A heat transfer coefficient, *htc* of 20 W/m²K, with the environment, at a temperature of 20°C, was defined for both tool and workpiece. The contact between the two objects, at the tool-chip interface, was defined by a shear model with a friction factor *m* of 0.6 and adopting a *htc* of 100000 W/m²K.

Table 30. Cutting speed and feed rate implemented in the FEM models.

Test	f_Z [μm/tooth]	→	f [mm/s]	V_C [m/min]	→	ω [rad/s]
A	2.5	→	1.008	30	→	1267
B	2.5	→	1.345	40	→	1690
C	5.0	→	2.017	30	→	1267
D	5.0	→	2.689	40	→	1690
E	10.0	→	4.034	30	→	1267
F	10.0	→	5.379	40	→	1690
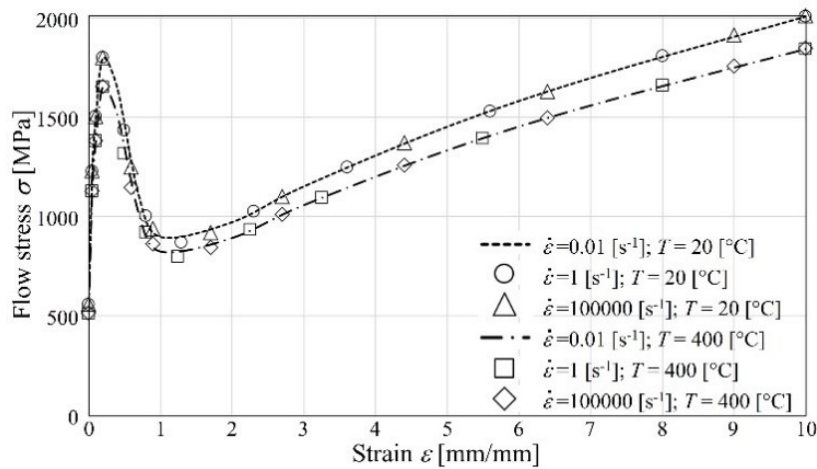
Fig. 128. Inconel 625 σ_{Init} function Vs. strain for different strain rate and temperature values.

The selected flow stress law $\sigma(\varepsilon,\dot{\varepsilon},T)$, implemented in the FEM environment, is the modified Johnson-Cook (J-C) model that is the typical one employed when simulating machining operation of nichel-chromium based alloys [206, 207]. It describes the plastic material behavior as a function of strain ε, strain rate $\dot{\varepsilon}$ [s^{-1}], temperature T [°C], and it is represented by **Equation 60**:

$$\sigma(\varepsilon,\dot{\varepsilon},T) = [A + B\varepsilon^n]\left[1 + C\,ln\left(\frac{\dot{\varepsilon}}{\dot{\varepsilon}_0}\right)\right]\left[1 - \left(\frac{T-T_r}{T_m-T_r}\right)^m\right]\left[M + (1-M)\left(tanh\left(\frac{1}{(\varepsilon+p)^r}\right)\right)^S\right] \qquad \textbf{Eq. 60}$$

Where $\dot{\varepsilon}_0$ [s^{-1}] is the reference strain rate, T_r and T_m [°C] are the environment and material melting temperatures respectively, while the other parameters are material related constants. As visible in **Equation 60**, the first three parts of it in squared backets are related to the effects of ε, $\dot{\varepsilon}$, and T on the material plasticity, while the last one is a hyperbolic function permitting to correctly represents the chip segmentation [208, 209]. The material constants for Inconel 625 proposed in [206] are reported in **Table 31**, while its behavior as a function of strain at different strain rates and temperatures is depicted in **Figure 128**.

Table 31. IN625 Johnson-Cook material constants from [206].

A [MPa]	B [MPa]	C	n	m	$\dot{\varepsilon}_0$ [s^{-1}]
559	3000	0.00021	0.5	2	1670
T_m [°C]	T_r [°C]	M	p	r	S
1350	20	0.2	0	0.65	10

5.2.2 Model calibration

With the intent of verifying the flow stress parameters of **Table 31**, an initial FEM simulation, truthfully reproducing Test E (V_C = 30 m/min; f_Z = 10 μm/tooth*rev), was setup following the novel methodology described in section 5.2.2. For this reason, the flow stress parameters has been defined as σ_{Init}. The resulting cutting force during the tool rotation of this simulation was then compared with the one estimated by the analytical model, as reported in **Figure 129**.

Fig. 129. Analytic and FEM F_C comparison by the implementation of σ_{Init}.

143

The evolution of the simulated cutting force, throughout the tool rotational angle, shows a trend that corresponds with the one predicted by the analytical model, enforcing the suitability of the proposed 2D FEM approach. On the contrary, the discrepancy of the F_C values is clearly observable. In particular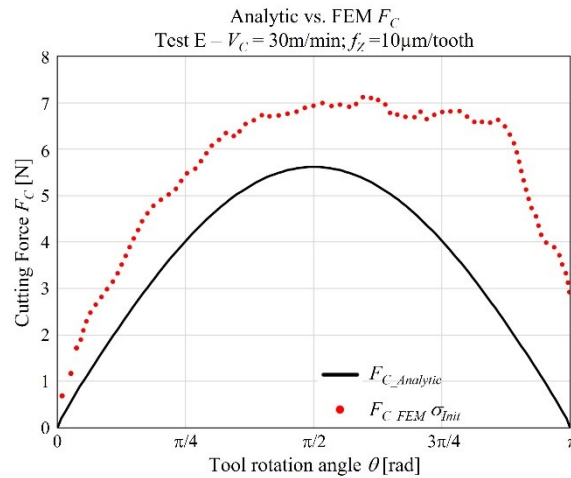, the F_C resulting from the simulation is greater than the analytical one. This can be ascribed to the fact that the parameters of σ_{Init} presented in [206] are derived from Hopkinson Split Bar tests of rolled and annealed material, that is characterized by different mechanical and physical properties respect to the specimens machined in this work, that were produced by AM process with intrinsic higher porosity and lower density. Therefore, to correctly estimate the cutting forces by simulation, an optimization of the J-C model parameters is mandatory.

Equation 60 reveals that flow stress is defined by a total number of 12 parameters. A concurrent optimization of these all is a time and energy consuming iterative process. Hence, since each bracket-squared part has a determined significance in the material behavior description, for improving the optimization procedure, the following assumption have been made.

- The strain rate has a minimal effect on the material behavior, as demonstrated by the experimental data. The low value of the C constant in the J-C model was kept constant as in the original model [206].
- At high temperatures, Inconel 625 alloys retain high mechanical characteristics, thus, flow stress curves remain close one to each other even when the temperature is varying, as observable in **Figure 128**. For this reason, the *m* parameter was maintained equal to 2, as proposed in [206].
- The hyperbolic function mainly affects the material softening behavior in the primary shear zone leading to the simulation of chip segmentation, but its effect on the cutting force peak is neglectable. Since the objective of this work is to correctly estimate F_C, the constants values related to this part of the model were kept unchanged.

Subsequent to these assumptions, **Equation 60** becomes:

$$\sigma(\varepsilon, \dot{\varepsilon}, T) = [A + B\varepsilon^n]\left[1 + C\ln\left(\frac{\dot{\varepsilon}}{\dot{\varepsilon}_0}\right)\right]\left[1 - \left(\frac{T-T_r}{T_m-T_r}\right)^2\right][F(tanh(\varepsilon))] \qquad \textbf{Eq. 61}$$

Where *F(tanh(ε))* represents the unchanged hyperbolic function, and the only parameters need to be optimized are *A*, *B*, and *n*.

The F_C peak values in **Figure 129** are 5.617 N and 7.623 N for the analytic (F_{CMA}) and FEM (F_{CMF}) models respectively. This leads to a percentage error $e_\%$ (**Equation 62**) in the F_C estimation by FEM of 25.7 %:

$$e_\% = \frac{|F_{CMA}-F_{CMF}|}{F_{CMA}} \cdot 100 = \frac{|4.716-5.928|}{4.716} \cdot 100 = 25.7\% \qquad \textbf{Eq. 62}$$

Assuming that material flow stress is the only factor influencing the FEM results, and considering the overestimation of the simulated forces, σ_{Init} was multiplied for a factor *K*

defined in **Equation 63**, obtaining a new set of reduced flow stress curves to be tested and fitted.

$$K = 1 - e_\% = 1 - 0.257 = 0.743 \qquad\qquad \textbf{Eq. 63}$$

For fitting the reduced flow stress values, an optimization of *A*, *B*, and *n* parameters was performed by the application of the PSO algorithm. The error function *Err(σ)* to be minimized was the normalized difference between *K* times σ_{Init} and the desired optimized flow stress law σ_{Opt}, for each strain and temperature, as defined in **Equation 64**:

$$Err(\sigma) = \sum_{i,j} \left(\frac{|K \cdot \sigma_{Init}(\varepsilon_i, T_j) - \sigma_{Opt}(\varepsilon_i, T_j)|}{K \cdot \sigma_{Init}(\varepsilon_i, T_j)} \right) \begin{array}{l} i = 0 \div 10 [\frac{mm}{mm}] \\ j = 20 \div 800 [°C] \end{array} \qquad \textbf{Eq. 64}$$

σ_{Init} (**Equation 60** with the parameters of **Table 31**), **Equation 61** and **Equation 64** were implemented in a Matlab® function. By the application of the PSO toolbox search algorithm, *Err(σ)* was minimized by iteratively varying *A*, *B*, and *n* values allowing their calibration. The optimization process was performed considering a population of 100 particles and 1000 iterations. The domains for *A*, *B*, and *n*, were set to [300÷800], [1000÷4000], and [0.1÷0.7] respectively. The calibrated values are *A* = 415, *B* = 2229, *n* = 0.4998. Therefore, the J-C model parameters of σ_{Opt} are the ones reported in **Table 32**. **Figure 130** shows the comparison between σ_{Init} and the optimized flow stress σ_{Opt}.
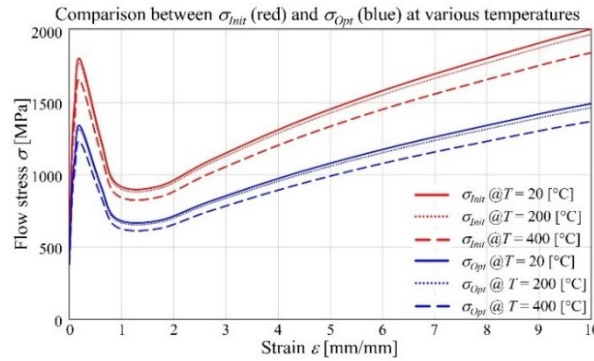

Fig. 130. Optimized and **[206]** flow stress comparison at different temperatures for Inconel 625.
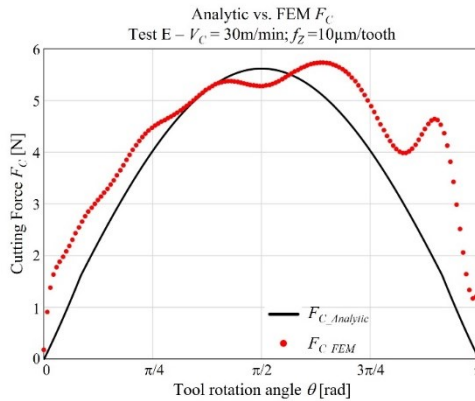

Fig. 131. Comparison between analytic and FEM F_C with σ_{Opt} for Test E.

145

Table 32. Johnson-Cook material constants for LB-PBF Inconel 625 (σ_{Opt}).

A [MPa]	B [MPa]	C	n	m	$\dot{\varepsilon}_0$ [s⁻¹]
415	2229	0.00021	0.4998	2	1670

T_m [°C]	T_r [°C]	M	p	r	S
1350	20	0.2	0	0.65	10

The optimized flow stress σ_{Opt}, reproposed in **Equation 65**, was then implemented in a FEM simulation reproducing Test E, giving encouraging results. As visible in the comparison amongst analytic and simulated F_C (**Figure 131**), both trend and module agree, with a $e_\%$ of peaks of 0.74 %.

$$\sigma(\varepsilon, \dot{\varepsilon}, T) = [415 + 2229\varepsilon^{0.4998}]\left[1 - \left(\frac{T-20}{1350-20}\right)^2\right]\left[1 + 0.00021\, ln\left(\frac{\dot{\varepsilon}}{\dot{\varepsilon}_0}\right)\right]\left[0.2 + (1 - 0.2)\left(tanh\left(\frac{1}{(\varepsilon)^{0.65}}\right)\right)^{10}\right]$$

Eq. 65

5.2.3 Model results

The validation of the simulation procedure and of the flow stress of **Equation 65** was carried out by the comparison of analytic and FEM F_C peaks for the whole experimental tests. The analytical model was calibrated on the experimental data as described in section 4.2. The **Table 33** lists the cutting force values, the experimental data and the model prediction both.

Table 33 Experimental cutting force and analytical model.

Test	f_z [µm/tooth*rev]	V_C [m/min]	F_{CExp} [N]	$F_{CAnalitic}$ [N]	$e_\%$
A	2.5	30	2.143	2.197	2.5
B	2.5	40	2.297	2.340	1.9
C	5.0	30	3.430	3.070	10.5
D	5.0	40	3.547	3.103	12.5
E	10.0	30	5.510	5.617	1.9
F	10.0	40	5.217	5.270	1.0

The results of the experimental tests in terms of maximum cutting force are listed in **Table 33**, where the average experimental peaks and the analytical model peaks are compared. **Figures 132-133** show the comparison between analytical and FEM cutting force for tests A, B, C, D, and F respectively. It is possible to appreciate the evolution of F_C along θ as well. The cutting force trends are in good agreement, confirming once again the validity of the established 2D FEM technique. The only discrepancy, that is common to all the presented tests, is the higher value of the FEM F_C respect to the analytical one, at θ values closed to π. This condition represents a position of the cutting edge nearby the disengagement from the workpiece. At this point, it can be experimentally observed that $h(\theta)$ is tiny, conducting to a F_C reduction, as correctly described analytically. On the other hand the simulation does not show this thickness reduction with a resulting F_C increasing. This is due to a wrong evalua-

tion of the chip segmentation. For solving this aspect, further studies should be done to optimize $F(tanh(\varepsilon))$ in **Equation 61**. **Table 34** reports the comparison of F_{CMA} and F_{CMF} with percentage errors. The low values of these latter indicate the capability of the implemented σ_{Opt} to correctly forecast the cutting forces.

Table 34. Analytic F_{CMA} and FEM F_{CMF} peak force comparison.

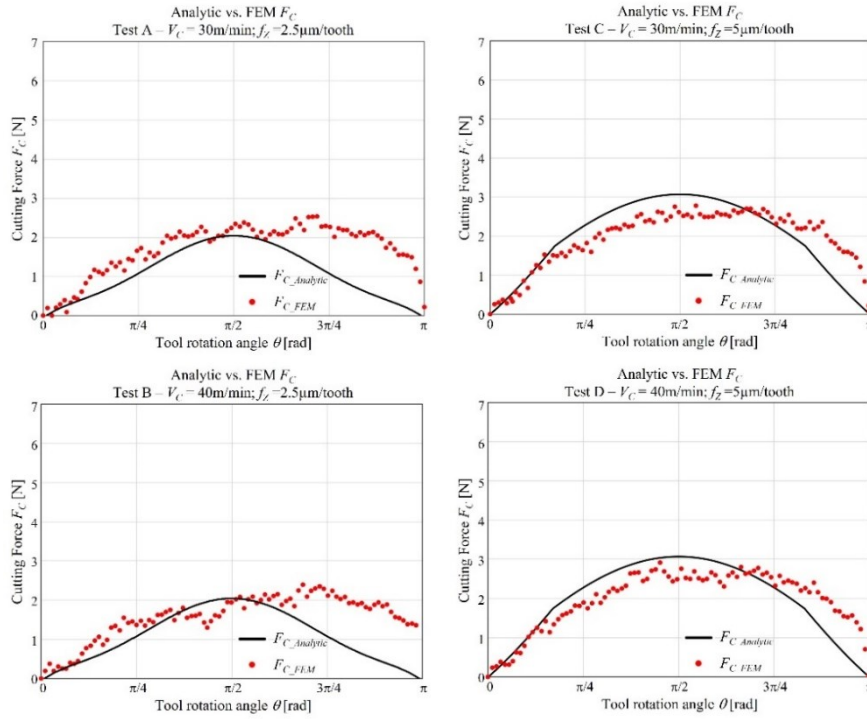| Test	F_{CMA} [N]	F_{CMF} [N]	$e_\%$
A	2.197	2.536	15.4
B	2.340	2.394	2.30
C	3.070	2.780	9.44
D	3.103	2.914	6.09
E	5.617	5.575	0.74
F	5.270	4.815	8.61

Fig. 132. Analytic and FEM FC, with σ_{Opt}, comparison for tests A, B, C, D.
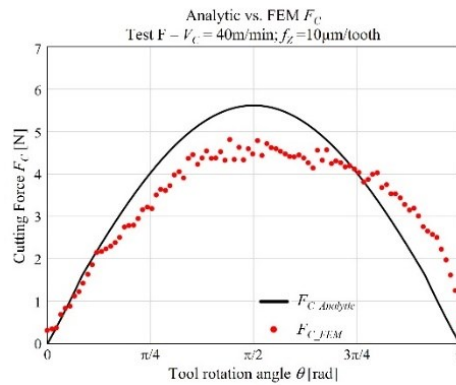

Fig. 133. Analytic and FEM FC, with σ_{Opt}, comparison for test F.

147

5.3 Conclusions

This chapter presented the formulation of an analytical force model for slot micro milling which considers the concurrent presence of different cutting regimes i.e. ploughing and shearing. This analytical model feature allows successfully applying the force model on a wide range of process parameters including high feed rate cases. A model refinement procedure is described and applied on an experimental case, micro milling of an additive fabricated Inconel 625 superalloy where material behavior in cutting is considered as unknown. An accurate load measurement system provides collecting cutting force data useful for the model assessment. The experimental investigation of the cutting regimes transiting from shearing to ploughing allowed identifying a MUCT value that is equal to 2.5 μm. This parameter offers an important information about the machinability of the additively fabricated Inconel 625 superalloy and, at the same time, it covers a key role as an analytical model input. After the model refinement procedure, the model offers a good prediction of the tangential and radial components of the cutting forces. The percentage error of the prediction is calculated for each test by considering the resultant cutting force. The proposed analytical force model offers reliable prediction in accord with the experimental data. This first version of the analytical model was finally published on an international journal **[19]**, visible in **Figure 133**. The model calibration and the comparison among two alternatives optimization strategies was presented at the international conference CIRP CMMO 2021 **[21]** and the abstract is visible in **Figure 134**.

PRODUCTION PROCESS

Analytical force modelling for micro milling additively fabricated Inconel 625

Andrea Abeni[1] · Dario Loda[1,2] · Tuğrul Özel[2] · Aldo Attanasio[1]

Abstract

In recent years, miniaturization of components has been concerned with several industrial fields including aerospace, energy, and electronics. This phenomenon resulted in increasing demand of micro-components with complex shape and high strength, often in high-temperature environment. Nickel-based superalloys such as Inconel 625 are a class of material suitable to aforementioned applications and can be successfully processed with Additive Manufacturing (AM). Moreover, micro-milling can be employed to manufacture micro-scale features on the additively fabricated parts or to achieve better surface finishes, as required for high-precision mechanical assemblies. In micro machining, it is possible to notice a lack of scientific study focusses on the material removal behavior of difficulty-to-cut alloys produced via Additive Manufacturing. This paper describes an analytical cutting force model suitable also for AM'd parts which considers the presence of ploughing- and shearing- dominated cutting regimes. A refinement procedure of the cutting force model was defined and applied by performing an experimental work on Inconel 625 samples fabricated by LaserCUSING™. A search algorithm was employed to develop an iterative methodology to determine the unknown cutting force model parameters. The model was successfully utilized to predict how the cutting force is affected as the process parameters change.

Keywords Micro milling · Cutting force model · Nickel-based superalloy · Minimum cutting thickness · Selective laser melting

Figure 133. Published paper on international journal **[19]**.

18th CIRP Conference on Modeling of Machining Operations

Modeling of cutting force in micro-end-milling process with experimental validation on additive manufactured Nickel-based superalloy

Andrea Abeni[a]*, Dario Loda[a,b], Tuğrul Özel[b], Aldo Attanasio[a]

[a]University of Brescia, Via Branze 38, 25123 Brescia, Italy
[b]Rutgers University, Industrial & Systems Engineering, Piscataway, New Jersey, USA

* Corresponding author. Tel.: +39 030 3715584. E-mail address: andrea.abeni@unibs.it

Abstract

Nowadays aerospace, microelectronics, biotechnology industries require small sized components with complex shape and high mechanical properties, often operating in aggressive environment. In this framework, Additive Manufacturing (AM) of Nickel-based superalloys is an interesting and cost effective process. Fewer design constraints and the weight reduction achievable through the topology optimization are the most relevant AM advantages. Furthermore, micro-scale features on the additively fabricated parts can be manufactured by using micro machining. Subtractive processes ensure to achieve high-precision mechanical coupling due to better surface finishes and tighter tolerances. A lack of scientific studies focusses on the material removal behavior of difficulty-to-cut alloys produced via Additive Manufacturing is evident. This work describes a machining analytical force models which considers the presence of ploughing- and shearing- dominated cutting regimes. The undefined cutting force model parameters and the Minimum Uncut Chip Thickness (MUCT) can be identified through proper experimental tests. The refinement procedure of the model was utilized to characterize Inconel 625 samples fabricated by LaserCUSING[TM]. The cutting force data were elaborated with an iterative methodology based on a search algorithm. The model successfully predicted how the cutting force changes as a function of the process parameters.

Keywords: Analytical model; Micro machining; Inconel 625; MUCT; Cutting force

Figure 134. Published paper on conference proceedings **[21]**.

The analytical model was calibrated also on Ti6Al4V alloy samples fabricated by LB-PBF process. The experimental analysis favorites the embedding between micro milling and additive manufacturing in order to integrate their respective advantages. The analytical model was successfully calibrated by considering the cutting regime transition, a key feature of micro machining processes. The model tuning required the computation of the Minimum Uncut Chip Thickness and the calculation of the unknown parameters of the model through PSO algorithm. The model was subsequently applied to predict the cutting force measured during microchannel performed by following an experimental CCD full factorial plan. A good matching between experimental data and model prediction was finally achieved as the major research output. The results were discussed at the international conference CIRP BIOM 2022 and the abstract of the publication is visible in **Figure 135**.

Available online at www.sciencedirect.com

ScienceDirect

Procedia CIRP 110 (2022) 8–13

www.elsevier.com/locate/procedia

ELSEVIER

V CIRP Conference on Biomanufacturing

Analytical modeling of micro-milling operations on biocompatible Ti6Al4V titanium alloy

Andrea Abeni[a*], Cristian Cappellini[b], Paola Serena Ginestra[a], Aldo Attanasio[a]

[a]*University of Brescia, Department of Mechanical and Industrial Engineering, V. Branze 38, Brescia 25123, Italy*
[b]*Free University of Bolzano, Faculty of Science and Technology, Piazza Università 5, Bolzano 39100, Italy*

* Corresponding author. Tel. 030 3715712; fax: 030 3712448. *E-mail address:* andrea.abeni@unibs.it

Abstract

Among the biocompatible materials, Ti6Al4V titanium alloy is widely spread due to its properties, such as corrosion and fatigue resistance combined with low density. Ti6Al4V can be processed by Additive Manufacturing technologies, such as Power Bed Fusion (PBF). The biomedical applications require good surface finishing to ensure biocompatibility with tissues and organs. Machining is an adequate process to ensure low final roughness of components. The necessity to realize miniaturized features implicates the usage of micro mills with diameter lower than one millimeter. It implicates several issues, such as size effects, higher than expected cutting forces, rapid tool wear which can be addressed by experimental tests and process modeling. This work reports the results of micro-milling performed on additively manufactured samples in Ti6Al4V. PBF process was utilized to manufacture the samples by employing laser source (PBF-LB). The machining center was equipped with a loadcell to acquire cutting force signal. An analytical cutting force model was calibrated on the experimental data with the purpose of predicting loads on the tool by considering ploughing- and shearing- regimes. Specific machining tests were performed to calculate the Minimum Uncut Chip Thickness (MUCT) and to calibrate the unknow parameters of the model, while further tests allowed to verify the reliability of the model about the cutting force prediction. The elaboration of the cutting force data was performed by an iterative methodology based on the Particle Swarm Optimization (PSO) algorithm.

Keywords: Biomanufacturing; Ti6Al4V alloy; Micro machining.

Figure 135. Published paper on conference proceedings **[22]**.

Once the model reliability was demonstrated, the model was enhanced by considering the effects of tool run-out phenomena for the evaluation of the asymmetrical behavior of machining forces in micro-milling operations. The proposed model concerns the topology evolution of the cross-sectional area of the chip, and the optimization of dedicated cutting coefficients for ploughing and shearing contributions. The detection of these latter was achieved minimizing the difference in the comparison of experimental cutting forces, acquired during an extensive machining campaign of Ti6Al4V and the forces estimated by the analytical model, by the application of a PSO algorithm. The modeled forces result to be in good agreement with the experimental ones, underlining the reliability of the proposed methodology. In this manner, once that the tool run-out parameters and the MUCT value are known, it is possible to exploit the analytical model for predicting the micro-milling forces, avoiding the need of expensive and time-consuming experimental tests. The results were discussed at the

international conference CIRP CMMO 2022 and the abstract of the publication is visible in **Figure 136**.

Available online at www.sciencedirect.com

ScienceDirect

www.elsevier.com/locate/procedia

16th CIRP Conference on Intelligent Computation in Manufacturing Engineering, CIRP ICME '22, Italy

Modelling of micro-milling by considering tool run-out and ploughing regime

Cristian Cappellini[a*], Andrea Abeni[b], Aldo Attanasio[b]

aFaculty of Science and Technology, Free University of Bolzano, P.zza Università 5, Bolzano, 39100, Italy
bUniversity of Brescia, Department of Mechanical and Industrial Engineering, V. Branze 38, Brescia 25123, Italy

* Corresponding author. Tel.: +39-+39-0471-017114; *E-mail address:* cristian.cappellini@unibz.it

Abstract

The accuracy in micro-milling is strongly affected by the phenomena of tool run-out. The discordance between the tool edge effective and theoretical trajectories increases the tool wear and it negatively affects the quality of the machined surface. The tool run-out should be considered in machining modelling in order to accurately predict how the cutting force changes as the process parameters change. This paper describes the structure of an analytical model which computes the cutting force by considering the tool run-out and the concurrent presence of ploughing- and shearing- dominated cutting regimes. The model was finally calibrated by considering micro-machining on difficult-to-cut material.
© 2022 The Authors. Published by Elsevier B.V.
Peer-review under responsibility of the scientific committee of the 16th CIRP Conference on Intelligent Computation in Manufacturing Engineering.

Keywords: Tool run-out; Micro-milling; Analytical Model.

Figure 136. Published paper on conference proceedings.

This chapter discusses also about a novel 2D FEM setup for forecasting cutting forces when micromilling additive manufactured Inconel 625 alloys parts. The flow stress parameters of modified Johnson-Cook model of this material were optimized by means of a PSO algorithm. The derived flow stress was then implemented in 2D FEM simulations, and the resulting forces were compared with the ones calculated by an analytic model. This comparison gave good superposition, in terms of forces peaks and trends, underlining the prediction capability of the FEM methodology and furnishing a reliable tool, avoiding the needs of costly and time-consuming experimental tests. On the other hand, due to a not calibrated chip segmentation model, an overestimation of FEM loads was observed when tool is disengaging from workpiece. Therefore, to correctly represent forces in this last phase, further development of this work will be the optimization of chip breakage.

Conclusions

The PhD project output can be summarized as follow:

- A standard testing procedure useful to verify the performance of a micro-milling system (i.e., milling machine, tool, tool holder, material, and process parameters) has been assessed. It was employed to qualify the CNC Machining Center Kern Pyramid Nano in order to ensure it suitability to perform high precision micro-milling tests. A deep focus was dedicated to the load measurement system in order to assess its dynamic performances at high frequencies. A range of spindle speed was defined to avoid resonance phenomenon which have a bad impact on the performance of the load cell. The procedure can be considered reliable and suitable for checking the status of a milling machine and related measurement system, with the possibility to detect machine issues and to correct them.
- A robust procedure to test the micro-machinability was developed and applied on a wide range of AM materials. The Minimum Uncut Chip Thickness was individuated by considering how the Specific Cutting Force changes as the feed rate changes. The relation between forces and the characteristics of the AM materials is discussed by considering microstructure, building orientation and mechanical properties. Further tests were designed and performed with different purposes: the thin-walls cut were performed to collect data at different feed rate and cutting speed in order to asses analytical and numerical models; the machining of constant depth micro-slots was performed to investigate the dynamic effects, to study the final surface finishing and to collect cutting force data useful for the calibration of models.
- About PBF 17-4 PH stainless steel, the results showed a transition from shearing to ploughing at the 30-35% of the effective tool edge radius. The identification of an optimal feed per tooth range allows to reduce cutting forces and consequently the tool wear rates. The study of the surface finishing demonstrated as the highest values of roughness were measured on the surface of the channels machined at low feed rates. The dimension of the burrs followed the same trend. Therefore, a high value of the feed rate is recommended to reduce the extension of the burrs and assure a correct mechanical coupling between the micro-sizes components.
- About Inconel 625, The MUCT resulted equal to 2.5 μm. The parameter was employed in the analytical model calibration, ensuring the correct modelling of the transition behavior. The micro-slots fabrication was combined with some micromachining of thin-wall with 0° helix angle in order to perform quasi-orthogonal cutting tests. Cutting force data were collected at different cutting speed and feed rate in order to complete the calibration of the analytical model and also to perform numerical simulation.
- About Ti6Al4V, the experimental tests were performed to compare the micro-machinability of several AM samples, such as Laser Based PBF, Beam Based PBF and

wrought samples. Furthermore, the building orientation of AM process was investigated to model its effect on micro-machinability. The surface roughness of the as-received, as built and machined workpieces was measured to investigate the effects of the process parameters on the surface final finishing. It is possible to notice a ploughing dominated regime at low feed per tooth values (< 2.0 μm/tooth). This deformation mechanism is observed to be equivalent for PBF samples and mill-annealed ones with a visible difference between the specific cutting pressure during ploughing. At lower feed per tooth values the specific cutting force is higher for the PBF samples than the mill-annealed ones. In that case, the data showed a behavior transition of the material at the 40% of the effective tool edge radius. Furthermore, the statistical analysis carried out on the process parameters showed that the cutting speed has no influence on the specific cutting forces, regardless of the sample production process. Contrarily, higher cutting speeds have been found to improve the surface roughness of all the samples.

- The micro-machinability of AlSi10Mg was investigated by testing several samples in different condition and built with different orientation. If compared with Ti64, the machinability of AlSi10Mg resulted more affected by the sample fabrication process. The materials with fine microstructure exhibits SCF higher than the materials with coarse microstructure. The gravity cast sample machining was affected by BUE phenomena, which does not regard PBF micro-machining, but T6 treatment increases the micro-machinability of the cast alloy. The treatment aligns the microstructure of wrought and AM samples.

- During the PhD project, a geometrical description of the process was integrated in the structure of a micro-machining model, able to consider the concomitant presence of different cutting regimes. The model refinement procedure involves AI algorithm in order to calibrate the unknown parameters. It provided a reliable prediction of the cutting force (percentage error ranging between 0.9% and 12.4%) in a wide range of process parameters. The model was validated by calibrating it also on the data collected while machining LB-PBF Ti6Al4V with a different tool geometry and size (from Ø 0.8 mm to Ø 0.5 mm)

- A second release of the model allow to improve its reliability by considering also the tool run-out effect on trajectories and, consequently, in cutting force signal. The model prediction well fits the experimental data in several cutting condition, but the variability of the tool run-out phenomenon increase the error about prediction in some tests.

- A novel 2D FEM modeling strategy was applied to the prediction of the material behavior while micro-machining additive manufactured Inconel 625 alloys parts. The flow stress parameters of modified Johnson-Cook model of this material were optimized by means of a PSO algorithm. The derived flow stress was then implemented in 2D FEM simulations, and the resulting forces were compared with the ones calculated by an analytic model. The numerical model offers good prediction

and the flow stress law can be employed to model high speed cutting processes which involves high strain rates.

The possible development of this research involves the modeling of the process. Currently, a new approach to model tool run-out is under testing. It avoids direct measurements on the sample, with a considerable improvement of the reliability and an important time saving. Furthermore, the numerical modeling strategy will be employed to calibrate also the second part of the flow stress model, by comparing the chip morphology of the samples collected during the test. The calibrated model will allow to predict the effective segmentation of the chip as a function of the process parameters. Other information, such as residual stress, can be investigated through the FEM modeling of the process. At the same time, some experimental tests will be performed to investigate the tool wear phenomenon in micro-machining, in order to set-up a reliable numerical model able to modify the tool geometry as a function of the tool rate. The final target is develop a wide knowledge about machinability in micro-size range of materials, with a special focus on AM materials and their peculiarities.

References

[1] Dornfeld D, Mina S, Takeuchi Y (2006) Recent Advances in Mechanical Micromachining. CIRP Annals - Manufacturing Technology. 55:745–768

[2] Alting L, Kimura F, Hansen HN, Bissacco G (2003) Micro Engineering. CIRP Annals - Manufacturing Technology 52 (2): 635-657.

[3] Childs T, Maekawa K, Obikawa T, Yamane Y (2000) Metal Machining, Theory and Applications

[4] Ozturk S, Altan E (2012) Slip-Line Metal Cutting Model with Negative Rake Angle. J. Braz. Soc. Mech. Sci. & Eng. 34(3)

[5] Dhanorker A, Özel T (2008) Meso/micro scale milling for micro-manufacturing. International Journal of Mechatronics and Manufacturing Systems 1(1): 23-42.

[6] Attanasio A (2017) Tool run-out measurement in micro milling. Micromachines 8:221

[7] Davoudinejad A, Tosello G, Parenti P, Annoni M (2017) 3D finite element simulation of micro end-milling by considering the effect of tool run-out. Micromachines 8(187):1–20

[8] Kaynak Y, Tascioglu E (2018) Finishing machining-induced surface roughness, microhardness and XRD analysis of selective laser melted Inconel 718 alloy. Procedia Cirp 71:500-504

[9] Yamazaki T (2016) Development of A Hybrid Multi-tasking Machine Tool: Integration of Additive Manufacturing Technology with CNC Machining. Procedia CIRP 42:81–86

[10] Ni C, Zhu L, Zheng Z, Zhang J, Yang Y, Hong R, et al (2020) Effects of machining surface and laser beam scanning strategy on machinability of selective laser melted Ti6Al4V alloy in milling. Mater Des 194:108880.

[11] Al-Rubaie KS, Melotti S, Rabelo A, Paiva JM, Elbestawi MA, Veldhuis SC (2020) Machinability of SLM-produced Ti6Al4V titanium alloy parts. J Manuf Process 57:768–86.

[12] Hojati F, Daneshi A, Soltani B, Azarhoushang B, Biermann D (2020) Study on machinability of additively manufactured and conventional titanium alloys in micro-milling process. Precis Eng 62:1–9.

[13] Milwaki JO (2017) Additive manufacturing of metals: from fundamental technology to rocket nozzles, medical implants, and custom jewelry. Springer series in materials science. Switzerland: Springer

[14] Townsend A, Senin N, Blunt L, Leach RK, Taylor JS (2016) Surface texture metrology for metal additive manufacturing: a review. Precis Eng 46:34–47.

[15] Bhavar V, Kattire P, Patil V, Khot S, Gujar K, Singh R (2014) A review on powder bed fusion technology of metal additive manufacturing. 4th Int. Conf. Exhib. Addit. Manuf. Technol 1–2.

[16] Balázs BZ, Geier N, Takács M, Davim, JP (2021) A review on micro-milling: recent advances and future trends. The International Journal of Advanced Manufacturing Technology, 112(3), 655-684.

[17] Abeni A, Lancini M, Attanasio A (2019) Characterization of machine tools and measurement system for micromilling. Nanotechnology and Precision Engineering 2:23–28.

[18] Abeni A, Ginestra PS, Attanasio A (2021) Micro-milling of Selective Laser Melted Stainless Steel. In Selected Topics in Manufacturing; Lectures Notes in Mechanical Engineering; Springer: Cham, Switzerland 1–12.

[19] Abeni A, Loda D, Özel T, Attanasio A (2020) Analytical force modelling for micro milling additively fabricated Inconel 625. Prod.Eng 14:613–627.

[20] Abeni A, Ginestra PS, Attanasio A (2022) Comparison Between Micro Machining of Additively Manufactured and Conventionally Formed Samples of Ti6Al4V Alloy. In Selected Topics in Manufacturing; Lectures Notes in Mechanical Engineering; Springer: Cham, Switzerland 91–106.

[21] Abeni A, Loda D, Özel T, Attanasio A (2021) Modeling of cutting force in micro-end-milling process with experimental validation on additive manufactured Nickel-based superalloy. Procedia CIRP 102:222-227.

[22] Abeni A, Cappellini C, Ginestra PS, Attanasio A (2022) Analytical modeling of micro-milling operations on biocompatible Ti6Al4V titanium alloy. Procedia CIRP 110:8-13.

[23] Attanasio A, Abeni A, Özel T, Ceretti E (2019) Finite element simulation of high speed micro milling in the presence of tool run-out with experimental validations. The Int. Journal of Adv. Man. Tech. 100(1-4):25-35.

[24] Attanasio A, Ceretti E, Outeiro J, Poulachon G. (2020) Numerical simulation of tool wear in drilling Inconel 718 under flood and cryogenic cooling conditions. Wear 458:203-403.

[25] Abeni A, Cappellini C, Attanasio A (2021). Finite element simulation of tool wear in machining of nickel-chromium based superalloy. ESAFORM 2021 - 24th International Conference on Material Forming.

[26] Abeni A, Metelli A, Cappellini C, Attanasio A (2021) Experimental Optimization of Process Parameters in CuNi18Zn20 Micromachining. Micromachines 12(11):1293.

[27] Korner C (2016) Additive manufacturing of metallic components by selective electron beam melting - a review. Int Mater Rev. 61:361–77.

[28] KARndowski JJ, Seifi M (2016) Metal Additive Manufacturing: A Review of Mechanical Properties. Annual Review of Materials Research. 46:151-186.

[29] Herzog D, Seyda V, Wycisk E, Emmelmann C (2016) Additive manufacturing of metals. Acta Mater 117:371–92.

[30] Goodridge R, Ziegelmeier S (2017) Powder bed fusion of polymers. In Laser additive manufacturing 181-204.

[31] Zhang X, Liou F (2021) Introduction to additive manufacturing. In Additive Manufacturing 1-31.

[32] Halada GP, Clayton CR (2005) The intersection of design, manufacturing, and surface engineering. In Handbook of Environmental Degradation of Materials 321-344.

[33] Pontes AJ (2021) Designing for additive manufacturing. Design and Manufacturing of Plastics Products: Integrating Traditional Methods With Additive Manufacturing 249.

[34] Behera, A (2021) 3-D print battery. In Nanobatteries and Nanogenerators 11-29.

[35] Babuska TF, Krick BA, Susan DF, Kustas AB (2021) Comparison of powder bed fusion and directed energy deposition for tailoring mechanical properties of traditionally brittle alloys. Manufacturing Letters 28:30-34.

[36] Kumaran M, Senthilkumar V, Sathies T, Panicker CJ (2022) Effect of heat treatment on stainless steel 316L alloy sandwich structure fabricated using directed energy deposition and powder bed fusion. Materials Letters, 313,131766.

[37] Liu M, Kumar A, Bukkapatnam S, Kuttolamadom M (2021) A review of the anomalies in directed energy deposition (DED) Processes & Potential Solutions-part quality & defects. Procedia Manufacturing, 53:507-518.

[38] Plessis A, Yadroitsava I, Yadroitsev I (2020) Effects of defects on mechanical properties in metal additive manufacturing: A review focusing on X-ray tomography insight. Materials and Design 187, 108385.

[39] Melia MA, Duran JG, Koepke JR, et al. (2020) How build angle and post-processing impact roughness and corrosion of additively manufactured 316L stainless steel. Mater Degrad 4(21).

[40] Lou S, Jiang X, Sun W, Zeng W, Pagani L, Scott PJ (2019) Characterization methods for powder bed fusion processed surface topography Precision Engineering 57:1-15.

[41] Zhang Y, Wu L, Guo X, Kane S, Deng Y, Jung Y-G, et al. (2017) Additive manufacturing of metallic materials: a review. J Mater Eng Perform 27:1–13.

[42] Liu C, Yan D, Tan J, Mai Z, Cai Z, Dai Y, et al. (2020) Development and experimental validation of a hybrid selective laser melting and CNC milling system. Addit Manuf 36:101550.

[43] Galati M, Minetola P, Rizza G (2019) Surface roughness characterization and analysis of the electron beam melting (EBM) process. Materials 12(13):2211.

[44] Bai Y, Zhao C, Yang J, Hong R, Weng C, Wang H (2021) Microstructure and machinability of selective laser melted high-strength maraging steel with heat treatment. J Mater Process Technol 288:116906.

[45] Li J, Cui X, Hooper GJ, Lim KS, Woodfield TBF (2020) Rational design, bio-functionalization and biological performance of hybrid additive manufactured titanium implants for orthopaedic applications: A review. J. Mech. Behav. Biomed. Mater. 105, 103671.

[46] Zhao B, Wang H, Qiao N, Wang C, Hu M (2017) Corrosion resistance characteristics of a Ti-6Al-4V alloy scaffold that is fabricated by electron beam melting and selective laser melting for implantation in vivo. Mater. Sci. Eng. C. 70:832–841.

[47] Koutiri I, Pessard E, Peyre P, Amlou O, De Terris (2018) Influence of SLM process parameters on the surface finish, porosity rate and fatigue behavior of as-built Inconel 625 parts. J. Mater. Process. Technol. 255:536–546.

[48] Vaithilingam, J., Prina, E., Goodridge, R.D., Hague, R.J.M., Edmondson, S., Rose, F.R.A.J., Christie, S.D.R. Surface chemistry of Ti6Al4V components fabricated using selective laser melting for biomedical applications. Mater. Sci. Eng. C 67, 294-303 (2016).

[49] Ginestra P, Ceretti E, Lobo D, Lowther M, Cruchley S, Kuehne S, Villapun V, Cox S, Grover L, Shepherd D, Attallah M, Addison O, Webber M (2020) Post processing of 3D printed metal scaffolds: A preliminary study of antimicrobial efficiency. Procedia Manufacturing 47:1106-1112.

[50] Fousova M, Vojtˇech D, Doubrava K, Daniel M, Lin CF (2018) Influence of inherent surface and internal defects on mechanical properties of additively manufactured Ti6Al4V alloy: comparison between selective laser melting and electron beam melting. Materials 11:537.

[51] Bagehorn S, Wehr J, Maier HJ (2017) Application of mechanical surface finishing processes for roughness reduction and fatigue improvement of additively manufactured Ti-6Al-4V parts. Int J Fatigue 102:135–42.

[52] Todai M, Nakano T, Liu T, Yasuda HY, Hagihara K, Cho K, Ueda M, Takeyama M (2017) Effect of building direction on the microstructure and tensile properties of Ti-48Al-2Cr-2Nb alloy additively manufactured by electron beam melting. Additive Manufacturing 13:61-70.

[53] Ginestra P, Ferraro RM, Zohar-Hauber K, Abeni A, Giliani S, Ceretti E (2020) Selective laser melting and electron beam melting of Ti6Al4V for orthopedic applications: A comparative study on the applied building direction. Materials 13(23), 5584:1-23.

[54] Attar E. Simulation of selective electron beam melting processes (2011) Der Technischen Fakultat der Universitat Erlangen-Nurnberg zur Erlangung des Grades. PHD Thesis.

[55] Yap CY, Chua CK, Dong ZL, Liu ZH, Zhang DQ, Loh LE, et al (2015) Review of selective laser melting: materials and applications. Appl Phys Rev 2, 041101.

[56] Uçak N, Çiçek A, Aslantas K (2022) Machinability of 3D printed metallic materials fabricated by selective laser melting and electron beam melting: A review. Journal of Manufacturing Processes, 80:414-457.

[57] Matilainen VP, Piili H, Salminen A, Nyrhil¨a O (2015) Preliminary investigation of keyhole

phenomena during single layer fabrication in laser additive manufacturing of stainless steel. Phys Procedia 78:377–87.

[58] Savalani MM, Pizarro JM (2016) Effect of preheat and layer thickness on selective laser melting (SLM) of magnesium. Rapid Prototyping Journal 22(1):115–22.

[59] Yasa E, Deckers J, Kruth JP, Rombouts M, Luyten J (2010) Investigation of sectoral scanning in selective laser melting. ASME 2010 10th Bienn. Conf. Eng. Syst. Des. Anal. 4:695–703.

[60] Chlebus E, Gruber K, Kuznicka B, Kurzac J, Kurzynowski T (2015) Effect of heat treatment on the microstructure and mechanical properties of Inconel 718 processed by selective laser melting. Mater Sci Eng A 639:647–655.

[61] Spierings AB, Herres N, Levy G (2011) Influence of the particle size distribution on surface quality and mechanical properties in AM steel parts. Rapid Prototyp J 17:195–202.

[62] Sofia D, Barletta D, Poletto M (2018) Laser sintering process of ceramic powders: the effect of particle size on the mechanical properties of sintered layers. Addit Manuf 23:215–24.

[63] Murray SP, Pusch KM, Polonsky AT, Torbet CJ, Seward GGE, Zhou N, et al. (2020) A defect-resistant Co–Ni superalloy for 3D printing. Nat Commun 11:4975.

[64] Milberg J, Sigl M (2008) Electron beam sintering of metal powder. Prod Eng 2:117–22.

[65] Rafi HK, Karthik NV, Gong H, Starr TL, Stucker BE (2013) Microstructures and mechanical properties of Ti6Al4V parts fabricated by selective laser melting and electron beam melting. J Mater Eng Perform 22:3872–83.

[66] Stephenson DA, Agapiou JS (2016) Metal cutting theory and practice. third ed. Boca Raton: CRP Press, Taylor & Francis Group.

[67] Abeni A, Ceretti E, Özel T, Attanasio A (2019) FEM simulation of micromilling of CuZn37 brass considering tool run-out. Procedia CIRP 82:172-177.

[68] Kruth J, Badrossamay M, Yasa E, Deckers J, Thijs L, Van Humbeeck J (2010) Part and material properties in selective laser melting of metals. In: 16th Int Symp Electromachining 1–12.

[69] Shunmugavel M, Polishetty A, Goldberg M, Singh R, Littlefair G (2017) A comparative study of mechanical properties and machinability of wrought and additive manufactured (selective laser melting) titanium alloy - Ti-6Al-4V. Rapid Prototyp Journal 23(6):1051–6.

[70] Tebaldo V, Faga MG (2017) Influence of the heat treatment on the microstructure and machinability of titanium aluminides produced by electron beam melting. J Mater Process Technol 244:289–303.

[71] Korner C, Group F (2016) Additive manufacturing of metallic components by selective electron beam melting - a review. Int Mater Rev 61:361–77.

[72] Kasperovich G, Haubrich J, Gussone J, Requena G (2016) Correlation between porosity and processing parameters in TiAl6V4 produced by selective laser melting. Mater Des 105:160–70.

[73] Kasperovich G, Hausmann J (2015) Improvement of fatigue resistance and ductility of

TiAl6V4 processed by selective laser melting. J Mater Process Technol 220:202–14.

[74] Herzog D, Bartsch K, Bossen B (2020) Productivity optimization of laser powder bed fusion by hot isostatic pressing. Addit Manufacturing 36:101494.

[75] Cunningham R, Nicolas A, Madsen J, Fodran E, Anagnostou E, Sangid MD, et al (2017) Analyzing the effects of powder and post-processing on porosity and properties of electron beam melted Ti-6Al-4V. Mater Res Lett 5(7):516–25.

[76] Sartori S, Bordin A, Ghiotti A, Bruschi S (2016) Analysis of the surface integrity in cryogenic turning of Ti6Al4V produced by direct melting laser sintering. Procedia CIRP 45:123-6.

[77] Sartori S, Moro L, Ghiotti A, Bruschi S (2016) On the tool wear mechanisms in dry and cryogenic turning additive manufactured titanium alloys. Tribol Int 105:264-73.

[78] Martínez-Maradiaga D, Mishin OV, Engelbrecht K (2020) Thermal properties of selectively laser-melted AlSi10Mg products with different densities. J Mater Eng Perform 29:7125-30.

[79] Dang J, Cai X, Yu D, An Q, Ming W, Chen M (2020(Effect of material microstructure on tool wear behavior during machining additively manufactured Ti6Al4V. Arch Civ Mech Eng 20:4.

[80] O'Sullivan D, Cotterell M (2001(Temperature measurement in single point turning J Mater Process Technol 118(1-3):301-8.

[81] Liu C, He Y, Wang Y, Li Y, Wang S, Wang L, et al (2019) An investigation of surface topography and workpiece temperature in whirling milling machining. Int J Mech Sci 164:105182.

[82] Tan JHK, Sing SL, Yeong WY (2020) Microstructure modelling for metallic additive manufacturing: a review. Virtual Phys Prototyp 15(1):87-105.

[83] Cooke S, Ahmadi K, Willerth S, Herring R (2020) Metal additive manufacturing: technology, metallurgy and modelling. J Manuf Process 57:978-1003.

[84] Ahmadi M, Karpat Y, Acar O, Kalay YE (2018) Microstructure effects on process outputs in micro scale milling of heat treated Ti6Al4V titanium alloys. J Mater Process Technol 252:333-47.

[85] Bordin A, Bruschi S, Ghiotti A, Bucciotti F, Facchini L (2014) Comparison between wrought and EBM Ti6Al4V machinability characteristics. Key Eng Mater 611-612:1186-93.

[86] Facchini L, Magalini E, Robotti P, Molinari A (2009) Microstructure and mechanical properties of Ti-6Al-4V produced by electron beam melting of pre-alloyed powders. Rapid Prototyp J 15(3):171–8.

[87] Drstvensek I, Zupanic F, Boncina T, Brajlih T, Pal S (2021) Influence of local heat flow variations on geometrical deflections, microstructure, and tensile properties of Ti-6Al-4 V products in powder bed fusion systems. J Manuf Process 65:382–96.

[88] Gong H, Rafi K, Gu H, Janaki Ram GD, Starr T, Stucker B (2015) Influence of defects on mechanical properties of Ti-6Al-4V components produced by selective laser melting and electron beam melting. Mater Des 86:545-54.

[89] Khorasani AM, Gibson I, Awan US, Ghaderi A (2019) The effect of SLM process parameters

on density, hardness, tensile strength and surface quality of Ti-6Al-4V. Addit Manuf 25:176-86.

[90] Tucho WM, Cuvillier P, Sjolyst-Kverneland A, Hansen V (2017) Microstructure and hardness studies of Inconel 718 manufactured by selective laser melting before and after solution heat treatment. Mater Sci Eng A 689:220-32.

[91] Balachandramurthi AR, Moverare J, Dixit N, Pederson R (2018) Influence of defects and as-built surface roughness on fatigue properties of additively manufactured alloy 718. Mater Sci Eng A 735:463-74.

[92] Deng D, Peng RL, Brodin H, Moverare J (2018) Microstructure and mechanical properties of Inconel 718 produced by selective laser melting: sample orientation dependence and effects of post heat treatments. Mater Sci Eng A 713:294–306.

[93] Bruno J, Rochman A, Cassar G (2017) Effect of build orientation of electron beam melting on microstructure and mechanical properties of Ti-6Al-4V. J Mater Eng Perform 26:692-703.

[94] Zhou L, Mehta A, Schulz E, McWilliams B, Cho K, Sohn Y (2018) Microstructure, precipitates and hardness of selectively laser melted AlSi10Mg alloy before and after heat treatment. Mater Charact 143:5–17.

[95] Li H, Ramezani M, Li M, Ma C, Wang J (2018) Tribological performance of selective laser melted 316L stainless steel. Tribol Int 128:121–9.

[96] Salonitis K, D'Alvise L, Schoinochoritis B, Chantzis D (2016) Additive manufacturing and post-processing simulation: laser cladding followed by high speed machining. Int J Adv Manuf Technol 85:2401-11.

[97] Lu Y, Wu S, Gan Y, Huang T, Yang C, Junjie L, et al (2015) Study on the microstructure, mechanical property and residual stress of SLM Inconel-718 alloy manufactured by differing island scanning strategy. Opt Laser Technol 75:197-206.

[98] Prashanth KG, Scudino S, Eckert J (2017) Defining the tensile properties of Al-12Si parts produced by selective laser melting. Acta Mater 126:25-35.

[99] Attar H, Calin M, Zhang LCC, Scudino S, Eckert J (2014) Manufacture by selective laser melting and mechanical behavior of commercially pure titanium. Mater Sci Eng A 593:170–7.

[100] Qiu C, Adkins NJE, Attallah MM (2013) Microstructure and tensile properties of selectively laser-melted and of HIPed laser-melted Ti-6Al-4V. Mater Sci Eng A 578:230-9.

[101] Bourell D, Kruth JP, Leu M, Levy G, Rosen D, Beese AM, et al (2017) Materials for additive manufacturing. CIRP Ann 66:659-81.

[102] Lizzul L, Sorgato M, Bertolini R, Ghiotti A, Bruschi S (2020) Influence of additive manufacturing-induced anisotropy on tool wear in end milling of Ti6Al4V. Tribol Int 146:106200.

[103] Segebade E, Gerstenmeyer M, Dietrich S, Zanger F, Schulze V (2019) Influence of anisotropy of additively manufactured AlSi10Mg parts on chip formation during orthogonal cutting. Procedia CIRP 82:113–8.

[104] Hrabe N, Quinn T (2013) Effects of processing on microstructure and mechanical properties of a titanium alloy (Ti–6Al–4V) fabricated using electron beam melting (EBM), part 2: energy input, orientation, and location. Mater Sci Eng A 573:271-7.

[105] Formanoir C, Michotte S, Rigo O, Germain L, Godet S (2016) Electron beam melted Ti–6Al–4V: microstructure, texture and mechanical behavior of the as-built and heat-treated material. Mater Sci Eng A 652:105–19.

[106] Simonelli M, Tse YY, Tuck C (2014) Effect of the build orientation on the mechanical properties and fracture modes of SLM Ti–6Al–4V. Mater Sci Eng A 616:1–11.

[107] Wang C, Tan X, Liu E, Tor SB (2018) Process parameter optimization and mechanical properties for additively manufactured stainless steel 316L parts by selective electron beam melting. Mater Des 147:157-66.

[108] Zhao X, Li S, Zhang M, Liu Y, Sercombe TB, Wang S, et al (2016) Comparison of the microstructures and mechanical properties of Ti–6Al–4V fabricated by selective laser melting and electron beam melting. Mater Des 95:21-31.

[109] Ming W, Chen J, An Q, Chen M (2019) Dynamic mechanical properties and machinability characteristics of selective laser melted and forged Ti6Al4V. J Mater Process Technol 271:284-92.

[110] Zhao Y, Sun J, Li J, Yan Y, Wang P (2017) A comparative study on Johnson-Cook and modified Johnson-Cook constitutive material model to predict the dynamic behavior laser additive manufacturing FeCr alloy. J Alloys Compd 723:179-87.

[111] Alaghmandfard R, Dharmendra C, Odeshi AG, Mohammadi M (2020) Dynamic mechanical properties and failure characteristics of electron beam melted Ti-6Al-4V under high strain rate impact loadings. Mater Sci Eng A 793:139794.

[112] Maconachie T, Leary M, Zhang J, Medvedev A, Sarker A, Ruan D, et al (2020) Effect of build orientation on the quasi-static and dynamic response of SLM AlSi10Mg. Mater Sci Eng 788:139445.

[113] Alaghmandfard R, Chalasani D, Hadadzadeh A, Amirkhiz BS, Odeshi A, Mohammadi M (2020) Dynamic compressive response of electron beam melted Ti–6Al–4V under elevated strain rates: microstructure and constitutive models. Addit Manuf 35:101347.

[114] Pang Z, Liu Y, Li M, Zhu C, Li S, Wang Y, et al (2019) Influence of process parameter and strain rate on the dynamic compressive properties of selective laser-melted Ti-6Al-4V alloy. Appl Phys A 125:90.

[115] Liu Y, Xu H, Zhu L, Wang X, Han Q, Li S, et al (2021) Investigation into the microstructure and dynamic compressive properties of selective laser melted Ti–6Al–4V alloy with different heating treatments. Mater Sci Eng A 805:140561.

[116] Xiao L, Song W, Hu M, Li P (2019) Compressive properties and micro-structural characteristics of Ti–6Al–4V fabricated by electron beam melting and selective laser melting. Mater Sci Eng A 764:138204.

[117] Geiger M, Kleiner M, Eckstein R, Tiesler N, Engel U (2001) Microforming. CIRP Annals - Manufacturing Technology 50(2):445-462.

[118] Masuzawa T (2000) State of the Art of Micromachining. CIRP Annals Manufacturing Technology 49(2):473-488.

[119] Darwish S, Ahmed N, Alahmari AM (2016) A comparison of laser beam machining of micro-channels under dry and wet mediums. Int. J. Adv. Manuf. Technol. 83(9-12):1539-1555.

[120] Egashira K, Masuzawa T (1999) Microultrasonic Machining by the Application of Workpiece Vibration. CIRP Annals - Manufacturing Technology 48(1):131-134.

[121] Bissacco G, Hansen HN, Slunsky J (2008) Modelling the cutting-edge radius size effect for force prediction in micro milling. CIRP Ann. Manuf. Technol 57:113–116.

[122] Bissacco G, Hansen H N, De Chiffre L (2006) Size Effects on Surface Generation in Micro Milling of Hardened Tool Steel. CIRP Annals - Manufacturing Technology 55(1):593-596.

[123] Cheng K, Huo D (2013) Micro-cutting: fundamentals and applications. West Sussex: John Wiley & Sons.

[124] Liu X, DeVor RE and Kapoor S G (2005) An Analytical Model for the Prediction of Minimum Chip Thickness in Micromachining. Jour. Manuf. Sci. Eng 128(2): 474-481.

[125] Egashira K, Hosono S, Takemoto S (2011) Fabrication and cutting performance of cemented tungsten carbide micro-cutting tools. Precision Engineering 34(4):547-553.

[126] Le Coz G, Piquard R, D'Acunto A, Bouscaud D, Fischer M, Laheurte P (2020) Precision turning analysis of Ti-6Al-4V skin produced by selective laser melting using a design of experiment approach. Int J Adv Manuf Technol 110:1615–25.

[127] Khaliq W, Zhang C, Jamil M, Khan AM (2020) Tool wear, surface quality, and residual stresses analysis of micro-machined additive manufactured Ti–6Al–4V under dry and MQL conditions. Tribol Int:106408.

[128] Varghese V, Mujumdar S (2021) Micromilling-induced surface integrity of porous additive manufactured Ti6Al4V alloy. Procedia Manuf 53:387–94.

[129] Ji H, Gupta MK, Song Q, Cai W, Zheng T, Zhao Y, et al (2021) Microstructure and machinability evaluation in micro milling of selective laser melted Inconel 718 alloy. J Mater Res Technol 14:348–62.

[130] Allegri G, Colpani A, Ginestra PS, Attanasio A (2019) An experimental study on micromilling of a medical grade Co-Cr-Mo alloy produced by selective laser melting. Materials 12:2208

[131] Bruschi S, Tristo G, Rysava Z, Bariani PF, Umbrello D, De Chiffre L (2016) Environmentally clean micromilling of electron beam melted Ti6Al4V. J Clean Prod 2016;133:932–41.

[132] Le Coz G, Fischer M, Piquard R, D'Acunto A, Laheurte P, Dudzinski D (2017) Micro cutting of Ti-6Al-4V parts produced by SLM process. Procedia CIRP 58:228–32.

[133] Rysava Z, Bruschi S (2016) Comparison between EBM and DMLS Ti6Al4V machinability characteristics under dry micro-milling conditions. Mater Sci Forum 836–37:177–84.

[134] Oliveira Campos F, Araujo AC, Jardini Munhoz AL, Kapoor SG (2020) The influence of additive manufacturing on the micromilling machinability of Ti6Al4V: a comparison of SLM and commercial workpieces. J Manuf Process 2020;60:299–307.

[135] Assis CLF, Mecelis GR, Coelho RT 2020 An investigation of stainless steel 316L parts produced by powder bed fusion submitted to micro-end milling operations. Int JAdv Manuf Technol 109:1867–80.

[136] Ni C, Zhu L, Zheng Z, Zhang J, Yang Y, Yang J, et al (2020) Effect of material anisotropy on ultra-precision machining of Ti-6Al-4V alloy fabricated by selective laser melting. J Alloys Compd 848:156457.

[137] Bai Y, Zhao C, Zhang Y, Chen J, Wang H (2021) Additively manufactured CuCrZr alloy: microstructure, mechanical properties and machinability. Mater Sci Eng A 819:141528.

[138] Sadiq MA, Hoang NM, Valencia N, Obeidat S, Hung WNP (2018) Experimental study of micromilling selective laser melted Inconel 718 superalloy. Procedia Manuf. 26:983–92.

[139] Rysava Z, Bruschi S, Piska M, Zidek J (2018) Comparing the performance of micro-end mills when micro-milling of additive manufactured Ti-6Al-4V titanium alloy. MM Sci J 2018:2543–6.

[140] Özel T, Olleak A, Thepsonthi T (2017) Micro milling of titanium alloy Ti-6Al-4V: 3-D finite element modeling for prediction of chip flow and burr formation. Prod. Eng. 11(4–5):435–444.

[141] Dornfeld D, Min S, Takeuchi Y (2006) Recent Advances in Mechanical Micromachining. CIRP Annals - Manufacturing Technology 55 (2):745-768.

[142] Srinivasa YV, Shunmugam MS (2013) Mechanistic model for prediction of cutting forces in micro end-milling and experimental comparison. International Journal of Machine Tools & Manufacture 67:18–27.

[143] Attanasio A, Garbellini A, Ceretti E, Giardini C (2015) Force modelling in micromilling of channels. Int J Nano manuf 11(5–6):275–296.

[144] Moges TM, Desai KA, Rao PVM (2018) Modeling of cutting force, tool deflection, and surface error in micro-milling operation. The International Journal of Advanced Manufacturing Technology 98(9-12):2865-2881.

[145] Martellotti M (1941) An analysis of milling process, ASME J.Manuf. Sci. Eng. 63:677–700.

[146] Bao W (2000) Modeling micro-end-milling operations. Part I:analytical cutting force model, Int. J. Mach. Tools Manuf. 40:2155–2173.

[147] Bao W, Tansel IN (2000) Modeling micro end milling operations. Part II: tool run-out, Int. J. Mach. Tools Manuf 40:2175–2192.

[148] Gelfi M, Attanasio A, Ceretti E, Garbellini A, Pola A (2015) Micromilling of lamellar Ti6Al4V: cutting force analysis. Mater Manuf Process 31(7):919–925.

[149] Liu K, Li XP, Rahman M (2003) Characteristics of high speed micro-cutting of tungsten carbide, J. Mater. Process. Technol. 140:352–357.

[150] Son SM, Lim HS, Ahn JH (2005) Effects of the friction coefficient on the minimum cutting thickness in micro cutting, Int. J. Mach. Tools Manuf. 45:529–535.

[151] Fang N (2003) Slip-line modeling of machining with a rounded edge tool—part I: new model and theory, J. Mech. Phys. Solids 51:715–742.

[152] Fang N, Jawahir IS (2002) An analytical predictive model and experimental validation for machining with grooved tools incorporating the effects of strains, strain-rates, and temperatures, CIRP Ann. Manuf. Technol. 51:83–86.

[153] Vogler MP, Kapoor SG, DeVor RE (2004) On the modeling and analysis of machining performance in micro end milling, part II: cutting force prediction. ASME Journal of Manufacturing Science and Engineering 126(4):695–705.

[154] Jin X, Altintas Y (2012) Prediction of micro-milling forces with finite element method, J. Mater. Process. Technol. 212:542–552.

[155] Rodríguez P, Labarga JE (2013) A new model for the prediction of cutting forces in micro-end-milling operations. Journal of Materials Processing Technology 213:261–268.

[156] Malekian M, Park SS, Jun MBG (2009) Modelling of dynamic micro-milling cutting forces. Int. J. Mach. Tools Manuf. 49(7-8):586-598.

[157] Chen W, Teng X, Huo D, Wang Q (2017) An improved cutting force model for micro milling considering machining dynamics. International Journal of Advanced Manufacturing Technology 93(9-12):3005-3016.

[158] Zhang X, Yu T, Wang W (2018) Dynamic cutting force prediction for micro end milling considering tool vibrations and run-out. Proceedings of the Institution of Mechanical Engineers, Part C: Journal of Mechanical Engineering Science 0 (0):1-14.

[159] Thepsonthi T, Özel T (2015) 3-D finite element process simulation of micro-end milling Ti-6Al-4V titanium alloy: experimental validations on Chip flow and tool Wear. J Mater Process Tech. 221:128–145

[160] Johnson GR, Cook WH (1983) A constitutive model and data for metals subjected to large strains, high strain rates and high temperatures. Proceedings 7th International Symposium on Ballistics: 541-547

[161] Holmquisti TJ, Johnson GR (1991) Determination of constant and comparison of results for various constitutive models. Int. Conf. on Mech. and Ph. Behavior of Mat. 1(3): 853-860.

[162] Rule WK, Jones SE (1998) A revised form for the Johnson-Cook strength model. International Journal of Impact Engineering. 21(8): 609-624.

[163] Wu HY, Lee WB, Cheung CF, S. To, Chen YP (2005) Computer simulation of single-point diamond turning using finite element method. J Mater Process Technol 167:549–554.

[164] Ee KC, Dillon Jr OW, Jawahir IS (2005) Finite element modeling of residual stresses in machining induced by cutting using a tool with finite edge radius. Int J Mech Sci 47:1611–1628.

[165] Strenkowski JS, Carroll JT (1985) A finite element model of orthogonal metal cutting. J Eng Ind 107:349–354.

[166] Guo YB, Liu CR (2002) FEM analysis of mechanical state on sequentially machined surfaces. Mach Sci Technol 6:21–41

[167] Calamaz M, Coupard D, Girot F (2008) A new material model for 2D numerical simulation of serrated chip formation when machining titanium alloy Ti-6Al-4V. Int J Mach Tools Manuf 48:275–288.

[168] Sima M, Ozel T (2010) Modified material constitutive models for serrated chip formation simulations and experimental validation in machining of titanium alloy Ti-6Al-4V. Int J Mach Tools Manuf 50:943–960 58.

[169] Calamaz M, Coupard D, Girot F (2010) Numerical simulation of titanium alloy dry machining with a strain softening constitutive law. Mach Sci Technol 14:244–257 59.

[170] Calamaz M, Coupard D, Nouari M, Girot F (2011) Numerical analysis of chip formation and shear localization processes in machining the Ti-6Al-4V titanium alloy. Int J Adv Manuf Technol 52:887–895.

[171] Ducobu F, Rivière-Lorphèvre E, Filippi E (2014) Numerical contribution to the comprehension of saw-toothed Ti6Al4V chip formation in orthogonal cutting. Int J Mech Sci 81:77–87.

[172] Özel T, Altan T (2000) Process simulation using finite element method—prediction of cutting forces, tool stresses and temperatures in high-speed flat end milling. International Journal of Machine Tools and Manufacture 40(5):713-738.

[173] Umbrello D (2008) Finite element simulation of conventional and high speed machining of Ti6Al4V alloy. Journal of materials processing technology 196(1-3):79-87.

[174] Afazov SM, Ratchev SM, Segal J (2010). Modelling and simulation of micro-milling cutting forces. Journal of Materials Processing Technology, 210(15):2154-2162.

[175] Jomaa W, Daoud M, Songmene V, Bocher P, Châtelain JF (2014) Identification and validation of Marusich's constitutive law for finite element modeling of high speed, In:

Proceedings of the ASME 2014 International Mechanical Engineering Congress and Exposition IMECE2014, Montreal, QC, Canada, November 14-20

[176] Menezes PL, Avdeev IV, Lovell MR, Higgs CF III (2014) An explicit finite element model to study the influence of rake angle and friction during orthogonal metal cutting. Int J Adv Manuf Technol 73:875–885.

[177] Ucun I, Aslantas K, Bedir F (2016) Finite element modeling of micro-milling: numerical simulation and experimental validation. Mach Sci Technol. 20(1):148–172.

[178] Shi Z, Li Y, Liu Z, Qiao Z (2018) Determination of minimum uncut chip thickness during micro-end milling Inconel 718 with acoustic emission signals and FEM simulation. The International Journal of Advanced Manufacturing Technology 98(1–4):37–45.

[179] Zhou Y, Sun H, Li A, Lv M., Xue C, Zhao J (2019) FEM simulation-based cutting parameters optimization in machining aluminum-silicon piston alloy ZL109 with PCD tool. Journal of Mechanical Science and Technology 33(7):3457-3465.

[180] Sahoo P, Patra K, Szalay T, Dyakonov AA (2020) Determination of minimum uncut chip thickness and size effects in micro-milling of P-20 die steel using surface quality and process signal parameters. The International Journal of Advanced Manufacturing Technology 106(11):4675-4691.

[181] Shi Y, Von Wagner U, Mahr F, et al (2009) Influence of themachine structure on micromilling process. PAMM 9(1):701-2.

[182] Park SS, Malekian M (2009) Mechanistic modeling and accurate measurement of micro end milling forces. CIRP Annals Manufacturing Technology. 58(1):49-52.

[183] Garbellini A, Lancini M, Attanasio A et al (2015) Testing procedure for evaluating the performance of a micro-milling process. Proceedings of the 8th International Conference on Leading Edge Manufacturing in 21st Century.

[184] Smith DA, Smith S, and Tlusty J (1998) High Performance Milling Torque Sensor. ASME Journal of Manufacturing Science 120(3):504-510.

[185] Park SS, Altintas Y (2004) Dynamic Compensation of Spindle Integrated Force Sensors with Kalman Filter. J. Dyn. Sys., Meas., Control 126(3):443-452.

[186] Lee SW, Mayor R, Ni J (2006) Dynamic analysis of a mesoscale machine tool. J Manuf Sci Eng 128(1):194-203.

[187] Kalinski KJ, Galewski MA (2011) Chatter vibration surveillance by the optimal-linear spindle speed control. Mech Syst Signal Process 25(1):369-383.

[188] Ozasahin O, Altintas Y (2005) Prediction of frequency response function (FRF) of asymmetric tools from the analytical coupling of spindle and beam models of holder and tool. Int. J. Machine Tools & Manufacture 92:31-40.

[189] Gagnol V, Le T, Ray P (2011) Modal identification of spindle-tool unit in high-speed machining. Mech. Syst. Sig. Proc. 25(7):2388-2398.

[190] Zaghbani I, Songmene V (2009) Estimation of machine-tool dynamic parameters during machining operation through operational modal analysis. Int. J. Mach. Tools & Manuf. 49(12-13):947-957.

[191] Fotsch D, Ewins D J (2002) Application of MAC in the frequency domain. Proceedings of the International Modal Analysis Conference 2:1225-1231.

[192] Chrzanowski W, Neel EAA, Armitage DA, Knowles JC (2008) Effect of surface treatment on the bioactivity of nickel-titanium. Acta Biomaterialia 4(6):1969-1984.

[193] Trosch T, Strößner J, Völkl R, Glatzel U (2016) Microstructure and mechanical properties of selective laser melted Inconel 718 compared to forging and casting. Materials Letters, 164(1):428-431.

[194] Sharman ARC, Hughes JI, Ridgway K (2006) Workpiece Surface Integrity and Tool Life Issues When Turning Inconel 718 Nickel Based Superalloy. Machining Science and Technology 8(3):399-414.

[195] Patel K, Fei J, Liu G, Özel T (2019) Milling investigations and yield strength calculations for nickel alloy Inconel 625 manufactured with laser powder bed fusion process. Production Engineering. 13(6):693–702.

[196] Shankar V, Bhanu Sankara Rao K, Mannan SL (2001) Microstructure and mechanical properties of Inconel 625 superalloy. Journal of Nuclear Materials 288:222-232.

[197] Lai X, Li H, Li C, Lin Z, Ni J (2008) Modelling and analysis of micro scale milling considering size effect, micro cutter edge radius and minimum chip thickness. International Journal of Machine Tools and Manufacture. 48(1):1-14.

[198] Wang H, Zhao B, Liu C, Wang C, Tan X, Hu M (2016) A comparison of biocompatibility of a titanium alloy fabricated by electron beam melting and selective laser melting PLoS ONE 11(7):0158513.

[199] Koike M, Greer P, Owen K, Lilly G, Murr LE, Gaytan SM, Martinez E, Okabe T (2011) Evaluation of titanium alloys fabricated using rapid prototyping technologies-electron beam melting and laser beam melting. Materials 4(10):1776-1792.

[200] Riviere-Lorphevre E, Letot C, Ducobu F, Dehombreux P, Filippi E (2017) Dynamic simulation of milling operations with small diameter milling cutters: effect of material heterogeneity on the cutting force model. Meccanica 52:35–44.

[201] Gelfi M, Attanasio A, Ceretti E, Garbellini A, Pola A (2015) Micromilling of lamellar Ti6Al4V: cutting force analysis. Mater Manuf Process 31(7):919–925.

[202] Eberhart R, Kennedy J (1995) A new optimizer using particle swarm theory. Proceedings of the Sixth International Symposium on IEEE 1995:39-43.

[203] Raja SB, Baskar N (2011) Particle swarm optimization technique for determining optimal machining parameters of different work piece materials in turning operation. The International Journal of Advanced Manufacturing Technology 54(5-8):445-463.

[204] Ciurana J, Arias G, Özel T (2009) Neural network modeling and particle swarm optimization (PSO) of process parameters in pulsed laser micromachining of hardened AISI H13 steel. Materials and Manufacturing Processes 24(3):358-368.

[205] Wang Z, Denlinger E, Michaleris P, Stoica AD, Ma D, Beese AM (2017) Residual stress mapping in Inconel 625 fabricated through additive manufacturing: Method for neutron diffraction measurements to validate thermomechanical model predictions. Mater Des 113:169-177.

[206] Hokka M, Leemet T, Shrot A, Bäker M, Kuokkala VT (2016) Modelling of the dynamics behaviour of hard-to-machine alloys. EPJ Conf; 226:04009.

[207] Arrazola PJ, Kortabarria A, Madariaga A, Esnaola JA, Fernandez E, Cappellini C, Ulutan D, Özel T (2014) On the machining induced residual stresses in IN718 nickel-based alloy: experiments and predictions with finite element simulation. Simul Model Pract Theory 41:87-103.

[208] Melkote SN, Grzesik W, Outeiro J, Rech J, Schulze V, Attia A, Arrazola PJ, M'Saoubi R, Saldana C (2017) Advances in material and friction data for modelling of metal machining. CIRP Ann Manuf Technol 66:731-754.

[209] Farahani HK, Ketabchi M, Zangeneh S (2017) Determination of Johnson-Cook plasticity model parameters for Inconel718. J Mat Eng Perf 26(11):5284-5293.

Appendix A - Extra activities

In this final appendix of the PhD thesis will be presented three publications about machining but not inherent with micro-machinability of AM parts. The first publication regards a 3D-FEM model of micro-milling of lead-free brass alloy. The model considers also the tool run-out effect on the tool edge trajectories. It allowed to predict cutting forces, burr formation, stress and temperature distribution.

The second publication is a conference proceeding. It deals with the FE modeling of drilling process. An innovative code was developed to update the tool geometry by considering how the tool wear phenomena induces its modification. The worn tool was utilized to simulate drilling in order to register how torque and force in axial direction changes due to tool wear.

The last publication regards an industrial case history. Micro-machinability of CuNi18Zn20 was deeply investigated by performing experimental tests in a wide range of process parameters. A samples was designed in order to model some microfeatures commonly employed in horology industrial field. The machining of these features with different parameters offers an interesting perspective about the windows of machinability of the alloy.

CrossMark

Finite element simulation of high speed micro milling in the presence of tool run-out with experimental validations

Aldo Attanasio[1] · Andrea Abeni[1] · Tuğrul Özel[2] · Elisabetta Ceretti[1]

Abstract
Micro milling process of CuZn37 brass is considered important due to applications in tool production for micro moulding and micro replication technology. The variations in material properties, work material adhesion to tool surfaces, burr formation, and tool wear result in loss of productivity. The deformed chip shapes together with localized temperature, plastic strain, and cutting forces during micro milling process can be predicted using finite element (FE) modeling and simulation. However, tool-workpiece engagement suffers from tool run-out affecting process performance in surface generation. This work provides experimental investigations on effects of tool run-out as well as process insight obtained from simulation of chip flow, with and without considering tool run-out. Scanning electron microscope (SEM) observation of the 3D chip shapes demonstrates ductile deformed surfaces together with localized serration behavior. FE simulations are utilized to investigate the effects of micro milling operation, cutting speed, and feed rate on forces, chip flow, and shapes. Predicted cutting forces and chip flow results from simulations are compared with force measurements, tool run-out, and chip morphology revealing reasonable agreements.

1 Introduction

The demand for miniaturized end-products has been continuously increasing in biomedical, automotive, aerospace, and electronics industries [1]. Among different processes commonly used to produce these products, micro turning and micro milling provide high flexibility, high accuracy, and economic efficiency due to high material removal rates, low set-up costs, and low material waste [2–4]. Micro milling is among the most versatile machining processes that allow wide spread of miniature components possessing micrometric dimensions. The most successful application of this technology is certainly in the dies and moulds industry for fabrication of tooling to be used in micro moulding and micro replication processes, due to viability of high accuracy geometric

dimensions and superior surface finishes at a rather low production cost.

On the other hand, as in macro scale processes [5], the performance of micro milling is affected by a large number of factors and technical issues. In the recent decades, a large number of publications are dedicated to understand micro milling processes. These are mainly concerned with miniature machine tool development, process modeling to achieve a greater understanding about cutting force generation and mechanistic modeling [6–9], chatter vibrations [10], workpiece defects and surface quality, tool edge effects [11], tool run-out effects [12, 13], thermal stability [14], and many other issues. Last several years, researchers also dealt with the possibility of implementing predictive process models with finite element (FE) simulations [13, 15–18], a useful capability to refine the knowledge about force generation and chip formation in micro milling.

In micro milling, tool diameters are typically smaller than 1 mm, tool edge roundness is about a few micrometres, and the chip thickness has the same order of magnitude with edge roundness [19]. At this length scale, ploughing, size effect, burr formation, rapid tool wear, higher than expected cutting forces, and tool run-out cannot be neglected being the most common micro milling related issues [3, 20–22].

✉ Aldo Attanasio
aldo.attanasio@unibs.it

1 Department of Mechanical and Industrial Engineering, University of Brescia, V. Branze 38, 25123 Brescia, Italy

2 Industrial and Systems Engineering, Rutgers University, Piscataway, NJ, USA

Springer

Among all of these issues in micro milling process, tool run-out is certainly the most important issue causing geometrical inaccuracies, workpiece defects, and burr formation and deserves more attention [12, 13, 20, 21, 23]. This phenomenon occurs due to the sum of the geometrical displacements of the tool axis, the spindle axis, and the tool-holder axis from the ideal axis of rotation [12]. The ratio between this offset and the feed per tooth could be easily high in high speed micro milling (typically rotational speeds that are higher than 10,000 rev/min and up to 100,000 rev/min). The deviation of the tool edge trajectories involves an asymmetric cutting condition. A change of undeformed chip thickness, a load imbalance between the flutes, a decrease of the tool life, and a reduction in workpiece quality are the main consequences of tool run-out.

The development of a good model for describing cutting operation on a micro scale is essential to understand how all process variables influence the final product quality. In fact, the traditional experimental approach runs into several difficulties at this scale. Measuring tool temperature and tool wear, evaluating chip morphology, and determining the cutting force values are challenging tasks. Finite element (FE) simulations can be applied to predict these process variables reasonably well, to analyze the generated surfaces and to optimize the machining parameters.

The main objective of this research was to develop and validate a FE model for simulating micro milling process of lead free brass due to the lack of publications available on this relevant topic. Secondly, the aims were to develop a new procedure to define tool run-out parameters based on experimental testing, Kronenberg cutting force model [24], and to develop FE simulation of micro milling in the presence of tool run-out.

To reach the pursued objectives, experimental tests consisting of micro milling operations under orthogonal conditions were performed. Orthogonal milling configuration was obtained by cutting a thin wall brass structure with an end mill with a helix angle equal to zero (Fig. 1). In this configuration, the total force can be represented in a plane (2D cutting) by two components (i.e., thrust and cutting force components or Fx and Fy components in an XY coordinate system). Moreover, a complete 3D FE model for orthogonal milling was presented. Material behavior in high deformation rate, hardening, and thermal softening is considered even though the thermal softening could be neglected due to the low temperature involved during the micro cutting operation. Cutting forces and chip morphology obtained from FE simulations were compared with experimental results for model validation. Micro milling tests were properly designed to obtain an orthogonal cutting configuration and to allow the comparison with FE simulation predictions. It should be noted that the force measurement system has been tested for accuracy on the load cell to ensure its validity for the desired bandwidth [23].
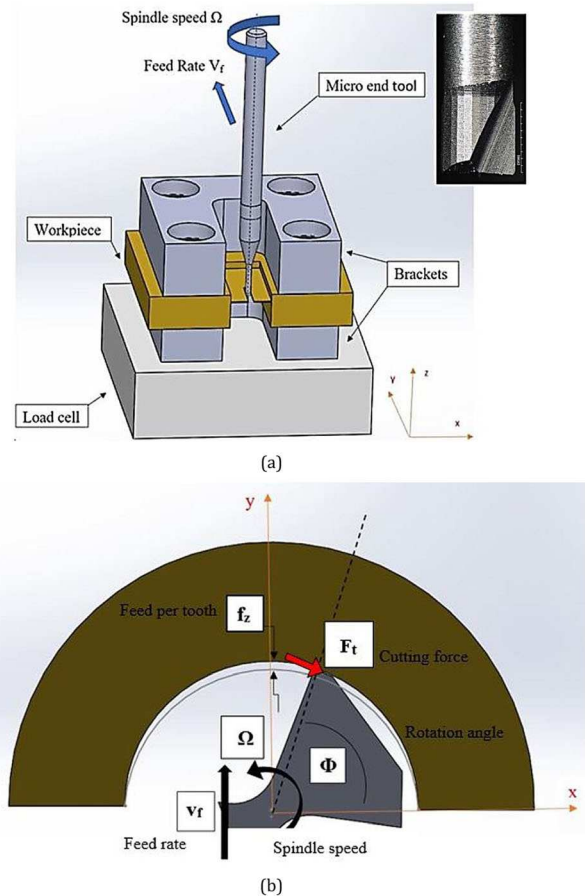

Fig. 1 **a** Orthogonal milling process in 3D configuration. **b** 2D configuration of cutting with a zero helix angle micro end mill

2 Experimental approach

Full immersion micro milling of brass (CuZn37) was performed by using the nano-precision 5-axis machining center Kern Pyramid Nano (± 0.3 μm precision). The experimental setup together with tool and workpiece geometries, positioning, and movements is illustrated in Fig. 1. A prismatic workpiece (30 mm × 26 mm × 5 mm) was blocked between two aluminum brackets and fixed on a three-component load cell (Kistler 9317C) with four bolts. Two machining operations were executed: (i) roughing to prepare a thin wall on the workpiece and (ii) orthogonal milling of the thin walled workpiece. After roughing, the workpiece was heat-treated for stress relief. FE simulations were only concerned with the second operation. A workpiece with 144 μm ± 6 μm thin wall was obtained by using four-flute and 6-mm diameter end mills. Two-flute micro end mills with a rake angle of $\gamma = 0°$ and a helix angle of $\beta = 0°$ from SECO company (103L008R005-MEGA-64-T) were used to cut the thin wall without engaging the tool bottom under dry cutting conditions. The tool material was tungsten carbide (WC/Co) with (Ti,Al)N coating. Tool geometrical details were measured using 3D digital optical microscope Hirox RH-2000

(measurement accuracy of 0.8 μm). The tool diameter was measured as $\varnothing = 782$ μm ± 4 μm and tool edge radius was measured as $r_\beta = 4.7$ μm ± 0.4 μm. Only the side cutting edge of the tool was engaged with the workpiece. The cutting conditions allowed this machining process to be considered approximately as orthogonal cutting.

Different cutting speeds were used with the aim of investigating their influence on tool run-out and cutting force values. A new tool was used for each test to avoid tool wear effects. Tool advance per rotation in x-direction was kept equal to 10 μm/tooth. The process parameters are summarized in Table 1. During machining, some chip samples were collected and then investigated using a scanning electron microscope (SEM).

A force measurement and data acquisition system that consists of a piezoelectric 3-component force sensor (Kistler 9317C) connected to charge amplifiers (Kistler 5015A) which receives three charge signals proportional to the cutting force as input and returns amplified voltage signals as output was used. This force measuring system accuracy is approximately equal to 0.1 N [12] which is sufficient for capturing forces in micro milling.

In micro milling processes, force signals oscillate of a few Newtons in few milliseconds to overcome the very small feed rate so to maintain adequate productivity [23]. High sampling rates are necessary to avoid aliasing distortions. In this work, the maximum tooth passing frequency was 1 kHz (as indicated in Table 1) and the sampling rate was fixed at 50 kHz. It is a good trade-off between acceptable data size and acquisition quality. Furthermore, a limited bandwidth could distort the force signals, as discussed in references [20, 21, 23]. When tooth passing frequencies overlap the load cell natural frequencies, the ideal condition of unity gain and low phase delay is not guaranteed. The modal parameters of the clamping system (load cell fixed on machining center, workpiece, and brackets) were detected using impact testing by measuring the output forces in each direction. Firstly, only the load cell was hit three times in order to validate the

Table 1 Micro milling process parameters

Cutting parameters	Test 1	Test 2	Test 3
Cutting speed, v_c [m/min]	50	62.5	75
Tooth passing frequency [Hz]	664	848	1000
Axial depth of cut, a_p [μm]	139	150	143

procedure. The natural frequency was experimentally determined (average values Fx 5156 Hz, Fy 4991 Hz) and compared with the value declared by Kistler (5000 Hz), finding a good matching.

In Fig. 2a, the frequency response function (FRF) shows the peak around the natural frequency of the load cell. Subsequently, the entire system was tested with the same methodology. The frequency response of the force sensing system is influenced by the stiffness and the mass of each component. The measured natural frequencies of the clamping system decrease from 5000 Hz (i.e., the natural frequency of the load cell) to 2145 Hz for x- and 2192 Hz for y-directions (Fig. 2b). A smaller bandwidth is the result of the dominant mode decrease, but it remains larger than maximum tooth passing frequency of 1 kHz.

Figure 3 reports the measured cutting forces for each cutting condition. Lower and upper bounds of experimental charts are built with a confidence level equal to 68%. The high scattering of cutting force of test 3 together with the higher values with respect to test 1 and test 2 can be related to the experimental set-up. The thin-wall cut with a higher cutting speed undergoes to greater vibrations which strongly affect the force measurements.

3 Finite element model

In literature, there are several 2D and 3D finite element simulation models reported for the micro milling process. A majority of the 3D FE simulation work considers workpiece as
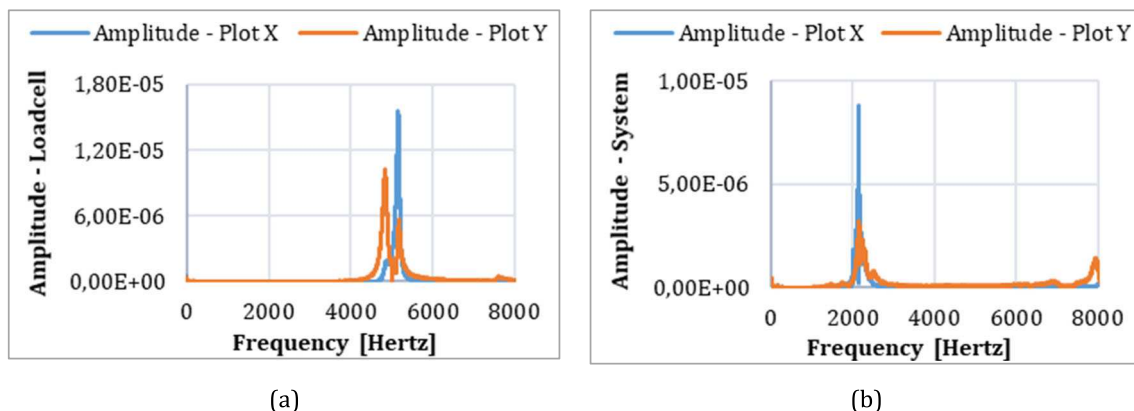

(a)

(b)

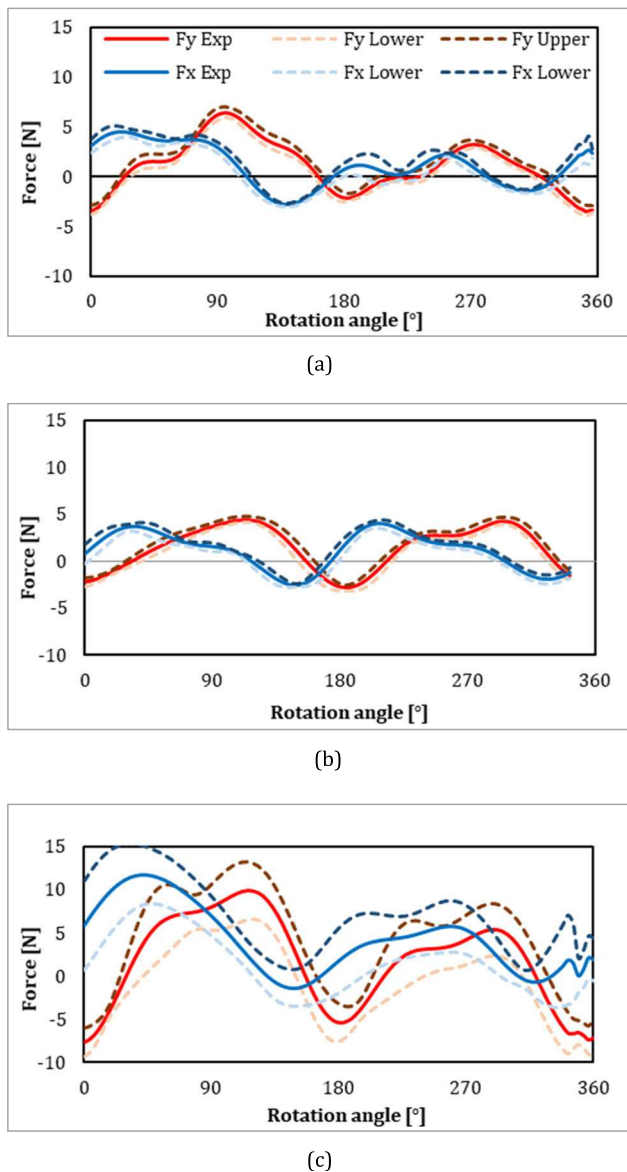**Fig. 2** FRF analysis of natural frequency tested on **a** the load cell and **b** the entire system

(a)

(b)

(c)

Fig. 3 Measured cutting forces: **a** test 1, **b** test 2, and **c** test 3

FE simulations of micro milling are divided into two groups: (i) FE simulations without considering tool run-out and (ii) FE simulations with considering tool run-out. For each experimental condition, both configurations have been modeled and simulated using DEFORM-3D. The tool run-out offset was created in the tool-workpiece engagement by adjusting the rotation and x, y, z offset settings in the FEM simulations simultaneously so that the simulation model exactly represents the cutting tool edge and the workpiece engagement in the presence of tool run-out.

All of the FE simulations include 3D workpiece geometry with visco-plastic deformable material assumption and a 3D micro milling tool geometry as rigid body. Figure 4a shows the simulation set-up as summarized below. FE simulation begins when tool cutting edge is in contact with the workpiece, assuming an initial cutting force equal to zero and a temperature of 20 °C. Between two consecutive steps, a time increment of 5E-07 s has been set. At the beginning of the simulation, workpiece mesh has about 44,000 tetrahedral elements. This number was increased up to 200,000 to ensure a high-quality mesh during FE simulations. A minimum element size was kept constant as 1.3 μm. The highest mesh density region was placed around the tool-workpiece contact zone and allowed to follow the chip developed by the milling process. The heat generated by the workpiece deformation was allowed to transfer along the tool path surface and the lateral surfaces. The external surface temperature was fixed at 20 °C. Some boundary nodes were fixed in the three directions as shown in Fig. 4a (red nodes), but surfaces perpendicular to the z-axis were allowed to move in order to examine the workpiece deformation also in z-direction. Figure 4b shows the configuration considered with tool run-out and Fig. 4c shows a typical cutting force plot for one full period when two flutes are engaged with the workpiece indicating the run-out effect on the cutting force.

The tool geometry, designed by using a CAD model, was meshed into 210,000 tetrahedral elements with a minimum size of 0.8 μm, concentrated around the active tool cutting edge.

For FE simulations with negligible tool run-out, only one flute cutting was modeled. In the case with considerable tool run-out, cutting with both flutes was simulated in order to underline the differences related to cutting forces and chip morphology between the first and the second edge cut. In particular, for each tool flute cutting, a simulation was designed changing workpiece geometry and tool movement details by considering tool run-out effects.

The CuZn37 material constitutive model was implemented by using Johnson-Cook [25] law. The flow stress is defined as shown in Eq. (1):
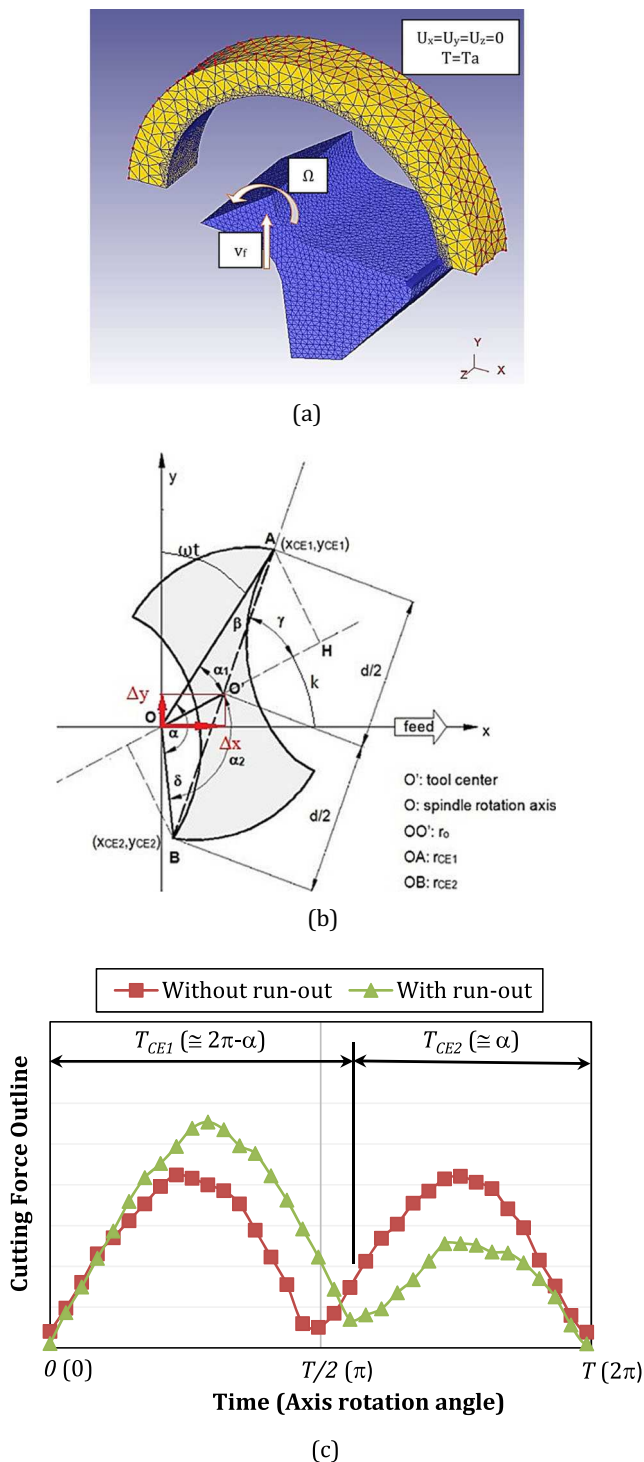
visco-plastic with continuous chip formation [13, 15, 17, 18], but only few publications studied 2D elastic-visco-plastic workpiece deformations and serrated chip formation in micro milling process [16] due to the computational limitations. The difficulty arises in elastic-visco-plastic FE simulation models for 3D micro milling process when simulations do not converge with high-solution accuracy. Therefore, in this study, FE simulations of micro milling were developed by using the visco-plastic workpiece assumption and performing a thermo-mechanical analysis in DEFORM-3D software. A finite element model in 3D was developed instead of a 2D model to capture the 3D chip formation and a more accurate representation of the micro milling process in the simulation results.

(a)

(b)

(c)

Fig. 4 Micro milling: **(a)** FEM 3D model with boundary conditions; **(b)** configuration with tool run-out; **(c)** outline curves of cutting force for a two-flute micro end mill without and with tool run-out

$$\sigma = [A + B\varepsilon^n]\left[1 + Cln\frac{\dot{\varepsilon}}{\dot{\varepsilon_0}}\right]\left[1-\left(\frac{T-T_0}{T_m-T_0}\right)^m\right] \quad (1)$$

where σ is the flow stress, ε is the true strain, $\dot{\varepsilon}$ is the true strain rate, $\dot{\varepsilon_0}$ is the reference true strain rate, T is the work temperature, T_m is the material melting temperature ($T_m =$

916 °C), and T_0 is the room temperature ($T_0 = 20$ °C). This model defines the combined contribution of hardening, strain rate, and temperature on the material behavior. Due to the low temperature reached in micro milling, the thermal softening term has a little influence; nevertheless, in this study, it was also considered. The J-C model constants are shown in Table 2.

In each case, workpiece geometry was designed as a half-ring (external diameter = 1000 μm) with a depth in *z*-direction of 139 μm for test 1, 150 μm for test 2, and 143 μm for test 3, respectively, as measured in experimental tests (see Table 1). The arch-shaped curve represents the undeformed geometry as a result of the previous cut. It was designed using equation set Eq. (2) (Table 3) for micro milling simulations without tool run-out and equation set Eq. (3) (Table 3) for micro milling simulations with tool run-out [7].

The equation set Eq. (3) shall contain some terms in addition to the equation set Eq. (2) in order to consider tool run-out. In Fig. 4b, the problem geometry is shown. The symbols r_{CE1} and r_{CE2} are the radii of the first (A) and the second (B) cutting edge and they are equal to the distance between the tool edges (A and B) and the spindle center (O), and α is the phase angle of the cutting edges ($A\hat{O}B$ angle). For the estimation of r_{CE1}, r_{CE2}, and α, a modified version of the procedure proposed in reference [12] was utilised. The tool run-out model assumes that:

– the spindle error is neglected;
– there is no inclination between the tool and the spindle axes (tilt effects are negligible).

The nano-precision machining center (Kern Pyramid Nano) used in this study guarantees this assumption. Under this hypothesis, the resolution of the geometrical problem [12] allows to derive the values of r_{CE1}, r_{CE2}, and α from the measurements of the major cutting edge radius (r_{CE1}), of the tool diameter ($\overline{AB}$ in Fig. 4a) and of the cutting force. The major cutting edge radius and the tool diameter can be measured by a microscope, while the cutting force can be measured using a load cell.

The phase α can be measured indirectly from force signals. In fact, the change of cutting edge phase from π to α causes a different cutting time between the two flutes. Referring to Fig. 4c, where an example of cutting force signal for a two-flute micro end mill with tool run-out is reported, the cutting time of the first cutting edge (T_{CE1}) is higher than that of the second cutting edge (T_{CE2}).

Table 2 Johnson-Cook model constants [25]

A	B	C	n	m
112	505	0.009	0.42	1.68

Table 3 Equation sets representing the arch-shaped curve without (Eq. (2)) and with (Eq. (3)) tool run-out

Equation set Eq. (2)	Equation set Eq. (3)
$x = r \cdot \cos(\omega \cdot t)$ $y = r \cdot \sin(\omega \cdot t) + \frac{f \cdot t}{60}$	**(a)** $x_{CE1} = r_{CE1} \cdot \cos(\omega \cdot t)$ **(a)** $y_{CE1} = r_{CE1} \cdot \sin(\omega \cdot t) + \frac{f \cdot t}{60}$ **(b)** $x_{CE2} = r_{CE2} \cdot \cos(\omega \cdot t + \alpha)$ **(b)** $y_{CE2} = r_{CE2} \cdot \sin(\omega \cdot t + \alpha) + \frac{f \cdot t}{60}$

The cutting time of each tooth depends on the cutting-edge phase angle (α) and can be estimated by using Eq. (4) and Eq. (5):

$$T_{CE1} = T \cdot \frac{2\pi - \alpha}{2\pi} \qquad (4)$$

$$T_{CE2} = T \cdot \frac{\alpha}{2\pi} \qquad (5)$$

where $T = T_{CE1} + T_{CE2}$ is the total cutting period. To estimate the periods (i.e., T, T_{CE1}, and T_{CE2}), a Matlab script was developed. The filtered F_x experimental force signal was fit by means of a Fourier series utilizing the Curve Fitting application of Matlab®. Once defined the fitting curve coefficients, utilizing the Matlab function "fminbnd", it is possible to locate the minima of this curve which correspond to the valleys of the force signal. In this manner, the periods T, T_{CE1}, and T_{CE2} are identified and the corresponding values of α can be calculated by using Eq. (5). More details on the procedure are reported in reference [12]. Cutting times and phase angles estimated for each test applying the above procedure are given in Table 4.

The radius of first cutting edge (r_{CE1}) can be in theory directly measured as the half of the channel width on the workpiece. The uncertainty of the measurement at this scale, high elastic recovery effects of CuZn37 brass, and the burr formation do not allow applying the previous assumption. For this reason, a new parameter namely Δr (i.e., the increment of tool radius due to tool run-out) was introduced. Once Δr value is defined, it is possible to calculate the radius of first cutting edge (r_{CE1}) by using Eq. (6):

$$r_{CE1} = \frac{\overline{AB}}{2} + \Delta rr \qquad (6)$$

Table 4 Matlab estimation of the cutting time of each tooth and corresponding phase angle

	Ω [RPM]	T_{CE1} [ms]	T_{CE2} [ms]	α [°]
Test1	19,920	1.5202	1.4919	178.311
Test2	24,960	1.2180	1.1997	178.600
Test3	30,000	1.0001	0.9999	179.986
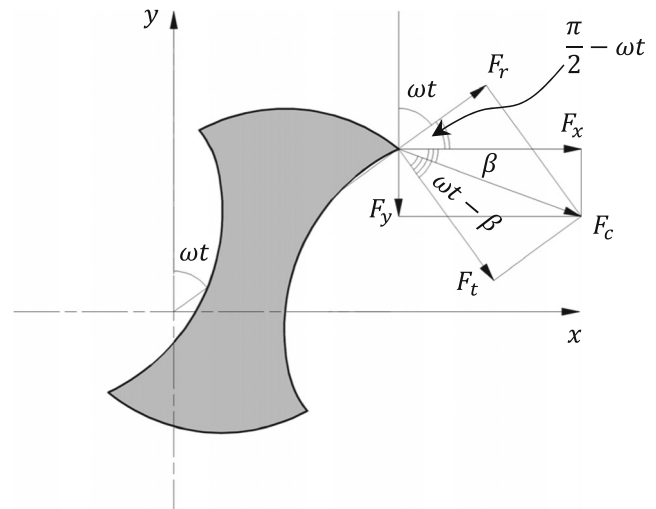
Fig. 5 Cutting force decomposition

The tool diameter ($\overline{AB}$) can be fixed at 0.782 mm (i.e., the average of the measurements). As demonstrated in reference [10], by using the law of sines on triangle AOB (Fig. 4b), β and δ are determined. Then, with the law of cosines, the radius of the second cutting edge ($r_{CE2} = \overline{OB}$) can be calculated. Finally, the tool run-out length ($r_0 = \overline{OO'}$) is determined by using the law of cosines on triangle OO'B. When all the tool run-out parameters are determined, it is possible to calculate how to offset the tool center compared to the spindle center for the FE simulation purposes.

Three different values of Δr were used in order to investigate its effect on the loads: $\Delta r = 0.5$ μm, $\Delta r = 1$ μm, and $\Delta r = 2$ μm. For each test, the best radius increment value was selected by comparing the experimental forces with an analytical prediction. The force prediction was performed using the Kronenberg model [24]. It allows calculating the tangential force component F_t as the product between the cutting pressure (K_S) and the instantaneous chip section (S), as expressed in Eq. (7):

$$F_t = S \cdot K_S \qquad (7)$$

The cutting pressure depends on the instantaneous chip section. The Eq. (8) defines this relation:

$$K_S = K_{S0} \cdot S^{\left(-\frac{1}{m}\right)} \qquad (8)$$

where the specific cutting pressure K_{S0} and m are the function of the tool-workpiece pair and they must be experimentally estimated. The instantaneous chip section is the product between the chip thickness and the axial depth of cut (Table 1). The chip thickness is influenced by tool run-out. It is necessary to distinguish between h_{CE1} (the instantaneous chip thickness of first cutting edge) and h_{CE2} (the instantaneous chip
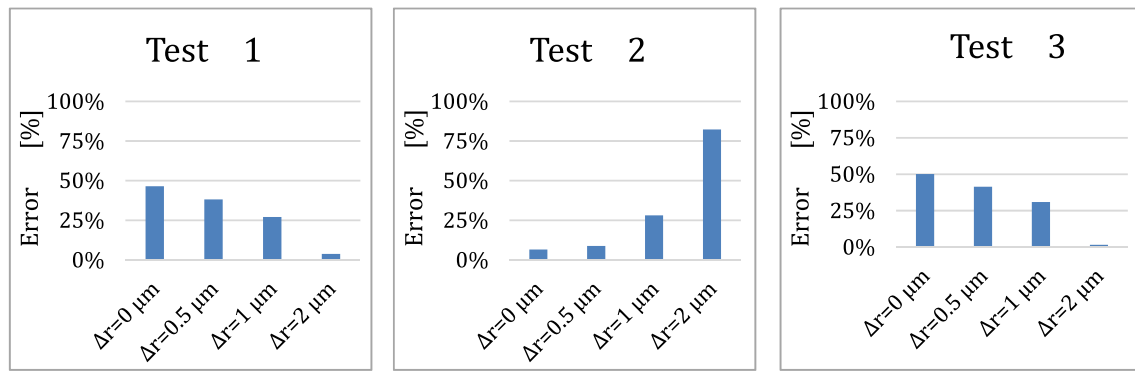
Fig. 6 The error on force predictions of the analytical model

thickness of the second cutting edge). It is possible to demonstrate (see [7]) that the different chip thicknesses can be calculated by using Eq. (9) and Eq. (10).

$$h_{CE1} = \sqrt{(r_{CE1}\sin(\omega t) + \Delta s_{CE1})^2 + (r_{CE1}\cos(\omega t))^2} - r_{CE2} \ \text{for} \ 0 \le \omega t < \alpha \tag{9}$$

$$h_{CE2} = \sqrt{(r_{CE2}\sin(\omega t) + \Delta s_{CE2})^2 + (r_{CE2}\cos(\omega t))^2} - r_{CE1} \ \text{for} \ \alpha \le \omega t < 2\pi \tag{10}$$

The predicted tangential force component (F_t) must be compared with the experimental one. F_t can be calculated from the cutting force (F_c) for each time instant. As a first approximation, the geometrical model is illustrated in Fig. 5. The cutting force (F_c) can be calculated by the experimental components F_x and F_y by using Eq. (11):

$$F_c = \sqrt{F_x^2 + F_y^2} \tag{11}$$

The angle β is defined as the angle between F_c and F_x. The Eq. (12) allows calculating this angle.

$$\beta = \left|\arctan\left(\frac{F_y}{F_x}\right)\right| \tag{12}$$

The cutting force (F_c) can be decomposed in its tangential (F_t) and orthogonal (F_r) components. F_t can be obtained by Eq. (13):

$$F_t = F_c \cdot \cos(\omega t - \beta) \tag{13}$$

Once estimated the experimental tangential component (F_t) of the cutting force, a comparison with the Kronenberg prediction was done by matching the maximum values.

For each test condition, the Δr value providing the minimum error estimated according to Eq. (14) was selected as best value. Figure 6 shows the calculated errors for each test for the different Δr values.

$$Error = \left(\left|\frac{\frac{F_{t,exp, \ A}}{F_{t,exp, \ B}} - \frac{F_{t,\Delta r, \ A}}{F_{t,\Delta r, \ B}}}{\frac{F_{t,exp, \ A}}{F_{t,exp, \ B}}}\right|\right) \tag{14}$$

For test 2, the best prediction was achieved by implementing $\Delta r = 0$ µm. For test 1 and test 3, the best results are guaranteed by the maximum increment, $\Delta r = 2$ µm.

Therefore, test 2 simulation was elaborated by implementing the FE model which neglects run-out effect. Test 1 and test 3 were simulated by using the model which considers run-out effects with an increment $\Delta r = 2$ µm.

Table 5 Tool run-out parameters

Run-out parameters	Test 1	Test 2	Test 3
Tool radius [µm]	391 ± 2	391 ± 2	391 ± 2
Δr [µm]	2	0	2
r_{CE1} [µm]	393.00	391.00	393.00
r_{CE2} [µm]	389.06	391.00	389.00
r_0 [µm]	6.087	0	2.000
γ [°]	71.23	0	1.275
$\Delta x(t_1^*)$	5.734	0	0.044
$\Delta y(t_1^*)$	2.042	0	2.000
$\Delta x(t_2^*)$	−5.792	0	−0.045
$\Delta y(t_2^*)$	−1.872	0	−2.000

Table 6 Thermal and mechanical properties of materials

Properties	CuZn37	WC(Co)	(Ti,Al)N
Thermal conductivity (Ns^{-1} °C^{-1})	370	59	f(T)
Heat capacity (Nmm^{-2} °C^{-1})	3.272	15	f(T)
Thermal exp. Coeff.(°C^{-1})	2.2e-05	5e-06	9.4e-06
Young's modulus (MPa)	1.1e+05	6.5e+05	6.0e+05
Poisson's ratio	0.33	0.25	0.25

Table 7 Friction modeling

Eq. (19) Sticking condition	Eq. (20) Sliding condition
$\tau_f = m \cdot k$	$\tau_f = \mu \cdot p$
if $\mu \cdot p > m \cdot k$	if $\mu \cdot p < m \cdot k$

For test 1 and test 3, the distance between O and O′ (i.e., r_0) was decomposed in x and y components, called Δx and Δy. Because of rotating tool movement, $\Delta x(t)$ and $\Delta y(t)$ change in time and can be calculated as:

$$\Delta x\,(t) = r_0 \cdot cos(k) \tag{15}$$

$$\Delta y\,(t) = r_0 \cdot sin(k) \tag{16}$$

where the time-dependent angle κ can be calculated with Eq. (17), obtained by a geometrical analysis of Fig. 4b:

$$k\,(t) = \frac{\pi}{2} - \alpha_1 - \omega t \tag{17}$$

In this equation, $\kappa(t)$ depends also on angle α_1, which can be obtained by Eq. (18).

$$\alpha_1 = \arccos\left[\frac{r_0 + \frac{AB}{2}cosy}{r_{CE1}}\right] \tag{18}$$

These results were used for both workpiece design and tool center shift compared to spindle center. Equation (3a) was used to design the workpiece profile in the simulation of the passes where the tool is engaged with r_{CE2} (tool edge B is working) and vice versa; Eq. (3b) was used when the tool was engaged with r_{CE1} (tool edge A is working).

In FE simulations without run-out, tool was positioned with its center O′ overlapped to the spindle rotation center O and then a rotation around O ≡ O′ was set. In FE simulations with tool run-out, tool center O′ was initially offset by $\Delta x(t^*)$ and $\Delta y(t^*)$, calculated at different time (t_1^* and t_2^*) for simulation of tool edge A and tool edge B: the first edge starts to engage the workpiece when $\omega t_1^* = 0$; the second edge starts to engage the workpiece when $\omega t_2^* = 2\pi - \alpha$. Then, the tool

rotation was set around spindle center O, from 0° to 180°. In Table 5, the parameters of each test for the FE simulation design considering tool run-out are summarized.

As previously explained, the movement was assigned to the tool, using speeds according to the experimental values. The tool boundary conditions allow transferring heat throughout the entire body. The heat transfer conduction coefficient between tool and workpiece plays a key role in chip formation thermodynamics [15, 18]. This parameter was set equal to 10^5 N s^{-1} mm^{-1} °C^{-1}. It is higher than usual value, and it is necessary to generate sufficient temperature in the short duration of the simulation (about 0.001 s). The heat exchange was also allowed between the chip-tool system and the environment. All material properties for the workpiece, the tool, and the coating are given in Table 6.

The friction between workpiece and tool was modeled using the hybrid model available in DEFORM-3D, which considers both sticking and sliding contacts [15, 18] by Eq. (19) and Eq. (20) (Table 7).

In these equations, τ_f is the frictional stress, k is the shear yield stress, and p is the interface pressure. The shear friction factor m was set equal to 0.9 and the Coulomb friction coefficient μ was fixed at 0.4 [15]. The chip curvature brings a contact also between itself and the workpiece, that contact was modeled by the sliding condition with a Coulomb friction coefficient of 0.1.

4 4. Comparison of predicted cutting forces and chip shapes

It was observed that the FE simulations of micro milling achieve a good prediction of the experimental forces. For simulation without considering tool run-out, test 2 is used because the run-out was minimum in this experiment (the least tool run-out condition). In Fig. 7a, b, a comparison between simulated and experimental force results for test 2 is presented showing reasonably good agreements.

In Fig. 8, the same comparison between experimental and finite element method (FEM) results is shown for
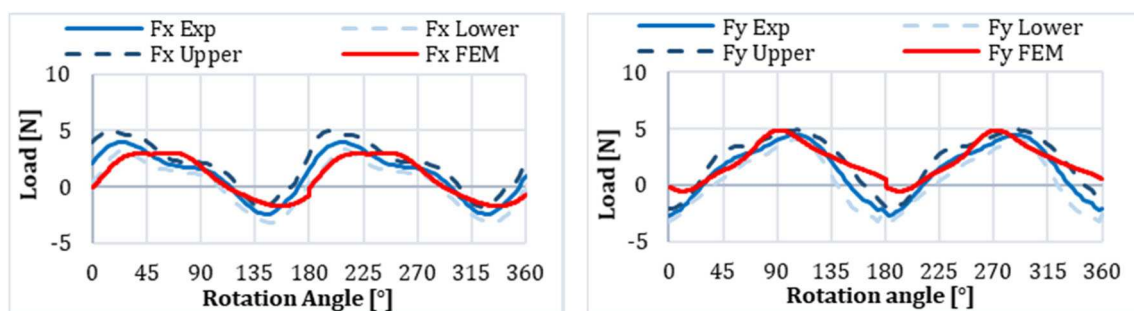

Fig. 7 Comparison of predicted and experimental forces (test 2—no tool run-out considered)
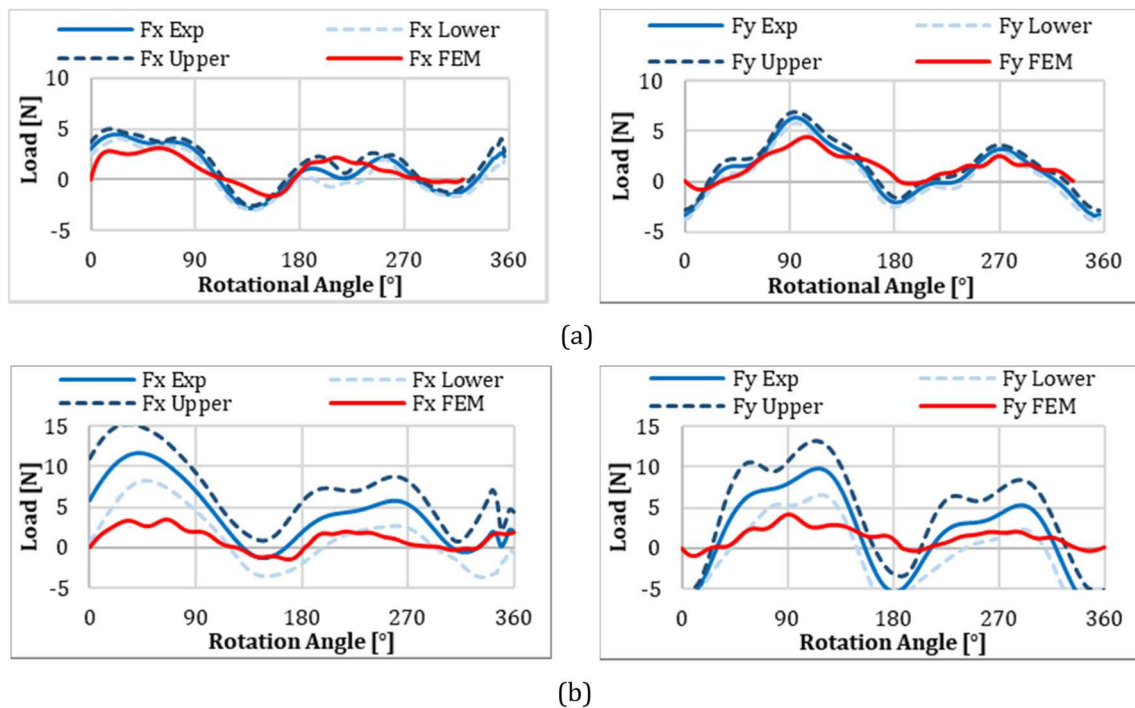
**Fig. 8** Comparison of predicted and experimental forces (**a**) test 1; **b**) test 3 (tool run-out considered)

test 1 (Fig. 8a) and test 3 (Fig. 8b) considering tool run-out due to a value of Δr equal to 2 μm. It is evident that the model validity for test 3 is not satisfactory. Experimental loads for this test are significantly higher than the force values of test 1 and test 2. A possible explanation for this can be related to the experimental set-up. The thin-wall cut with higher cutting speed undergoes to greater vibrations which affect the force measurements. Furthermore, considering the simulation results, it is well-known how, at the high cutting speed (i.e., higher strain rates), the material constitutive law expressed by the Johnson-Cook model underestimates

the actual flow stresses and, as a consequence, the predicted cutting forces.

In addition, reasonably good results are obtained for the chip shapes from the FE simulations. Figure 9 shows the comparison between simulated and experimental chip shapes for test 2. It is possible to observe that the simulation is able to predict the some chip segmentation as well.

Simulated chip body also shows significant effective strain but a low temperature as shown in Fig. 10 shows indicating that plastic deformation is large but heat generated in this micro milling process with such small feed per tooth values is not very high (around 50 °C).

Fig. 9 The comparison between a SEM image of a chip sample (**a**) and a part of the simulated chip shape (**b**) for test 2
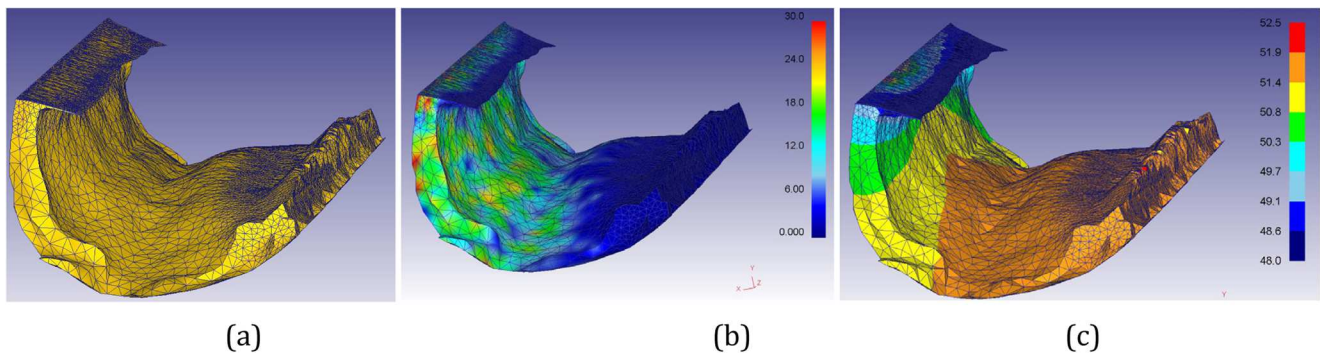

(a)

(b)
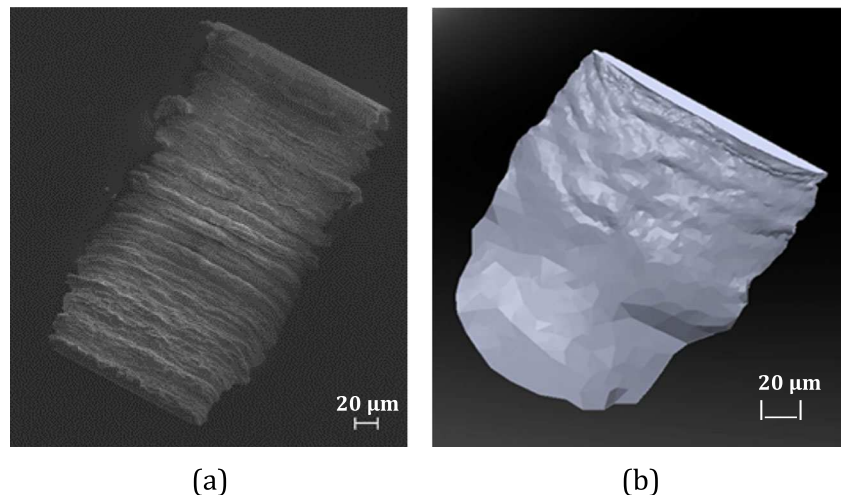
Fig. 10 **a** Simulated chip geometry with deformed mesh, **b** predicted effective strain distribution, and **c** predicted temperature distribution in °C

5 Conclusions

This study presents an experimental and finite element simulation-based investigations about the effect of tool run-out on 3D orthogonal micro milling configuration. The size of the tool run-out deviation does not result in direct connection to the cutting speed and it remains in the magnitude order of few micrometres. The cutting forces are significantly influenced by tool run-out and this effect can be reliably predicted by the FE simulation model coupled with tool run-out. This methodology relies on measurement of tool run-out from orthogonal micro-milling tests and on measuring cutting forces generated by two flutes of the micro end mill. It was shown that while FE simulations accurately predict cutting forces in the presence of no tool run-out effect, the improved FE simulation methodology by considering tool motion with calculated tool run-out results in reasonably good cutting force predictions as well. It is also noted that the qualitative comparison of predicted chip flow and chip shapes and the measured chip shapes yields in reasonably good results. A more quantitative analysis of experimental chip samples as compared with predicted chips is required for further validating the mechanism of chip formation when considering tool run-out in micro milling processes.

Publisher's Note Springer Nature remains neutral with regard to jurisdictional claims in published maps and institutional affiliations.

References

1. Dornfeld D, Mina S, Takeuchi Y (2006) Recent advances in mechanical micromachining. CIRP Ann Manuf Technol 55:745–768
2. Cheng K, Huo D (2013) Micro cutting: fundamentals and applications. John Wiley & Sons, Chichester
3. Bissacco G, Hansen HN, Slunsky J (2008) Modelling the cutting edge radius size effect for force prediction in micro milling. CIRP Ann Manuf Technol 57:113–116
4. Özel T, Bartolo P, Ceretti E, Ciurana J, Rodriguez CA, Lopes Da Silva JV (2016) Biomedical devices: design, prototyping and manufacturing. Wiley, Hoboken
5. Karagiannis S, Stavropoulos P, Ziogas C, Kechagias J (2013) Prediction of surface roughness magnitude in computer numerical controlled end milling processes using neural networks, by considering a set of influence parameters: an Aluminium alloy 5083 case study. Proc Inst Mech Eng B J Eng Manuf 228(2):233–244
6. Annoni M, Pusterla N, Rebaioli L, Semeraro Q (2015) Calibration and validation of a mechanistic micromilling force prediction model. J Manuf Sci Eng 138:11001–11012
7. Attanasio A, Garbellini A, Ceretti E, Giardini C (2015) Force modelling in micromilling of channels. Int J Nanomanuf 11(5–6):275–296
8. Gelfi M, Attanasio A, Ceretti E, Garbellini A, Pola A (2015) Micromilling of lamellar Ti6Al4V: cutting force analysis. Mater Manuf Process 31(7):919–925
9. Riviere-Lorphevre E, Letot C, Ducobu F, Dehombreux P, Filippi E (2017) Dynamic simulation of milling operations with small diameter milling cutters: effect of material heterogeneity on the cutting force model. Meccanica 52:35–44
10. Wang JJ, Uhlmann E, Oberschmidt D, Sung CF, Perfilov I (2016) Critical depth of cut and asymptotic spindle speed for chatter in micro milling with process damping. CIRP Ann Manuf Technol 65(1):113–116
11. Uhlmann E, Oberschmidt D, Kuche Y, Löwenstein A (2014) Cutting edge preparation of micro milling tools. Procedia CIRP 14:349–354
12. Attanasio A (2017) Tool run-out measurement in micro milling. Micromachines 8:221
13. Davoudinejad A, Tosello G, Parenti P, Annoni M (2017) 3D finite element simulation of micro end-milling by considering the effect of tool run-out. Micromachines 8(187):1–20
14. Mamedov A, Lazoglu I (2016) Thermal analysis of micro milling titanium alloy Ti-6Al-4V. J Mater Process Technol 229:659–667
15. Thepsonthi T, Özel T (2015) 3-D finite element process simulation of micro-end milling Ti-6Al-4V titanium alloy: experimental validations on Chip flow and tool Wear. J Mater Process Technol 221:128–145
16. Thepsonthi T, Özel T (2016) Simulation of serrated chip formation in micro-milling of titanium alloy Ti-6Al-4V using 2D elasto-viscoplastic finite element modeling. Prod Eng Res Dev 10(6):575–586
17. Ucun I, Aslantas K, Bedir F (2016) Finite element modeling of micro-milling: numerical simulation and experimental validation. Mach Sci Technol 20(1):148–172

18. Özel T, Olleak A, Thepsonthi T (2017) Micro milling of titanium alloy Ti-6Al-4V: 3-D finite element modeling for prediction of chip flow and burr formation. Prod Eng 11(4–5):435–444

19. Biermann D, Kahnis P (2010) Analysis and simulation of size effects in micromilling. Product Eng Res Dev 4(1):25–34

20. Park SS, Malekian M (2009) Mechanistic modeling and accurate measurement of micro end milling forces. CIRP Ann Manuf Technol 58:49–52

21. Malekian M, Park SS, Jun MBG (2009) Modeling of dynamic micro-milling cutting forces. Int J Mach Tools Manuf 49:586–598

22. Altintas Y, Jin X (2011) Mechanics of micro-milling with round edge tools. CIRP Ann Manuf Technol 60(1):77–80

23. Korkmaz E, Gozen BA Bediz B, Ozdoganlar OB (2017) Accurate measurement of micromachining forces through dynamic compensation of dynamometers. Precis Eng 49:365–376

24. Kronenberg M (1966) Machining science and application. Pergamon Press

25. Johnson GJ, Cook WH (1983) A constitutive model and data for metals subjected tool large strains, high strain rates and high temperatures. Proc 7th international Symposium on Ballistics 541–547

Finite element simulation of tool wear in machining of nickel-chromiumbased superalloy

Andrea Abeni, Cristian Cappellini and Aldo Attanasio

Andrea Abeni. Department of Mechanical and Industrial Engineering, University of Brescia, V. Branze 38, Brescia, 25123, Italy
Corresponding author: Andrea Abeni. E-mail address: andrea.abeni@unibs.it
Cristian Cappellini. Faculty of Science and Technology, Free University of Bolzano, P.zza Università 5, Bolzano, 39100, Italy
Aldo Attanasio. Department of Mechanical and Industrial Engineering, University of Brescia, V. Branze 38, Brescia, 25123, Italy

Abstract. The phenomenon of tool wear strongly affects the efficiency of machining and the quality of machined products. The experimental approach to investigate tool wear requires several time consuming tests. Finite Element Methods (FEM) can be utilized to predict tool wear and tool life as function of process parameters and tool geometry. The commercial software for Finite Element Analysis (FEA) are limited by the impossibility to update the geometry of the worn tool. This research utilizes a self-released subroutine in order to modify the tool geometry in DEFORM 3D simulations by considering the volume reduction of the tool. The model was validated with experimental data obtained by drilling tests on Inconel 718 using conventional metal working fluids (MWF). The correct profile of the simulated worn tool was individuated by comparing the prediction of the simulation with the real tool geometry. The FEM simulation allowed to predict how torque changes during the tool life. In a predictive maintenance perspective, the model can be implemented to optimize the tools replacement.

Keywords. Drilling, Flank Wear, FEM-Simulation, Subroutine

1 Introduction

Nickel-chromium based superalloys, and in particular Inconel 718, are widely used in high temperature and extremely corrosive environments, such as jet engines parts, gas turbine components, and rocket motors in the aerospace industry, due to their ability to maintain proper mechanical characteristics also in extreme conditions [1]. The retain of these properties, combined with low thermal conductivity, high chemical affinity with cutting tool materials, and the presence of abrasive carbide particles, makes Inconel 718 a difficult-to-cut material, and it brings to a very pronounced tool wear [2,3]. The amount of tool wear heavily affects machining forces, cutting efficiency, residual stresses and surface roughness of the machined product, and the tool life itself [4-6]. Moreover, when drilling is considered, due to its internal machining nature and to the higher difficulty of the chip to be removed from the cutting zone, stronger mechanical and thermal loads on tool and workpiece are generated if compared with external machining (turning and milling) [7], making the tool wear control more prominent. The evolution of tool wear can be assessed by means of several experimental tests, but these are expensive and time consuming [8]. To overcome this costly approach, Finite Element Methods (FEM) can be utilized. The capability of FEM to predict cutting forces, torques, and surface integrity as a function of process parameters and tool geometry for different machining operations has been demonstrated by numerous research [7-9]. The limits of the commercial software for Finite Element Analysis (FEA) are related to the impossibility of updating the geometry of the worn tool, and consequently the effects of it on forces and workpiece quality are not foreseeable [10]. In order to surmount this lack, in this work, a self-released subroutine able to modify the tool geometry in DEFORM 3D simulations by considering the volume reduction of the tool is presented. The validation of the model has been performed by the comparison of simulation results with the experimental data obtained by drilling tests of Inconel 718 with conventional metal working fluids (MWF) lubrication [11]. The resulting simulated worn tool geometry, in agreement with the real tool geometry, has been used to perform FEM drilling simulations and to predict how torque changes as a function of the tool wear. The good comparison between simulated and experimental values demonstrated that, in a predictive maintenance perspective, the model can be profitably

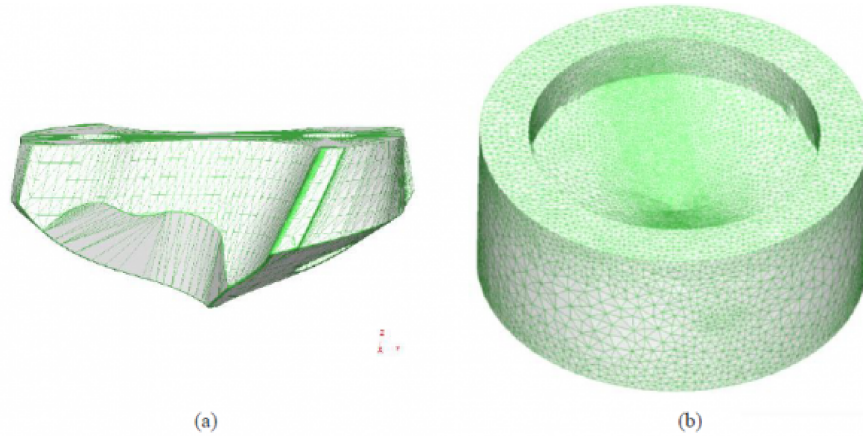implemented to optimize the tools replacement.

Fig. 1. The 3D CAD geometry of the tool (a) and the workpiece (b).

2 FE simulations of tool wear

2.1 FE drilling model

The three dimensional CAD geometries of tool and workpiece are illustrated in Figure 1. The helicoidal drill design (Figure 1a) must comply with the actual tool shape. The workpiece (Figure 1b) is modeled as a cylinder with a hole which replicates the profile of the drill. In DEFORM-3D, the FEM modelling of the chip formation is based on the chip separation criterion [12]. The fracture criterion defines a variable and a critical value of breakage. The contact between the tool cutting edge and the workpiece determines a crack in an element of the mesh if the variable reaches the critical value. Tools can be modeled as a rigid body while workpieces visco-plastic behavior can be defined as flow stress dependent on strain, strain rate and temperature. The software allows to select the fracture criterion between various models [13]. They include the Cockcroft-Latham criterion, which is defined by the Equation 1.

$$\int_0^{\bar{\varepsilon}_f} \sigma_1 \, d\bar{\varepsilon} = D \tag{1}$$

where $\bar{\varepsilon_f}$ is the effective strain; σ_1 is the maximum principal stress; D is a material constant. The thermal proprieties of the workpiece, the tool and the coating materials were defined in terms of thermal conductivity, heat capacity, emissivity and thermal expansion. The relative movement between tool and workpiece is achieved by assigning a feed speed and a rotation speed to the tool. The workpiece is fixed by adding a constrain to the nodes of mesh which belongs to the external side surface of the cylinder. FEM simulation of drilling requires the definition of the friction between tool and workpiece. Several researchers adopted shear model in machining [14, 15], which is defined by Equation 2.

$$\tau_f = m \cdot k \tag{2}$$

where τ_f is the tangential stress, k is the shear yield stress and m is the shear friction factor. It must be determined

through tribological test or it can be assumed by literature. The FEM analysis considers also the heat exchange between objects. The simulator requires the heat conduction coefficient h_{cond} across the tool-workpiece interface and the convection coefficient h_{conv} to perform the thermal simulation. In machining, a high value of h_{cond} is usually used to reach steady state in a short time [16]. Furthermore, h_{conv} strongly depends on the cutting fluid proprieties and temperature and it can be experimentally determined.

2.2 Tool wear modeling

The simulation of tool flank wear (*VB*) is performed by using a subroutine written in Fortran language [10]. It iteratively calculates the incremental wear (*ΔVB*) and subsequently it reconstructs the worn tool flank. The procedure includes a preliminary Lagrangian simulation to reach the thermo-mechanical steady state. At the beginning of the chip formation mechanism, the contact area with the tool surface increases. The increasing is limited by the chip curvature. It determines the separation between chip and the rake surface of the drill.
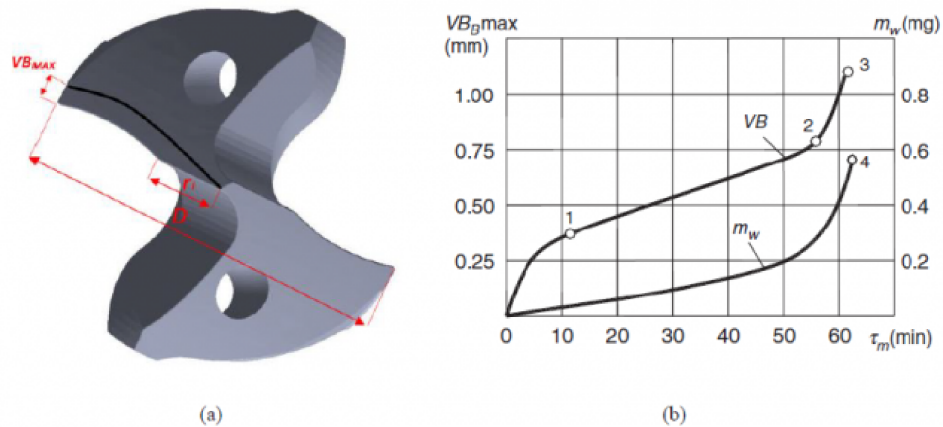
Fig. 2. The scheme of the tool wear on flank as function of distance from the drill center (a) and a typical trend of VB in time [17] (b)

The mechanical steady state is guaranteed only if the tool-chip contact area is constant, while the thermal steady state is ensured by a constant temperature of the cutting edge nodes. The steady state of drilling constitutes the starting point for the wear calculation. The modification of the tool flank geometry depends on time and on the distance r between the drill center and each mesh node which belongs to the cutting edge. Several researches demonstrated as usually the flank wear linearly increases from the chisel edge to the begin of the curved part of the cutting edge ($r<r_l$). Furthermore, the flank of wear remains constant (VB_{MAX}) along the curved part until the drill periphery ($r\geq r_l$). A schematization of the worn profile is shown in Figure 2a. One of the achievements of this work is to demonstrate the validity of this morphology of the worn tool also by comparing the geometrical model outlined with others.

About the time, the duration of the drilling must be discretized in interval of time (*Δt*). The subroutine calculates the tool wear increment along the curved part of the cutting edge (*ΔVB_MAX*) with a periodicity of *Δt*. The code requires the experimental tool wear rate (*dW(t)/dt*) to correctly update the cutting edge geometry for each time instant. Figure 2b shows a typical trend of the flank wear as a function of the time. The trend was identified in several researches [17, 18] and it can be divided into three stages. The first region is characterized by an accelerated wear, while in the second region the wear linearly depends on time. In the third and last stage, the wear rate increases drastically until the end of the tool life. Once the tool wear rate is known, it can be used to calculate *ΔVB_MAX* for the i-th iteration through

Equation 3:

$$\Delta VB_{MAX\,i} = \frac{dW(t_i)}{dt} \cdot \Delta t \qquad (3)$$

Once the ΔVB_{MAX} is known, it can be used to calculate the width of the wear on flank along the entire cutting edge. Different computation strategy can be adopted in order to calculate different morphology of the worn flank. The procedure to update the tool mesh as function of $VB(r)_i$ is the most critical part of the subroutine. The mesh nodes which belongs to the flank, the rake and the cutting edge must be identified in order to calculate the local rake angle (γ) and the local clearance angle (α). As the wear VB, also γ and α depends on the distance r. The subroutine calculates the angles with the purpose to compute a local wear volume (LWV) in correspondence of each node of the cutting edge [10]. Since the LWV depends on the local VB, α and γ, the FEM is capable to compute the actual loss of volume due to wear on flank. Finally, the subroutine deletes all the nodes contained in the LWV. A new tool geometry is extrapolated by the updated mesh and it is used for the further iteration.

3 Study case

An experimental study case was used to test the reliability of the procedure. In particular, the study case was designed with the purpose to simulate different profile of wear on flank and to compare them with the experimental profile. The drilling tests were performed by Chen and Liao [11] with a multi-layer TiAlN PVD coated tungsten carbide drills manufactured by Guhring. Table 1 summarizes the geometrical features of the drill. The tests consist in pecked-drilling of Inconel 718 samples with a constant cutting speed equal to 13.2 m/min and a constant feed rate equal to 40 mm/min. Metal working fluid (MWF) was employed to lubricate and to evacuate the chip. During the drilling, the torque and the thrust force were acquired by using a Kistler 9273 dynamometer.

Table 1. Geometrical features of the drill.

Diameter [mm]	10.5	Point angle [°]	140
Chisel edge angle [°]	48	Back taper angle [°]	5
Margin width [mm]	0.26	Web thickness [mm]	0.53
Edge radius [μm]	40	Helix angle [°]	35

An optical microscope and a scanning electronics microscope (SEM) were utilized to inspect the tool wear condition. The SEM images allowed to evidence the development of micro-cracks distributing along the chipping area. The propagation of the cracks determined a progressive damage of the cutting edge. A crater wear was formed on the tool rake and the flank wear gradually increases. Finally, the wear rate increases drastically until the end of the tool life. Figure 3a shows the worn flank after 600 seconds of machining. The width of the wear lip was periodically measured on the curved section of the cutting edge, where it was maximum (VB_{MAX}). The trend of VB_{MAX} is illustrated in Figure 3b. For the first ten minutes, the wear rate was constant, and it was equal to $4.4\cdot10^{-4}$ mm/s. At the end of the drilling tests, the wear rate increased to $1.2\cdot10^{-4}$ mm/s.

The drilling tests were simulated with the FEM model described in section 2. The tool was modeled as a rigid body and meshed with 200k tetrahedral elements, setting a maximum size of 0.3 mm. The elements with minimum size were located around the cutting edge and the ratio between minimum size and maximum size was set equal to ten. The multi-layer TiAlN PVD coating was added. The workpiece was meshed with more than 100k elements with a size ranging from 0.05 to 0.5 mm. The thermo-viscoplastic behavior of Inconel 718 was selected from the DEFORM database, such as the proprieties of the materials which constitutes the tool [10]. Table 2 summarizes the critical value *D* of the Cockcroft-Latham criterion. The table expresses also the shear friction factor *m* and the convention coefficient h_{conv} of the lubricant. The first was determined through tribological tests [10], while the second was calculated by Outeiro et al. [7].

<div align="center">Table 2. Critical value, friction factor and convention coefficient</div>

D	500
m	0.1
hconv	0.930 KW/m^{2}K

The subroutine was utilized each 45 s to generate a worn geometry of the drill. The experimental wear rate was replicated, included the acceleration after 10 minutes of machining. Three different profile of wear on flank along the cutting edge were tested. The first model utilized the increment ΔVB_{MAX} to calculate the flank wear on the curved part of the cutting edge, where the width of wear profile is considered constant. Along the linear section of the cutting edge, the actual increment of wear is lower. Equation 4 allows to calculate the wear $VB(r)_i$ at the i-th iteration.
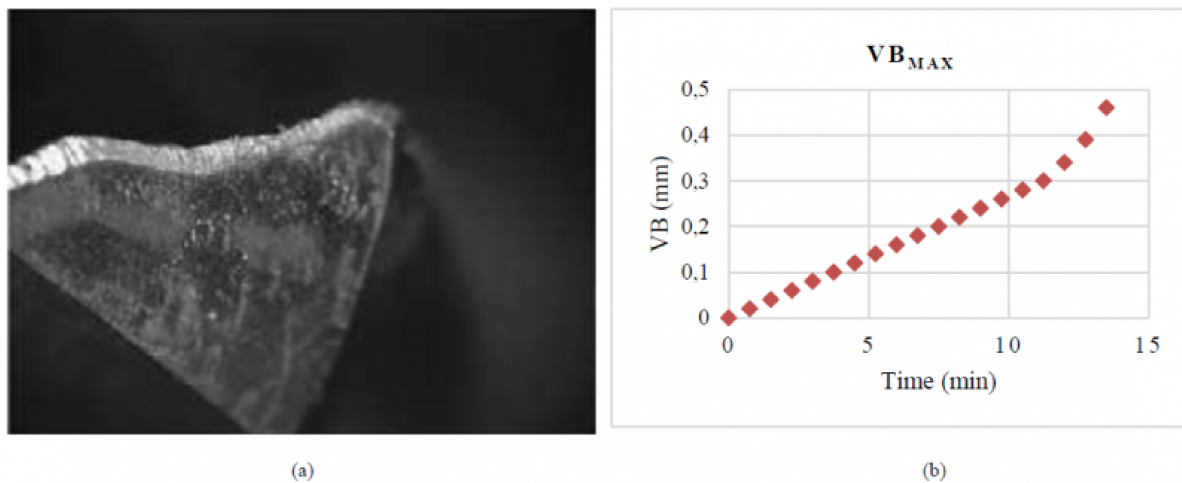

<div align="center">(a)　　　　　　　　　　　　　　　　(b)</div>

<div align="center">Fig. 3. The wear on tool flank after 10 minutes (a) and the trend of VBMAX (b)</div>

$$\begin{cases} VB(r)_i = VB(r)_{i-1} + \Delta VB_{MAX\,i} & r \geq r_l \\ VB(r)_i = VB(r)_{i-1} + \frac{r}{r_l} \cdot \Delta VB_{MAX\,i} & r < r_l \end{cases} \tag{4}$$

A second geometrical model of tool wear provides a constant wear along the curved part of cutting edge with a discontinuity located where the cutting edge becomes linear. It is expressed by Equation 5 and it depends also on the diameter of the drill (D)

$$\begin{cases} VB(r)_i = VB(r)_{i-1} + \Delta VB_{MAX\,i} & r \geq r_l \\ VB(r)_i = VB(r)_{i-1} + \frac{2r}{D} \cdot \Delta VB_{MAX\,i} & r < r_l \end{cases} \tag{5}$$

The third model was based on the hypothesis of linearity along the entire cutting-edge profile. The Equation 6 allows to calculate the wear $VB(r)_i$ at the i-th iteration.

$$VB(r)_i = VB(r)_{i-1} + \frac{2r}{D} \cdot \Delta VB_{MAX\,i} \qquad \forall r \tag{6}$$

4 Results and discussion

The thermo-mechanical steady-state was reached after a drill rotation equal to 180°. The temperature of the tool cutting edge and the torque rapidly increase during the first 45°. Subsequently the torque reaches an equilibrium point at 10.7 Nm. The cutting edge temperature reached a peak of 320 °C in the correspondence of the most stressed nodes. Figure 4 compares the tool wear predictions after 675 s, developed with the models explained in section 3. The time corresponds to a width of the wear on flank equal to 0.3 mm. According to ISO standards, it is considered a limit for the tool life. The profile elaborated by the subroutine based on Equation 4 does not provide any discontinuity along the cutting edge. As expected, the subroutine provides a constant wear on flank with a width of 0.3 mm in the curved section, as visible in Figure 4a. The second subroutine utilized Equation 5 and it computes a point of discontinuity where the curvature of the cutting edge change (Figure 4b). The linear section results less worn as compared with the first FE prediction. Finally, an other continuous geometry was designed by the code implemented on Equation 6. Moreover, the wear increases as the distance from the drill center increases also along the curved section of the cutting edge as a consequence of the cutting speed increasement (Figure 4c). The actual tool [11], visible in Figure 3a, shows a good correspondence with the geometry showed in Figure 4a. The curved section of the cutting edge compensates the increasing of the cutting speed avoiding an undesired increase of the stress. The first model was utilized to simulate the evolution of the wear with a period of 45s. The progression of the wear is compatible with the experimental evidences and in particular with the VB trend shown in Figure 3b. The computational time to elaborate each step is lower than 500 s. The elevated computational rate can be considered adequate to integrate the subroutine in a commercial FE software.
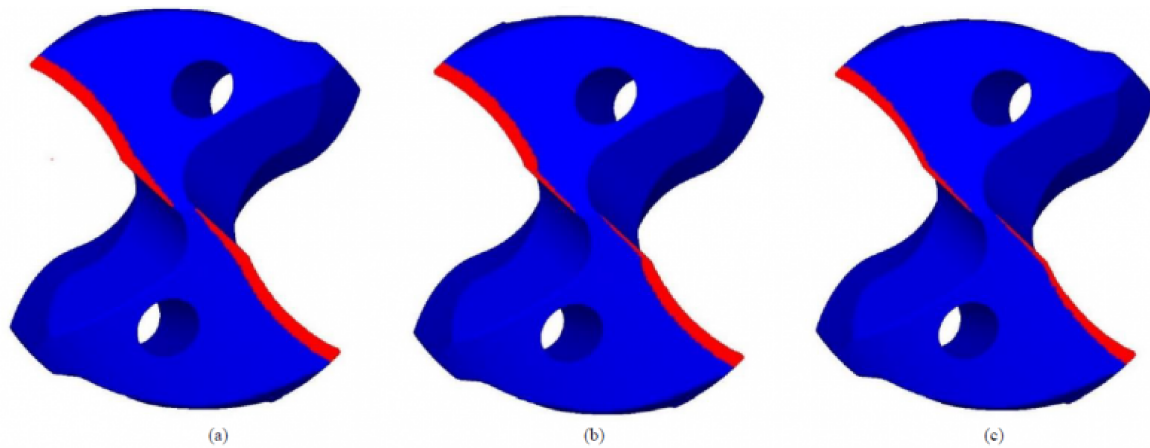
Fig. 4. A comparison of the different wear flank profile after 675 s. The constant wear on curved cutting edge (a), the discontinuity wear on the point of curvature change (b) and the linear wear profile (c).
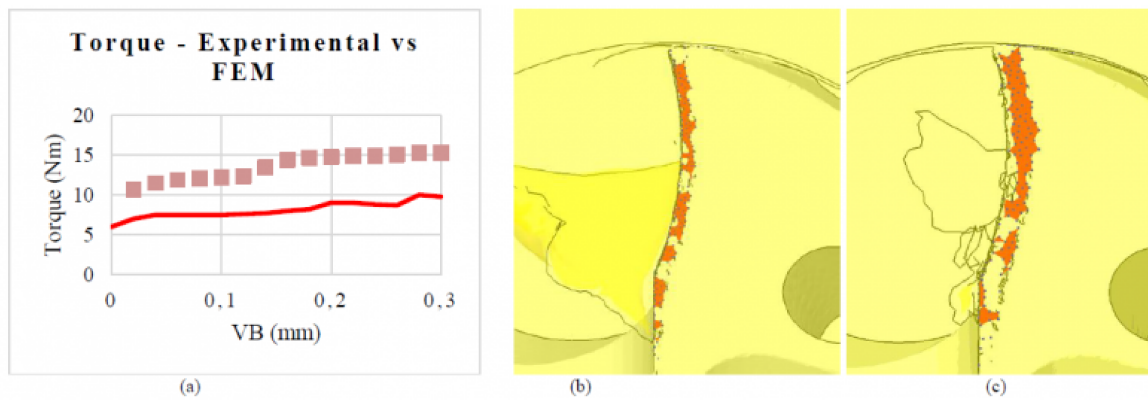

Fig. 5. The torque dependence on the flank wear (a), the contact point on flank after 360 s (b) and after 675 s (c).

The new geometries were utilized to perform Lagrangian simulations to investigate the wear effect on drilling of Inconel 718. The Figure 5a shows the comparison between experimental e FE prediction about torque. Generally, the FEM seems to overestimate the torque. A possible explanation is an overestimation of the friction coefficient in the FEM model. Furthermore, the torque increasement as the wear increases was correctly simulated. This trend is determined by the increasement of the contact zone along the tertiary shear zone which determines an increasement of the cutting force. The contacts between workpiece and flank after 360 s is visible in Figure 5b, while the contacts after 675 s is visible in Figure 5c.
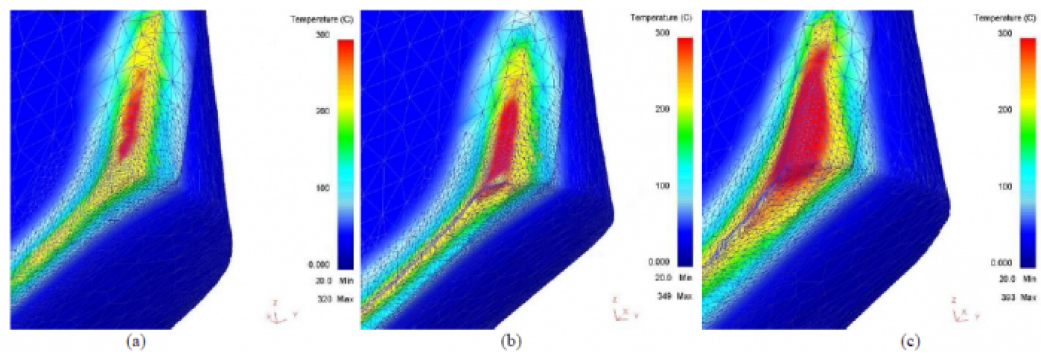
Fig. 6. The temperature distribution on the tool surface in steady state condition on the new tool (a); after 360 s (b); after 675 s (c).

The model can predict also the increment of the tool temperature determined by tool wear. Fig. 6 shows the cutting edge, the flank and the face of one cutting flute in different wear conditions. The increment of the red-colored high temperature zone around the tool corner is well visible. The maximum value of temperature progressively increased from 320 °C to 349 °C after 360 s (Fig.6a and Fig.6b). The tool heating becomes faster for larger tool wear and the temperature reaches an absolute maximum of 393 °C. Also the tool face and flank temperature is affected by tool wear.

5 Conclusion

In this paper, the development and application of a self-released subroutine, in DEFORM-3D FE simulation software, capable to modify the tool geometry as a function of the volume reduction due to wear has been presented. Its validation has been performed by the comparison of the worn tool geometry simulation results with the experimental data of drilling tests of Inconel 718, in terms of drilling torque evolution. The good agreement between simulations and experimental tests demonstrated the effectiveness of the presented subroutine and, in a predictive maintenance perspective, its suitable implementation in the tool replacement optimization phase.

Bibliography

[1] Pajuri, U. M. R. Methuku, S. Siripragada, S. S. Sangishetty, Y. Gunda, R. K. Finite element simulations of machinability parameters in turning of Inconel 718. Materials Today: Proceedings, 2020, https://doi.org/10.1016/j.matpr.2020.08.275.

[2] Dudzinski, D. Devillez, A. Moufki, A. Larrouquère, D. Zerrouki, V. Vigneau, J. A review of developments towards dry and high speed machining of Inconel 718 alloy. International Journal of Machine Tools & Manufacture, 2004, 44, 439-456.

[3] Olovsjo, S. Nyborg, L. Influence of microstructure on wear behaviour of uncoated WC tools in turning of Alloy 718 and Waspaloy, Wear, 2012, 282-283, 12-21.

[4] Toubhans, B. Fromentin, G. Viprey, F. Karaouni, H. Dorlin, T. Machinability of inconel 718 during turning: Cutting force model considering tool wear, influence on surface integrity. Journal of Materials Processing Technology, 2020, 285.

[5] Holmberg, J. Wretland, A. Berglund, J. Beno, T. A detailed investigation of residual stresses after milling Inconel 718 using typical production parameters for assessment of affected depth. Materials Today Communications, 2020, 24.

[6] Hao, Z. Gao, D. Fan, Y. Han, R. New observations on tool wear mechanism in dry machining Inconel 718. International Journal of Machine Tools & Manufacture, 2011, 51, 973-939.

[7] Outeiro, J. C. Lenoir, P. Bosselut, A. Thermo-mechanical effects in drilling using metal working fluids and cryogenic cooling and their impact in tool performance. Production Engineering, 2015, 9, 551-562.

[8] Ucak, N. Cicek, A. Oezkaya, E. Aslantas, K. Finite element simulations of cutting force, torque, and temperature in drilling of Inconel 718. Procedia CIRP, 2019, 82, 47-52. [9] Liu, Y. Xu, D. Agmell, M. M' Saoubi, R. Ahadi, A. Stahl, J. E. Zhou, J. Numerical and experimental investigation of tool geometry effect on residual stresses in orthogonal machining of Inconel 718. Simulation Modelling Practice and Theory, 2021, 106.

[10] Attanasio, A. Ceretti, E. Outeiro, J. C. Poulachon, G. Numerical simulation of tool wear in drilling Inconel 718 under flood and cryogenic cooling conditions. Wear, 2020, 458-459.

[11] Chen, Y. C. Liao, Y. S. Study on wear mechanisms in drilling of Inconel 718 superalloy. Journal of Materials Processing Technology, 2003, 140(1-3), 269-273.

[12] Ducobu, F. Rivière-Lorphèvre, E. Filippi, E. Material constitutive model and chip separation criterion influence on the modeling of Ti6Al4V machining with experimental validation in strictly orthogonal cutting condition. International journal of mechanical sciences, 2016, 107, 136-149.

[13] Poláková, I. Zemko, M. Rund, M. Džugan, J. Using DEFORM Software for Determination of Parameters for Two Fracture Criteria on DIN 34CrNiMo6. Metals, 2020, 10(4), 445.

[14] Manoranjan, K. S. Narayanan, V. H. Kumar, T. M. Ashwin, R. Sekar, K. V. Investigation of friction models in the machining of Inconel 625 Super Alloy using FEM. IOP Conference Series: Materials Science and Engineering 2019, 577(1). doi:10.1088/1757-899X/577/1/012098

[15] Melkote, S. N. Grzesik, W. Outeiro, J. Rech, J. Schulze, V. Attia, H. Saldana, C. Advances in material and friction data for modelling of metal machining. CIRP Annals, 2017, 66(2), 731-754.

[16] Abeni, A. Ceretti, E. Özel, T. Attanasio, A. FEM simulation of micromilling of CuZn37 brass considering tool run-out. Procedia CIRP, 2019, 82, 172-177. [17] Astakhov, V. P. Tribology of metal cutting. Elsevier, Oxford (UK), 2006.

[18] Trent, E. M. Wright, P. K. Metal Cutting, fourth ed., Butterworth–Heinemann Editor, Boston, 2000.

Article

Experimental Optimization of Process Parameters in CuNi18Zn20 Micromachining

Andrea Abeni [1], Alessandro Metelli [1], Cristian Cappellini [2] and Aldo Attanasio [1,*]

[1] Department of Mechanical and Industrial Engineering, University of Brescia, Via Branze 38, 25123 Brescia, Italy; andrea.abeni@unibs.it (A.A.); alessandro.metelli@unibs.it (A.M.)
[2] Faculty of Science and Technology, Free University of Bolzano, Piazza Università 1, 39100 Bolzano, Italy; cristian.cappellini@unibz.it
[*] Correspondence: aldo.attanasio@unibs.it; Tel.: +39-331-613-3181

Abstract: Ultraprecision micromachining is a technology suitable to fabricate miniaturized and complicated 3-dimensional microstructures and micromechanisms. High geometrical precision and elevated surface finishing are both key requirements in several manufacturing sectors. Electronics, biomedicals, optics and watchmaking industries are some of the fields where micromachining finds applications. In the last years, the integration between product functions, the miniaturization of the features and the increasing of geometrical complexity are trends which are shared by all the cited industrial sectors. These tendencies implicate higher requirements and stricter geometrical and dimensional tolerances in machining. From this perspective, the optimization of the micromachining process parameters assumes a crucial role in order to increase the efficiency and effectiveness of the process. An interesting example is offered by the high-end horology field. The optimization of micro machining is indispensable to achieve excellent surface finishing combined with high precision. The cost-saving objective can be pursued by limiting manual post-finishing and by complying the very strict quality standards directly in micromachining. A micro-machining optimization technique is presented in this a paper. The procedure was applied to manufacturing of main-plates and bridges of a wristwatch movement. Cutting speed, feed rate and depth of cut were varied in an experimental factorial plan in order to investigate their correlation with some fundamental properties of the machined features. The dimensions, the geometry and the surface finishing of holes, pins and pockets were evaluated as results of the micromachining optimization. The identified correlations allow to manufacture a wristwatch movement in conformity with the required technical characteristics and by considering the cost and time constraints.

Keywords: micromilling; process optimization; ANOVA; surface finishing

1. Introduction

The horology industry represents one of the major manufacturing sectors for micromachining. In particular, micromilling and microdrilling finds several applications in the manufacturing of the mechanical watches. Although quartz watches based dominate the watch market, the business turnover related to mechanical watches is meaningfully higher [1]. The standard size of a wristwatch movement is very limited, with a diameter ranging from 17 mm to 36 mm and a thickness lower than 4 mm. In the low volume of the caliber are assembled some hundreds of miniaturized components, such as wheels, shafts, levers, screws, springs and bushing. The components are mounted inside the case of the mechanical movement, which is composed by a main plate and the bridges. All the parts have pockets, micro-holes and micro-pins to mechanically constrain the miniaturized components. The micromachining of these features must comply with tight dimensional and geometrical tolerances. Furthermore, the surface finishing assumes a crucial role in order to reduce the frictional effects and to guarantee adequate visual appearance.

Among the manufacturing processes, micromilling is one of the most flexible and fastest way to produce complex tridimensional microfeatures with high dimensional accuracy [2]. It can be successfully applied to a wide variety of materials by using micro-scaled mill with diameters in a sub-millimeter range with different coatings [3]. Micromilling is a subtractive process characterized by a contact between the tool cutting edge and the workpiece along a defined path. As in conventional-size milling, the cutting speed, the feed rate, and the depth of cut are the most meaningful process parameters. The research of the best combinations of these parameters is crucial to guarantee high precision, flexibility, excellent surface finishing, tight geometrical and dimensional tolerances with a low material scrap in the micrometric magnitude scale [4,5]. The selection of the process parameters must also consider the tool deflection effect, defined also as tool run-out effect [6]. The high ratio between the tool length and its diameter results in a drastic reduction of the tool shank section modulus. Form and feature geometric errors on the machined component and distortion of cutting forces are the most undesired effects of tool deflection [7,8]. The component assembly and the product functioning are strongly correlated to the machining optimization. Surface roughness, holes and pins geometrical accuracy (dimension and circularity), burrs extension and their distribution must be controlled by optimizing the process parameters [9].

In contrast with conventional scale milling, when performing a micromilling operation, particular attention must be paid to size and surface effects, since they strongly affect the chip formation and the related surface quality. In micromilling, in fact, the dimensions of uncut chip thickness and work material grain size are comparable. Grain-size effects influence the chip typology, leading to a quasi-shear extrusion chip and cutting force increase, when the grain size decreases [10,11]. Moreover, this process is characterized by a relatively small ratio between the depth of cut (*DOC*) and the cutting-edge radius (r_0) [12]. It results in negative rake angles, increasing the compressive stresses on the work material that reduces the chip brittle fracture, by enhancing the material plasticity. An increment of the negative rake angle favorites the contact between the back cutting surface and the work-piece surface, altering the shearing cutting mode into extrusion cutting, ploughing, or roughing in which the workpiece material undergoes to scraping, squeezing, and grooving instead of been correctly cut [13–15]. Additionally, indentation effects can take place, consistently rising the surface hardness and cracks propagation [16,17]. The amount of residual chips at the bottom and side of the micro-slot may affect the surface quality. These effects may result in higher size and number of burrs and rapid wear of the micro-milling tool [18]. The burrs can be defined as the residual material that overhangs outside the workpiece edge after machining. Several deburring processes are currently employed in the industrial processes, but the removal may require several minutes and damage the machined features. Therefore, the burr minimization on microparts during micromilling is more desirable and advisable compared with the deburring [19]. Several investigations were published about the thematic of the burr reduction [20–22]. The effect of the process parameters was quantitively or qualitatively computed by considering different work-piece materials, such as Inconel 718 [23], stainless steel AISI 316L [24] and Ti-6Al-4V [25]. The experimental researches revealed different behaviors for different materials.

On the other hand, there is a lack of information on machinability at microscale of the materials commonly employed in watch movements. Nickel silver, brass and gold are some of the materials used to produce main plate and bridges, but the CuNi18Zn20 is probably the most common alloy in the horology field due to its grey appearance, higher mechanical properties, and better corrosion resistance than other brass alloys [26]. CuNi18Zn20 is a free lead brass alloy characterized by a single α-phase microstructure. Several studies were performed on the machinability of lead free brasses, revealing their difficult to be machined due to the high ductility of α-phase, leading to extended burrs formation and low surface quality, when conventional cutting processes are performed [27,28]. Amongst these, the results related to the analysis of CuZn38As brass alloy are of great interest, since it is mainly composed by an α-phase microstructure (98%) and shows a machinability

comparable with CuNi18Zn20 [29]. This study underlined that to reduce the machined surface roughness and to achieve better dimensional tolerances, low feed rate must be employed. However, although a wide documentation can be found on their machinability, in literature there are not papers which deals with the issues which afflicts the watch making industry, where micromachining conditions are employed. In this case, low feed rate and depth of cut, combined with high cutting speed are suggested [30–32], but no bibliographic references concerning the processing of CuNi18Zn20 can be found. This paper deals with the optimization of finishing operations in micromachining of microfeatures on CuNi18Zn20 samples. The optimization process was performed using a microtool with a standard geometry, therefore the obtained results can aid the manufacturers in the choice of the process parameters; An experimental approach was adopted by designing a prototype which included some ad hoc features in a limited volume. The selected features consist in microholes, micropins and pockets. In watchmaking industry, microholes are necessary to couple the bridges and the main plate with the jewels that binds the shafts of the wheels. The diameters usually are equal to few hundreds of micrometers while the required tolerances are reduced to few tens of micrometers to ensure the correct mechanical coupling. Pins ensure the fixing between the main plate and the bridges, and their dimension is comparable with the diameter of the holes. The cylindricity of pins is an imperative requirement to avoid an uncorrected interference with the holes into the bridges. Finally, pockets are fabricated to house the wheels in the caliber structure and their depth is crucial for a corrected wheels positioning.

The micromachining of the listed features was repeated several times by varying the process parameters on three levels and testing all the possible combinations. The outputs were evaluated in terms of diameter, circularity and cylindricity of pins and holes. Moreover, S_a, S_{sk}, and S_{ku} roughness parameters of the pocket surfaces were measured in order to examine the surface quality [33]. The correlation between process parameters and outputs was analyzed by means of Analysis of Variance (ANOVA) technique. The burrs extension was checked by using a multifocal 3D microscope. Finally, an optimal parameters set was selected by considering also the time production necessary to fabricate each prototype.

2. Materials and Methods

Micromachining tests were executed by using a five axis Nano Precision Machining Centre KERN Pyramid Nano equipped with a Heidenhain iTCN 530 numeric control. It is visible in Figure 1a. The spindle reaches a maximum rotational speed of 50 krpm with a maximum torque of 1.5 Nm. The machining center operates in a controlled environment with a temperature of $20 \pm 0.5\,°C$ and humidity of 35% to guarantee the maximum accuracy and precision [34]. The micromill features are summarized in Table 1.


| (a) | (b) |

Figure 1. The KERN Pyramid Nano Ultraprecision machining center (**a**); the SECO 905L008-MEGA-T micromill (**b**).

Table 1. Features of micromill SECO 905L008-MEGA-T.

Propriety	Value
Manufacturer	SECO
Code	905L008-MEGA-T
Nominal diameter [μm]	800
Number of flutes	2
Measured diameter [μm]	795 ± 1
Measured cutting-edge radius [μm]	6 ± 0.8
Helix angle [°]	20
Rake angle [°]	4
Material	Tungsten Carbide
Material coating	Titanium Nitride

A SECO 905L008-MEGA-T sample is visible in Figure 1b. The actual diameters and the actual cutting-edge radius were measured by using a 3D multifocal microscope Hirox RH-2000 which guarantees an accuracy of 0.8 μm. The micromachining was performed on CuNi18Zn20 samples. The alloy is characterized by brightness (i.e., the intensity of light emanating from the machined surface which depends on the final roughness), good elasticity, excellent mechanical resistance and good machinability and it finds wide applications in watchmaking industry. The experimental tests consist in the micromachining of a self-designed prototypal geometry. It is shown in Figure 2. The prototype dimension is 9 mm × 6 mm × 0.9 mm and it was manufactured in two steps:

- A rough machining to cut a block from a sheet with a thickness of 1.2 mm. A 3 mm diameter end-mill was utilized to machine the blank.
- The two-flutes 0.8 mm diameter micromill was employed to machine a 0.5 mm thickness pocket by leaving three pins. The diameters of the pins are Φ 0.6 mm, Φ 1 mm and Φ 2 mm. The same micromill was employed to machine a through-hole with a diameter equal to Φ 1 mm on the Φ 2 mm pin. The CAM set allowed to perform a normal attack to the surface of the workpiece.

(a)	**(b)**
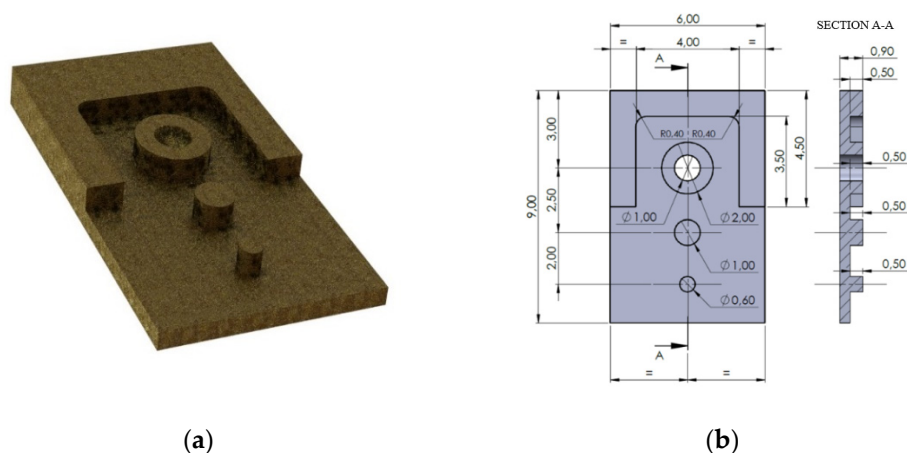
Figure 2. The micromachined prototype: (**a**) a 3D render; (**b**) the 2D dimensioned drawing.

The listed features were identified as critical parts commonly micromachined on a wristwatch caliber. The prototypes were machined 27 times by changing the depth of cut (*DOC*), the feed per tooth (f_Z) and the cutting speed (V_C) on three levels (Table 2) in a 3^3 complete factorial plan. Table 3 summarizes the values of the process parameters. Machining was performed in lubricated condition by using emulsified oil and monitoring the tool wear to ensure that is neglectable.

Table 2. List of the values of the micromilling process parameters.

Process Parameter	Value A	Value B	Value C
Depth of cut *DOC* [μm]	50	100	150
Feed per tooth f_Z [μm/rev*tooth]	5	10	15
Cutting speed V_C [m/min]	30	40	50

Table 3. List of the process parameters and production time.

Test	*DOC* [μm]	f_Z [μm/rev*t]	V_C [m/min]	Time [s]	Test	*DOC* [μm]	f_Z [μm/rev*t]	V_C [m/min]	Time [s]
1	50	5	30	686	15	150	10	30	149
2	100	5	30	326	16	100	15	30	129
3	150	5	30	283	17	50	15	40	205
4	50	10	30	359	18	100	10	40	143
5	50	5	40	521	19	150	10	40	116
6	100	5	40	265	20	100	15	40	104
7	150	5	40	215	21	50	15	50	179
8	50	10	40	280	22	100	10	50	121
9	50	5	50	433	23	150	10	50	100
10	100	5	50	216	24	100	15	50	91
11	150	5	50	175	25	150	15	30	106
12	50	10	50	238	26	150	15	40	85
13	50	15	30	255	27	150	15	50	74
14	100	10	30	183					

Micromachining was performed with the final purpose of identifying the best process parameter set, by considering the features of the machined workpiece and the constraints related to the productivity. Production time oscillates between 74 s and 686 s with an average time of 224 s. The data are collected in Table 3.

Low feed rates combined with low depths of cut determine very low productivity. Moreover, the 80% of the tests have a production time between 74 s and 283 s, which can be considered a reasonable processing time. The process parameters sets 1, 2, 4, 5, 9 can not be considering efficient, however the tests were performed in order to have a benchmark for the quality of the other machined samples.

A coordinate measuring machine, a multifocal 3D microscope and an autofocus 3D laser probe were employed to check the quality of machining on the samples. The CMM optical machine Mitutoyo Quick Scope was employed to measure the diameter and the circularity of the pins and the holes. The instrument guarantees an accuracy of 2.5 μm and each measure was repeated three times by changing the magnification. Hirox RH-2000 multifocal microscope was utilized to perform a visual inspection of the burrs and the shape of the features. The pin conicity was measured with the microscope. Lastly, in order to achieve information related to the machined surface quality, different roughness measurements were performed by means of the autofocus 3D laser probe Mitaka PF-60. In particular, the measured roughness parameters are S_a, S_{sk}, and S_{ku} that are the extension to a surface of the linear parameters R_a, R_{sk}, and R_{ku} respectively. Roughness S_a is defined as the difference in height of each point compared to the arithmetical mean of the surface, as reported in Equation (1).

$$S_a = \frac{1}{A} \iint |z(x,y)| dx \, dy \tag{1}$$

Roughness S_{sk} (skewness), reported in Equation (2), is calculated as the quotient of the mean cube value of height and the cube of the mean square deviation of the height S_q respect to the arithmetical mean of the surface

$$S_{sk} = \frac{1}{S_q^3 A} \iint z^3(x,y) dx \, dy \tag{2}$$

where S_q is (Equation (3))

$$S_q = \sqrt{\frac{1}{A} \iint |z^2(x,y)| dx \, dy}$$ (3)

Roughness S_{ku} (kurtosis), reported in Equation (4), is defined as the ratio between the mean fourth power of height and the fourth power of S_q within the sampling area.

$$S_{ku} = \frac{1}{S_q^4 A} \iint z^4(x,y) dx \, dy$$ (4)

Even if the measurements of these roughness parameters are time consuming, they represent more detailed data about the whole surface finishing. S_a furnish a global overview of the surface quality since, considering its definition, it is not significantly affected by scratches, contamination, and measurement noise. On the other hand, S_{sk} and S_{ku} values permit the assessment of the shape of valleys and peaks on the surface. In particular, S_{sk} leads to the estimation of the asymmetry of height discrepancies respect to the mean plane, being it suitable for abrasion evaluation in case of sliding surfaces. Negative values of S_{sk} suggest the surface is mainly constitute of valleys, that are useful for lubrication purposes, while positive S_{sk} values indicate that primarily peaks and asperities characterize the surface. A more detailed measure of peaks and valleys sharpness is provided by S_{ku} where, a smooth surface is individuated by a value lower than 3, while above this value the surface shows sharp asperities. The high precision along the surfaces requested to guarantee accurate contact between the component faces in horology, makes the evaluation of roughness parameters an attractive technique for quality assessment in watchmaking industry [35]. The sampling area A employed in these measurements was selected on the base of the pocket and it was equal to 1 mm × 1 mm.

3. Results

3.1. Qualitative Analysis

An initial qualitative inspection of the surface of the machined samples was accomplished employing the microscope Hirox RH-2000 with a magnification of X250. In Figure 3 the effects of the process parameters variation on the quality of three significant examples is shown (Test 1, 9 and 27).
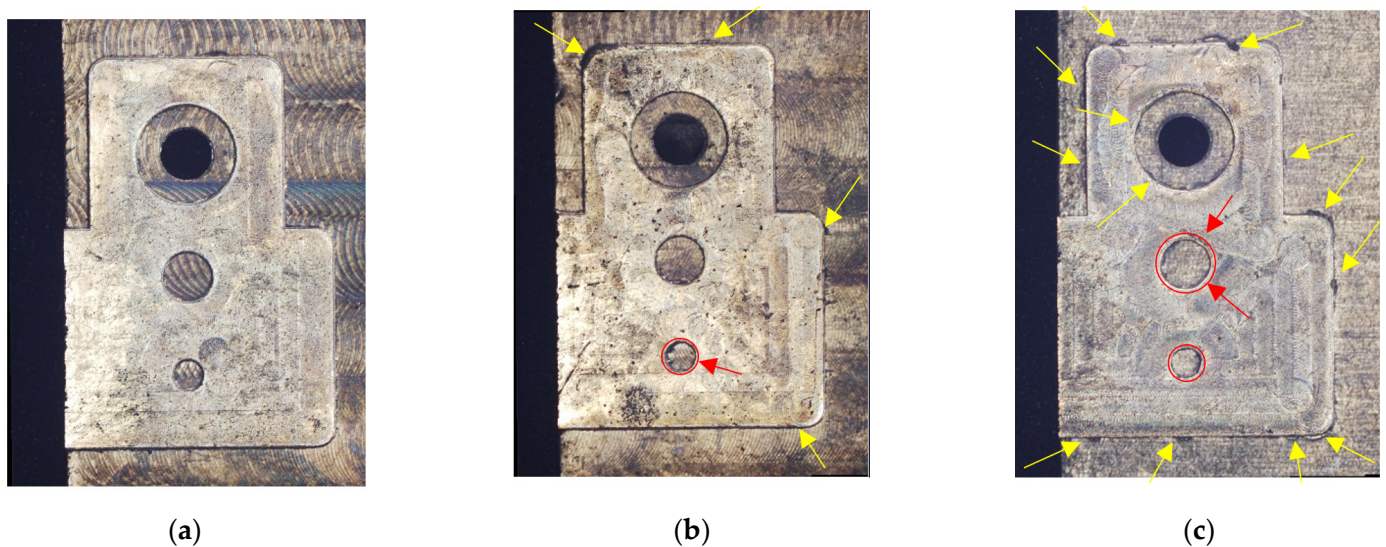

(a)   **(b)**   **(c)**

Figure 3. Quality of the machined surface for three different tests: (**a**) Test 1; (**b**) Test 9; (**c**) Test 27.

The sample in Figure 3a, namely Test 1, was obtained employing the minimum value of depth of cut, feed per tooth and cutting speed. The machined surface results to be of excellent quality since there is no burrs formation and the circularity of holes and pins is

optimal. The values of these latter, in fact, have a deviation from the nominal value that is lower than 2 µm.

In Figure 3b, the surface aspect of Test 9 is observable. This sample was milled utilizing the same depth of cut and feed per tooth, but the cutting speed was raised from 30 m/min to 50 m/min. As a consequence, more burrs are present respect to Test 1 (marked by the yellow colored arrows), but in any case, their reduced dimensions do not prejudice the mechanical coupling between parts.

The last sample in Figure 3c is related to Test 27 in which the maximum values of depth of cut, feed per tooth and cutting speed were applied. In this case, a wide diffusion of burrs with dimensions that are not negligible is present. Similar distributions of the burrs were detected in the samples of Test 25, and Test 26. The totality of these three tests were performed by employing a value of the depth of cut of 150 µm and a value of the feed per tooth of 15 µm, hence the application of the maximum value of depth of cut in conjunction with the maximum value of the feed per tooth is not suitable to answer to surface quality requirements. Moreover, the dimensions and the shape of pins and holes for Test 27 are not acceptable. In particular, the shape of the machined pin with a diameter of 0.6 mm is irregular, as marked by the red colored circles and arrows. Analogous defects were observed in the samples processed with a feed per tooth of 10 µm in conjunction with a cutting speed of 40 m/min and 50 m/min, and in the samples machined with a feed per tooth of 15 µm irrespective to the cutting speed.

Following this preliminary qualitative examination, a quantitative evaluation of the quality of the machined feature results was conducted. In order to correlate the machining parameters with the experimental measurements, analyses of variance of these latter were performed as well.

3.2. Quantitative Analysis, ANOVA and Optimization

Quantitative measurements of diameters of the three pins and of the hole, and their circularities were achieved by means of the CMM machine Mitutoyo Quick Scope, while Hirox RH-2000 microscope was employed for estimating the conicity of the pins. Amongst the realized features, the pins with a nominal diameter of 1 mm and 2 mm presented low variability and high precision, whereas the manufacture of the hole and of the smaller pin exhibited the most important criticalities.

With the aim of evaluating how the employed process parameters affect the specimen quality, an analysis of variance (ANOVA), for each measured machined feature, namely hole diameter, the smaller pin diameter, circularity, and conicity, and roughness parameters, was performed. This technique allows to understand the influence of the variation of the process parameters on material machinability as well, and it is mandatory to optimize the micromilling operation.

The hole diameter values for each test are visible in Figure 4. In this graph, the nominal and the average values of the diameter are also plotted. The average diameter is equal to 1.014 mm and, around it, considering the accuracy of ±2.5 µm of the CMM machine, upper and lower bounds were constructed. For this reason, the points that are contained in the band can be approximated with the mean value. The offset between nominal and average value is equal to 14 µm, indicating a low accuracy of the process with a percentage error of 1.4 %. On the other hand, the data are good placed inside the band, underlining high repeatability but, due to their positioning, the dependency of the hole diameter from the process parameters is not deductible. A deeper knowledge of the dependency was achieved by the related ANOVA, which results are reported in Table 4.
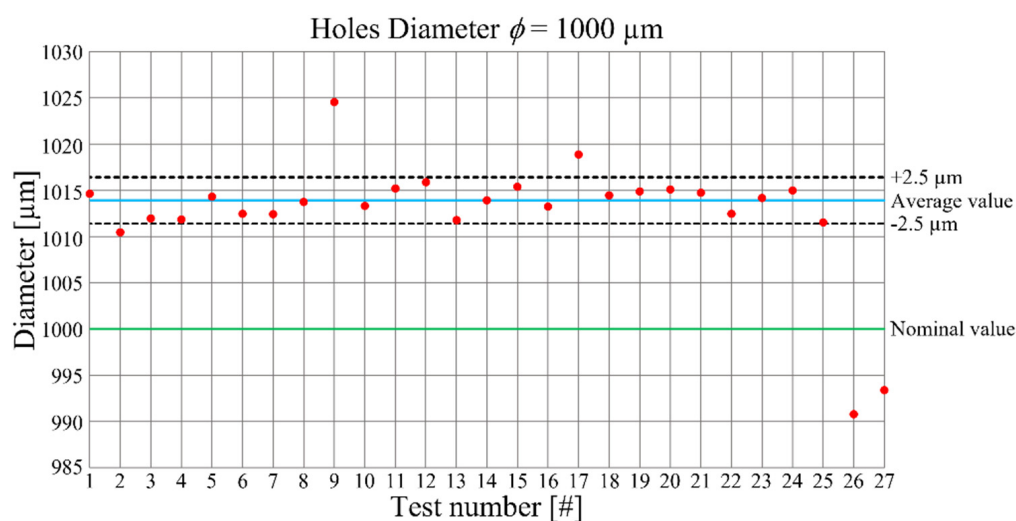
Figure 4. Hole diameters as a function of the performed tests.

Table 4. Analysis of variance of hole diameter $\varphi_H = 1.000$ mm.

Source	DoF	Seq SS	Adj SS	Adj MS	F	P
DOC	2	0.0002108	0.0002108	0.0001054	5.20	0.036
f_z	2	0.0001415	0.0001415	0.0000707	3.49	0.081
V_C	2	0.0000077	0.0000077	0.0000039	0.19	0.830
$DOC*f_z$	4	0.0003732	0.0003732	0.0000933	4.60	0.032
$DOC*V_C$	4	0.0001228	0.0001228	0.0000307	1.51	0.286
f_z*V_C	4	0.0000782	0.0000782	0.0000196	0.96	0.477
Error	8	0.0001622	0.0001622	0.0000203		
Total	26	0.0010965				

The performed ANOVA underlines that the hole diameter is mainly affect by the depth of cut and by its interaction with the feed per tooth, while the single effect of this latter is of low influence. In particular, a reduction of both depth of cut and feed per tooth leads to an increase of the hole diameter, as it is observable from the relative main effects plot in Figure 5 in which the negligible effect of the cutting speed is visible as well. The reason of this behavior is imputable to the tool run-out effect. An increase in depth of cut and feed per tooth, in fact, causes an increment of the cross-sectional area of the chip with a rise in the cutting forces. Due to the small ratio between tool diameter and tool length, in the presence of high cutting forces, the deflection of the tool axis respect to the spindle axis becomes not negligible [6], carrying out to a reduction of an internal feature as the hole diameter.

Figure 6 shows the pin diameter measurements as a function of experimental test number. The average pin diameter is equal to 0.593 mm with an offset from the nominal value of 7 μm. The value of the percentage error is 1.2% which is comparable with the one related to the hole diameter. The precision of the pins is lower than the precision of the holes.
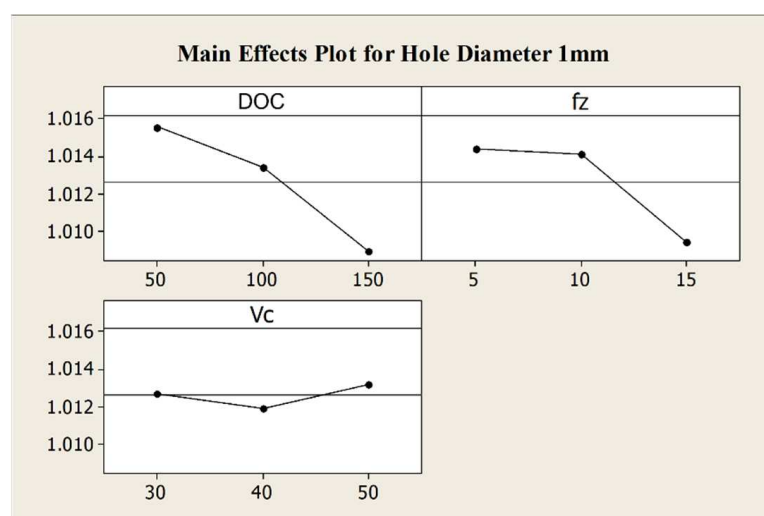
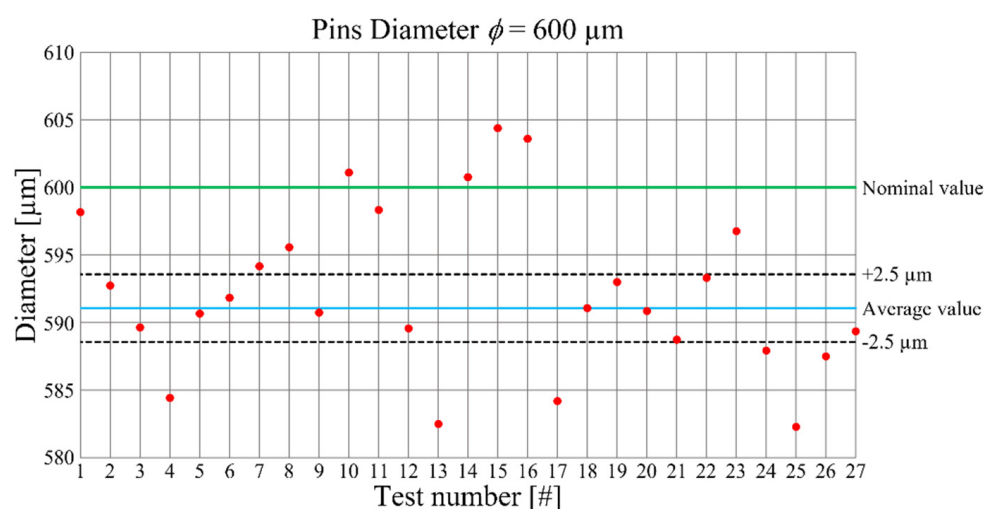**Figure 5.** Main effects plot for the hole diameter.

Figure 6. Pin diameters as a function of the performed tests.

The analysis of variance of the pin diameter (Table 5) does not show a clear dependency of if from the process parameters. For this reason, the main effects plot is not reported, and the cutting conditions must be further investigated by increasing the range of variability.

Table 5. Analysis of variance of pin diameter φ_P = 0.600 mm.

Source	DoF	Seq SS	Adj SS	Adj MS	F	P
DOC	2	0.0001344	0.0001344	0.0000672	1.56	0.269
f_z	2	0.0001940	0.0001940	0.0000970	2.24	0.168
V_C	2	0.0000248	0.0000248	0.0000124	0.29	0.758
DOC*f_z	4	0.0001173	0.0001173	0.0000293	0.68	0.626
DOC*V_C	4	0.0000915	0.0000915	0.0000229	0.53	0.718
f_z*V_C	4	0.0000344	0.0000344	0.0000086	0.20	0.932
Error	8	0.0003457	0.0003457	0.0000432		
Total	26	0.0009421				

Pin circularity is depicted in Figure 7 where a small dispersion of the experimental measurements, except the ones at higher depth of cut, feed per tooth and cutting speed, is visible, indicating an acceptable precision in the analyzed process parameters variation range.
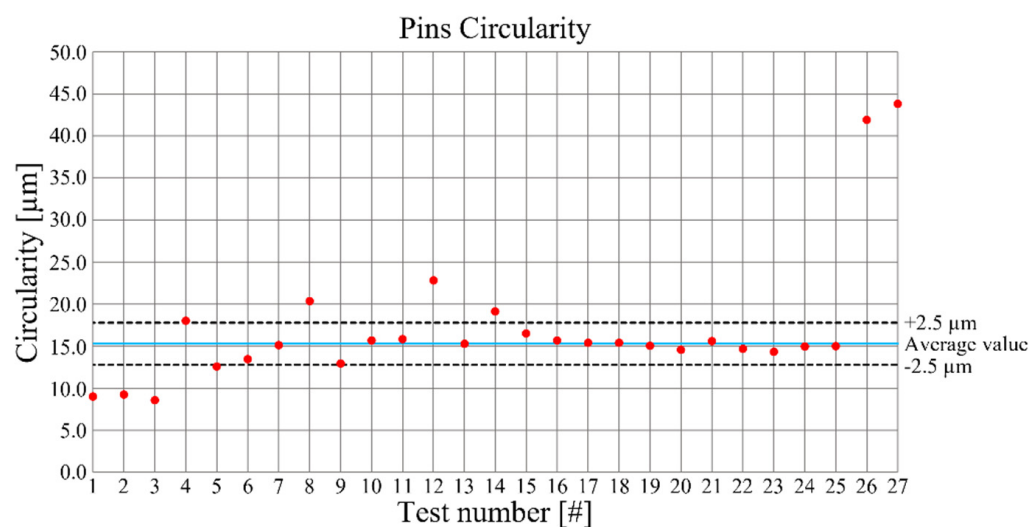
Figure 7. Pin circularities as a function of the performed tests.

As underlined by the ANOVA results in Table 6, the pin circularity is heavily affected by the feed per tooth and its interaction with the depth of cut. In particular, the main effects plot in Figure 8 shows that pin circularity increases when feed per tooth and depth of cut grow.

Table 6. Analysis of variance of pin circularity.

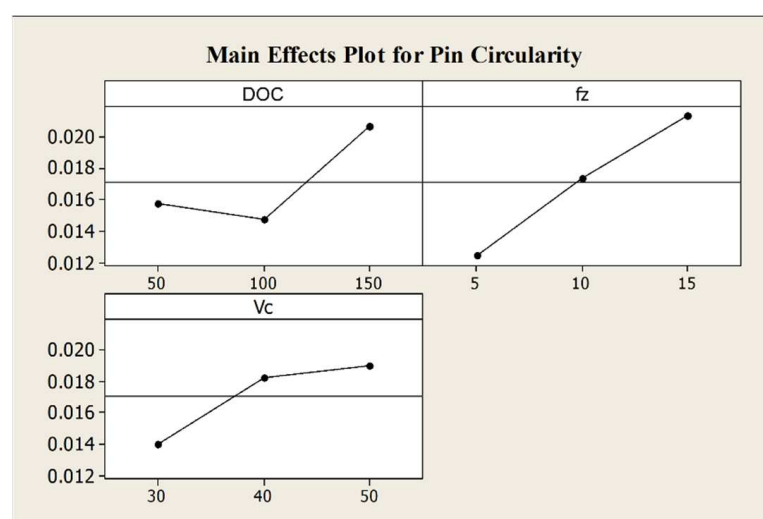| Source	DoF	Seq SS	Adj SS	Adj MS	F	P
DOC	2	0.0001792	0.0001792	0.0000896	2.84	0.117
f_z	2	0.0003530	0.0003530	0.0001765	5.59	0.030
V_C	2	0.0001263	0.0001263	0.0000631	2.00	0.198
DOC*f_z	4	0.0005390	0.0005390	0.0001347	4.26	0.039
DOC*V_C	4	0.0001299	0.0001299	0.0000325	1.03	0.449
f_z*V_C	4	0.0000988	0.0000988	0.0000247	0.78	0.568
Error	8	0.0002528	0.0002528	0.0000316		
Total	26	0.0016789				

Figure 8. Main effects plot for pin circularity.

The conicity of the pins was assessed by the evaluation of the tilt of the lateral surface in comparison to the normal direction respect to the pocket surface. The related tilt angle ranges between 0° and 0.5° for all the tests, as shown in Figure 9.
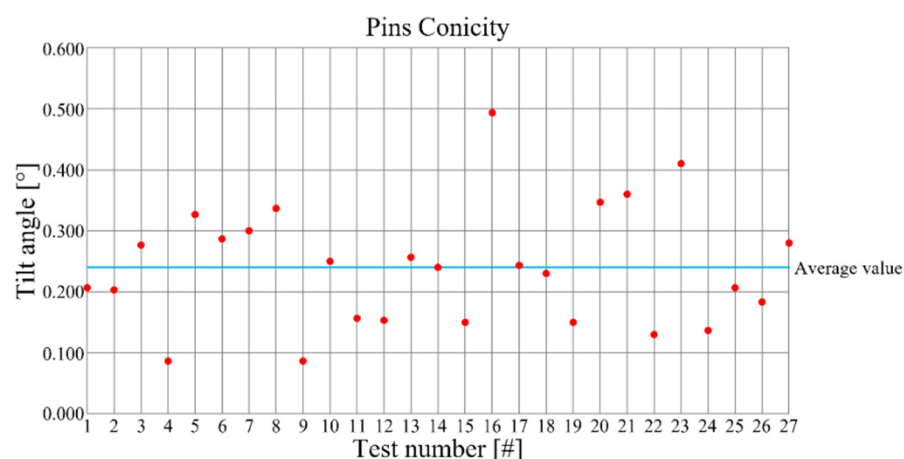
Figure 9. Pin conicities as a function of the performed tests.

　　The pin conicity does not shows any dependencies from the considered process parameters (ANOVA results in Table 7). Also in this case, the influence of cutting parameters need to be further investigated and the main effects plot is not shown. In any case, the value of the inclination angle of the lateral surface does not prejudice the mechanical coupling of pin with other parts.

Table 7. Analysis of variance of pin conicity.

Source	DoF	Seq SS	Adj SS	Adj MS	F	P
DOC	2	0.00415	0.00415	0.00208	0.16	0.852
f_z	2	0.02214	0.02214	0.01107	0.87	0.455
V_C	2	0.01105	0.01105	0.00553	0.43	0.662
$DOC*f_z$	4	0.01823	0.01823	0.00456	0.36	0.831
$DOC*V_C$	4	0.05746	0.05746	0.01437	1.13	0.407
f_z*V_C	4	0.03742	0.03742	0.00936	0.74	0.593
Error	8	0.10167	0.10167	0.01271		
Total	26	0.25214				

　　The machined surface was evaluated analyzing the roughness parameters S_a, S_{sk}, and S_{ku} that provide information about the overall quality and sharpness of the asperities.

　　All the considered roughness parameters result to be independent from the cutting speed while, varying from the specific parameter, the depth of cut and the feed per tooth have noticeable effects, as highlighted from the analysis results in Tables 8–10.

Table 8. Analysis of variance of roughness parameter S_a.

Source	DoF	Seq SS	Adj SS	Adj MS	F	P
DOC	2	0.437391	0.437391	0.218696	104.56	0.000
f_z	2	0.204669	0.204669	0.102335	48.93	0.000
V_C	2	0.001188	0.001188	0.000594	0.28	0.760
$DOC*f_z$	4	0.096272	0.096272	0.024068	11.51	0.002
$DOC*V_C$	4	0.012273	0.012273	0.003068	1.47	0.298
f_z*V_C	4	0.015411	0.015411	0.003853	1.84	0.214
Error	8	0.016732	0.016732	0.002092		
Total	26	0.783938				

Table 9. Analysis of variance of roughness parameter S_{sk}.

Source	DoF	Seq SS	Adj SS	Adj MS	F	P
DOC	2	5.64	5.64	2.82	1.60	0.261
f_z	2	11.714	11.714	5.857	3.32	0.049
V_C	2	3.945	3.945	1.972	1.12	0.374
DOC*f_z	4	2.646	2.646	0.662	0.37	0.821
DOC*V_C	4	5.827	5.827	1.457	0.82	0.545
f_z*V_C	4	2.894	2.894	0.723	0.41	0.797
Error	8	14.132	14.132	1.766		
Total	26	46.797				

Table 10. Analysis of variance of roughness parameter S_{ku}.

Source	DoF	Seq SS	Adj SS	Adj MS	F	P
DOC	2	917.7	1249	624.5	4.32	0.033
f_z	2	890.2	976.9	488.4	3.38	0.062
V_C	2	2157.5	2157.5	1078.8	1.39	0.303
DOC*f_z	4	1566.9	1566.9	391.7	0.51	0.733
DOC*V_C	4	2382.6	2382.6	595.7	0.77	0.574
f_z*V_C	4	2393.8	2393.8	598.5	0.77	0.572
Error	8	6195.3	6195.3	774.4		
Total	26	20,667.8				

More in detail, roughness S_a is heavily affected from the depth of cut, the feed per tooth, and their interaction. Moreover, as observable from main effects and interaction plot in Figure 10, the higher the aforementioned process parameters or their interaction, the higher the roughness S_a.

(**a**)

(**b**)
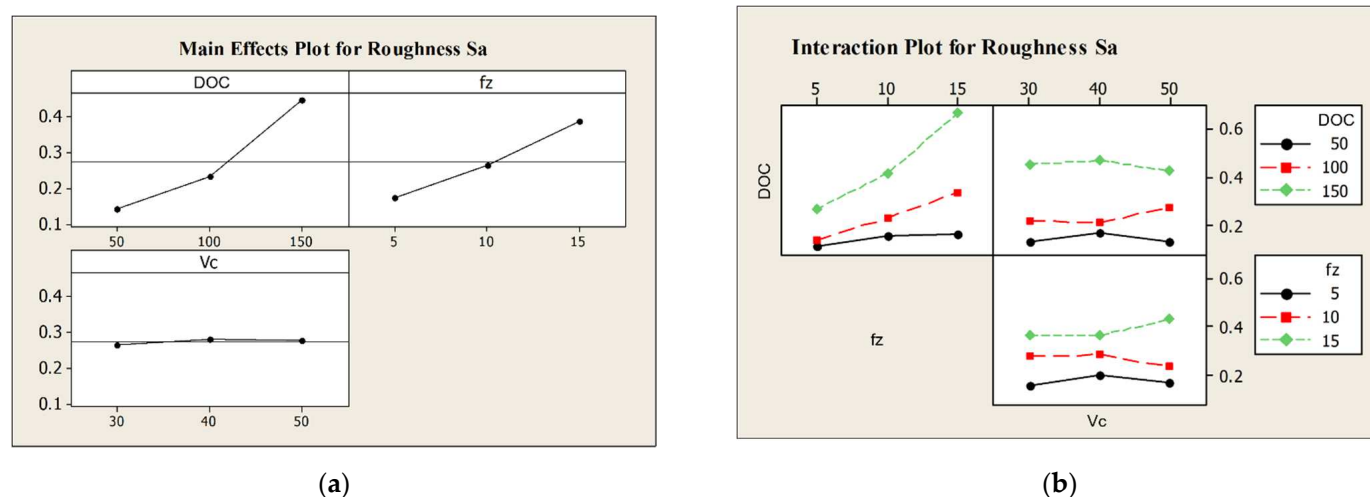
Figure 10. (**a**) Main effects plot for roughness parameter S_a; (**b**) Interaction plot for roughness parameter S_a.

The feed per tooth strongly influences the roughness S_{sk} while the depth of cut has only a marginal effect. Additionally, Figure 11 illustrates that the value of S_{sk} decreases when the feed per tooth and the depth of cut increase, meaning that with a reduction of the process parameters a surface with more asperities is expected.
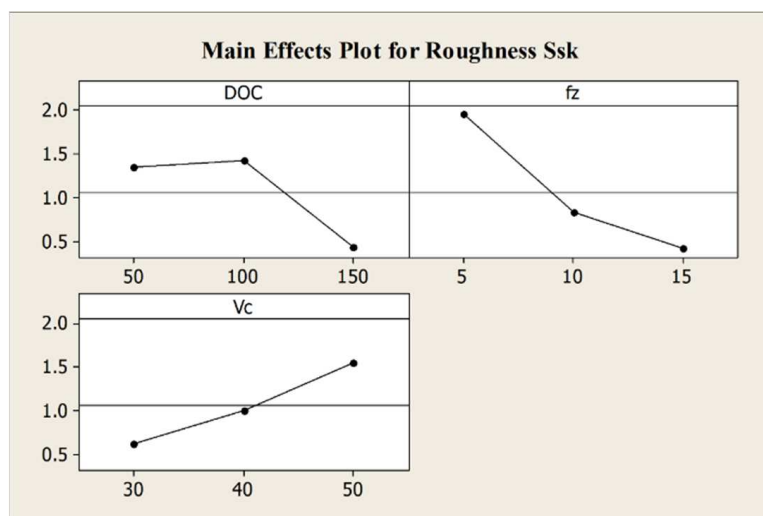
Figure 11. Main effects plot for roughness parameter S_{sk}.

The influence of depth of cut and feed per tooth is confirmed from the analysis results for S_{ku} as well, where the increase of the process parameters leads to a decrease of S_{ku} value and, as a consequence, to a smoother surface. The main effects plot for S_{ku} in Figure 12 shows this behavior.
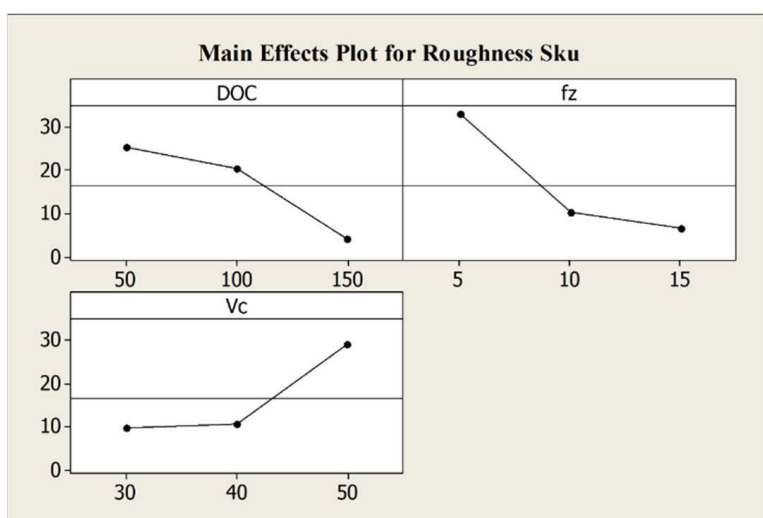

Figure 12. Main effects plot for roughness parameter S_{ku}.

The outcomes of the previously presented analyses indicates that the roughness S_a must be taken into account to perform the optimization of the process parameters set. Hole and pin diameters, in fact, have good precision and their accuracy can be managed by adjusting their offsets respect to the required nominal values. Moreover, circularity and conicity of the pins do not compromise the mechanical coupling.
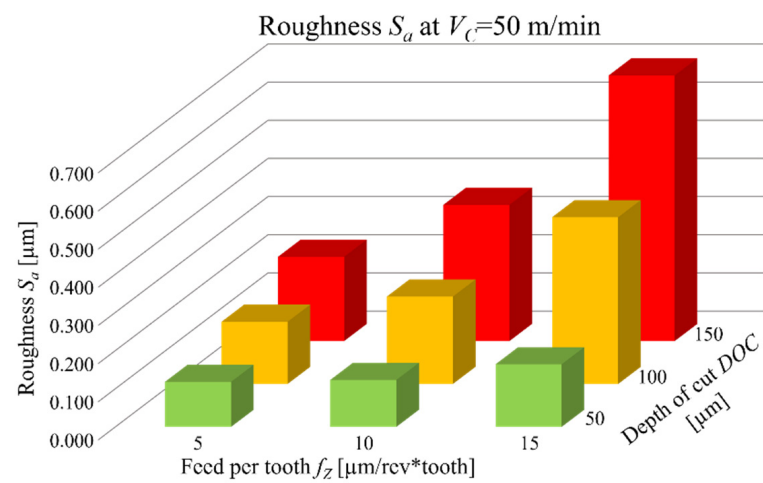
The variation of roughness S_a ranges from a minimum value of 0.111 μm to a maximum value of 0.696 μm. S_a measurements are summarized in Figure 13, where they are distributed in three graphs corresponding to the three different cutting speeds.
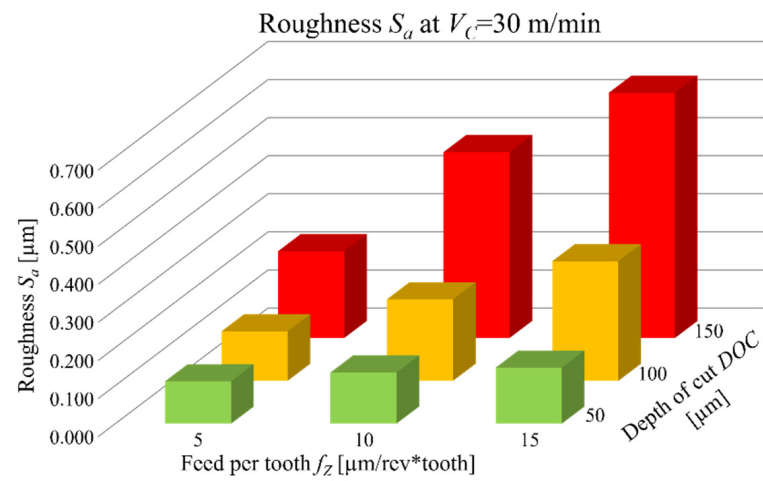
(**a**)
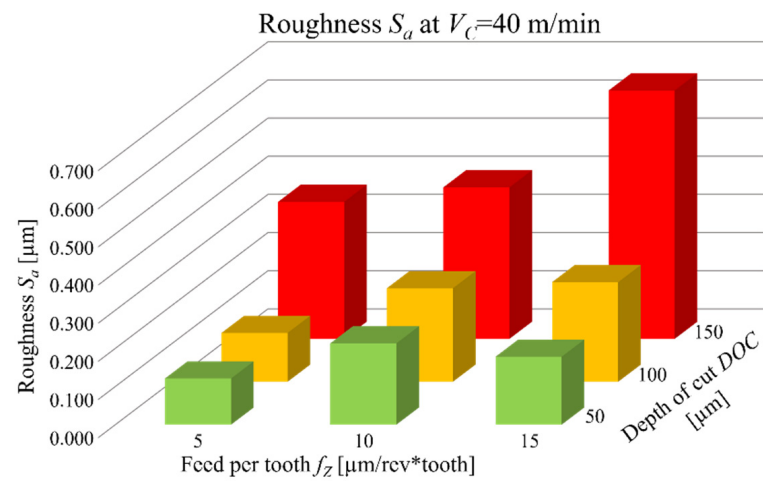
(**b**)

(**c**)

Figure 13. Roughness S_a behavior as a function of *DOC* and f_Z: (**a**) at 30 m/min; (**b**) at 40 m/min; (**c**) at 50 m/min.

As already underlined, low values of depth of cut and feed per tooth, that have the greatest influence on S_a, lead to the best surface quality, thus the lowest process parameters values should be employed to achieve high levels of finishing. On the other hand, the process optimization must warrant an acceptable production time (T_P). In Figure 14 the correlation between roughness S_a and production time for the performed tests is showed.
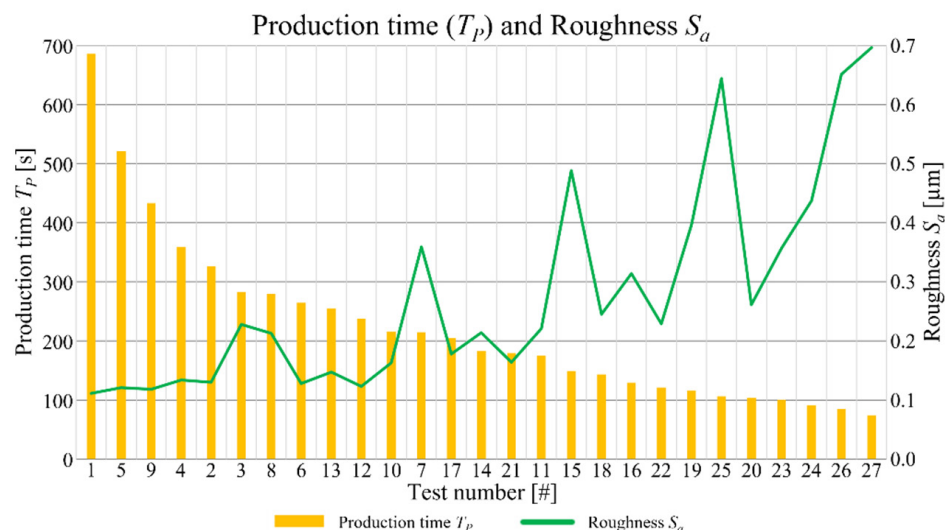
Figure 14. Production time (T_P) and roughness S_a as a function of the experimental tests.

For a better interpretation of the graph in Figure 14, the order of the experimental tests is rearranged from the one requesting the highest production time to the one requiring the lowest. The trend underlined by the graph is that reducing the production time a grow of the roughness is detected. Hence, a compromise between them is necessary, in order to optimize the process parameters selection. Tests 17, 14, and 21 individuate the best deal. Related to these tests, the roughness S_a varies between 0.164 and 0.214 µm while the production time ranges amongst 179 s and 205 s. Tests 17 and 21 were both accomplished employing the minimum value of the depth of cut (DOC = 50 µm) and the maximum value of the feed per tooth (f_Z = 15 µm) leading to a pin diameter that is far from the nominal value of 0.600 mm with, in addiction, an irregular shape. Moreover, the hole diameter for the Test 17 is outside the band of the measurement accuracy (Figure 4), meaning a loss of precision for this combination of parameters. Finally, considering the good compromise between production time and final surface roughness, and the compliance of dimensional and geometrical tolerances, the outcomes of this optimization reveals that the optimized process parameters are those of Test 14. This test is characterized by the application of central level values of both feed per tooth (f_Z = 10 µm) and depth of cut (DOC = 100 µm) at the lowest cutting speed (V_C = 30 m/min), providing a pin diameter of 600.8 + 2.5 µm, with low values of circularity (19.1 µm) and conicity (24%), a roughness S_a equal to 0.214 µm and a production time equal to 183 s. A reduction of feed per tooth and depth of cut, maintaining the lowest cutting speed, shows a better value of surface roughness than the one of Test 14, but the production times are higher than the acceptable value of 283 s. On the other hand, keeping at low cutting speed value and using the highest ones for the other parameters, leads to quick production times, but to a compromised roughness. This can be explained considering the elevated chip cross-sectional area and the related high cutting energy required. The increase of this latter, generates higher cutting temperatures, favoring a ductile chip formation, rather than a brittle one, that decreases the surface quality.

In order to validate the entire procedure of optimization, a functioning wristwatch movement was fabricated in the laboratories of the University of Brescia. A first set of main plate and bridges were machined by using the process parameters suggested by a catalogue. The result is not considerable acceptable due to several issues:

- The workpieces profiles show large burrs that compromises the mechanical coupling between the bridges and the main plates and between the machined parts and the jewels;
- Pins show bulging distortion and the cylindricity tolerance is not respected;
- Micro-holes circularity is not adequate;
- The surface roughness is elevated, and it affects the movement functionality.

The same parts were subsequently manufactured by employing the optimized process parameters, id est a depth of cut DOC = 100 μm, a feed per tooth f_Z = 10 μm, and a cutting speed V_C = 30 m/min, were tested by the machining of a new main plate and bridges. The quality of results considerably increases as visible in Figures 15 and 16. The new pins on the movement do not exhibit bulging effects and reveals good circularity (Figure 15a). This latter is excellent for the new radial holes as well (Figure 15b). The burrs observable in the original main plate are totally absent in the new configuration, and the regularity of the holes guarantees the correct jewels assembly (Figure 16).
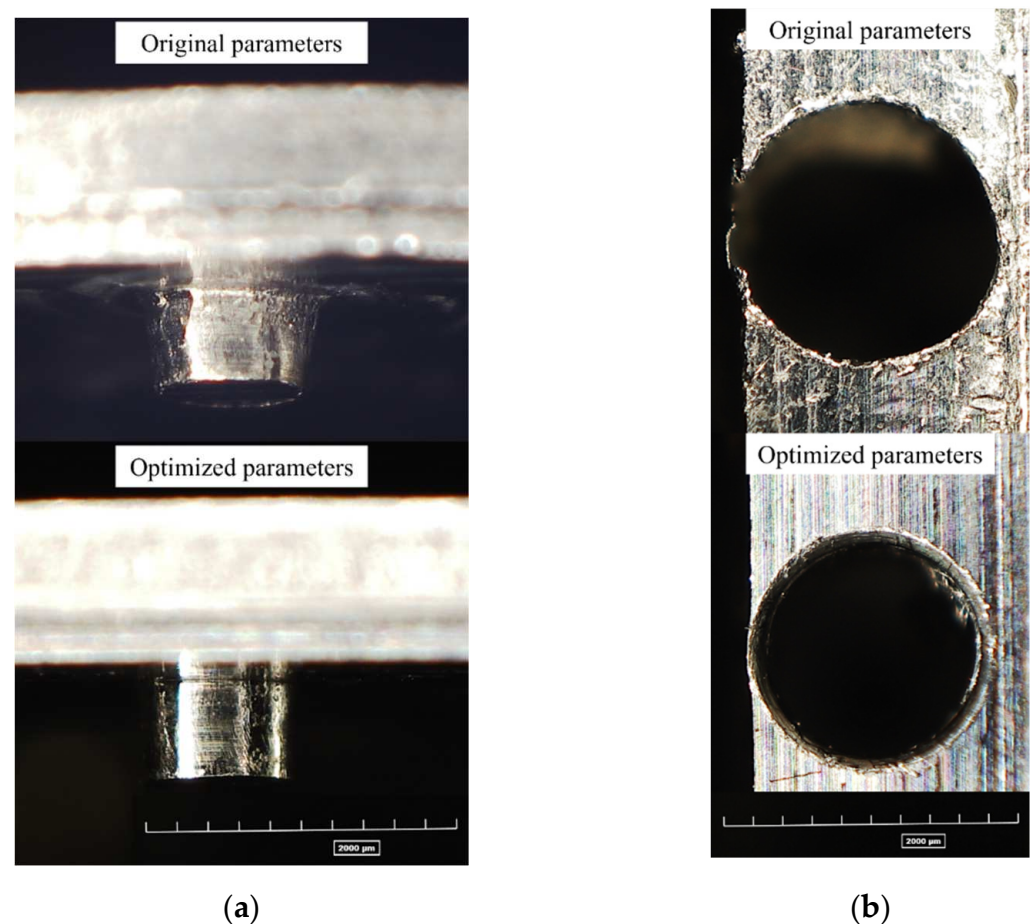

(**a**) (**b**)

Figure 15. Results comparison between original and optimized process parameters for: (**a**) pin conicity; (**b**) hole diameter and circularity.

The quality characteristics of the realized features resulted to be improved by the application of the optimized process parameters respect to the ones suggested by the tool catalogue, revealing the functionality of the proposed optimization method. For completeness, it is important to underline that the tool geometry employed in the experimental campaign is unique, and the variability window of the process parameters is ascribable to finishing operations. Hence, in the case of a different tool geometry, and operation, such as roughing, the employment of the identified optimized parameters should not be applicable. Due to the prominent nature of size and surface effects in micromachining, the modification of ratio between uncut chip thickness and tool edge radius alters the chip

formation mechanism, varying CuNi18Zn20 machinability. In order to select the most suitable process parameters, when machining setup differs from the one employed in this work, this behavior must be considered.

Figure 16. Comparison between the features machined with: (**a**) original process parameters; (**b**) optimized process parameters.

4. Conclusions

The paper described an experimental approach to a problem of optimization of cutting process parameters in a complex micro-machining case. As results of the experimental campaign of 27 prototypes machining, it was evidenced that the employment of the highest depth of cut and feed per tooth induced to excessive burrs distribution. Moreover, the final geometry showed irregularities in the tests with $f_Z = 10$ μm combined with $V_C = 40$–50 m/min, and $f_Z = 15$ μm unrelatedly the cutting speed. A critical size for the machining of microfeatures was individuated as 1 mm. The features in submillimeter dimensional scale requires machining with low feed rates and low cutting speeds.

The conicity of pins does not result a critical tolerance while a lack of accuracy emerged about the offset between the nominal and the effective diameters of pins and holes. The size of the deviation does not depend on the process parameters and it is equal to the 1.5% of the nominal diameter. A possible cause is the micro mill run-out due to the evidence that the holes show higher then expected diameters. Vice versa, the pins have lower then expected diameters due to tool eccentricity. A strong correlation between roughness and depth of cut emerged by the data analysis. The trend is not commonly reported in conventional scale machining. The chatter vibrations were identified as a possible explanation of this scale effect. The depth of cut increasement implicates higher cutting forces which can determines the vibrations of the workpiece. The roughness resulted directly correlated also to the feed rate.

References

1. Su, S.; Du, R. Signature analysis of mechanical watch movements. *Mech. Syst. Signal Process.* **2007**, *21*, 3189–3200. [CrossRef]
2. Gherman, L.; Gleadall, A.; Bakker, O.; Ratchev, S. Manufacturing Technology: Micro-machining. In *Micro-Manufacturing Technologies and Their Applications*; Fassi, I., Shipley, D., Eds.; Springer Tracts in Mechanical Engineering; Springer: Cham, Switzerland, 2017; pp. 97–127.
3. Mijušković, G.; Cica, D. Investigation, modeling, and optimization of surface roughness in micro-milling of graphite electrodes. *Int. J. Adv. Manuf. Technol.* **2021**, *117*, 579–590. [CrossRef]
4. Schorderet, A.; Herzog, R.; Jacquod, N.; Marchand, Y.; Prongué, C. Productivity Increase of High Precision Micro-Milling by Trajectory Optimization. In Proceedings of the HSM 15th International Conference on High Speed Machining, Prague, Czech Republic, 8–9 October 2019.
5. Zhang, X.; Yu, T.; Dai, Y.; Qu, S.; Zhao, J. Energy consumption considering tool wear and optimization of cutting parameters in micro milling process. *Int. J. Mech. Sci.* **2020**, *178*, 105628. [CrossRef]
6. Attanasio, A. Tool Run-Out Measurement in Micro Milling. *Micromachines* **2017**, *8*, 221. [CrossRef] [PubMed]
7. O'Toole, L.; Kang, C.W.; Fang, F.Z. Precision micro-milling process: State of the art. *Adv. Manuf.* **2021**, *9*, 173–205. [CrossRef]
8. Huo, D.; Chen, W.; Teng, X.; Lin, C.; Yang, K. Modeling the Influence of Tool Deflection on Cutting Force and Surface Generation in Micro-Milling. *Micromachines* **2017**, *8*, 188. [CrossRef]
9. Zhou, M.; Chen, Y.; Zhang, G. Force prediction and cutting-parameter optimization in micro-milling Al7075-T6 based on response surface method. *Micromachines* **2020**, *11*, 766. [CrossRef]
10. Simoneau, A.; Ng, E.; Elbestawi, M.A. Grain Size and Orientation Effects When Microcutting AISI 1045 Steel. *CIRP Ann.* **2007**, *56*, 57–60. [CrossRef]
11. Wu, X.; Li, L.; He, N.; Yao, C.; Zhao, M. Influence of the cutting edge radius and the material grain size on the cutting force in micro cutting. *Precis. Eng.* **2016**, *45*, 359–364. [CrossRef]
12. Abeni, A.; Loda, D.; Özel, T.; Attanasio, A. Analytical force modelling for micro milling additively fabricated Inconel 625. *Prod. Eng.* **2020**, *14*, 613–627. [CrossRef]
13. Shi, Z.; Li, Y.; Liu, Z.; Yang, Q. Determination of minimum uncut chip thickness during micro-end milling Inconel 718 with acoustic emission signals and FEM simulation. *Int. J. Adv. Manuf. Technol.* **2018**, *98*, 37–45. [CrossRef]
14. Przestacki, D.; Chwalczuk, T.; Wojciechowski, S. The study on minimum uncut chip thickness and cutting forces during laser-assisted turning of WC/NiCr clad layers. *Int. J. Adv. Manuf. Technol.* **2017**, *91*, 3887–3898. [CrossRef]
15. Lee, Y.J.; Wang, H. Current understanding of surface effects in microcutting. *Mater. Des.* **2020**, *192*, 108688. [CrossRef]
16. Nix, W.D.; Gao, H. Indentation size effects in crystalline materials: A law for strain gradient plasticity. *J. Mech. Phys. Solids* **1998**, *46*, 411–425. [CrossRef]
17. Durst, K.; Backes, B.; Göken, M. Indentation size effect in metallic materials: Correcting for the size of the plastic zone. *Scr. Mater.* **2005**, *52*, 1093–1097. [CrossRef]
18. Chen, Y.; Wang, T.; Zhang, G. Research on parameter optimization of micro-milling Al7075 based on edge-size-effect. *Micromachines* **2020**, *11*, 197. [CrossRef] [PubMed]
19. Wu, X.; Du, M.; Shen, J.; Jiang, F.; Li, Y.; Liu, L. Experimental research on the top burr formation in micro milling. *Int. J. Adv. Manuf. Technol.* **2021**, 1–10. [CrossRef]
20. Aurich, J.C.; Bohley, M.; Reichenbach, I.G.; Kirsch, B. Surface quality in micro milling: Influences of spindle and cutting parameters. *CIRP Ann.* **2017**, *66*, 101–104. [CrossRef]
21. Chen, N.; Zhang, X.; Wu, J.; Wu, Y.; Li, L.; He, N. Suppressing the burr of high aspect ratio structure by optimizing the cutting parameters in the micro-milling process. *Int. J. Adv. Manuf. Technol.* **2020**, *111*, 985–997. [CrossRef]
22. Abeni, A.; Ginestra, P.S.; Attanasio, A. Micro-milling of Selective Laser Melted Stainless Steel. In *Selected Topics in Manufacturing*; Ceretti, E., Tolio, T., Eds.; Lectures Notes in Mechanical Engineering; Springer: Cham, Switzerland, 2021; pp. 1–12.
23. Lu, X.H.; Jia, Z.Y.; Wang, H.; Feng, Y.X.; Liang, S.Y. The effect of cutting parameters on micro-hardness and the prediction of Vickers hardness based on a response surface methodology for micro-milling Inconel 718. *Measurement* **2019**, *140*, 56–62. [CrossRef]
24. Hajiahmadi, S. Burr size investigation in micro milling of stainless steel 316L. *Int. J. Light. Mater. Manuf.* **2019**, *2*, 296–304. [CrossRef]
25. Aslantas, K.; Ekici, E.; Çiçek, A. Optimization of process parameters for micro milling of Ti-6Al-4V alloy using Taguchi-based gray relational analysis. *Measurement* **2018**, *128*, 419–427. [CrossRef]
26. Isler, P. Watches: Mechanical materials. In *Encyclopedia of Materials: Science and Technology*, 2nd ed.; Buschow, K.H.J., Cahn, R.W., Flemings, M.C., Ilschner, B., Kramer, E.J., Mahajan, S., Veyssière, P., Eds.; Elsevier: Amsterdam, The Netherlands, 2003; pp. 1–17.
27. Johansson, J.; Persson, H.; Ståhl, J.E.; Zhou, J.M.; Bushlya, V.; Schultheiss, F. Machinability Evaluation of Low-Lead Brass Alloys. *Procedia Manuf.* **2019**, *38*, 1723–1730. [CrossRef]
28. Nobel, C.; Klocke, F.; Lung, D.; Wolf, S. Machinability Enhancement of Lead-Free Brass Alloys. *Procedia CIRP* **2014**, *14*, 95–100. [CrossRef]
29. Zoghipour, N.; Tascioglu, E.; Atay, G.; Kaynak, Y. Machining-induced surface integrity of holes drilled in lead-free brass alloy. *Procedia CIRP* **2020**, *87*, 148–152. [CrossRef]

30. Sun, Z.; To, S. Effect of Machining Parameters and Tool Wear on Surface Uniformity in Micro-Milling. *Micromachines* **2018**, *9*, 268. [CrossRef] [PubMed]
31. Muhammad, A.; Gupta, M.K.; Mikołajczyk, T.; Pimenov, D.Y.; Giasin, K. Effect of Tool Coating and Cutting Parameters on Surface Roughness and Burr Formation during Micromilling of Inconel 718. *Metals* **2021**, *11*, 167. [CrossRef]
32. Chen, Z.; Wu, X.; Zeng, K.; Shen, J.; Jiang, F.; Liu, Z.; Luo, W. Investigation on the Exit Burr Formation in Micro Milling. *Micromachines* **2021**, *12*, 952. [CrossRef]
33. D'Urso, G.; Giardini, C.; Quarto, M. Characterization of surfaces obtained by micro-EDM milling on steel and ceramic components. *Int. J. Adv. Manuf. Technol.* **2018**, *97*, 2077–2085. [CrossRef]
34. Abeni, A.; Lancini, M.; Attanasio, A. Characterization of machine tools and measurement system for micromilling. *Nanotechnol. Precis. Eng.* **2019**, *2*, 23–28. [CrossRef]
35. Serje, D.; Pacheco, J.; Diez, E. Micromilling research: Current trends and future prospects. *Int. J. Adv. Manuf. Technol.* **2020**, *111*, 1889–1916. [CrossRef]